GUIDED SELF-ASSEMBLY OF MONOLAYER PROTECTED NANOCLUSTERS ON FUNCTIONALIZED SURFACES

A THESIS
SUBMITTED TO THE
UNIVERISTY OF PUNE
FOR THE DEGREE OF
DOCTOR OF PHILOSOPHY
IN
PHYSICS

BY
MOHAMMED ASLAM

Physical and Materials Chemistry Division
National Chemical Laboratory
Pune – 411 008

July 2002

DEDICATED
TO
O'BA AND AMMA

DECLARATION

I hereby declare that the thesis entitled "**Guided Self-assembly of Monolayer Protected Nanoclusters on Functionalized Surfaces**" submitted for Ph.D. degree to the University of Pune has been carried out at National Chemical Laboratory, under the supervision of Dr. K. Vijayamohanan. The work is original and has not been submitted in part or full by me for any degree or diploma to this or any other University.

Date: 26/07/2002 **(Mohammed Aslam)**

Physical & Materials Chemistry Division
National Chemical Laboratory
Pune – 411 008

NCL

Dr. K. Vijayamohanan

Scientist

Physical & Materials Chemistry Division

National Chemical Laboratory

Pune – 411008, INDIA

Tel: 91-020-5893300 Extn: 2270

Res: 91-020-5893307

Fax: 91-020-5893044

Email: viji@ems.ncl.res.in

CERTIFICATE

This is to certify that the work incorporated in the thesis "**Guided Self-assembly of Monolayer Protected Nanoclusters on Functionalized Surfaces**" submitted by Mohammed Aslam was carried out by him under my supervision at National Chemical Laboratory, Pune. All the materials from other sources have been duly acknowledged in the thesis.

Date: 26/07/2002

(K. Vijayamohanan)
Research Guide

ACKNOWLEDGEMENT

This Doctoral thesis means much more to me, a Himalayan dream of my *late* father (O'Ba) coming true. This is not just the words in these pages but each word acknowledges my deep gratitude to all those who played a pivotal role in the same and without whom this thesis would not have been possible.

Dr. K. Vijayamohanan has been more than a guide to me, a huge green shadowy tree. He is the only person responsible for introducing me to the fascinating world of SAMs and nanoparticle assemblies. Thank you so much Sir for being there with all these words of encouragement, inspiration, wisdom and optimism that always helped me to see the bright side of things. You kept me going when my faith was faltering. Another person whom I must thank is **Dr. I.S. Mulla**, for all his help and also being kind and considerate throughout. Thank you Sir for being always on my side. I can never forget the kind help of Dr. P. Ganguly, *Former HOD Physical Chemistry Division*, who supported me in my worst time. I must salute him for his timely help. The co-operation and help from Dr. S.K. Date, Head Physical Chemistry Division is also gratefully acknowledged.

I also thank the Director, NCL for providing me the infrastructured facilities and the CSIR for financial support. My heartful gratitude to Drs. Murali Sastry, T. Pradeep, Srinivasan, K. Sridhar, P.A. Joy, S.D. Sathey, K.R. Patil, and Anil Kumar for their encouragement and help. Most helpful during my doctoral work were Dr. Sainkar, Dr. Mandale, Rajesh, Dr. Mohan Bhadbhade and Mrs. Iyer. I thank you all. Help from Punekar and Koshy is gratefully acknowledged.

I can never forget the working atmosphere of our Lab. (*Nanogroup*!), thanks to my seniors Drs. Varsha, Krishanu, Sudrik and Sushama for their help and teaching professional research style to me. Thanks to all my Labmates, Trupti, Nirmalya, Jadab, Gopu, Niranjan, Girish, Deepali, Pradeep who created a pleasant atmosphere to work.. Yes, I know, the same is said in every thesis, but it just happens to be true. I can never forget "Sat. Seminars", "Weekly reports", "Daily plans" and late night experiments with music and the marathon efforts to capture "the Only computer".

My sincere thanks to my in-law parents, my brothers Shafeeque, Saleem, my brothers-in-law Iqbal, Anees, and especially my mother who have always stood beside me.

Finally, a grateful thanks to *Shagufta* without whose support this would have never been possible. She is the person who supported me in each and every respect during this work.

The value of this thesis remains to be judged by those who read it. At least for me personally, working has been a rewarding experience.

(M. Aslam)

CONTENTS

CHAPTER – 1

Guided Assembly, Properties, and Applications of Organized Nanoclusters on Self-assembled Monolayers*

This chapter presents a critical review of the preparation and characterization of monolayer-protected nanoclusters and their different methods of organization on various substrates. Different features of the self-assembly of organized nanoparticles on suitable supports are investigated to harness their potential applications in molecular electronics. The objectives of the present study and the overall organization of the present investigation are mentioned in the end.

* A part of this chapter has been published in **Appl. Biochem. Biotech.** *96 (1-3)*, 25-39 (2001) and another part in **Proceedings of Chem. Sci.** *113(5/6)*, 659-670 (2001).

1. INTRODUCTION

The emergence of nanotechnology as a unique and powerful interdisciplinary research activity during this decade has clearly seen the realization of the Feynman's prophecy (*there's plenty of room at the bottom, 1959*)[1] through the collective effort of physicists, chemists, biologists and electronic engineers leading to several cutting edge applications affecting our day-to-day life. For example, several nanoparticle-based applications such as solar cells, controlled drug-delivery systems, selective molecular sensing, light emitting diodes, single electron transistors and memory devices etc. have been demonstrated in the recent past using different types of advanced materials.[2,3] The functional parts of many of these devices contain organized hybrid materials with artificially created characteristic dimensions, less than about 200 nm. More significantly, as conventional lithography starts reaching its fundamental limit, new post-lithographic techniques like nanopatterning with high resolution have been realized by few groups using dip-pen nanolithography, soft lithography etc.[3a,e] which allow inexpensive computer systems with mole quantities of logic elements that are molecular in both size and precision but interconnected in complex and highly specific patterns.

One of the preeminent areas of nanotechnology where a great deal of research on new materials occurs is the controlled assembly of nanoparticles in two and three-dimensions (2D and 3D) using molecular interconnects.[2-8] These organized architectures have attracted extensive attention in diverse fields due to their fundamental and technological implications, despite challenges involved in the organization of ordered arrays of nm size particles also known as quantum dots.[4-8] The characteristic features of such nanoscale architectures include size and shape dependent quantum effects due to low dimensionality, collective behavior due to the control of interparticle distance and the directional electron transfer arising from the controllable multifunctional nature of organic interconnects, all contributing to the unique behavior which is vastly

different from that of either the single molecule or the bulk phase.[9] The interest also arises due to the unusual physicochemical properties of nanoparticles arising primarily due to the confinement of electrons within particles of dimensions smaller than the bulk electron delocalization length i.e., quantum confinement.[10]

As a part of the drive towards miniaturization, several methodologies have been developed recently for constructing ordered assemblies of nanoparticles.[2a,b,4-6,8] One general strategy utilizes a bifunctional ligand, where a self-assembled monolayer is formed with one end adsorbed on the substrate while the other is used to anchor size selective nanoparticles. For naked colloidal particles prepared instantaneously, this type of sequential anchoring mechanism is rather efficient, especially if electrostatic or adsorptive interactions are utilized.[5-8] Also, for monolayer-protected nanoclusters (MPCs) there has been very limited success so far probably due to the steric hindrance that renders the process very tedious and technologically challenging. Although mixed monolayers can create controlled amount of disorder in these systems, polydispersity in size and charge on clusters can cause defects and competing tunneling pathways which may alleviate the enhancement of the optical/electronic response. The extent of disorder possible in such self-assemblies implies limitations for applications where, the spontaneous organization of molecules, molecular clusters and aggregate structures can adversely affect the performance.

Since self-assembly techniques can offer the potential to fabricate nanoscale elements without the direct use of conventional lithographic techniques, it naturally becomes inexpensive and faster to create nanoscale features. Nevertheless, the practical realization of electronic circuits of reasonable functionality and complexity using this methodology will need the ability to controllably break the symmetry typically found in self-assembled networks so that nanometer-size building blocks can be assembled into specific

device configurations. Towards the goal of a self-assembly technique which can be used to realize robust electronic devices and circuits, we have demonstrated the fabrication of highly ordered nanoscale arrays using a guided self-assembly technique on a self-assembled monolayer (SAM) functionalized metal surface. Specifically, we have developed a process that allows high-quality close-packed arrays of Au MPCs (5 nm in diameter) to be formed on hydrophobic Au substrates. The local ordering at the nanometer scale is provided by a chemically driven self-assembly process, while the arbitrary global pattern is defined by the patterned template.

1.2. SELF-ASSEMBLED MONOLAYERS (SAM)

The term 'self-assembly' involves the arrangement of atoms, molecules or even aggregates of molecules into ordered functional entities without the intervention of mankind towards an energetically stable form.[11] For example, the spontaneous formation of a monolayer of alkanethiol molecule on a smooth gold surface often denoted as 2D self-assembled monolayer (2D SAM) is induced by strong chemisorption between the head group of selected organic molecules and the substrate. They have been recently utilized for studying the phenomena like distance-dependent electron transfer[12], the mechanism of single electron transistor[13] and the observation of molecular events like Coulomb staircase.[14] More significantly, the strong interchain interaction ensures tight packing and stability of the monolayers leading to several applications including chemical sensing,[15] control of surface properties such as wettability and friction,[16] corrosion protection,[17] patterning,[18] semiconductor surface passivation[19] and optical second harmonic generation.[20] In addition, similarity of these ultrathin films with lipid bilayer membranes have encouraged the application of these 2D structures as model systems to investigate a host of biological processes such as bioenergetics of photosynthesis and protein adsorption.[21]

Transfer of a well-packed monolayer from aqueous solution surface (air/water interface) to solid substrate - LB Method[22] - involves cumbersome equipment and time consuming procedures while no such special film balance or procedure is required for self-assembly; indeed the method has been sarcastically referred by some as "molecular beaker epitaxy".[23] Appropriately selected head groups (--SH for the case of alkane thiols) are held together by strong attraction (chemisorption or nearly covalent bond formation involving ~ 60 kcal/mol) of a selectively functionalized substrate surface enabling the ordering of methylene chains due to van der Waals interactions. The outer methyl group of the hydrocarbon tail causes hydrophobicity of SAM and hence contact angle measurements with water can be used to probe SAM formation.[24] SAM formed in this manner are long lasting and stable since the compact nature prevents solvent or impurity penetration. In contrast, LB films are less stable due to non-equilibrium preparation and also because they are maintained mainly by only van der Waal's interactions; some imperfections (pin holes or large defects due to substrate heterogeneity) remain in both films due to impurities and boundaries between domains of the substrate and film forming materials.

Like thiol groups, long chain carboxylic acids also form SAM on glass, alumina and silver oxide surfaces, and the time required to form a complete monolayer increases with decreasing concentration; in comparison, higher concentration is needed for glass than for alumina (0.002 vs 0.0002 M). During SAM formation of carboxylic acids on silver oxide surface, the two oxygen of carboxylates bind to the surface nearly symmetrically with a chain tilt angle from the surface normal of 15-25^{o}.[25] In contrast, on CuO and Al_2O_3 surfaces, the carboxylate group links asymmetrically with nearly zero tilt angle. In all the cases, procedures are easy, economical, and avoid complexities like reorganization upon transfer in the case of LB films. Non-adsorbed molecules are removed by copious rinsing from the solvent used to get a defect free SAM as shown in Figure 1.1. During the last 15 years, most of the important aspects

of SAM formation like kinetics, mechanism, steric effects on packing and applications even in fields like tribology, adhesion, biology and microelectronics[21,26-28] have been studied extensively and several excellent reviews are available.[24,29,30]

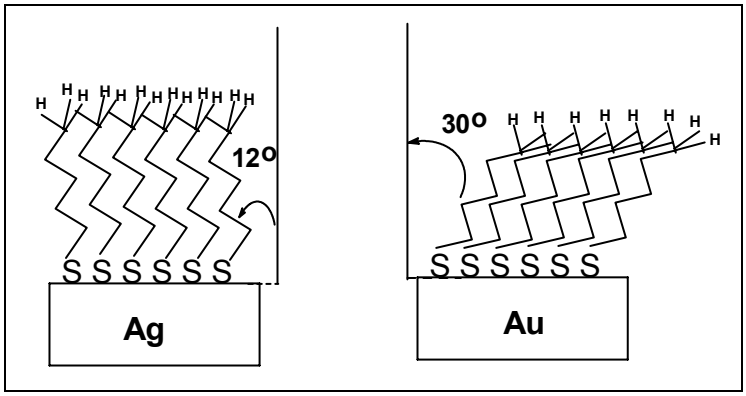

Figure 1.1 Schematic representation of the SAM formation of alkanethiol on Gold and Silver surfaces indicating tilt angles 30° and 12°, respectively. The angles are drawn with respect to the surface normal.

1.2.1 Structure and Bonding

Due to the exciting potential applications of SAMs a comprehensive picture has emerged about the structure and bonding of SAMs especially on Au (111) surface. Substrate-headgroup bonding, interaction between alkyl chains and the orientation of the tail group are three main parameters of control during SAM formation. Although the nature of bonding may be purely covalent, polar or ionic depending on the specific headgroup-substrate interaction, apparent pinning of the headgroup is caused by strong chemisorption energy (~60 kcal/mole) on the substrate surface. Once these molecules are there on the surface, the close packing starts via the interchain van der Waal's interaction (<10 kcal/mol) and this could be controlled by the length of the methylene chain. Terminal functionalities can be a wide range of groups such as –OH, -CN, -COOH, $-NH_2$ etc. or a simple $-CH_3$ tail group.

More important results about the structure of SAM can be obtained by diffraction and microscopic techniques including STM, AFM and He

diffraction.[31] Electron diffraction[32-33] of alkane thiolates on Au (111) shows hexagonal symmetry of S atoms with S--S spacing of 4.97 Å and a calculated area per molecule of 21.4 $Å^2$ while He diffraction and AFM results unravel a $\sqrt{3}X\sqrt{3}$ $R30^o$ over-layer structure.[34-35] Recent He diffraction however shows evidence of a rectangular primitive unit mesh with dimensions of 8.68 x 10.02 Å containing four chains equivalent to a c (4x2) superlattice as confirmed by STM.[36-37]

One of the salient features of above picture is the possibility of limited mobility of the molecules causing surface atom rearrangement. STM studies confirm that island structure formed during SAM formation by alkanethiol on gold surface exhibit macroscopic shape changes over a period of minutes and it has been concluded that these shape changes are associated with mobile defects in the gold surface making Au-S bond labile.[38] Migration of thiolates between neighbouring hollow sites is required to remove defects from the organization. Actually, migration can be possible through the on-top or the bridge sites. It is possible that the thiolate which is chemically bonded to the on-top site (neutral gold-thiolate molecule) can move to a hollow site leaving a defect and STM studies suggest that some pinholes in the monolayer can be observed following this mechanism.[39] These pinholes are shown to disappear with annealing of the monolayers at 373 K.[39,40] The extent of Au coverage by SAM due to pinholes and other defects can be conveniently investigated by measuring the faradaic response of the [$Fe(CN_6)^{3-}$/ $Fe(CN_6)^{4-}$] redox couple in aqueous solution by cyclic voltammetry employing SAM coated substrate as working electrode. The cathodic and anodic peak currents at the electrode are completely suppressed due to the presence of defect free SAM.[41] Although several other techniques are available to study the mechanism and kinetics of SAMs, more efforts are focused recently to design multifunctional molecules with tailored electrical and optical properties[42] so that unique hierarchical nanostructures can be designed.

1.2.2 Monofunctional vs. Bifunctional Molecules

Among the broad spectrum of substrates and functional groups used for the SAM formation, long chain alkanethiols and disulfides on gold are the most widely studied and well-characterized systems.[24,29] Although ω-terminated alkanethiol derivatives have been extensively investigated, the formation of monolayer is also possible with disulfides, diselenides and sulfur containing π-systems etc.[43] In this way, the SAM acts as a model organic surface. By systematically varying the terminal functional group of the alkanethiol, the surface properties of the organic film can be altered and an array of model organic surfaces with different chemical characteristics can be prepared. For example, a methyl (-CH_3) terminated alkanethiol film represents a non-polar surface while a hydroxyl (–OH) terminated alkanethiol film represents a more polar surface. By varying the chemical nature of the terminal functional group, one can observe changes in the wettability, film order, and solvent interactions that can be correlated with the molecular structure of the interface.[24,29]

Utilization of bifunctional SAM with different terminal functional groups is usually on the basis of properties like packing, stability, electron transfer and so forth, which the SAM of simple n-alkylthiols does not exhibit. Generally the functional groups at the end position are larger than the methyl group of simple alkylthiols. The SAMs having large tail groups would not pack with good order as alkylthiols because of much reduced repulsion between backbones of the nearest adsorbents which is attributed to larger separation compared with that of alkylthiol SAMs. Thus the enhancement of the packing or ordering of the SAMs having large tail group is required,[44] particularly for applications.

The synthesis of organic assemblies with a wide range of surface functionalities is the first step for designing organo-inorganic materials for molecular electronics. The mere presence of a suitable monolayer can make metals and semiconductors compatible with biological systems, thus suggesting the usefulness of monolayers in designing biomolecular systems.

For example, the alkanethiols terminated with functional group such as carboxylic acid and amine are much more important in controlling the surface properties and immobilisation of foreign molecules like cytochrome-c on the SAM surface.[44,45] A control of the terminal functional groups on SAM is attractive for the designing of chemical sensors[46] and also for the modification of surface properties towards application in nanotribology,[47] wetting[48] and adhesion.[49] The self-organization of metal (Ag, Au) and semiconducting nanoclusters (CdS, CdSe) on SAMs with dithiol functionalities gives rise to interesting nanostructures.[22,50-55] Similarly, the effective utilization of the functionalized interface of SAMs in two-dimensional reactions has been demonstrated recently by forming multilayers of zirconium phosphonate and copper dithiol.[56,57] Additionally, SAMs have been found to be valuable for preparing chiral-functionalized surfaces of oligopeptides for intended applications in molecular electronics.[58]

1.2.3 Tailoring of Properties

A careful manipulation of the chemical structure of the monolayer constituting the SAM renders it amenable to a large variety of diverse applications. The chemical properties can be fine tuned by selecting different type of terminal functional groups and the ease of formation and flexibility in structure can be utilized to study the wetting, tribology, adhesion, molecular recognition and related phenomena. This is a model system with controllable permeability to study the ion transfer as well as distant-dependent electron transfer.[12] Organo-inorganic materials tailored in this fashion are extremely important in nanotechnology to construct electronic devices like sensor arrays, single electron devices etc. by virtue of their size and shape-dependent electrical, optical and magnetic properties. These, in turn can affect the optimization of charge separation and carrier transport to the level necessary for the band gap engineering of these hybrid materials. In addition, SAM formation represents one type of methodology to build complex structures[24] at

nanometer scale by tailoring organic molecules and nanoclusters systematically via self-assembly to form unique superstructures with desired functions and properties. This intrinsic flexibility of creating organized nanostructures with SAMs is helpful to most technological applications.

1.2.4 Control of length Scale

The crucial dimension in SAMs is the thickness normal to the plane of the monolayer: A control of the alkyl chain length can provide easy access to vary monolayer thickness often at the scale of 0.1 nm. The long chain alkanethiols are adsorbed preferably over the shorter chains[41] and the change in chain length is expected to affect the kinetics as well as the quality of monolayers. Investigations related to the effect of chain length on monolayer properties for a series of n-alkanethiols show that for long chain thiols monolayers are arranged in a crystalline environment and as chain length decreases, the intrachain as well as the interchain interaction energy decreases (for example, the intrachain van der Waal's interaction per methylene unit decreases by 0.2 kcal/mol).[59] In effect, the coverage decreases, and molecules residing on low energy surface sites are likely to be thermally desorbed. Heterogeneous electron transfer at the monolayer modified electrode shows that current decreases rapidly with chain length as expected for nonadiabatic electron transfer.[60] Other than long chain alkane thiols, rigid rod like[61], conjugated,[62] and purely aromatic thiols[63] have also been employed for SAM formation. Although a high density of packing is observed for these molecules, the stability as well as the rate of formation of SAM is slower compared to that of n-alkane thiols.[61a]

1.2.5 Geometric Constraints

It is necessary to understand the packing and ordering of complex molecules in SAMs using different parameters affecting the spontaneous

monolayer formation in order to unravel the adsorbate-adsorbate interactions. If molecules have aromatic ring, alkyl chains and fused rings, the contribution of these parts to the equilibrium molecular packing and ordering in the SAM would be important. Simple planar π-system tends to spontaneously aggregate in layers, usually with herringbone structure. Similarly, paraffin spontaneously assembles in pseudohexagonally close-packed layer structure. In both cases, there usually is more than one possible stable packing arrangement and in some cases these arrangements have about the same stabilization energy.[64] Forming a chemical bond between π-ring and alkyl chains results in more complex system and it is not clear if this will spontaneously self-assemble in layered structure. Some molecules do form stable 2D layer, while others undergo bulk crystallization. The features that will determine the layered structure formation in these molecules are: (a) a minimum mismatch of different molecular parts; (b) an epitaxial matching between the sublattices of different molecular parts and finally (c) bonding flexibility, not affecting the criteria a and b.

When rod-like diacetyle molecule, π-system or phenoxy group is introduced to break the cylindrical symmetry of all-trans alkyl chains, the contact angle increases to 47^{o} and this is found to be more for shorter molecules.[29] The overall packing depends on the relative energy contribution of various interaction including the van der Waal's interactions, the conformation changes, π-π interaction etc. In a recent study[43] the geometrical constraint present in the naphthalene disulfide (NDS) due to the presence of rigid naphthalene ring, which can force two sulfur atoms to a fixed distance is compared with diphenyl disulfide (DDS) and diphenyl diselenide (DDSe). Considering the constraint imposed by the naphthalene ring on two sulfur atoms for NDS, it is obvious that even if the S-S bond dissociates during chemisorption, the two sulfur atoms must retain the bonding distance of 2.4 Å (i.e., the actual S-S distance in the compound). On the contrary, DDS and DDSe leads to two separate molecules once the S-S bond is broken. Hence,

for NDS, even if one sulfur occupies the normal 3-fold hollow site, the inherent rigidity of the naphthalene ring may direct the other sulfur to a possible *quasibridge site* as the distance between a 3-fold hollow and bridge site (2.4 Å) is comparable to an S-S distance in NDS. In contrast, DDS and DDSe, free from such structural constraints, can form a normal overlayer with an S-S distance of 5 Å.

1.3. MONOLAYER PROTECTED CLUSTERS (MPCs)

One of the important applications of SAM is the nanoparticle stabilization where the molecules form covalent bonds on the particle surface,[65] to avoid particle growth and agglomeration by different mechanism like Ostwald ripening, air oxidation etc. In contrast to the two-dimensional SAM on different structures as discussed above, these clusters can be viewed as 3D SAM[66] formed on the curved surface of the metal or semiconductor, which leads them to extra stability. Of particular interest is the regulated assembly of these monolayer-protected nanoclusters of same size, self-organised in crystalline arrays of one, two or three dimensions or in fractal form to generate superstructures.[55,67]

Synthesis of monodispersed nanoparticles in desired compositions, sizes and morphologies are the basic requirements for the self-assembly. More significant, is the long-term stability in both solution phase and in powder form, especially for the fabrication of nanodevices without any encapsulation. New methods for the synthesis and stabilization are being continuously tried due to the need for making stable clusters with as narrow size distribution as possible (less than 5% standard deviation) to meet strongest application criteria.[68] However, the understanding towards the mechanism of formation of monodispersed particles and its time-dependent changes with respect to the presence of other ions and solvent nature is not clear and several groups are trying to bridge these lacunae. Parameters, like purity, concentration of

reagents, ionic strength, solvent dielectric constant, rate and sequence of the addition of reagents and temperature are known to significantly affect the reproducibility in shape and size distribution.[69]

1.3.1 Classification

Different classification schemes for MPCs are possible depending upon the size, shape and properties of nanoclusters. Further grouping is also possible based on the nature of organic capping molecule. Most of the classifications are not rigid, as the primary objective is the convenience of grouping together similar systems to study their structure and behavior.

1.3.1.1 Metallic Clusters

Noble metal like Au, Ag, Cu, Pt etc. are the simplest nanoclusters stabilized by monolayers (cartoon shown in Figure 1.2). Comparison of the 3D SAM to the classical 2D SAM[24,29] demonstrates the intrinsic differences due to surface curvature; the packing density of the alkane thiolate chains bonded to the Au cluster surface (62-68 %) is nearly twice of that found on flat Au (111) (33%). There has been significant concentration (10-25%) of chain end gauche defects in case of 3D SAMs which is absent in 2D monolayers.[70] Several groups have prepared various types of Au, Ag, Cu, Pd and Pt nanoclusters using two-phase method and its other variants.[10c,71]

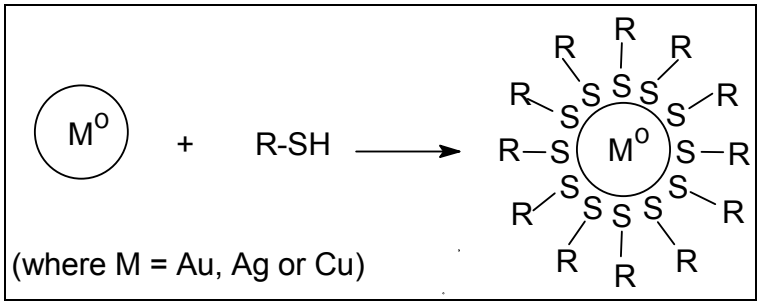

Figure 1.2 Schematic cartoon for the capping of a nanoparticle by alkanethiol molecule (i.e. the 3D SAM formation or MPCs synthesis), where R is $CH_3(CH_2)_n$.

1.3.1.2 Semiconducting and Insulating Clusters

In comparison to metallic nanoparticles, where the property is mainly characterized by mean free path of the electrons, properties of semiconducting nanoparticle depends totally on the Bohr's radius (the electron-hole separation as characterized by excitonic diameter). This is a characteristic length scale, depending on which the material can show many new properties controlled also by its dielectric constant. For semiconductor nanoparticles this is distinctly reflected in the variation in band structure that is size sensitive as manifested by the change in optical and electrical properties.[3f,72] Exploitation of this concept is believed to open the door for the manufacturing of ultrahigh density integrated circuits and information storage devices based on the presence or absence of individual electrons.[73]

Thus a great deal of research has been devoted in the last decade to synthesize semiconducting nanoparticles of varied size and shape especially in a controllable dispersion. One most common route involves the use of strong medium to support and stabilize particles including inorganic (e.g. glass and ceramics)[74] and polymer matrices[75] where the particles are embedded in the supporting media to form nanocomposite structures. Another approach entails the use of inverse micelles[76] or micro emulsions[77] as nanoreactors for synthesis. In addition, several semiconducting nanoparticles have also been generated by using amphiphilic monolayers at the air/water interface by the controlled reaction of the metal cations at the polar head region with appropriate reagents like H_2S.[78] The main limitations of these methods are that only small amount can be prepared and that some of the particles lack long term stability, especially when solvents are removed.

Organic monolayer-protected semiconductor nanoclusters,[79,80] akin to metal counterparts have demonstrated better stability in both solution and dry form. More significantly, by surface exchange or coupling reactions it can be

further functionalized to get suitable functional groups on the organic layer to manipulate surface energy states of electrons and holes. This means that the electronic structure can be tailored to modulate the macroscopic properties like photoluminescence and optical absorption.[81] Another important property of concern is the photochemical characteristics[72] for solar energy conversion and photochemical reaction catalysis. Because the electronic energy distribution is dependent upon the specific molecular structure and physical dimension, several examples have been demonstrated to show that it can be regulated at the molecular level.[72]

1.3.1.3 Heterostructure & Core-shell clusters

Design of building blocks with unique structure and composition is one of the important steps in the progress of nanotechnology. In this regard, nanoparticles with core-shell morphologies represent a new type of constructional unit consisting of two dissimilar compositional and structural domains. The aim of such modification is augmented chemical and physical properties and a broad spectrum of applications normally not possible with their single counterparts. Many types of nanoparticles could fit into the core-shell category[82] as core and shell of different materials in close interaction, including inorganic-organic, inorganic-inorganic, organic/organic or inorganic/biological core shell combinations.[2-8,71,76,82-83]

The core-shell synthesis typically involves tailoring the surface properties of particles, often accomplished by coating or encapsulating them within a shell of a preferred material. This coating can alter the charge, functionality, and reactivity of the surface along with improving the stability and dispersibility of the core. Also such compositions have been reported to show enhanced optical,[84] catalytic,[85] and magnetic properties. Due to the large difference between the intrinsic fermi levels of the core and the conduction band energies of the n-type shell (3.5 eV), mobile electrons that diffuse within

the shell will be retarded if the trapping energy $E_{tr} = E_f(core) - E_{CB}(shell)$ >> kT. Such metal-semiconductor particles have potential applications both as information storage element and as electronic circuit components. For example, Au-SiO_2 core-shell particles prepared through citrate reduction of Au salt followed by aminosilane functionalized silica coating show enhanced optical properties.[84] Similarly Au@SnO2 has been exploited as an electronic component with specific functions as the thin semiconducting shell around small metal particles may lead to composite particles with high electronic capacitance and low leakage rate.[86]

Apart from the synthetic routes in which initial reducing agents like alcohol, hydroxylamine or formaldehyde have been used as to form Pd-Pt,[87] Au-Pd,[88] Pd-Ag[89] and Pd-Cu[90] core-shell particles, a more recent and emerging route is through the alkanethiolate monolayer shell formation. The core metal of MPCs can be varied as demonstrated by the reports with Ag, Au core-shell particles[91] and alloys (Au/Ag, Au/Cu, Au/Ag/Cu, Au/Pt, Au/Pd and Au/Ag/Cu/Pd) so called monolayer protected alloy cluster (MPAC) cores.[91b] These MPCs and MPACs are air/solvent-stable and are obtained in high yield. Nevertheless, careful studies have recently revealed that the core metal in MPACs appear to be partly radially segregated and exhibit enhanced stability relative to their single-metal counterparts.[91b]

1.3.2 Preparation

A variety of nanoparticle preparation methods are known right from the period of Michael Faraday[92a] where superfine or ultrafine particles were prepared either alone or using supports (gelatin, agar, gum, albumin etc.) for catalytic purposese.[9a,92] For example, stable 12 nm Au particles were prepared during late 50's by reducing aqueous gold chloride with sodium citrate or other reducing agents.[93] However, the credit for preparing the stable monolayer protected metallic nanoclusters in powder form goes to Brust et al,[65] where the

alkanethiol monolayers (3D SAM) as capping agents were organised in situ for the first time. Further extensive work[94,95] has revealed the stabilization of metallic and semiconducting nanoclusters could be achieved with chemisorbed alkanethiols and several analogous molecules.

1.3.2.1 Brust method

In Brust method, the metal (Au, Ag, Cu, Pt etc.) salt in aqueous medium is reduced by strong reducing agents like $NaBH_4$, N_2H_4 etc., at the aqueous-organic interface, in the presence of a surface-passivating agent in organic medium. Vigorous stirring causes instantaneous transfer of the clusters to the organic phase through SAM formation with long chain organic thiols, amines, acids etc. present in the organic phase. A systematic variation of parameters like nature and the concentration of reducing agent, ratio of metal salt to capping agent, temperature, pH, and ionic strength can be used to control the size, shape. These capped nanoclusters can be separated from the solvent after thorough washing, stored as dried powders, and redispersed on demand in suitable solvent.[83]

In addition, borohydride reduction of gold chloride in alkaline aqueous medium using a bifunctional molecule as surface passivating agent[94] have produced nanoparticles with a surface functionality from amines to carboxylic. Au and Ag nanoparticles with dialkyl disulfides surface passivating agents have been generated with $NaBH_4$ reduction.[96] Advantage of using dialkyl disulfide is that two ($RSSR^{'}$) distinct functional groups can be utilized and mixed SAMs will be formed with homogeneous distribution of functional groups. The application of different capping agents will allow a fine control over the size and shape of these nanoparticles. In one of the examples, Pt nanoparticles with cubic, tetrahedral, polyhedral, irregular prismitic shape were generated when surface passivating agent concentration along with Pt concentration was varied during the reductive nanoparticle formation.[97]

1.3.2.2 Other Methods

The advantage of solution state synthesis is that it is very cheap and bulk quantity of nanoparticles can be produced without any specialized laboratory apparatus. The nanoparticles can also be synthesized using other methods including gas phase reaction,[98] laser ablation,[99] electrodeposition[100] etc. Another useful strategy similar to Brust method for preparing nanocluster includes reaction in a constrained environment such as inverse micelles, dendrimers, polymers, and silicates sols[101] where the capping agent arrests the growth of particles limiting the size.

Uncapped nanoclusters have limited stability and their high surface energy causes them to agglomerate in solution/solid state due to Ostwald ripening and other growth modes. However, these clusters can be stabilized electrostatically or sterically[102] and the stabilization occurs through the involvement of electrical double layer consisting organized cations, anions and solvent molecules. Agglomeration of the highly charged particles is avoided by the Coulombic repulsion which decreases exponentially with increasing interparticle distance.

1.3.3 Characterization

The characterization of nanoparticles aims to quantify the particle size, shape, distribution, overall composition and impurity contents. A variety of techniques have been applied to get valuable information about the structure, kinetic and thermodynamic stability and mechanistic aspects of the monolayers on the cluster surface. These techniques useful to characterize various parts of MPCs are shown in Fig.1.3. Surface composition is also probed although this is a formidable task. The techniques used for characterization should have no damaging interaction and must reveal subtle features like the conformation and orientation with respect to different functional groups on nanocluster surface.

Also, some of the techniques require specific environment like MPC/solution, MPC/ultra high vacuum (UHV) interface, and hence the possibility of reorganization of organic molecule due to change in environment has to be considered during analysis. In brief, no single method of characterization provides complete insight and hence the application of various techniques is essential; some of them are mentioned below (Figure 1.3).

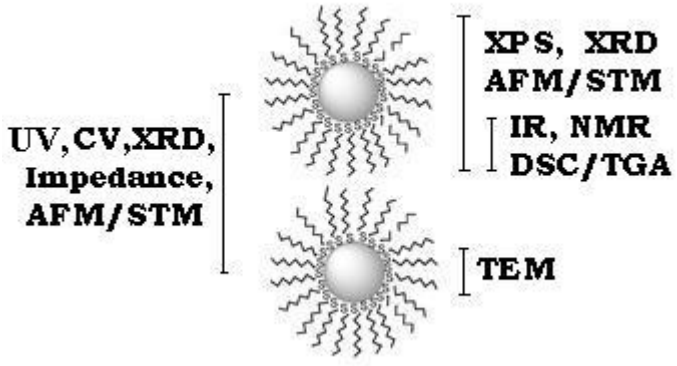

Figure 1.3 The scheme indicating the various techniques to be used to characterize various parts of monolayer-protected nanoclusters.

1.3.3.1 UV-visible Spectroscopy (UV-vis spectroscopy)

UV-vis spectroscopy is a valuable technique to qualitatively determine the size and degree of aggregation of nanoparticles. This technique is particularly effective in characterizing nanometer sized metallic MPCs like Au, Ag and Cu etc. because the surface plasmon shows its characteristic resonance in the visible region. More specifically, since absorption maximum (λ_{max}) for surface plasmon depends on the size, shape of particles and also the interparticle separation, it is possible to analyze these concepts. For example, dodecanethiol capped Au MPCs (2.6-5 nm) reveals strong plasmon band at around 520 nm which decays exponentially into visible region. Interestingly, for smaller particles (core size), the intensity of the band is also found to

decrease.[103] For alloy clusters, the surface plasmon position and intensity are intermediate to those of corresponding single metal MPCs[104] and similarly for nanorods an additional band corresponding to longitudinal plasmons appears at higher wavelength.[105] In addition, for very small particles (1-2 nm), molecule like properties and transitions to discrete LUMOs[106] could be used to estimate the HOMO-LUMO "gap" energies as a function of size.[107]

1.3.3.2 X-ray Diffraction (XRD)

X-ray diffraction is an important method to characterize crystalline nanoclusters. For example, XRD indicates that the alkanethiolate-gold nanocrystal has fcc lattice with a mean lattice constant within 2% of the bulk value (a=0.409 nm). In a recent study Zanchet et al[108] has shown that in addition to bulk fcc structure (particle size 2.6-3.2 nm), some particles reveal decahedral (1.7 nm) and icosahedral (≤1.3 nm) structures depending on the particle size. More interestingly, few of these sample fractions condense reversibly to form ordered crystals or superlattices with long-range translational and orientational order.

The x-ray studies of several cases of ordered nanocrystals have also suggested that the image arise from a bcc superlattice viewed along a [101] axis. The model for this shows orientation of 54.7^{o} with respect to (010) rows of the superlattice in which nine (111) gold planes (0.235 nm interplane spacing) are evident.[71] The (111) plane in such ordered lattices corresponds to diffraction form Au lattice planes within the nanocrystal. Further structural information can be obtained from the small-angle and long-angle region of diffraction studies. The long-range 2θ values show broadened peaks whose shapes and intensities arise from the diffraction of the finite number of atomic planes indexed to fcc Au, in individual Au nanoparticles. The clear sequence of diffraction peaks in small-angle region reveals the structure of 3D superlattice,

into which the fractionated samples of passivated nanoclusters crystallize.[83a] Despite such useful information from x-ray studies, a complete determination of the structure and composition of nanoclusters in particular, the exact interaction between the metal nanocluster surface and 'stabilizing ligands' is still a daunting task.

1.3.3.3 Transmission Electron Microscopy (TEM)

The most widely used technique for characterizing nanoclusters is high-resolution transmission electron microscopy (HRTEM), which provides direct visual information on the size, shape, dispersion and structure. Potential drawbacks of this techniques include: (a) electron beam-induced structural rearrangements, aggregation or decomposition; (b) the inherent problem in interpreting two-dimensional images of 3D samples and (c) problem with sampling (only a small number of clusters can be analyzed and counted which may not be representative of the sample as a whole). Despite these limitations, TEM has been the technique of choice due to atomic-level resolution and the possible selected area electron diffraction.

TEM studies have shown that casting of dilute alkanethiolate Au MPC solution leads to a semiordered islands and chains of clusters with uniform core-core spacing of about one alkanethiolate chainlength.[71] Images of naked nanoclusters[109] of similar size display a bilayer structure and unusual self-organization features of chains and rings where the top-layer nanoparticles are roasted in 2-fold saddle rather than 3-fold hollow sites, probably due to the balance between local electrostatic repulsion and dispersion forces between neighbouring particles. Alkanethiolate-MPCs prepared under condition of excess thiol show ordered features while films of thiol deficient preparation tend to contain a mixture of widely scattered MPCs with large clumps and patches (6 nm). Such different morphology of the TEM samples probably reflects a complex amalgamation of differing, polarity-based level of adhesion of MPCs to

one another and to the substrate surface during evaporation of the solvent and thus are tenuous to interpret in simple structural terms.

Most of the core size of the alkanethiol-MPCs from TEM images appears to be relatively small (< 3 nm) and they do have a nearly uniform size distribution. The average MPC core diameter decreases strongly when prepared using reaction mixtures rich in thiol relative to gold.[103b,110] This dependency is qualitatively sensible given that the eventual MPC core size is determined by the competing processes of core growth by the encasing monolayer ligand shell. Larger excess of thiol enhances the rate of passivation, yielding smaller nanoparticles. The same trend has been observed for arenethiolate nanoclusters.[110b] High resolution TEM studies can be particularly useful to study the faceting, crystallinity and ordering in these nanocrystals.

1.3.3.4 X-ray photoelectron spectroscopy (XPS or ESCA)

X-ray photoelectron spectroscopy (XPS or ESCA) is a surface analytical tool where a sample is exposed to monochromatic x-ray and the properties of inner-shell electron are probed. According to photoelectric effect, when a material is exposed to electromagnetic radiation of sufficiently high energy, the emission of electron is observed. The kinetic energy of the estimated electron is given by $E_{kin} = h\nu - E_B$, where E_B is the binding energy of the electrons in the atom which can give valuable structural information. XPS is one of the most powerful tools to study monolayers on MPCs (3D SAM) as it can give significant information about the nature of chemical state of elements at the surface of MPCs, the average number of ligands per core can be derived from combined analysis of XPS and TGA studies.[66]

Although self-assembled monolayers (SAMs) of alkylthiols on planar gold (2D SAMs) and on gold MPCs (3D SAMs) have been intensely studied [hostetler etal Terrill etal], the actual nature of the Au-S bonding remains

ambiguous. Comparison of the X-ray photoelectron spectroscopy (XPS) spectra of 2D and 3D SAMs and a "reference" Au(I) complex, sometimes referred to as Au(I) thiolate polymers, provides detailed insight into this problem. High-resolution XP spectra and Au $4f_{7/2}$ and S $2p_{3/2}$ binding energies (B.E.) in 2D SAMs, 3D SAMs and the Au(I) thiolate complexes reveal the S atom in the SAM systems bears a charge of about 0.2e. The 2D and 3D SAMs exhibit similar XPS characteristics and are both distinguishable from the Au(I) complex.[111] In brief, Au $4f_{7/2}$ B.E. appears very near to Au(0) (83.9 eV) and S $2p_{3/2}$ B.E. is consistent with a RS^- ligand (161.9 eV). Like 2D SAM, 3D SAMs gives energies distinctive of Au(0) and a surface thiolate indicating that the bond is somewhere between RS-M and RS^- — M^+.[112] These results also indicate that as many as one third of the Au atoms in the MPC bear alkanethiolate ligand[103b] and for the smallest cores only an increased B.E is seen.

This technique is also useful for analyzing mixed monolyers on MPC surfaces. The angle-dependent studies can give valuable information about the atomic distributions in MPC surface. Nevertheless, in all these applications the limitations such as beam-induced damage on the monolayer and carbon contamination from XPS chamber are to be kept in mind during the XPS analysis.

1.3.3.5 Cyclic Voltammetry (CV)

CV is one of the most valuable techniques to study the electronic properties of MPCs. It is a simple technique where the potential is linearly varied at a definite rate between two fixed potential values and the resulting current response is plotted against the applied potential. An approximate estimation of differential capacitance for SAM itself can give significant information about adsorbate packing and intermolecular interaction. This technique has significant applications in the area of MPC, their assemblies, as

CV data can provide a mean to evaluate the MPC energetics and monolayer coverage using appropriate solvent and supporting electrolyte. These MPCs show a single electron transfer process in an aqueous system ($\Delta E \approx 60$ mV; $I_{pa}/I_{pc} \approx 1$), and a surface coverage of 1.85×10^{-10} mol/cm^2 on Pt surface. Electrode reactions of redox-functionalized nanoclusters (e.g. ferrocene, anthraquinone) are unusual, in that many equivalents of redox charge per MPC can be delivered, under diffusion control, to the electrode/solution interface. MPCs functionalized with two different redox groups exhibit voltammetry of two different groups occurring independent of each other.[113]

The electrochemical studies at high resolution also have shown quantized double layer charging in MPCs (diffusing nanoelectrodes). The capacitance is associated with the ionic space charge formed around an MPC dissolved in the electrolyte solution, upon electronic charging of the core. Because of the small subattofarad (aF) capacitance (C_{CLU}) of an MPC, charging of tiny capacitor by single electron occurs in the potential interval ($\Delta V = e/C_{CLU}$) that exceeds k_BT.[114] These potential intervals are seen sometime in voltammetry of MPC solution depending on the size. This quantized double layer charging is analogous to STM based “coulomb staircase” experiments using MPC. The spacing of these current peaks on the potential axis reflects the nature of MPC core charging process. An even peak spacing indicates metal-like core whose charging is controlled by electrostatic (i.e. double layer) principles. These studies reveal that the MPC properties can be tuned as a function of surface coverage, core size and the relative chain length.

1.3.3.6 Impedance Studies

The impedance method is based on the measurement of the response of an electrochemical cell with the material concerned as working electrode to a small amplitude alternating potential. It can give valuable information about surface coverage, dielectric constant and electron transfer behavior of MPCs

both in solution and solid state. The response is often analyzed by the complex impedance presentation and the results are interpreted in terms of suitable equivalent circuits. With the help of appropriate double-layer models (primitive Helmholtz parallel plate model, Gouy-Chapman model, Stern model etc.)[115] both faradaic and nonfaradaic processes at electrode/MPC interface can be investigated. Each MPC has a finite capacitance, separated from every other MPC by an organic medium which serves as a tunnelling barrier. The equivalent circuit of an MPC in solution looks like Figure 1.4 (a), where R_{CT} is charge transfer resistance and C_{MPC} is the tiny capacitance of MPCs which establish a double-barrier tunnel junction in solution. When these MPCs are anchored on an electrode surface the equivalent circuit becomes like (b).[2a,116] The interfacial capacitance C_{DL} has two components, C_{SAM} and C_{EL} which can account for the contributions from the electrode surface with and without adsorbed MPCs, respectively. The capacitance modulation with electrode potential is in agreement with CV studies, the MPC surface coverage (C_{SAM}/C_{MPC}) being 1.23 x 10^{-11} mol/cm^2. Assuming hexagonal close packing, the interparticle distance is found to be 3.95 nm, slightly larger than the average physical diameter of 3.5 nm for sum of core and monolayer diameter, representing a surface coverage of roughly 0.8 of a monolayer. The transfer rate constant can be determined using $k=1/sC_{SAM}R_{CT}$, approximately 20 per second.

Equivalent circuit description of the MPC-solution interface provides a simple way to determine the double-layer structure, estimation of surface coverage, double-layer capacitance, dielectric constant of the monolayer and heterogeneous electron transfer rate constant of the MPC assembly. The main limitation is the model dependence of the calculated parameters as all the values can be misleading if incorrect equivalent circuit is used.

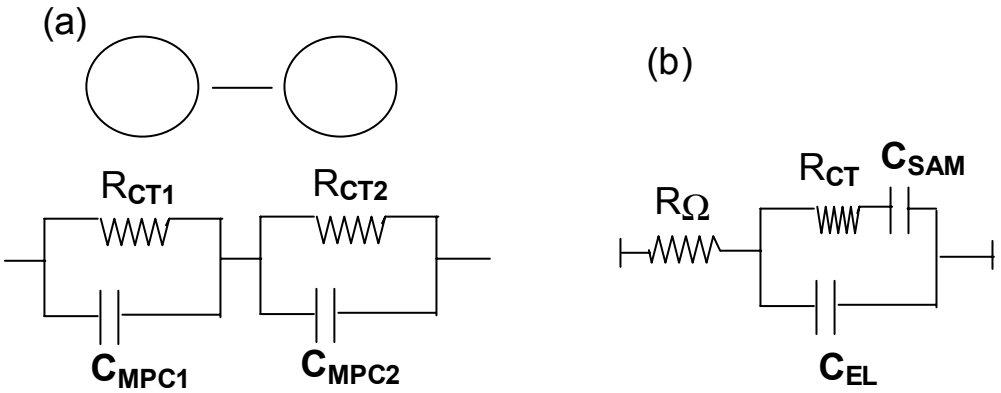

Figure 1.4 Equivalent circuit for the nanoparticles (a) in solution (b) after organization on surface. $R_{CT1,CT2}$, C_{MPC1}, C_{MPC2} indicates the resistance and capacitance respectively, of two adjacent nanoclusters in solution. After attaching the nanoclusters to surface the capacitance includes the component C_{SAM} due to the nanoclusters.

1.3.3.7 Thermogravimetry/Differential Scanning Calorimetry (TG/DTA/DTG/DSC)

Thermogravimetry is an important tool to study the stability of MPCs along with useful information about the Au core – thiol ratio. Thermal decomposition of Au MPCs leads to the loss of organic part[66,103b] finally leading to a residue of Au powder. Considering the average core size of Au MPCs, the TGA results give average number of ligands per MPCs as 4.7/ligands/nm^2.[103b] TG results confirm that MPC ligand coverage is more than 50%. This is greater than the ligand/Au surface atoms in 2D Au(111) surface (~33%). Theoretical calculations also indicates that this high coverage results from larger ligand/Au binding ratios on core edges and vertexes.[117] The alkanethiolate MPC decomposes at around 260^{o}C.[103b] The mass loss occurs in single step beginning at 230, 266, 310^{o}C for C8, C12 and C16-thiolate-Au MPCs respectively, corresponding to the quantitative loss of the alkanethiolate chains. The temperature dependence of the mass loss indicates that the thermal stability of Au MPCs increases with increasing chainlength.[66]

A related technique, DSC is very powerful to study the phase transitions in alkanethiolate-MPC monolayers. Phases of Au MPCs studied in the temperature range of –100^{o}C to 100^{o}C show that for smaller chains (≤C8-

thiolate MPCs) no phase transition is observed while for C12 and C16-thiolate MPCs a broad endotherm is seen corresponding to enthalpies of 6.5 kJ/mol for C12 and 14 kJ/mol for C16-thiolate monolayers respectively. The melting heats of pure C12 and C16-thiolate are smaller (37 and 50 kJ/mol, respectively) so that these melting transitions involve only a portion, not all of the hydrocarbon chains. The temperature dependence studies reveal that as the chain length of capping organic molecule increases the phase transition temperature increases.[103b]

1.3.3.8 Nuclear Magnetic Resonance (NMR)

NMR spectroscopy is particularly useful to determine the structure and dynamics of monolayers on MPC. Studies of order-disorder transitions are possible in MPCs using NMR and IR. ^{1}H and ^{13}C NMR resonances of MPCs are characteristically broad relative to those of free alkanethiols,[103b,118] the factors include spin-spin relaxation (T_2) broadening, a distribution in chemical shifts due to differences in Au-SR binding sites, and a gradient in monolayer packing density from near core to chain terminus with associated dipolar broadening.[118b]

For example, ^{13}C NMR studies show that in both solution and solid-state, the resonance of the first three C next to the sulfur headgroup disappears upon binding to gold, indicating a strong interaction with the surface. For C12-thiolate MPC a broad resonance appears at 4.2 ppm for the C next to the sulfur headgroup. For C8-thiolate MPCs the ^{13}C resonance in solution and solid-state is same while C18-thiolate MPCs show downfield shift by 4.5 ppm in solid-state. This indicates that chains crystallize into an extended all-trans conformation, while the high conformational order, alongwith reduced methylene proton line width in C18-thiolate MPCs indicates that the chains are undergoing large amplitude motion about their large axes. Molecular mobility increases towards the unbound ends which have a higher populations of

gauche conformations.[118a] In a variable temperature dependent ^{1}H NMR study of C18-thiolate, it has been shown that as the temperature increases, disorder (increase in gauche bond population) propagates from the chain terminus to the middle of the chains leading to eventual chain melting.

1.3.3.9 Fourier Transform Infra-red Spectroscopy

Infrared spectroscopy is a general tool to study monolayers, especially their orientation, packing and density. Detailed information about the packing, functional groups can, in principle, be obtained with polarized light, since the adsorption in the vicinity of a molecular vibration frequency is dictated in general by the relative orientation of the electric field and the dipole transition moment. In comparison to 2D SAM which has *ca.* 10^{13} molecules/cm^2, the density of monolayers will be more in 3D SAMs and hence the use of attenuated total reflection (ATR) and grazing-angle (GA) becomes proximate.

Comparative vibrational spectroscopic studies have shown that[29] alkanethiolate chains of 2D SAM are typically in all-trans, zig-zag configuration, while chain conformation in solid-state MPC films are mostly all-trans containing significant (5.25%) gauche defect concentration at both inner and terminal chain ends, especially for longer chainlengths and above the chain melting temperature. Monolayer ordering in solid-state MPC samples are also associated with interdigitation of chain domains (or bundles) or neighbouring cluster molecules.[118] Also hydrogen bonding becomes an important structural component in MPC with polar monolayers.[119a] In contrast, monolayers of dissolved alkanethiolate MPCs exhibit disorder comparable to that of liquid alkanes. These MPCs have proved to be only rough analogies of 2D SAM due to the high proportion of classically defined MPCs core surface defect sites.[119b]

1.3.3.10 Scanning Probe Microscopies (AFM/STM)

While standard methods of measurement and characterization are routinely employed for investigation, the increasing use of scanning probe microscopy (spatial resolution 0.1 nm), combined with high-resolution electron microscopy has enabled direct images of structure to be obtained. Scanning probe microscopies are now employed at low temperature, under vacuum or in a magnetic field to image nanoparticles. In a STM measurement, an atomically sharp tip is brought very close (≤10Å) to the surface and on application of a small potential difference (~1V) between the surface and the tip, the generated tunnelling current is monitored during scanning of the tip on the surface. The STM experiments can be done either in (a) constant current or (b) constant height mode. The samples for STM should have few desirable criteria such as (1) good electrical conductivity, (2) atomically flat surface, and (3) limited surface mobility. Compared to STM, AFM is purely mechanical, a cantilever tip attached to a spring is dragged across the sample. The increase or decrease in the height of the tip is measured yielding the surface height profile as a function of distance. The advantage is that one can carry out measurements on non-conducting samples. AFM is good at determining the particle height but is poor at determining its diameter.[120] Likewise, AFM cannot differentiate shape differences, or image of particles that are spatially close.

The STM measurement performed on C12-thiolate Au MPCs on HOPG surface shows clusters as spherical protrusions lying along the step edges. Clusters are not seen on smooth HOPG surface and are pushed aside by the scanning tip. For different chainlengths no such big corresponding difference in size is observed. The average size lies in the range 3.9 to 4.5 nm and percentage for C8, C12, and C16 falls in the regime of 52%, 58% and 68% respectively.[66] Advantage of using STM data over TEM is that TEM measures only core diameter while STM measures the overall cluster dimension (organic molecule and core diameter). Convolution of the particle size with the STM tip

dimension may cause the STM image to overestimate the true cluster size, while AFM measurements indicate slightly smaller particles. The images of C12-thiolate MPCs on flat mica surface show that the aggregates have more width than their height and no significant difference in height is observed for small and large aggregates indicating that the groups consist of a single layer of clusters.

1.3.3.11 Other methods

One of the important properties of MPC is there room temperature conductivity. Solid-state electronic conductivity measurement on dry powders of MPCs reveals that they are electronically conducting presumably due to the electron tunnelling through the intervening monolayers. Besides the techniques described above, several special characterization techniques such as He, electron and neutron diffraction,[121] surface plasmon spectroscopy (SPS/SPR),[122] magnetoelectrochemistry,[123] secondary ion mass spectroscopy (SIMS)[124] etc. have been applied for investigation of nanoparticles to get valuable information.

1.4. ORGANIZATION OF NANOCLUSTERS, WHY AND HOW?

One of the important challenges in nanoscience and nanotechnology is the precise organization of structures with subnanometer resolution on surfaces to generate functional architectures.[125] For this, self-assembly has proven to be one promising technique that can work. Although, nanoparticles have been assembled on a wide variety of substrates by highly ingenious means, true nanoengineering requires precise control on exact location of the nanoparticle on the surface. This requirement is finally becoming a reality with STM/AFM modulated ordering of the adsorbed particles which brings several novel applications.[9-10] If particles are truly monodispersed (variation in particle size

distribution less than 1%), theoretical calculations based on Huckel-type tight binding models can be adopted to estimate the configurational disorder of arrays.[126]

Depending on the chemical nature of the surface and the cluster, there are several methods to organize nanoclusters into arrays. These include: (1) Covalent attachment on suitably modified surface,[50-55] (2) Electrostatic organization of clusters using control of surface charge,[127] (3) hydrophobic organization using van der Waals interaction and (4) a combination of some of these especially in biomolecules; out of these studies, covalent and hydrophobic assemblies are scanty despite their important role in many biological processes. Indeed, layer-by-layer self-assembly has been recognized as a subfield of colloidal chemistry and the exponential increase in research publications as listed at a website[128] shows the emerging importance of this thrust area.

1.4.1 Substrates/SAM/Cluster interactions

Generally, the electronic structure of metals and semiconductors dictates its properties and this can be varied by doping, albeit to certain narrow limits only, as the original structure needs to be preserved. To achieve the desired properties, one can design/tune solid surface accordingly via the control of surface properties, because the electron transport through devices depends critically on the properties of surfaces and interfaces through which the electron passes. By chemisorption and self-assembly one can glue specifically designed molecules to metal, semiconductor or insulator surfaces to yield a hybrid system - “a combination of molecular and non-molecular worlds”.[129a] Nevertheless, when such structures will be used for applications, the problem of interrogating each unit separately using transfer of individual signals from nanocluster to substrate may pose new set of problems.[129b]

The substrate/SAM/cluster interactions are important for a variety of reasons. First, the electronic properties of solid substrates tuned in a desired and predictable way using SAMs can be harnessed for useful applications. Second, a systematic change in the interface (molecular/substrate) system corresponding to the variation in the molecular properties is thus possible. Third, tuning the properties would help to understand the substrate effect apart from the nanocluster and molecular effect and this can help us to make novel devices with several unusual properties. Once we select the particular molecule which adsorbs on the selected substrate, the chemical effects in the surface-bound substrate can be analyzed. Molecules with the capability to interact with the nanoclusters should be selected on the basis of their binding group (to the surface) - often the terminal headgroup, to alter the molecular properties.

1.4.1.1 Metallic Substrates (e.g., Au, Ag, Cu, Hg,)

Metallic substrates play a crucial role in SAM formation as well as cluster organization. In most cases Au (111) is used due to its inertness in ambient conditions compared to Ag and Cu so that the manipulation of nanocluster organization is possible with lesser contamination. Au, Ag and Cu surfaces can interact with thiol, disulfides and related functional groups due to a specific bonding interaction of the d-state of the metal with the s-state of the adsorbate. Gold is generally used due to its hydrophilic nature in vacuum, although, it can strongly adsorb these organic molecules from solution as well as air to make surface permanently hydrophobic.[130] Moreover, since Au does not have stable oxide on the surface,[131] it can be easily cleaned by removing physically and chemically adsorbed contaminants. Other metals like Ag, Cu and Hg are more reactive and hence are prone to easy oxidation in air. Similarly, prolonged immersion of Ag, Cu or Hg substrates in alkanethiol solutions leads to the formation of interfacial metal sulfides which can adversely influence the monolayer structure and quality.[132]

In case of Metal/SAM/Nanoparticles, the metallic particles maintain their discrete nature without any large scale clustering in contrast to the semiconducting nanoparticles which crystallize on SAM modified Ag surface.[133] The coverage is found to be greater than 95% in all the cases indicating densely packed and stable films of underlying SAM. When SAM is formed on the metallic substrate, the monolayer changes the dielectric function of the substrate and these changes are more effective for Ag and Cu as compared to Au. This can be described in terms of changes in surface work function of the metal caused by its adsorbate.[134] However, such adsorbate effect would depend on the ionic nature and the strength of the SAM-substrate bond. From the consideration of the electronegativity difference among S, Ag and Au, the Ag-S bond should be more ionic than Au-S bond. Therefore, SAM on Ag can affect the charge distribution at the adsorption site to a large degree than it would do in case of gold (dielectric function of Ag is much more affected than Au).[135]

When nanoparticles are introduced, they generally do not change the dielectric function of the underlying SAM, but change the dielectric function of the substrate. The dielectric function of the particle layer is sensitive to the chemical nature of the SAM, and to some extent to metal substrate.[136] In Metal/SAM/Nanoparticle interfaces, SAM perturbs the electronic details of the adsorbed particle layer, while the SAM dielectric function is less affected. At the same time, the substrate fermi level will change with the adsorption of particle and the organization gets altered alongwith the surface charge density of the nanoparticles. This charge density contributes to the interparticle interaction and is likely to depend on the size of the particle.[136] At the same time, the net charge on a nanoparticle attached through a SAM would be sensitive to the electrostatic or covalent nature of the particle-SAM bond. If the particle size changes, the organization will alter with respect to the electronic density and its interaction with SAM.

1.4.1.2 Semiconducting Substrates

In comparison with Metal/SAM/Nanoparticle interactions, the semiconductor/SAM/Nanoparticle junctions have more technological importance, although, the challenge lies in producing well controlled interfaces at the nanoscale for tailored electrical/optical properties compared to bulk metal/semiconductor systems. The nanocluster network on semiconductor surface gives a periodic lateral modulation of the electronic properties of the underlying substrate. The assembly can be formed/transferred into the substrate via selective etching using cluster as an etch mask or could be included by electronic interaction at the nanoparticle-substrate interface.[137] This junction is broadly classified into three categories which includes single electron tunnelling (SET), nanoscale Schottky barrier and nanoscale Ohmic contacts.

One of the significant issues apart from the useful electronic functions is the accurate positioning of the metallic nanoparticles on these substrates and some of the problems can be solved by pushing the clusters and locating them on the scanning probe tips. For semiconductor/SAM/Nanoparticle assemblies the substrate should be flat enough at the nanometer scale. A rough substrate may cause difficulty in imaging nanoclusters from the substrate itself. Chemical stability of these surfaces (i.e. resistive to oxidation upon air exposure) can be an important benefit when *ex-situ* processing of depositing nanoclusters is required, while the parent oxide layer may be removed through *in-situ* cleaving which ultimately removes the insulating layer and roughness. A well-known method employed nowadays preferentially is to anchor the nanoclusters in a closed-packed monolayer through the deliberate passivation of the surface (i.e. chemical self-assembly).[137b] This nanoscale ordering of clusters can be further combined with procedures which impose a large-scale pattern to break the symmetry of the uniformly ordered self-assembled elements in controlled ways.

Several examples are known for SAM formation on processed GaAs and HOPG substrates using dithiol molecules yielding a long-range order and nearly 80% particle coverage. These clusters show ordering with 7.9±0.6 nm spacing between neighbouring nanoclusters[137b] and the coupling to the semiconductor substrate is much stronger than the intercluster coupling.[137c] Therefore, it is possible to change the relative strength if the intercluster electronic coupling could be made much stronger than the nanocluster-to-semiconductor coupling, leading to uniquely patterned array structures like a "molecular ribbon".[138]

1.4.1.3 Insulating Substrates

In contrast to metal surfaces, SAM on an insulating surface shows high surface coverage and consequently a more ordered SAM is formed compared to that on metallic substrates.[139a] Careful inspection of insulating surfaces modified with Au particle reveals a number of important features about Au colloid-based cluster organization. At low coverage, the particles are randomly bound to the surface.[139b] This contrasts sharply with electrophoretically-deposited colloidal Au films where low coverage is manifested in close-packed, ordered structure.[140] Strong covalent bonds between organosilane sulfhydryl groups and the colloid surface prevent the particle migration on the organosilane film. Optical spectroscopy reveals that increased immersion times leads to increased numbers of isolated partices, rather than three-dimensional clusters, which can be easily discerned by Field Emission-SEM.[141a] In a related study,[141] the particle coverage and absorbance reveals a $t^{1/2}$ dependence, and the Beer's law is followed with modulation for surface-confined particles. However, as the derivatization time increases beyond a limit, both the absorbance and the particle coverage deviate from $t^{1/2}$ behavior and reach a plateau level (saturation). Analysis of interparticle spacings at this coverage indicates that repulsive forces govern particle assembly beyond the early time of diffusion-dominated regime.

1.4.2 Electrostatic Organization

Electrostatic interactions play an important role in many biological and chemical processes.[127a] Recently it has been shown that nanoparticle arrays can be constructed from the interaction of charged nanoparticles with oppositely charged (suitably functionalized) substrate bearing a chemical group that can selectively bind nanoparticles (e.g. a quaternary amine that binds with anionic particles.[2b,3c,42a] The formation of a colloidal layer is achieved by placing the surface functionalized substrate in a solution of nanoparticle for a sufficient time to adsorb onto the surface followed by equilibrium organization into a saturated monolayer with time. The density of the nanoparticle depends on factors such as size, charge, attachment method and the nature of the substrate.[142]

Interestingly, the electrostatic organization of citrate stabilized gold nanoparticles on amine and thiol functionalized surface reveals that bigger nanoparticles form 20 times less denser films.[2b,3c] Similar results were also confirmed through reflectrometric studies of negatively charged SiO_2 particles on aminopropyl triethoxysilane functionalized substrate.[143] The initial rate of nanoparticle adsorption was found to decrease with increasing particle size. The amine-functionalized substrates were found to bind nanoparticles at a slightly higher density than thiol functionalized substrate. The nanoparticle monolayer formation was found to be complete within few hours by QCM[144] and in these type of electrostatic organizations the pH plays an important role and the maximum cluster adsorption depends on the particle size and the curvature.[145] Several other examples of electrostatic organization are available using different type of biomolecules.[3e]

1.4.3 Covalent Organization

The layer-by-layer self-assembly of bifunctional organic molecules and nanoparticles onto substrates using covalent control is very simple. A well-cleaned substrate is primed by adsorbing a layer of bifunctional organic molecule. This substrate is then immersed into a dilute aqueous solution of metallic nanoparticles for a time, optimized for the adsorption of a monolayer, rinsed and dried. These operations are repeated to complete the self-assembly of metallic nanoparticles sandwiched onto the functionalized substrate. For example, the scheme given below (Figure 1.5) illustrates self-assembly of pentanedithiol and Ag nanoclusters onto Au (111) substrate. In this case the dithiol molecules form covalent bonds between Au (111) surface and Ag nanoparticles and a layer-by-layer organization of Ag nanoparticles can be confirmed using STM and AFM.

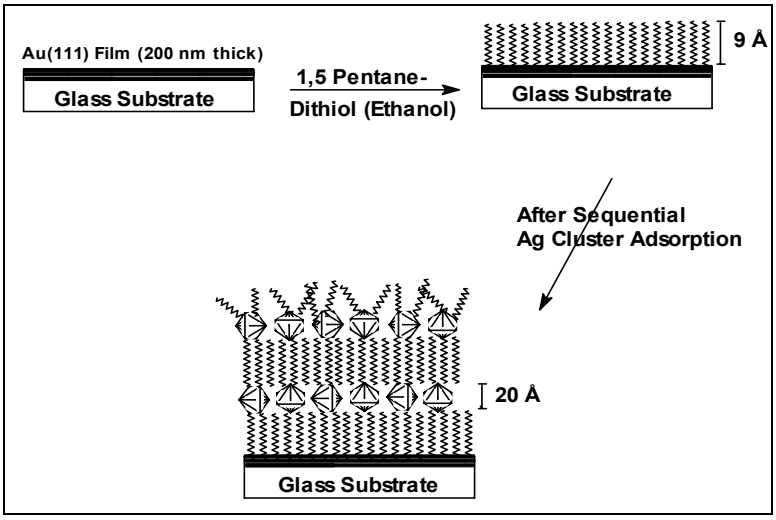

Figure 1.5 Cartoon of a layer-by-layer organization of Ag nanoclusters on Au (111) surface modified with 1,5-pentanedithiol after dipping the substrate in 1 mM ethanolic solution of the specified organic molecule for 24 h.

Instead of dithiol molecules, any bifunctional molecule containing –SH, -NH_2, -COOH, -CN, -S-S etc. can be used although the binding strength varies significantly with the type of cluster. For example, TiO_2[146] and Ag[53] nanoparticles can be preferentially linked using –COOH groups on the terminal side and similar selectivity can be used for attaching CdS and Pt clusters using

–SH terminal group.[55] These arrays demonstrate that nanoparticles do not aggregate and have relatively high coverage-usually about half a monolayer.[147] The first work of this type is illustrated by Colvin et al using CdS nanocrystals on dithiol functionalized Au (111) substrates with a high coverage.[50]

Although long range order is generally not observed for covalent assembly,[148] this method has fine control over particle spacing and in turn this affects the bulk properties such as conductivity. The properties of the self-assembled multilayers depends primarily on the choice of the building blocks used, their rational organization and integration along the axis perpendicular to the substrate. An advantage of this technique is that it can be potentially used to prepare complex patterns of various types of nanocrystals.[148] This approach has proven useful for locking-in structures in order to build test-case devices, such as single electron transistors, light emitting diodes (LEDs), molecular rectifiers etc.

1.4.4 Hydrophobic Organization

Hydrophobic organization is one of the thermodynamically driven self-organization processes which play a very crucial role in many biological systems. Hydrophobic forces are interactions arising due to the attractive force between surfaces of unequal charges where the dimension and geometry can cause these forces stronger. These forces drive the functional groups with similar configuration and free energies. For MPC organization the curvature of the nanocluster surface plays an important role because the magnitude of the attractive interaction is a function of the degree of hydrophobicity of the surface.[149]

Apart from the important role played in biological self-assembly, the hydrophobic forces are crucial in phenomena such as mineral floatation, wetting, coagulation and surfactant aggregation etc. These forces are found to

decrease exponentially (1.4 nm decay length) between two hydrophobic neutral surfaces and are 10 to 100 times stronger than van der Waals forces in a very short length scale (i.e. 0 to 10 nm).[150] This methodology was successful particularly for smaller nanoparticles (<10 nm)[151] because beyond this size threshold particles become increasingly prone to multilayer or three-dimensional aggregate formation. This aggregation tendency can be attributed to the rapid increase in van der Waals attraction and loss of mobility of alkane chains on the planar facets of the nanoparticles as a function of size.[118b]

1.4.5 Other modes

Superlattice formation through solvent evaporation was reported first by Bentzon *et al* in 1990.[152a] They observed ordered 3D array of iron oxide colloids when the particles were placed on a TEM grid. Later Malvaney observed the formation of an ordered hexagonal array of 14 nm Au particles through electrophoretic deposition.[151] This was followed by the work of Murray's group where 2D ordering for their semiconducting nanoparticles of CdS were reported to possess unique optical behavior. Similarly superlattice formation was also reported by Ohara et al[152b] using metallic nanoparticles with broad size distribution to demonstrate size dependent inter-particle dispersive attraction.

In comparison to covalently bound particles which form irreversible cross linking, the assembly is not stable since the driving force is only weak dispersive interaction; for narrower particle size distribution long-range order could be easily obtained. For example, Wang has revealed[152c] long-range order due to the narrow size distribution of Au particles. This is further confirmed by the results of Hostetler et al[103b] where thiol with shorter chain length causes substantial disorder. Molecular dynamic simulation by Landman[117] corroborated this picture for 3D superlattice formation for Au nanoparticles. According to these theoretical studies, longer chain length (≥ C12 thiol) capped Au

nanoparticles bundle in tetragonally distorted fcc lattice eventhough smaller thiols result bcc superstructure at room temperature.

In the same fashion, hcp superlattice of silver nanoparticles was reported by Harfenist et al[153a] using TEM results. These particles were however, icosahedral in shape, in contrast to that spherical particles which formed fcc superlattice with specific orientational ordering.[153b] In comparison to metal nanoparticles, semiconductor nanoparticles are characterized by substantially weaker interparticle dispersion and hence very narrow particle size distribution is necessary for superlattice formation, even for short range ordering. Murray[154] showed that for CdSe quantum dots a long range ordering could be achieved for the ultra narrow size distribution (± 3%). This is the first such report to form artificial bulk solid from the Q-dots. Another method for superlattice formation of nanoparticles is through LB technique at the air-water interface, where the superlattice reveals three distinct phases depending upon the extra conical volume available for monolayer extension.[155]

1.5. PROPERTIES OF SAM/NANOCLUSTER ASSEMBLIES

The organization of SAM/Nanocluster assemblies arises due to the motivation that it has potential to control electrical, optical and magnetic properties in bulk self-assembled materials although, the type of superlattices that can be prepared in this manner are quite limited. Fabrication of such structure requires weakly interacting nanoclusters with very narrow size distribution. These particles automatically organize themselves depending upon the Coulombic interaction between them. For example, monodispersed nanoparticles easily form array as they have only a narrow size distribution (standard deviation upto 3%).[147] Some of the unique properties of such assemblies are mentioned below;

1.5.1 Electronic Properties

When a metal nanocluster is organized on a SAM surface, the I-V curves show interesting behavior due to Coulomb blockade effect where single electron tunnelling occurs. The charging energy (namely, the energy barrier that has to overcome to transfer a single electron from the neutral nanocluster to a nearest neutral nanocluster) is dependent on the interparticle capacitance C ($E_c = e^2/2C$; where e is the fundamental unit charge and C is capacitance). When Au MPCs are organized on a dodecanethiol (DDT) SAM functionalized Au (111) surface using toluene dispersion with STM tip on top, a double tunnel junction is formed through the tip-gap nanocluster as first junction and cluster-insulator-metal substrate as second junction. This phenomenon has been frequently demonstrated by using STM/STS.[14]

Solution state electronic properties of MPCs show similar quantized double layer charging which is analogous to the classical "ensemble Coulomb Staircase" experiments of MPCs.[83a] However, in this case the capacitance is associated with the ionic space charge formed around MPCs dissolved in an electrolyte solution. Because of the small (10^{-18} F) capacitance of MPCs, charging of the tiny capacitor by single electrons can occur in definite potential intervals.

1.5.2 Optical Properties

The arrays of nanoparticles display unique optical properties which are distinct from their respective bulk properties and even individual counterparts. To manipulate the shape, size and chemical composition, array geometry provides a flexible platform through the rational design of metallic and semiconducting quantum dots. When particles are organized into film, the plasmon absorption is red shifted due to the coupling of plasmon frequencies of

the neighbouring nanoclusters when these clusters are arranged in close-packed region[156a] as predicted theoretically.[156b]

For example, the multilayers of thiol Au nanoclusters[83a,157] reveal that with more number of particles, the coupling of plasmon increases; too much of a long range order may give absorbance red-shifted by several hundred nm. An additional band at 650 nm apart from the original peak at 520 nm in the Au colloid multilayer[157] corresponding to the region of interparticle plasmon coupling, gradually increases in the wavelength indicating the growth of assembly.

In one of the examples, Natan et al[158] have demonstrated that Au assemblies on Si substrates show higher absorbance in the near infra-red (NIR) region depending on the cross-linker length. These films which might have applications as dichroic coating, show aggregation of particles after drying along with a red shift in λ_{max} and broadening. Information about the composition of the film, if Ag/Au array is formed, is lost due to the combination of individual plasmon into collective plasmon oscillation. In additon, the Ag/Au multilayers display an increase in the absorbance over the entire visible range (350-820 nm) corresponding to additional particle coverage with each cross-linker/nanoparticle.

1.5.3 Magnetic Properties

Nanoclusters of magnetic materials prepared with a variety of shapes and sizes exhibit strong size-dependent properties that may provide useful information of immense technological importance in magnetic storage and microelectronics.[159] For example, Co nanoclusters show moderate crystal anisotropy enabling the observation of effects of size, shape, internal crystal structure, and surface anisotropy. Suitable preparation strategies like that

reported by Murray[159a] are extremely useful for designing artificial nanostructures for magnetic devices.

Magnetic nanoclusters with narrow size distribution (< 10%) can be deposited from appropriate solvents selected for its polarity and boiling point to assemble into superlattices. The solvent polarity is chosen so that the interaction between the nanoparticles will become mildly attractive as the solvent evaporates and the dispersion becomes more concentrated. Similarly, the boiling point is selected to permit the nanoclusters enough time to find the equilibrium lattice sites before the solvent evaporates on the growing superlattice. These superlattices are held together by weak van der Waals and dipolar magnetic attraction. They may be made more rigid and robust by selecting organic capping functional groups that will crosslink under suitable conditions like exposure to radiation or heating.[159a,c] In one of the significant illustrations, Murray and coworkers have shown that heating such a superlattice to ~300 ^{o}C under inert atmosphere causes cross linking between the organic capping groups forming an amorphous matrix between the nanoclusters,[159c] while heating in vacuum leads to the desorption of organic molecules resulting controlled sintering to finally yield a fully inorganic solid.[159c]

One of the important findings of these studies is that for an hcp array of Co nanoclusters, each Co cluster acts as a single magnetic domain. When the temperature is decreased below a critical temperature (blocking temperature, T_b) the magnetic moment is pinned along an “easy” axis and this acts as ferromagnetic, while, above the blocking temperature, thermal fluctuations randomize the moments causing hysteresis. Interestingly, when a magnetic superlattice is cooled with well controlled anisotropies, the transition from ferromagnetic to superparamagnetic becomes very narrow.[159a,c] The width of the hysteresis loop is found to decrease significantly with the decrease in size

(i.e. the energy barrier decreases). This shows that the measurement at 5 K in comparison to 298 K (random magnetization), transfers the material from ferromagnetic to superparamagnetic state.[159a] Even simple diamagnetic clusters like Au and Pd show size dependent paramagnetism[159d,e] and more studies are necessary to unravel their complex susceptibility features.

1.5.4 Electrochemical Properties

Electrochemical studies of nanoclusters and their assemblies are important because when the nanoparticles are organized on a suitable substrate through various type of linkages described above, it is possible to estimate their surface coverage especially if they are redox active. For example, when potential is applied in the range of –0.8 to +0.8 V vs. SCE to the electrode, where Au nanoparticles are anchored through covalent linkage in 0.1 M aqueous buffer solution, Au nanoparticle array shows reversible redox behaviour.[2b] The double layer capacitance obtained from the voltammogram is proportional to the integral area of the conductive array, so that the area can be calculated if the capacitance/cm^2 is known. The redox activity is preferably due to the mechanism $Au_n^o \rightarrow Au_n^+ + e^-$ and the redox peak increases with the number of layers. An approximate estimation of the number of particles[3c] in one layer gives 1.8 x 10^{12} clusters/cm^2 and time-dependent CV estimates the dynamics of the nanoclusters on the gold surface through the peak potential shifts and shape variations.[2a] The cross linking agents are estimated to be 1.5 x 10^{-11} moles/cm^2 per layer and by knowing the coverage of Au nanoparticles, one can estimate that *approx.* 100 cross linking molecules are attached to the gold nanoparticles.[160a,b] Variation of physico-chemical properties of the nanoparticle array[160c] is possible using potential dependent changes of the redox-state of the linkers.

Impedance measurements of Ag nanoarrays[148] reveal change in electronic properties as a function of the interparticle separation. For example,

inductive behavior is clearly seen at smaller interparticle separation while as the particle separation increases the array becomes an insulator. As the separation decreases, the RC type tunnelling transport switches to coherent long-range transport. The major limitations of the electrochemistry are the potential induced reorganization of nanoarrays, changes due to solvent entrapment and etching of the nanoparticles due to cycling.

1.5.5 Other Properties

Apart from above interesting properties observed for these assemblies, the organized nanoparticle monolayers can also have a masking effect for the gold evaporation.[161] If the individual particles in an organized monolayer "stick together" (thin Au film evaporation), then the entire monolayer may be removed from the substrate in one piece.[161b] Electronic nanocluster based devices can be built taking advantage of the precise placement and engineering of nanoclusters leading the fabrication of sensors exploiting the properties of both the nanocluster and cross linking materials. In some cases, as the particle size increases metallic regions begin to appear (with increasing particle density or layer growth) and the light scattering and reflectance from the assemblies and these components become important. This scattering appears in the region 650-800 nm and reflectance occurs over the entire frequency range. This causes broadening in UV-Vis spectra due to the generation of multilayers.[141a,158a]

1.6. APPLICATIONS

Arrays prepared by self-assembly technique are attractive for several exciting applications due to the possibility of engineering the surfaces at the molecular level. The chemical properties can be fine tuned by selecting various sizes of nanoclusters and a large variety of flexibility in monolayers can be utilized to evaluate the theories of single electron tunnelling, optical

enhancement, molecular recognition and related phenomena. Some of the recent applications are mentioned below:

1.6.1 Conventional devices

During the past 24 years, the number of transistors integrated onto a single chip has increased by a factor of 16,000, or by a factor of four in every 3.4 years. The present size of microelectronic components is significantly below 1 micron, with the current generation of integrated circuits reaching 0.1μm features. This phenomenal increase in circuit capability is now known as Moore's Law. Compared to the ENIAC (which was first powered up fifty years ago) the present generation of microprocessors can compute 60,000 times faster using few milliwatt of the power with greater reliability.

Many times in the past two decades, the end of Moore's law has been predicted with the limiting factors being the increasing complexity of the integrated circuits on the inability of optical lithography to scale down dimensions smaller than the wavelength of light. So far, ingenious engineering (various optical and chemical tricks to lithography) simultaneously with the commitment of significant resources has been able to overcome these limitations by utilizing increasingly sophisticated computer algorithms to aid in the design of the circuits. However, as feature sizes shrink enormously into the nanometer size regime, fundamental limitations begin to appear including the impossibility of requiring a fraction of an electron to continue the scaling of a device into the nm domain, as well as more enigmatic quantum mechanical issues such as size quantization enabling significant gaps between allowed energy levels and the dependence of electron tunnelling through ultrathin insulating barriers.

Thus, if the exponential downscaling of electronic devices is to be continued beyond 2010 as per few forecasts, dramatic changes in device

design and operating principles are essential. Discussions regarding the absolute limits of electronic circuitry shows that[162] the ultimate performance of a Boolean logic computing machine is limited only by fundamental physical constants and the laws of thermodynamics. More specifically, Feynman's analysis shows that it is physically possible to perform calculations one billion times faster than the currently used microprocessors but using few watts of power. There are presumably huge rewards in store for pushing into the nanometer size range and learning how to harness quantum phenomena as the operating basis for electronic, optical, magnetic, and chemical technologies. Such nanostructures offer excellent future potential for enormous increase in information storage capacity and computational throughput, due to their packing density and the short information transit times. In addition, they offer greatly decreased voltage and power requirements for all types of optical sources (from high performance communications lasers to general illumination) although we need to fabricate functional nanostructures in huge quantities with extremely uniform and controlled size, shape, and composition distributions to enjoy these benefits in the future.

1.6.2 Molecular Electronics

Metal nanoclusters have proved to be one of the possible alternatives to semiconductor based integrated circuits, information storage devices etc.[2,3] A novel nanoelectronic component devised this year is a nanoscale transistor that can be switched between "on" and "off" states with a single electron and works efficiently at room temperature. The tiny field effect transistors (FETs) are individually controllable and can be integrated on a single chip. Prior to this study, nanoparticle FETs could not be turned on and off individually.[3b] Similarly, when an aqueous suspension of metallic nanoparticles in an alternating current field between two planar electrodes, the particles assembled into conducting microwires that grew from one electrode to the other.[163] The wires are not the nanowire type, their diameters are micrometers across, but the method

represents an easy way to create electrical connections in liquid environments. These wires could be used in wet electronic and bioelectronic circuits, including chemical sensors. In another key step toward single-molecule electronic devices, researchers wired a single molecule into an electrical circuit by chemically bonding the two molecular ends to metal conductors.[163b] Thus, current-voltage characteristics of the resulting circuit could be studied. A nanoparticle could be tethered to the ends of an octanedithiol molecular wire and then a conducting tip of an atomic force microscope was used to contact the nanoparticle, forming a circuit.

1.6.3 Micro Electromechanical Systems (MEMS)

Chemical control of the surface functionality and hence surface interaction is one of the key issues in the design, fabrication, and operation of microelectromechanical systems (MEMS). Since the majority of the current MEMS devices are made of silicon by surface micromachining, an attractive approach is to use the well-know alkyltrichloro silane or trimethoxy silane self-assembled monolayers (SAM) on oxidized silicon surfaces to control surface energy. While this approach has enjoyed some success in reducing adhesion in model MEMS structures (e.g. microgears), a major impediment to its commercial implementation is its lack of reliability. Assembly of organic monolayers directly onto the silicon surface via Si-O linkages by the reaction between an alcoholic functional group and a chlorinated Si surface seems to be more efficient,[164] since the resulting molecular monolayer is more stable as illustrated in a model MEMS structure of a cantilever beam array (CMA). Major advantages of this new approach for surface control in MEMS include simplicity, reproducibility, and reliability.

A similar approach to fabricate active MEMS devices from nanoparticles have been recently demonstrated by a three-step process utilizing an ink jet print head for the selective deposition of either semiconducting or metallic

nanoparticles (100 layer thick) on plastic/glass substrates.[165] The nanoparticles had very low melting temperature (<1000 ^{o}C) compared to bulk volume,[166] the reduction in melting temperature was even called nanotectic. When such materials were deposited at low temperature, it could withstand subsequent exposure to high heat and are essentially equivalent in terms of structure and morphology to what is traditionally created in a vacuum.

1.6.4 Newly emerging applications

Photonics is a newly emerging application for nanoclusters as the excitonic coupling in nanoparticle arrays can drive highly efficient interactions with photons though the structure is of subnanometer size. It is possible to envisage high efficiency in fully three-dimensional optical switches based on such interactions. For example, the quantum entanglement of two luminescent species interconnected by a suitable SAM molecule can form the basis of a quantum bit (Q-bit), the prerequisite for quantum computation. Similarly, the NLO effects of organic molecules can be coupled with size-confinement behavior of clusters using SAM methodology for harnessing new type of photonic materials. In the same fashion, some of the recent studies have shown that tiny nanoclusters of metallic gold (between 20 and 40 atoms) encapsulated by a common biomolecule displays distinctly chiral properties, a puzzling phenomena which needs explanation.[167]

A unified understanding of the electromagnetic interaction of nanoclusters and monolayer-cluster sandwich assemblies with tunable length scales will unravel several fundamental questions of photon-solid interactions within a fully quantum electrodynamic framework. In addition, investigations of resonant absorption phenomena as a function of material dimensionality, symmetry, and excitonic structure would give several surprises for photonic applications. For example, photon emission in confined and geometrically complex architectures are not well understood especially due to quantum

electrodynamic (QED) boundary effects and unknown entanglement of excited states through local, nanoscale geometries. Several of these optical nonlinearities will be probed in the coming years for nano-particle proximity effects using artificially prepared nanocluster-organic molecule assemblies with controlled size and spacing.[57-60]

1.7. CONCLUSIONS AND PERSPECTIVES

Thus SAM formation in two-dimension and three-dimension has proved to be one of the most useful concepts towards fulfilling the initial promise of nanoelectronic architectures. Ordered superstructures formed using monolayers and MPCs can harness the size and shape dependent electrical/optical properties for several unique electronic components. Although there are well-established methods to synthesize and organize selected nanocluster assemblies on various metallic, semiconducting and insulating substrates, several problems require immediate attention.

1.8. MOTIVATION, SCOPE AND ORGANIZATION OF THE THESIS

The thesis addresses some of the major issues of self-assembled monolayers and their efficient use for organization of nanoclusters, the motivation being both fundamental and technological application in nanotechnology. This includes preliminary studies of several SAM forming molecules on various substrates, their application towards 3D SAM formation and behavior of these self-assemblies on solid substrates carved through various types of linkages. Some amount of details have been provided about 2D SAM formation, their comparison with LB film and a brief overview about 3D SAM on cluster followed by the preparation and characterization of ultrathin film formation with alternating layers of organic interconnects and metal nanoparticles.[67,168] The work described in this thesis addresses the issues related to self-assembled monolayers and their utilization for organizing Au, Ag

and Cu nanoclusters (i.e. nanoarrays) using different modes of interaction. More specifically, the inherent flexibility in the selection of organic molecules with respect to chain length and functional groups is attractive for creating molecular level hybrid nanostructures to explore new properties and effects. Since the main focus is on functional nanostructures with metallic clusters, related self-assemblies using inorganic solids[56] or biosurfaces[169] are not included.

1.9. OBJECTIVES OF THE PRESENT STUDY

From the foregoing critical review of SAMs, MPCs and nanoparticle assemblies on various substrates it is clear that several limitations continue to exist preventing their wide utilization for various electronic applications. Hence, it will be interesting to study the organization of these functionalized surfaces with precise control on certain parameters like chainlength, aromaticity, nature of functional groups etc. in order to overcome some of the limitations in these systems. This is especially significant for designing hybrid systems for applications in molecular electronics since disorder induced by one of these variables can adversely affect the device performance. The specific objectives of the work embodied in this thesis are set out in this perspective as described below:

(a) To study the effect of π-system and constraints imposed by the fused aromatic rings on self-assembled monolayers and hence the formation with respect to long chain thiols as standard;

(b) To understand the application of bifunctional monolayers for solid-state material synthesis and the mechanism of nucleation of ceramic materials on functionalized surfaces;

(c) To design a system which will give well-ordered 2D arrays of MPCs;

(d) To investigate the electronic properties of these materials and their organizations at room temperature and low-temperature to unravel quantum level phenomena like Coulomb blockade;

(e) To explore the potential application of dithiol molecules with different chainlengths in 3D organization of metal nanoclusters;
(f) To reveal the array formation of metal clusters using different chainlength molecules;
(g) To examine the adsorption kinetics of nanoclusters on functionalized surfaces;
(h) To demonstrate the possibility of hydrophobic organization of nanoclusters and to compare with conventional routes of array formation.

The thesis consists of six chapters. Chapter one is a general introduction to the investigation giving a critical review about self-assembled monolayers and monolayer-protected nanoclusters, types of interactions used for the nanocluster assemblies (2D & 3D), need for such an organization and different protocols currently in vogue for nanocluster organization. A critical review about the guided assemblies of nanoclusters using diverse mode of interactions through organic monomolecular spacers is followed by their application for nanoelectronic and optoelectronic devices. The chapter ends by mentioning explicitly the existing lacunae, specific objectives, future prospects for next 10 years and finally with the synopsis of the thesis.

As monolayer formation plays a key role in defining/tuning the size and shape of nanoparticles, the effect imposed by the molecular structure in 2D is discussed in second chapter with several organic molecules of similar structures. The molecules are chosen on the basis of their geometrical similarity. Hence, it is interesting to compare and study SAM of small molecules, which lack the hydrophobic ordering influence of a hydrocarbon chain. More significantly, the effect of π-system on molecular level interchain interaction is evaluated. The geometric constraint imposed by the rigid naphthalene ring for Naphthalene disulfide (NDS), which inhibits the cleavage of S-S bond, is discussed which adversely affects the monolayer organization

and stability relative to the monolayers formed with diphenyl disulfide (DDS) and diphenyl diselenide (DDSe). The chapter is further extended to investigate the utility of SAM for the nucleation mechanism of ceramic thin films at functionalized surfaces.

In Chapter 3 we demonstrate the preparation and structural characterization of multilayered Ag nanocluster (1.9 ± 0.4 nm) arrays by the sequential self-assembly of C_5 and C_8-dithiol molecular interconnects on Au (111) substrate. Quartz crystal microbalance (QCM) results suggest high coverage of dithiol molecule (99%) as well as Ag nanocluster concentration (*ca.* 10^{11} clusters/cm^2) on the functionalized surface. The formation of silver nanocluster arrays was confirmed using Atomic Force Microscopy (AFM) while the low angle x-ray diffraction patterns reflect the long-range periodicity with an approximate interparticle spacing of 2.3 nm. The redox accessibility of these passivated clusters is confirmed since $1e^-$ transfer ($\Delta E \approx 60$ mV; $I_{pa}/I_{pc} \approx 1$) behavior is observed with an estimated surface coverage of *ca.* 1.95 x 10^{-10} mol/cm^2. The room temperature emission spectra (Photoluminescence) suggest the formation of minibands in the superlattice structure due to the electronic coupling between silver nanoclusters.

A novel method to organize the monolayer protected Au clusters using hydrophobic forces between the methyl ends of thiol functionalized Au (111) surfaces and MPCs is presented in chapter four. More specifically, hydrophobic organization of 4.8±0.5 nm core diameter Au clusters is demonstrated in contrast to the conventional covalent and electrostatic interactions where specific bifunctional molecules are used. QCM result shows a slow attainment of saturation coverage (10^{10} clusters/cm^2) of Au nanoclusters on SAM functionalized substrate and the equilibrium constant (K_{eq}) is three times less compared to that for the monolayer formation using dodecanethiol. The electronic and optical properties of these films show that the Au colloids maintain their individual characteristics without fusion to larger units, and the

current-voltage behavior shows significant non-linearity. Electrochemical studies illustrate the redox accessibility of these MPCs with a surface coverage of 2.15 x 10^{-9} mol/cm^2 on SAM functionalized surface.

A detailed study about the low temperature electronic properties of disordered Q-dot arrays is described in chapter five. The protected nanocluster arrays of Cu, Ag and Au reveal insulating to metallic transition at low temperatures. The disappearance of Kubo gap at low temperature in these systems, where the interparticle spacing (0.5-1 nm) is less than the nanocluster dimensions (10-15 nm), is explained to effect the transition due to strongly coupled charge fluctuations and cluster vibrations. For the same interparticle separation of Cu, Ag and Au clusters, the transition temperature is found to vary significantly, possibly due to the difference in localization arising from the lack of precise size distribution. Electronic properties of hydrophobically organized nanoclusters were studied using Kelvin probe method at room temperature. The I-V characteristic is chain-length dependent and the effect of π-cloud imposed by the presence of phenyl rings has been investigated.

Chapter six outlines a summary of all the major conclusions of the present study with respect to the organization of nanoclusters on a functionalized surface. The effect of π-system on self-assembly and application of SAM for solid-material synthesis is briefly summarized. The room temperature electronic properties of organized nanoclusters and low-temperature properties of disordered quantum-dot superstructures is briefly epitomized.

These studies have shown the clear significance of harnessing organic molecules to modulate cluster-cluster, cluster-molecule interactions during the preparation of hybrid nanostructures. More significantly, the electron transfer behaviour is not inhibited by the presence of these organic molecules and it is possible to choose suitable alkyl chains to control the electronic properties of

these metallic quantum dot arrays. Although few such superstructure assemblies with high degree of ordering have been demonstrated; some of them lack complete order due to the reorganizational capabilities of organic molecules. Another important limitation is the lack of precise control as compared to the use of sophisticated methods like molecular beam epitaxy (MBE). Nevertheless, this simple chemical method of preparation of such controlled architecture is useful to understand several important issues related to electron transfer in these hybrid assemblies and their applications.

1.10. REFERENCES

1. Feynman, R.P., in a lecture delivered at the *American Physical Society Metting*, **1959**.

2. (a) Chen, S. *J. Phys. Chem.B* **2001**, *104*, 663. (b) Pileni, M.P. *J. Phy. Chem.B* **2001**, *104*, 3358. (b) Shipway, A.N.; Lahav, M.; Willner, I. *Adv. Mater.* **2000**, *12*, 993. (c) Whetten, R.L.; Shafigullin, M.N.; Khoury, J.T.; Schaaff, T.G.; Vezmar, I.; Alvarez, M.M.; Wilkinson, A. *Acc. Chem. Res.* **1999**, *32*, 397. (d) Schmid, G.; Baumle, M.; Greekens, M.; Heim, I.; Osemann, C.; Sawitwoski, T. *Chem. Soc. Rev.* **1999**, *28*, 179.

3. (a) Feldheim, D.L. *Nature* **2000**, *408*, 45. (b) Gittins, D.I.; Bethell, D.; Schiffrin, D.J.; Nichols, R.J. *Nature* **2000**, *408*, 67. (c) Shipway, A.N.; Katz, E.; Willner, I. *ChemPhysChem* **2000**, *1*, 18. (d) Rao, C.N.R.; Kulkarni, G.U.; Thomas, P.J.; Edwards, P.P. *Chem. Soc. Rev.* **2000**, *29*, 27. (e) Mirkin, C.A. *Inorg. Chem.* **2000**, *39*, 2258. (f) Colvin, V. L.; Schlamp, M. C.; Allvisatos, A. P. *Nature* **1994**, *354*, 370. (g) Murray, C.B.; Kagan, C.R.; Bawendi, M.G. *Science* **1995**, *270*, 1335.

4. Markovich, G.; Leff, D.V.; Chung, S.W.; Soyez, H.M.; Dunn, B.; Heath, J.R. *Appl. Phys. Lett.* **1997**, *70*, 3107.

5. Lyon, L.A.; Pena, D.J.; Natan, M.J. *J. Phys. Chem. B* **1999**, *103*, 5826.

6. Peschel, S.; Schmid, G. *Angew. Chem. Int. Ed. Engl.* **1995**, *34*, 1442.

7. Andres, R.P.; Bein, T.; Dorogi, M.; Feng, S.; Henderson, J.I.; Kubiak, C.P.; Mahoney, W.; Osifchin, R.G.; Reinfenberger, R. *Science* **1996**, *272*, 1323.

8. Fendler, J.H. *Chem. Mater.* **1996**, *8*, 1616.

9. (a) Hayat, M.A. *Colloidal Gold: Principles, Methods and Applications*, Academic Press, NY 1989, vol.1.(b) Haberland, H. *Clusters of atoms and molecules*, Springer, NY 1994.

10. (a) Kreibig, U.; Bonnenmann, H.; Hormes, J. *Nanostructured metal clusters and colloids*: Handbook of surfaces and interfaces of materials, Vol. 3, 2001, Academic Press, San Diego, USA. (b) Alivisatos, A. P. *Science* **1996**, *271*, 933. (c) Collier, C. P.; Saykally, R. J.; Shiang, J. J.; Henrichs, S. E. Heath, J. R. *Science* **1997**, *277*, 1978.

11. Fecilla, P.; Dixon, R.P.; Slobodkin, G.; Alvi, D.S.; Waldeck, D.H.; Hamilton, A.D. *J. Am. Chem. Soc.* **1990**, *112*, 9408.

12. Becka, A.M.; Miller, C.A. *J. Phys. Chem.* **1993**, *97*, 6233.

13. Feldheim, D.L.; Keating, C.D. *Chem. Soc. Rev.* **1998**, *27*, 1.

14. Dorogi, M.; Gomez, J.; Osifchin, R.; Andres, R.P.; Reinfenberger, R. *Phy. Rev. B* **1995**, *52*, 9071.

15. Duan, C.; Meyerhoff, M.E. *Anal. Chem.* **1994**, *66*, 1369.

16. Bain, C.D.; Whitesides, G.M. *J. Am. Chem. Soc.* **1988**, *110*, 5897.

17. Laibinis, P.E.; Whitesides, G.M. *J. Am. Chem. Soc.* **1992**, *114*, 9022.

18. Prime, K.L.; Whitesides, G.M. *Science* **1991**, *252*, 1164.

19. Sagiv, J. *J. Am. Chem. Soc.* **1980**, *102*, 92.

20. Heflin, J.R.; Figura, C.; Marciu, D.; Liu, Y.; Claus, R.O. *Appl. Phys. Lett.* **1999**, *74*, 495.

21. Sigal, G.B.; Mrksich, M.; Whitesides, G.M. *J. Am. Chem. Soc.* **1998**, *120*, 3464.

22. Blodgett, K.B.; Langmuir, I. *Phys. Rev.* **1937**, *51*, 964.

23. Keller, S.W.; Kim, H.N.; Mallouk, T.E. *J. Am. Chem. Soc.* **1994**, *116*, 8817.

24. Ulman, A. *An Introduction to Ultrathin Organic Films: From Lamguir-Blodgett to Self-assembly*, Academic Press: Boston 1991.

25. Tao, Y.; Lee, M.; Chang, S. *J. Am. Chem. Soc.* **1993**, *115*, 9547.

26. Dubois, L.H.; Nuzzo, R.G. *Annu. Rev. Phy. Chem.* **1992**, *43*, 437.

27. Prime, L.K.; Whitesides, G.M. *Science* **1991**, *252*, 1164.

28. Krishnamoorthy, A.; Chanda, K.; Murarka, S.P.; Ramanath, G.; Ryan, J.G. *Appl. Phys. Lett.* **2001**, *78*, 2467.

29. Ulman, A. *Chem. Rev.* **1996**, *96*, 1533.

30. Bishop, A.R.; Nuzzo, R.G. *Curr. Opin. Colloid Interf. Sci.* **1996**, *1*, 127.

31. Z.L. Wang, *Characterization of nanophase Materials*, 1st ed.; Z.L. Wang ed.; Wiley-VCH: Weinheim, Germany, **2000**; vol.1 p.406.

32. (a) Strong, L.; Whitesides, G.M. *Langmuir* **1988**, *4*, 546. (b) Lee, K.A.B.; Johnson, S.C. *Langmuir* **1990**, *6*, 709.

33. Dubois, L.H.; Zegarski, B.R. *J.Chem. Phy.* **1993**, *98*, 678.

34. Chidsey, C.E.D.; Liu, G.; Rowntree, P.; Sooles, G. *J. Chem. Phy.* **1989**, *91*, 4421.

35. Alves, C.A.; Smith, E.L.; Porter, M.D. *J. Am. Chem. Soc.* **1992**, *114*, 1222.

36. Camillone III, N.; Chidsey, C.E.D. ; Liu, G.; Rowntree, P.; Sooles, G. *J. Chem. Phy.* **1993**, *98*, 3503.

37. Poirier, G.E.; Tarlov, M.J. *Langmuir* **1994**, *10*, 2853.

38. McCarley, R.L.; Dunaway, D.J.; Willicut, R.J. *Langmuir* **1993**, *9*, 2775.

39. Schonenberger, C.; Sondag-Heuthorst, J.A.M.; Jorritsma, J.; Fokkink, L.G.J. *Langmuir* **1994**, *10*, 611.

40. Bucher, J.P.; Santesson, L.; Kern, K. *Langmuir* **1994**, *10*, 979.

41. Porter, M.D.; Bright, T.B; Allara, D.L.; Chidsey, C.E.D. *J. Am. Chem. Soc.* **1987**, *109*, 3559.

42. (a) Shipway, A.N.; Willner, I. *Acc. Chem. Res.* **2001**, *34*, 421. (b) Collier, C.P.; Mattersteig, G.; Wong, E.W.; Luo, Y.; Beverly, K.; Sampaio, J.; Raymo, F.M.; Stoddart, J.F.; Heath, J.R. *Science* **2000**, *289*, 1172.

43. Bandyophadhyay, K.; Vijayamohanan, K. *Langmuir* **1998**, *14*, 6924.

44. Poirier, G.E. *Chem. Rev.* **1997**, *97*, 1117.

45. Lipkowski, J.; Ross, P.N. (Ed.), *Adsorption of molecules at metal surfaces*, NY, 1992.

46. (a) Finklae, H.O.; Avery, S.; Lynch, M.; Furtsch, T. *Langmuir* **1987**, *3*, 409. (b) Hartman, J.; Kelvin, M.J. *Chem. Phys.* **1989**, *91*, 4994.

47. (a) Finklae, H.O.; Hanshew, D.D. *J. Am. Chem. Soc.* **1992**, *114*, 3173. (b) Bain, C.D.; Whitesides, G.M. *Langmuir* **1989**, *5*, 1370. (c) Ulman, A.; Evans, S.D.; Shnidman, Y.; Sharma, R.; Eilers, J.E.; Chang, J.C. *J. Am. Chem. Soc.* **1991**, *113*, 1499.

48. Abbott, N.L.; Folker, J.P.; Whitesides, G.M. *Science* **1992**, *257*, 1380. (b) Chidsey, C.E.D.; Loiacono, D.N. *Langmuir* **1990**, *6*, 682.

49. Kaelble, D.H. *Physical Chemistry of Adhesion*, Wiley-Interscience; New York, 1971.

50. Colvin, V.L.; Goldstein, A.N.; Alivisatios, A.P. *J. Am. Chem. Soc.* **1992**, *114*, 5221.

51. Chumanov, G.; Sokolov, K.; Gregory, B.W.; Cotton, T.M. *J. Phys. Chem.* **1995**, *99*, 9466.

52. Grabar, K.C.; Smith, P.C.; Musick, M.D.; Davis, J.A.; Walter, D.G.; Dickson, M.A.; Guthrie, A.P.; Natan, M.J. *J. Am. Chem. Soc.* **1996**, *118*, 1148.

53. Bandyopadhyay, K.; Patil, V.; Vijayamohanan, K.; Sastry, M. *Langmuir* **1997**, *13*, 5244.

54. Garcia, M.E.; Baker, L.A.; Crooks, R.M. *Anal. Chem.* **1999**, *71*, 256.

55. Vijayasarathi, K.; Thomas, J.P.; Kulkarni, G.U.; Rao, C.N.R. *J. Phys. Chem. B* **1999**, *103*, 399.

56. Keller, S.W.; Johnson, S.A.; Brigham, E.S.; Yonemoto, E.H.; Mallouk, T.E. *J. Am. Chem. Soc.* **1995**, *117*, 12879.

57. Ansell, M.A.; Zeppenfeld, A.C.; Yoshimoto, K.; Cogan, E.B.; Page, C.J. *Chem. Mater.* **1996**, *8*, 591.

58. Strong, A.E.; Moore, B.D. *J. Mater. Chem.* **1999**, *9*, 1097.

59. Bain, C.D.; Troughton, E.D.; Tao, Y.T.; Evall, J.; Whitesides, G.M.; Nuzzo, R.G. *J. Am. Chem. Soc.* **1989**, *111*, 321.

60. Miller, C.; Cuendet, P.; Grätzel, M. *J. Phys. Chem.* **1991**, *95*, 877.

61. (a) Kwan, W.S.V.; Atanasoska, L.; Miller, L.L. *Langmuir* **1991**, *7*, 1419. (b) Kwan, W.S.V.; Cammarata, V.; Miller, L.L.; Hill, M.G.; Mann, K.R. *Langmuir* **1992**, *8*, 3003. (c) Sabatani, E.; Cohen-Boulakia, J.; Bruening, M.; Rubinstein, I. *Langmuir* **1993**, *9*, 2974. (d) Dhirni, A.; Zener, R.W.; Hsung, R.P.; Guyot-Sionnest, P.; Sita, L.R. *J. Am. Chem. Soc.* **1996**, *118*, 3319.

62. (a) Chang, S.C.; Chao, I.; Tao, Y. *J. Am. Chem. Soc.* **1994**, *116*, 6792. (b) Tour, M.J.; Jones, L.; Pearson, D.L.; Lamba, J.J.S.; Burgin, T.P.; Whitesides, G.M.; Allara, D.L.; Parikh, A.N.; Atre, S.V. *J. Am. Chem. Soc.* **1995**, *117*, 9529.

63. Hutchison, J.E.; Postlethwaite, T.A.; Murray, R.W. *Langmuir* **1993**, *9*, 3277.

64. Ulman, A.; Scaringe, R.P. *Langmuir* **1992**, *8*, 894.

65. Brust, M.; Walker, M.; Bethell, D.; Schiffrin, D.J.; Whyman, R. *J. Chem. Soc. Chem. Commun.* **1994**, 801.

66. Terril, R.H.; Postlethwaite, T.A.; Chen, C.H.; Poon, C.D.; Terzis, A.; Chen, A.; Hutchison, J.E.; Clark, M.R.; Wignall, G.; Londono, J.D.; Superfine, R.; Falvo, M.; Johnson, C.S.Jr.; Samulski, E.T.; Murray, R.W. *J. Am. Chem. Soc.* **1995**, *117*, 12537.

67. Sarathy, K.V.; Raina, G.; Yadav, R.T.; Kulkarni, G.U.; Rao, C.N.R. *J. Phys. Chem. B* **1997**, *101*, 9876.

68. Chaki, N.K.; Sudrik, S.; Sonawane, G.; Vijayamohanan, K. *Chem. Commun.* **2002**, 76.

69. Fendler, J.H.; Meldrum, F.C. *Adv. Mater.* **1995**, *7*, 607.

70. Hostetler, M.J.; Stokes, J.J.; Murray, R.W. *Langmuir* **1996**, *12*, 3604.

71. Whetten, R.L.; Khoury, J.T.; Alvaraz, M.M.; Murthy, S.; Vezmar, I.; Wang, Z.L.; Stephens, P.W.; Cleland, C.L.; Luedtke, W.D.; Landamn, U. *Adv. Mater.***1996**, *8(5)*, 428.

72. Henglein, A. *Chem. Rev.* **1989**, *89*, 1861.

73. (a) Devoret, M.H.; Esteve, D.; Urbina, C. *Nature* **1992**, *360*, 547. (b) Nakazato, K.; Ahmed, H. *Adv. Mater.* **1993**, *5*, 668.

74. (a) Salata, O.V.; Dobson, P.J.; Hull, P.J.; Hutchison, J.L. *Adv. Mater.* **1994**, *6*, 772. (b) Martucci, A.; Innocenzi, P.; Fick, J.; Mackenzie, J.D. *Non-Cryst. Solids* **1999**, *244*, 55.

75. (a) Wang, Y. *Acc. Chem. Res.* **1991**, *24*, 133. (b) Kane, S.R.; Cohen, R.E.; Silbey, R. *Chem. Mater.* **1996**, *8*, 1919.

76. (a) Fendler, J.H. *Chem. Rev.* **1987**, *87*, 877. (b) Liveri, V.T.; Rossi, M.; D'Arrigo, G.; Manno, D.; Micocci, G. *Appl. Phys. A* **1999**, *69*, 369.

77. Yang, J.P.; Qadri, S.B.; Ratna, B.R. *J. Phys. Chem.* **1996**, *100*, 17255.

78. (a) Meldrum, F.C.; Flath, J.; Knoll, W. *Langmuir* **1997**, *13*, 2033. (b) Wang, Y.; Herron, N. *J. Phys. Chem.* **1991**, *95*, 525.

79. (a) Steigerwald, M.L.; Brus, L.E. *Acc. Chem. Res.* **1990**, *23*, 183. (b) Nirmal, M.; Brus, L.; *Acc. Chem. Res.* **1999**, *32*, 407. (c) Empedocles, S.; Bawendi, M.G. *Acc. Chem. Res.* **1999**, *32*, 389.

80. (a) Alivisatos, A.P. *J. Phys. Chem.* **1996**, *100*, 13226. (b) Peng, X.; Wickham, J.; Alivisatos, A.P. *J. Am. Chem. Soc.* **1998**, *120*, 5343. (c) Bruchez, M., Jr.; Moronne, M.; Gin, P.; Weiss, S.; Alivisatos, A.P. *Science* **1998**, *281*, 2013. (d) Chan, W.C.W.; Nie, S. *Science* **1998**, *281*, 2016.

81. (a) Nosaka, Y.; Yamaguchi, K.; Miyama, H.; Hayashi, H. *Chem. Lett.* **1988**, *605*. (b) Fischer, C.H.; Henglein, A. *J. Phys. Chem.* **1989**, *93*, 5578. (c) Rogach, A.L.; Kornowski, A.; Gao, M.; Eychmuller, A.; Weller, H. *J. Phys. Chem. B* **1999**, *103*, 3065.
82. (a) Schneider, J.J. *Adv. Mater.* **2001**, *13*, 529. (b) Caruso, F. *Adv. Mater.* **2001**, *13*, 11.

83. (a) Templeton, A.C.; Wuelfing, M.P.; Murray, R.W. *Acc. Chem. Res.* **2000**, *33*, 27. (b) Steigerwald, M.L.; Alivisatos, A.P.; Gibson, J.M.; Harris, D.T.; Kortan, R.; Muller, A.J.; Thayer, A.M.; Duncan, T.M.; Douglass, D.C.; Brus, L.E. *J. Am. Chem. Soc.* **1998**, *110*, 3046.

84. Giersig, M.; Ung, T.; Liz-Marzan, L.M.; Mulvaney, P. *Adv. Mater.* **1997**, *9*, 570.

85. Ung, T.; Liz-Marzan, L.M.; Mulvaney, P. *J. Phys. Chem. B* **1999**, *103*, 6770.

86. Oldfield, G.; Ung, T.; Mulvaney, P. *Adv. Mater.* **2000**, *12(20)*, 1519.

87. (a) Wang, Y.; Toshima, N. *J. Phys. Chem. B* **1997**, *101*, 5301. (b) Tong, Y.Y.; Yonezawa, T.; Toshima, N.; van der Klink, J.J. *J. Phys. Chem.* **1996**, *100*, 730.

88. (a) Schmid, G.; West, H.; Malm, J.O.; Bovin, J.O.; Grenthe, C. *Chem. Eur. J.* **1996**, *2*, 1099. (b) Lee, A.F.; Baddeley, C.J.; Hardacre, C.; Ormerod, R.M.; Lambert, R.M.; Schmid, G.; West, H. *J. Phys. Chem.* **1995**, *99*, 6096.

89. (a) Michaelis, M.; Henglein, A.; Mulvaney, P. *J. Phys. Chem.* **1994**, *98*, 6931. (b) Esumi, K.; Wahabayashi, M.; Torigue, K.; *Colloids Surf. A* **1996**, *109*, 55.

90. Bradley, J.S.; Hilll, E.W.; Klein, C.; Chaudret, B.; Duteil, A. *Chem. Mater.* **1993**, *5*, 254.

91. (a) Collier, C.P.; Saykally, R.J.; Shiang, J.J.; Henrichs, S.E.; Heath, J.R. *Science* **1997**, *277*, 1978. (b) Hostetler, M.J.; Zhong, C.J.; Yen, B.K.H.; Anderegg, J.; Gross, S.M.; Evans, N.D.; Porter, M.; Murray, R.W. *J. Am. Chem. Soc.* **1998**, *120*, 9396.
92. (a) Faraday, M. *Philos. Trans. R. Soc. London* **1857**, *147*, 145. (b) Schmid, G.; Chi, L.F. *Adv. Mater.* **1998**, *10*, 515.

93. Turkevich, J.; Stevenson, P.C.; Hillier, J. *Discuss. Faraday Soc.* **1951**, 55.

94. Brust, M.; Fink, J.; Bethell, D.; Shiffrin, D.J.; Kiely, C. *J. Chem. Soc. Chem. Commun.* **1995**, 1655.

95. (a) Baum, T.; Bethell, D.; Brust, M.; Schiffrin, D.J. *Langmuir* **1999**, *15*, 866. (b) Brust, M.; Kiely, C.J.; Bethell, D.; Schiffrin, D.J. *J. Am. Chem. Soc.* **1998**, *120*, 12367. (c) Kiely, C.J.; Fink, J.; Brust, M.; Bethell, D.; Shiffrin, D.J. *Nature* **1998**, *396*, 444.

96. Porter, Jr., L.A.; Ji, D.; Westcott, S.L.; Graupe, M.; Czernuszewicz, R.S.; Halas, N.J. Lee, T.R. *Langmuir* **1998**, *14*, 7378.

97. Ahmadi,T.S.; Wang, Z.L.; Green, T.C.; Henglein, M.A.; M.A. El-Sayed, *Science* **1996**, *272*, 1924.

98. Andres, R.P.; Bielefeld, J.D.; Henderson, J.I.; Janes, D.B.; Kolagunta, V.R.; Kubiak, C.P.; Mahoney, W.J.; Osifchin, R.G. *Science* **1996**, *273*, 1690.

99. Chumanov, G.; Sokolov, K.; Gregory, B.W.; Cotton, T.M. *J. Phys. Chem.* **1995**, *99*, 9466.

100. (a) Jensen, T.R.; Schatz. G.C.; Van Duyne R.P.; *J. Phys. Chem. B* **1999**, *103*, 2394. (b) Gilbert, S.E.; Cavalleri, O.; Kern, K.; *J. Phys. Chem.* **1996**, *100*, 12123. (c) Urquhart, R.S.; Furlong, D.N.; Gengenbach, T.; Geddes, N.J.; Grieser, F. *Langmuir* **1995**, *11*, 1127.

101. (a) Esumi, K.; Suzuki, A.; Aihara, N.; Usui, K.; Torigoe, K. *Langmuir* **1998**, *14*, 3157. (b) Teranishi, T.; Kiyokawa, I.; Miyake, M. *Adv. Mater.* **1998**, *10*, 596. (c) Wuelfing, W.P.; Gross, S.M.; Miles, D.T.; Murray, R.W. *J. Am. Chem. Soc.* **1998**, *120*, 12696. (d) Spatz, J.P.; Roescher, A.; Moller, M. *Adv. Mater.* **1996**, *8*, 337. (e) Bharati, S.; Lev, O. *Chem. Commun.* **1997**, 2302.

102. Evans, D.F.; Wennerstrom, H. *The Colloid Domain; where Physics, Chemistry and technology Meet*: VCH: New York, 1994.

103. (a) Badia, A.; Demers, L.; Dickinson, L.; Morin, F.G.; Lennox, R.B.; Reven, L. *J. Am. Chem. Soc.* **1997**, *119*, 11104. (b) Hostetler, M.J.; Wingate, J.E.; Zhong, C.J.; Harris, J.E.; Vachet, R.W.; Clark, M.R.; Londono, J.D.; Green, S.J.; Stokes, J.J.; Wignall, G.D.; Glish, G.L.; Porter, M.D.; Evans, N.D.; Murray, R.W. *Langmuir* **1998**, *14*, 17 and references therein.

104. Hostetler, M.J.; Zhang, C.-J.; Yen, B.K.H.; Anderegg, J.; Gross, S.M.; Evans, N.D.; Porter, M.D.; Murray, R.W. *J. Am. Chem. Soc.* **1998**, *120*, 9396.

105. Link, S.; El-sayed, M.A. *J. Phys. Chem. B* **1999**, *103*, 8410.

106. (a) Logunov, S.L.; Ahmadi, T.S.; El-sayed, M.A.; Khoury, J.T.; Whetten, R.L. *J. Phys. Chem. B* **1997**, *101*, 3713. (b) Alvarez, M.M.; Khoury, J.T.; Schaaf, T.G.; Shafigullin, M.N.; Vezmar, I.; Whetten, R.L. *J. Phys. Chem. B* **1997**, *101*, 3706. (c) Schaaf, T.G.; Shafigullin, M.N.; Khoury, J.T.; Vezmar, I.; Whetten, R.L.; Cullen, W.; First, P.N.; Gutierrez, -W.C.; Ascensio, J.; Jose-Yacaman, M.J. *J. Phys. Chem. B* **1997**, *101*, 7885.

107. Chen, S.; Ingram, R.S. Hostetler, M.J.; Pietron, J.J.; Murray, R.W.; Schaaf, T.G.; Khoury, J.T.; Alvarez, M.M.; Whetten, R.L. *Science* **1998**, *280*, 2098.

108. Zanchet, D.; Hall, B.D.; Ugarte, D. *J. Phys. Chem. B* **2000**, *104*, 11013.

109. Fink, J.; Kiely, C.J.; Bethell, D.; Schiffrin, D.J. *Chem. Mater.* **1998**, *10*, 922.

110. (a) Leff, D.V.; Ohara, P.C.; Heath, J.R.; Gelbart, W.M. *J. Phys. Chem.* **1995**, *99*, 7036. (b) Chen, S.; Murray, R.W. *Langmuir* **1999**, *15*, 682.

111. Bourg, M.; Badia, A.; Lennox, R.B. *J. Phys. Chem. B*, **2000**,*104 (28)*, 6562.

112. Laibinis, P.E.; Whitesides, G.M.; Allara, D.L.; Tao, Y.-T.; Parikh, A.N.; Nuzzo, R.G. *J. Am. Chem. Soc.* **1991**, *113*, 7152.

113. (a) Ingram, R.S.; Murray, R.W. *Langmuir* **1998**, *14*, 4115. (b) Pietron, J.J.; Murray, R.W. *J. Phys. Chem. B* **1999**, *103*, 4440.

114. (a) Chen, S.; Ingram, R.S.; Hostetler, M.J.; Pietron, J.J.; Murray, R.W.; Schaaff, T.G.; Khoury, J.T.; Alvarez, M.M.; Whetten, R.L.; *Science* **1998**, *280*, 2098. (b) Ingram, R.S.; Hostetler, M.J.; Murray, R.W.; Schaaff, T.G.; Khoury, J.T.; Whetten, R.L.; Bigioni, T.P.; Guthrie, D.K.; First, P.N. *J. Am. Chem. Soc.* **1997**, *119*, 9279.

115. Bard, A.J.; Faulkner, L.R. *In Electrochemical Methods: Fundamentals and Applications,* John Wiley & Sons, New York: 1980, chapter 12.

116. Markovich, G.; Collier, C.P.; Henrichs, S.E.; Remacle, F.; Levine, R.D.; Heath, J.R. *Acc. Chem. Res.* **1999**, *32*, 415.

117. Luedtke, W.D.; Landman, U. *J. Phys. Chem.* **1996**, *100*, 13323. (b) Luedtke, W.D.; Landman, U. *J. Phys. Chem.B* **1998**, *102*, 6566.

118. (a) Badia, A.; Gao, W.; Singh, L.; Demers, L.; Cuccia, L.; Reven, L. *Langmuir* **1996**, *12*, 1262. (b) Badia, A.; Cuccia, L.; Demers, L.; Morin, F.; Lennox, R.B.; *J. Am. Chem. Soc.* **1997**, *119*, 2682.

119. (a) Templeton, A.C.; Chen, S.; Gross, S.M.; Murray, R.W. *Langmuir* **1999**, *15*, 66. (b) Templeton, A.C.; Hostetler, M.J.; Kraft, C.T.; Murray, R.W. *J. Am. Chem. Soc.* **1998**, *120*, 1906.

120. Mulvaney, P.; Giersig, M. *J. Chem. Soc. Faraday Trans.* **1996**, *92*, 3137.

121. (a) Brown, L. O.; Hutchison, J.E. *J. Phys. Chem. B* **2001**, *105(37)*, 8911. (b) Bodkev, F.; Hansen, M.F.; Koch, C.B.; Leffman, K.; Steen, M. *Phy. Rev. B* **2000**, *61(10)*, 6826.

122. Hutter, E.; Fendler,J.H.; Roy, D. *J. Phys. Chem. B* **2001**, *105(45)*, 11159.

123. Chen, S.; Yang, Y. *J. Am. Chem. Soc.* **2002**, *124(19)*, 5280.

124. Armelao, L.; Colombo, P.; Fabrizio, M.; Gross, S.; Silvia, T.E. *J. Mat. Chem.* **1999**, *9(11)*, 2893.

125. (a) Ivanisevic,A.; Im, J.; Lee, K.; Park, S.; Demers, L.M.; Watson, K.J.; Mirkin, C.A. *J. Am. Chem. Soc.* **2001**, *123*, 12424. (b) Decher, G. *Science* **1997**, *277*, 1232.

126. Remacle, F.; Collier, C.P.; Markovich, G.; Heath, J.R.; Banin, U.; Levine, R.D. *J. Phys. Chem. B* **1998**, *102*, 7727.

127. (a) Honig, B.; Nicholls, A. *Science* **1995**, *268*, 1144. (b) Caruso, F.; Lichtenfield, H.; Giersig, M.; Mohwald, H. *J. Am. Chem. Soc.* **1998**, *120*, 8523. (c) Tien, J.; Terfort, A.; Whitesides, G.M. *Langmuir* **1997**, *13*, 5349.

128. http://www.chem.fsu.edu/multilayers/

129. (a) Seker, F.; Meeker, K.; Kuech, T.F.; Ellis, A.B. *Chem. Rev.* **2000**, *100*, 2505. (b) Ashkenasy, G.; Cahen, D.; Cohen, R.; Shanzer, A.; Vilan, A. *Acc. Chem. Res.* **2002**, *35(2)*, 121.

130. Smith, T.J. *J. Colloid and Interf. Sci.* **1980**, *75*, 51.

131. Somorjai, G.A.; *Chemistry in Two Dimensions-Surfaces*; Cornell University Press: Ithaca, New York, 1982.

132. Laibinis, P.E.; Whitesides, G.M.; Allara, D.L.; Tao, Y.T.; Parikh, A.N.; Nuzzo, R.G. *J. Am. Chem. Soc.* **1991**, *113*, 7152.

133. (a) Hutter, E.; Fendler, J.H.; Roy, D. *J. Phys. Chem. B* **2001**, *105*, 11159. (b) Hutter, E.; Fendler, J.H.; Roy, D. *J. Appl. Phys.* **2001**, *90*, 1977.

134. (a) Walters, M.J.; Roy, D. *Appl. Spectrosc.* **1998**, *52*, 1554. (b) Lovell, M.A.; Walters, M.J.; Roy, D. *Phys. Chem. Chem. Phys.* **1999**, *8*, 1985.

135. (a) Bryant, M.A.; Pemberton, J.E. *J. Am. Chem. Soc.* **1991**, *113*, 8284. (b) Schoenfisch, M.H.; Pemberton, J.E. *J. Am. Chem. Soc.* **1998**, *120*, 4502.

136. Malinsky, M.D.; Kelly, K.L.; Schatz, G.C.; Van Duyne, R.P. *J. Am. Chem. Soc.* **2001**, *123*, 1471.

137. (a) Lee, T.; Liu, J.; Chen, N-P.; Andres, R.P.; Janes, D.B.; Reinfenberger, R. *J. Nanop. Res.* **2000**, *2*, 345. (b) Lee, T.; Liu, J.; Janes, D.B.; Kolagunta, V.R.; Dicke, J.; Andres, R.P.; Lauterbach, J.; Melloch, M.R.; McInturff, Woodall, J.M.; Reinfenberger, R. *Appl. Phys. Lett.* **1999**, *74*, 2869. (c) Lee, T.; Chen, N-P.; Liu, J.; Andres, R.P.; Janes, D.B.; Chen, E.H.; Melloch, M.R.; Woodall, J.M.; Reinfenberger, R. *Appl. Phys. Lett.* **2000**, *76*, 212.

138. (a) Andres, R.P.; Bein, T.; Dorogi, M.; Feng, S.; Henderson, J.I.; Kubiak, C.P.; Mahoney, W.; Osifchin, R.G.; Reinfenberger, R. *Science* **1996**, *272*, 1323. (b) Andres, R.P.; Kolagunta, V.R.; Kubiak, C.P.; Mahoney, W.J.; Osifchin, R.G. *Science* **1996**, *273*, 1690.

139. (a) Bandyopadhyay, K.; Patil, V.; Vijayamohanan, K.; Sastry, M. *Langmuir* **1997**, *13*, 5244. (b) Grabar, K.C.; Allison, K.J.; Baker, B.E.; Bright, R.M.; Brown, K.R.; Freeman, R.G.; Fox, A.P.; Keating, C.D.; Musick, M.D.; Natan, M.J. *Langmuir* **1996**, *12*, 2353.

140. Chen, R.J.; Zhang, Y.; Wang, D.; Dai, H. *J. Am. Chem. Soc.* **2001**, *123*, 3838.

141. (b) Musick, M.D.; Pena, D.J.; Botsko, S.L.; McEvoy, T.M.; Richardson, J.N.; Natan, M.J. *Langmuir* **1999**, *15*, 844. (a)Lyon, L.A.; Pena, D.J.; Natan, M.J. *J. Phys. Chem. B* **1999**, *103*, 5826.

142. Schmitt, J.; Machtle, P.; Eck, D.; Mohwald, H.; Helm, C.A. *Langmuir* **1999**, *15*, 3256.

143. Keller, S.W.; Johnson, S.A.; Brigham, E.S.; Yonemoto, E.H.; Mallouk, T.E. *J. Am. Chem. Soc.* **1995**, *117*, 12879.

144. In QCM, the change in the resonance frequency of a piezoelectric crystal on deposition of material on its surface is used to estimate the mass of the

material. It is extremely sensitive to minute mass changes and the instrument used in these studies had a mass resolution of ~ 10 ng/cm^2.

145. (a) Patil, V.; Sastry, M. *Langmuir* **1998**, *14*, 2707. (b) Gole, A.; Sathivel, C.; Lachke, A.; Sastry, M. *J. Chromatogr. A* **1999**, *848*, 485.

146. Rizza, R.; Fitzmaurice, D.; Hearne, S.; Hughes, G.; Spoto. G.; Ciliberto, E.; Kerp, H.; Schropp, R. *Chem. Mater.* **1997**, *9*, 2969.

147. Collier, C.P.; Vossmeyer, T.; Heath, J.R. *Annu. Rev. Phys. Chem.* **1998**, *49*, 371.

148. Heath, J.R.; Vossmeyer, T.; DeIonno, E.; Markovich, G. *In Nanostructures Materials: Clusters, Composites and Thin Films*, ed. V.M. Shalaev, M. Moskovits, ACS Symp. Ser. 670, pp. 1-6. Washington, DC, 1997.

149. (a) Israelachvili, J.N.; Pashley, R.M. *Nature* **1982**, *300*, 341. (b) Israelachvili, J.N.; Pashley, R.M. *J. Colloid and Interf. Sci.* **1984**, *98*, 500.

150. Pashley, R.M.; McGuiggan, P.M.; Ninham, B.W.; Evans, D.F. *Science* **1985**, *229*, 1088.
151. Giersig, M.; Mulvaney, P.; *J. Phys. Chem.* **1993**, *97*, 6334.

152. (a) Bentzon, M.D.; Tholen, A. *Ultramicroscopy* **1990**, *38*, 105. (b) Ohara, P.C.; Leff, D.V.; Heath, J.R.; Gelbart, W.M. *Phy. Rev. Lett.* **1995**, *75*, 3466. (c) Murthy, S.; Wang, Z.L.; Whetten, R.L. *Philos. Mag. L* **1997**, *75*, 321.

153. (a) Harfenist, S.A.; Wang, Z.L.; Whetten, R.L.; Vezmar, I. Alvarez, M.M. *Adv. Mater.* **1997**, *9*, 817. (b) Alvarez, M.M.; Khoury, J.T.; Schaaff, T.G.; Shafigullin, M.N. Vezmar, I.; Whetten, R.L. *Chem. Phys. Lett.* **1997**, *266*, 91.

154. Murray, C.B.; Kagan, C.R.; Bawendi, M.G. *Science* **1995**, *270*, 1335.

155. Schmid, G.; Lehnert, A. *Angew. Chem. Int. Ed. Engl.* **1989**, *28*, 780.

156. (a) Taleb, A.; Petit, C.; Pileni, M.P. *J. Phys. Chem. B* **1998**, *102*, 2214. (b) Blatchford, C.G.; Campbell, J.R.; Creighton, J.A. *Surf. Sci.* **1982**, *120*, 435.

157. (a) Brust, M.; Bethell, D.J.; Schiffrin, D.J.; Kiely, C. *Adv. Mater.* **1995**, *7*, 795. (b)Yabuki, S.; Mitzutani, F. *Electroanalysis* **1997**, *9*, 23. (c) Demaille, C.; Brust, M.; Tsionsky, M.; Bard, A.J. *Anal. Chem.* **1997**, *69*, 2323.

158. (a) Musick, M.D.; Keating, C.D.; Lyon, L.A.; Botsko, S.L.; Pena, D.J.; Holliway, W.D.; McEvoy, T.M.; Richardson, J.N.; Natan, M.J. *Chem. Mater.* **2000**, *12*, 2869. (b) Lyon, L.A.; Keating, C.D.; Fox, A.P.; Baker, B.E.; He, L; Nicewarner, S.R.; Mulvaney, S.P.; Natan, M.J. *Anal. Chem.* **1998**, *70*, 341. (c) Sanchez-Cortes, S.; Gracia-Ramos, J.V.; Morcillo, G.J. *J. Colloid and Interf. Sci.* **1994**, *167*, 428. (d) Freeman, R.G.; Grabar, K.C.; Allison, K.J.; Bright, R.M.; Davis, J.A.; Guthrie, A.P.; Hommer, M.B.; Jackson, M.A.; Smith, P.C.; Wlater, D.G.; Natan, M.J. *Science* **1995**, *267*, 1629.

159. (a) Sun, S.; Murray, C.B.; Weller, D.; Folks, L.; Moser, A. *Science* 2000, *287*, 1989. (b) Luborsky, F.E. *J. Appl. Phys.* **1961**, *32*, 171S. (c) Murray, C.B.; Sun, S.; Gaschler, W.; Doyle, H.; Betley, T.A.; Kagan, C.R. *IBM J. Res. & Dev.* **2001**, *45*, 47 and references therein. (d) Volokitin, Y.; Sinzig, J.; de Jongh, L.J.; Schmid, G.; Moiseev, I.I. *Nature* **1997**, *384*, 621. (e) Claus, P.; Bruckner, A.; Mohr, C.; Hofmeister, H. *J. Am. Chem. Soc.* **2000**, *122*, 11430.

160. (a) Lahav, M.; Shipway, A.N.; Willner, I. *J. Chem. Soc. Perkin Trans. 2* **1999**, 1925. (b) Gittins, D.L.; Bethell, D.; Nichols, R.J.; Schiffrin, D.J. *Adv. Mater.* **1999**, *11*, 737. (c) Bethell, D.; Brust, M.; Schiffrin, D.J.; Kiely, C. *J. Electroanal. Chem.* **1996**, *409*, 137.

161. (a) Burmeister, F.; Schafle, C.; Keilhofer, B.; Bechinger, C.; Boneberg, J.; Leiderer, P. *Adv. Mater.* **1998**, *10*, 495. (b) Burmeister, F.; Schafle, C.; Matthes, T.; Bohmisch, M.; Boneberg, J.; Leiderer, P. *Langmuir* **1997**, *13*, 2983.

162. Feynman, R.P. *Lectures on computation*. Ed. A.J.G. Hey and R.W. Allen. Reading, MA: Addison Wesley Longman, 1996.

163. (a) Hermanson, K.D.; Lumsdon, S.O.; Williams, J.P.; Kaler, E.W.; Velev, O.D. *Science* **2001**, *294*, 1082. (b) Cui, X.D.; Primak, A.; Zarate, X.; Tomfohr, J.; Sankey, O.F.; Moore, A.L.; Moore, T.A.; Gust, A.; Harris, G.; Lindsay, S.M. *Science* **2001**, *294*, 571.

164. Jun, Y.; Boiadjiev, V.; Major, R.; Zhu, X.-Y. *Proc. SPIE-Int. Soc. Opt. Eng.* **2000**, *4175*, 113.

165. Ridley, B.A.; Nivi, B.; Jacobson, J.M. *Science* **1999**, *286*, 746.

166. Buffat, Ph.; Borel, J.P. *Phys. Rev. A* **1976**, *13*, 2287.

167. Talapin, D.V.; Haubold, S.; Rogach, A.L.; Kornowski, A.; Haase, M.; Weller, H. *J. Phys. Chem.* **2001**, *105*, 2260.

168. Colvin, V.L.; Goldstein, A.N.; Alivisatios, A.P. *J. Am. Chem. Soc.* **1992**, *114*, 5221.
169. Kumar, A.; Abbott, N.L.; Kim, E.; Biebuyck, H.A.; Whitesides, G.M. *Acc. Chem. Res.* **1995**, *28*, 219.

Chapter 2

Structural Aspects of SAM formation of disulfides and the application of Monolayers for Ceramic thin Film formation*

This chapter primarily deals with SAM formation of aromatic disulfides which are lesser studied compared to longchain alkanethiols. A comparative investigation of the self-assembled monolayers of diphenyl disulfide (DDS), diphenyl diselenide (DDSe), and naphthalene disulfide (NDS) on polycrystalline gold films using STM, QCM, and electrochemical techniques is presented. The geometric constraint imposed by the aromatic ring plays an important role in controlling the microscopic structure, adversely affecting the monolayer organization and stability. In addition, one of the applications of SAM towards the solid state synthesis of zirconia films is illustrated using a bifunctional molecule.

* A part of the work discussed in this chapter has been published in: **J. Mater. Chem.** *14*, 1737-1741 (2000) and another part in **J. Colloid and Interf. Sc.** *234*, 410-417 (2001).

2.1 INTRODUCTION

During the past few years, preparation and characterization of ultrathin organic films obtained by self-assembly have received considerable attention for the modification of noble metal surfaces with a number of applications such as molecular recognition, non-linear optics, tribology, and photo-patterning methodology (chapter 1, section 2.1).[1-5] Among several functional groups known to form SAMs on the surface of noble metal and semiconducting substrates, different types of the thiol/disulfide monolayers on Au surfaces have received attention due to their simplicity and ease of preparation as illustrated in chapter 1.[2-4] Although compact monolayers on gold surfaces are generally formed by most organic thiol/disulfide compounds, the quality of the monolayer such as the absence of pinholes and other defects critically depends on the presence of a long hydrophobic tail. Structurally, the Au-S bonding pattern in both thiols and disulfides is the same except for an oxidative dissociation of the S-S bond for disulfides. While the nature of surface attachment is believed to involve a Au-thiolate interaction,[1-4] the possibility of thiolate group dimerization to form disulfides on gold surfaces has also been recently considered.[6] Most of the data obtained from different diffraction studies are consistent with a ($\sqrt{3}$ x $\sqrt{3}$)R30° overlayer structure formed during the chemisorption of thiol/disulfide on Au (111) surfaces and in such a model, each sulfur head group can occupy a three-fold site on underlying Au (111) surface with a separation of 5 Å. A detailed discussion of the structure and bonding of long chain alkanethiols have been included in chapter 1. With that background, we describes the comparative monolayer formation ability of diphenyl disulphide (DDS), diphenyl diselenide (DDSe), and naphthalene disulphide (NDS) in this chapter to get an insight into the relative degree of organization and change in the interactions of substrate head group.[7] DDS was selected on the basis of geometric similarity with respect to DDSe whereas, NDS was used in order to reflect the role of inherent rigidity of the naphthalene ring, so that S-S bond cleavage is sterically hindered.[8,9] Lastly, selenol/diselenide monolayers have not yet received

enough attention[10-12] despite their promising utility for a variety of applications such as photoresists, photocatalysts, preparation of semiconductor quantum dots, photon-induced electron transfer systems, etc.

Present studies show that naphthalene disulphide forms a compact monolayer (96% surface coverage) despite the fact that the hydrocarbon tail lacks the ordering influence.[8] DDS and DDSe were found to form similar monolayers under identical conditions with the molecular plane perpendicular to the surface although there are several important differences. For example, DDS dissociately chemisorbs on Au, while in both DDSe and NDS, the Se-Se and S-S bonds are preserved upon adsorption. Also, the number of pinholes and defects are found to be much less in DDS monolayers than in NDS and DDSe. Specifically, this chapter deals with the relative ability of SAM formation and the structure of these monolayers of NDS, DDS, and DDSe formed on polycrystalline gold by using QCM, STM, and cyclic voltammetry. These techniques are selected based upon their proven ability to effectively unravel the molecular level details of the structure[13-15] and the degree of organization of SAMs.

In the same fashion, the effective utilization of these functionalized interfaces of SAMs for solid state and biomimetic synthesis is an active area of research, as elucidated by the multilayer formation of zirconium phosphonate and sequentially adsorbed copper ions on dithiol functionalized surface.[16,17] The recent past has seen increasing interest in the utilization of functionalized interfaces for growing ceramic thin films at temperatures below 100 °C.[18-22] Dense and highly adherent polycrystalline films of oxides, hydroxides and sulfides have been prepared on plastic, glass and other substrates, from aqueous as well as non-aqueous solutions using ω-functionalized self-assembled monolayers as organic templates for controlled nucleation and growth.[18-24] Due to the structural as well as functional similarities of self-assembled monolayers to protein surfaces, this type of preparation strategy is

sometimes known as biomimetic synthesis as the monolayers play an important role by providing suitable functionalities necessary to initiate growth of the inorganic layers. For example, several studies have recently shown that by manipulation of surface energy through monolayer formation, nanophase morphology, crystal growth habit, orientation and even chirality can be controlled in both aqueous and non-aqueous media.[18-25]

The last part of this chapter deals with the role of SAM in controlling the nucleation mechanism of crystalline zirconia thin films through potentiodynamic cycling, at room temperature, on bare and SAM-covered gold surfaces to elucidate the differences between the mechanisms of ZrO_2 formation. The formation of ceramic materials on SAM surfaces, especially on thiol moieties, is important from a biomineralization point of view. As the preparation of thin films of zirconia will be especially useful for a variety of applications such as fuel cells, oxygen sensors, inorganic membranes for gas separations, optical coatings *etc.*, this novel method is expected to influence many such applications. In addition, the present method also implies the possibility of preparing fully stabilized (cubic) or partially stabilized (tetragonal and cubic) zirconia on functionalized surfaces at lower temperatures by using various additives in the electrolyte.

2.2 EXPERIMENTAL

2.2.1 Materials

NDS was prepared by a reported procedure[26] and its purity was monitored above 99.99% by GC-Mass and NMR studies. Double distilled water was passed through Milli-Q system to get deionized ultra pure water (R = 18 MΩ cm) and was used through out the experiment. Diphenyl disulfide, diphenyl diselenide, KCl, $ZrOCl_2.8H_2O$, KOH and all other chemicals used in this work

were purchased from Aldrich Co. and were used as received. All solvents were of reagent grade and were distilled following usual procedure before using.

2.2.2 Preparation of Substrate

Gold substrates for these experiments were prepared by the thermal evaporation onto clean glass substrates under high vacuum condition (pressure better than 10^{-6} torr) in an Edward E306 coating unit. Before deposition, glass substrates were cut into required size to use as electrode substrate. Visible contaminants were removed by wiping with tissue paper followed by chemical cleaning by immersion in 1:4 H_2O_2/concentrated H_2SO_4 (pirhana) at 70^oC for about 30 minutes, rinsed with double distilled water and blown dry in a stream of Ar. The glass slides were then placed in an oven at 105^oC for about 10-15 minutes. Substrates cleaned by this procedure were transformed to the vacuum evaporator for gold deposition. A 5 nm Cr-buffer layer was first deposited onto conventionally cleaned glass plates to improve the adhesion of the Au film. This procedure yields polycrystalline Au films with strong (111) texture. The surface roughness factor (R=actual/geometrical surface area) of gold was determined according to a standard procedure, where the charge required to cathodically reduce the oxide layer was used for the calculation.[9] In order to avoid surface contamination, all the substrates were stored in polypropylene containers until use.

2.2.3 Monolayer Formation

Before depositing SAMs the substrates were thoroughly cleaned by repeated 30 sec exposure to sulfochromic acid (saturated $K_2Cr_2O_7$ in concentrated H_2SO_4) at 323 K and to 3% HF. After this exposure the substrates were extensively rinsed with deionised water. Extensive pretreatment is likely to leave the gold surface oxidized which can not be removed by water rinsing. The cleaning with sulfochromic acid was performed for a few seconds, which is sufficient to remove the organic impurities but provides inadequate exposure to form oxide layer. After cleaning, the substrates were immediately transferred

into a deareated 1 mM solution of the appropriate compound in acetonitrile. The substrates were kept for 24 h in the deposition solution to get well organized crystalline film although 10-12 h are sufficient for the chemisorption. The longer incubation period generally allows the molecular film to assemble in a crystalline-like solid phase and also provides the possibility for the desorption of physisorbed and chemisorbed contaminants from the gold surface into the solution. The substrates were removed from the solution, washed repeatedly with the solvent and finally with absolute ethanol, and then dried in a stream of Ar prior to the measurement.

In case of ZrO_2 synthesis, first a SAM of the pentanedithiol was formed on the gold film by dipping it in 1 mM ethanolic solution for 24 h following established methods to obtain the equilibrium organization.[28,29] In the second step, the SAM-covered gold substrate was introduced in a 5 mM aqueous zirconyl oxychloride solution (pH 3.5) at ambient temperature for 24 h to ensure complete attachment of Zr^{4+} ions to the ω-terminal groups of the SAM. The treated substrate was then washed copiously with de-ionized water and dried under a flow of argon gas. Variation of the immersion time over 2–24 h as well as the concentration of the solution in the mM range produced identical results. In the final step, cyclic voltammetry was performed using the samples obtained from the second step as the working electrode, a large platinum flag as the counterelectrode and a saturated calomel (SCE) as the reference electrode in 1 M aqueous KCl solution. The potential was cycled between 1.2 and +0.8 V *vs.* SCE at a scan rate of 200 mV/s. To confirm Zr attachment on the SAM surface, cyclic voltammetry was also performed on the bare and SAM-covered gold substrates respectively, as working electrodes in a mixture of 1 M KCl and 5 mM $ZrOCl_2$ solution. After performing at least ten such cycles the samples were removed and washed with a gentle flow of de-ionized water and dried under Ar prior to characterization.

2.2.4 Quartz Crystal Microgravimetric (QCM) Measurements

An Elchema elctrochemical nanobalance (with 0.1 Hz resolution) interfaced with a computer was used to monitor the subtle mass changes during SAM formation. All the experiments were performed at room temperature using vacuum deposited 10-MHz Au-coated quartz crystals (0.2 cm^2 exposed area). Initially, the solvent was introduced in the vessel to stabilize the QCM frequency, and then a small measured amount (25 μL) of the specific compound was inserted with a syringe. The frequency change due to adsorption is directly proportional to the mass, and after conversion the mass is plotted against time. The blank experiment conducted with the solvent alone shows only a minor mass change as compared to the mass change after the monolayer formation.

2.2.5 Electrochemical Characterization

Cyclic voltammetry was carried out with a computer-interfaced PAR 283 potentiostat/galvanostat as described above using bare as well as SAM-covered Au as the working electrode under normal atmosphere. Impedance measurements were performed with a PAR 283 potentiostat/galvanostat and a PAR 5012 lock-in amplifier interfaced with a computer, in a solution containing 5 mM of the redox-active probe, $Fe(CN)_6^{-3/4}$. For the structural studies of SAM cyclic voltammetry was performed in an oxygen-free atmosphere (bubbling Ar gas) by using a three electrode cell: gold coated glass or respective SAM modified gold substrates as the working electrodes, a large area platinum flag counter electrode, and a saturated calomel reference electrode (SCE). The supporting electrolyte was 0.1M aqueous KOH. All potentials in the text are referred to SCE. Impedance measurements always used a 5 mV rms perturbation at the formal potential of the redox couple and readings were taken at five discrete frequencies per decade. The analysis was carried out using the commercially available program EQUIVALENT CIRCUIT written by

B.A. Boukamp (University of Twente) which determines the parameters of the assumed equivalent circuit by a weighted non-linear least-squares fit.

2.2.6 Scanning Tunnelling Microscopy

A homebuilt Scanning Tunnelling Microscope (STM) was used to probe the SAM formation.[32] STM studies were performed at room temperature in air and the instrument was operated in constant current mode of 200 pA at a bias voltage of +100 mV (substrate positive). Prior to these experiments the instrument was calibrated with highly oriented pyrolytic graphite (ZYA, Advanced Ceramic). Electrochemically etched tungsten tip was used as the probe. To ensure that the data collected were representative for the film morphology, multiple images were taken at different locations and scan ranges.

2.2.7 X-ray Photoelectron Spectroscopy (XPS)

The XPS measurements were carried out using a VG Scientific ESCA 3 MK II spectrometer operated at a pressure of better than 10^{-9} Torr using a monochromatic Mg-Kα source ($h\nu$ = 1253.6 eV) with the x-ray source operated at an electron takeoff angle (ETOA, defined as the angle between electron emission direction and surface parallel) of 54^{o}. The alignment of the binding energy was done using the C 1s binding energy of 284.6 eV as a reference. The core level spectra of C 1s, Au 4f, O 1s and S 2p orbitals were recorded at an overall instrumental resolution of ~ 1 eV. The X-ray flux was kept deliberately low in order to reduce beam-induced damage (electron power 70 W). The deconvolution of overlapping peaks in the final, high resolution spectra was accomplished using a standard curve-fitting algorithm. The line shape of all peaks was assumed to be Gaussian.

2.2.8 Other Measurements

The X-ray diffraction analysis of the films was carried out at room temperature using a Philips 1730 X-ray diffractometer at 40 kV and 30 mA (1200 W) with filtered Cu-Kα line (λ = 1.5404 Å). Scanning electron microscopy (SEM) of the sample was conducted on a Leica Stereoscan S-440 model microscope, operated at 20 kV accelerating voltage and 25 pA current.

2.3 STRUCTURAL STUDIES OF VARIOUS AROMATIC THIOLS

2.3.1 Quartz Crystal Microbalance (QCM)

In situ Quartz Crystal Microbalance (QCM) is considered to be an ideal tool for investigating the adsorption processes due to its high sensitivity ($\pm$ 0.1 ng) towards mass change.[33,34] The Sauerbrey equation, which relates the frequency change to mass loading can been used to determine the approximate amount of adsorbed molecules on the gold coated quartz crystal surface. However, several additional factors can also affect the oscillation frequency, like viscous damping, surface stress, energy disruption by nonshear coupling, etc.[34] The major limitation is that the frequency shift cannot be directly related to the absolute mass change and hence corrections by blank experiments (i.e., quartz crystal in the same environment without the adsorbing molecule) is needed for obtaining reliable kinetic information.

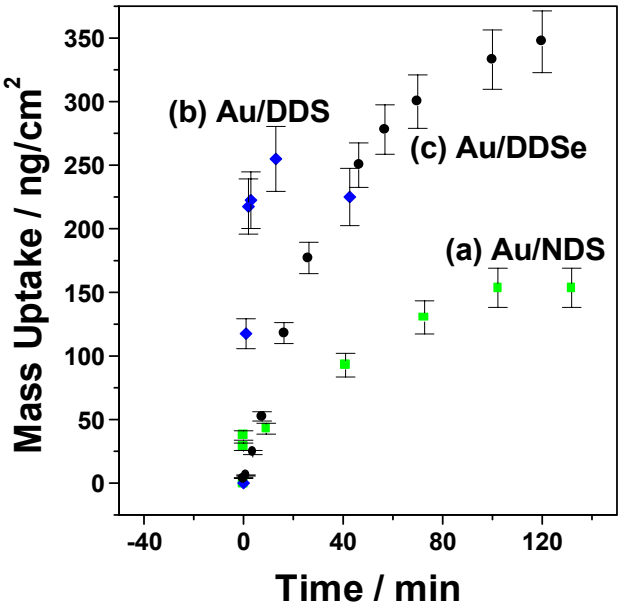

Figure 2.1 The mass change with time for NDS, DDS, and DDSe when gold-coated quartz crystals are exposed to 1 mM solution of these molecules in acetonitrile; the mass values used are after correction by performing a blank experiment. The error bars were determined on the basis of upper and lower values of the fluctuation of the frequency signal. (a) Au/NDS; (b) Au/DDS; (c) Au/DDSe.

Figure 2.1 shows the mass change with time for NDS, DDS, and DDSe, when the gold coated quartz crystal is exposed to 1 mM solution of these molecules in acetonitrile. The mass increase seems to attain a plateau value at about 150, 260, and 342 ng/cm^2 (corresponding to a time of 80 min) for monolayers of NDS, DDS, and DDSe, respectively. These values were obtained by subtracting the minor mass change (8 ng) from blank experiments with the solvent only. Although the three curves show similar features, especially in the initial region, the one corresponding to DDS is steeper than the others suggesting a faster adsorption rate than NDS or DDSe. An approximate estimation of the surface coverage shows that DDS adsorbs within a few seconds and covers most of the surface (surface coverage close to 0.9), while DDSe and NDS need about one hour for attaining the same coverage. In addition to the distinct kinetics of surface coverage, the difference in saturation coverage can be related to the molecular structure. The saturation coverage corresponding to the final mass uptake is similar for DDS and DDSe (0.92 and 0.99, respectively) while it is significantly lower for NDS (0.8). Since the

roughness of gold is identical in all cases, a more closely packed molecular assembly is suggested for DDS and DDSe relative to a more defective type of monolayer for NDS. This could be due to the easy relaxation appearing from bond cleavage for DDSe and DDS, while for NDS, the fused ring may impose constraints for side movement and a lesser interaction affinity of DDSe, than for the corresponding disulfides. These results underline the importance of intramolecular conformational changes in controlling the monolayer packing density and is in agreement with the results of Surface Enhanced Raman Spectroscopy (SERS) investigations.[27]

2.3.2 Cyclic Voltammetry (CV)

Considering the simple parallel plate capacitance model for the electrode-electrolyte interface which has been applied successfully for electrodes derived from long chain alkanethiol monolayers,[35-37] double layer capacitance studies can provide additional insights in the average structure of the self-organised assemblies. Fig.2.2a shows cyclic voltammograms of bare gold and the monolayer-coated electrodes (DDS, DDSe, and NDS) respectively, recorded at the scan rate of 0.5 V/s in the potential range from 0.0 to +0.8 V vs. SCE. An approximate calculation of the double layer capacitance from the nonfaradaic current measured at a 0.25 V constant potential indicates that a uniform and compact monolayer is formed due to the strong chemisorption of DDS, DDSe and NDS on the gold surface as shown by the decrease in double layer capacitance compared to bare gold. The differential capacitance decreases from 29 $\mu F/cm^2$ for bare gold to 7.3, 8.0, and 11.6 $\mu F/cm^2$ for DDS, DDSe and NDS functionalized substrates, respectively. Although these capacitance values are different from the relatively better values measured in 0.1 M aqueous NaF electrolyte for well defined oriented surfaces,[27] the decreasing order and relative change suggest that the capacitance values reflect monolayer compactness. For example, the monolayer formed for NDS shows disordered/defective organization compared

to DDS and DDSe pointing towards the importance of structure in controlling the degree of ordering. In addition, the average structure and quality of the monolayer assemblies could be compared by this method despite the limitation due to the estimation of capacitance, which is not very sensitive to monolayer defects.

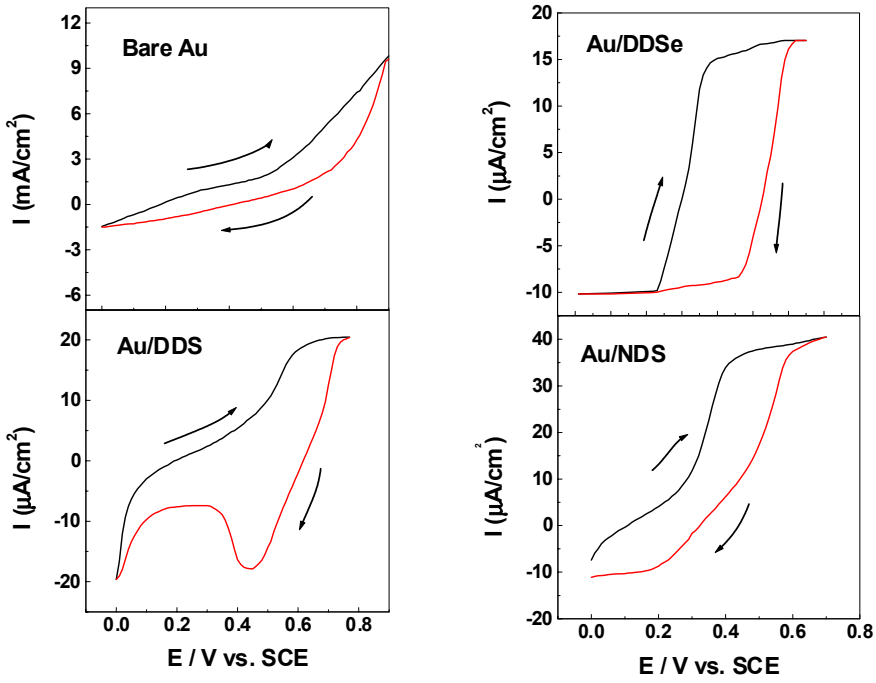

Figure 2.2a Cyclic voltammogram of bare gold and DDS, DDSe, and NDS-modified gold substrates in the range from 0 to +0.8 V in 0.1 M KOH (reference: SCE; counter electrode: platinum disk; scan rate: 0.5 V/s).

The voltammogram of bare gold electrode although not well defined, clearly indicates a marked increase in the current around +0.7 V vs. SCE, corresponding to the oxidation of polycrystalline Au as reported earlier[38] in alkaline medium (pH ≥ 14). Polycrystalline Au is known to give two flattened peaks at 1.15 to 1.2 V vs. SCE in alkaline medium, which correspond to the oxidation/reduction reactions of Au oxide. Sometimes organic impurities especially redox active ones are also known to give certain anomalous peaks at slightly different values. Also, holding the potential for long time at +1.0 V vs. SCE is known to give a sharp cathodic peak corresponding to the reduction

of the oxide film. We have not observed any of these features as the upper limit of the potential range during the anodic scan of +0.8 V vs. SCE. However, the fact that the increase of the current around +0.7 V vs. SCE (Fig. 2.2a) could be attributed to gold oxidation was verified by taking voltammograms beyond 1.2 V vs. SCE, where a strong cathodic peak was observed. In addition, by holding the potential at 1.2 V vs. SCE an increase in the height of the cathodic peak was found. However for the monolayer coated electrodes, the onset of oxygen evolution was found to adversely affect the film quality and hence the anodic limit was fixed to 0.8 V vs. SCE for all the further voltammograms. This is expected for Au oxide and subsequent oxygen evolution.

Compared to the voltammogram of bare gold, DDS modified electrode (Au/DDS) shows a drastic decrease in current (almost 100 times) due to the monolayer formation followed by a plateau region (above 0.6 V vs. SCE) during the anodic scan. Reverse scan gives a distinct cathodic peak at +0.43 V vs. SCE which might be attributed to the reduction of the oxide film formed in the forward scan, as known from the electrochemistry of gold in alkaline media.[38] Interestingly, there is no sharp cathodic peak for DDSe (Au/DDSe) although, the i-E response of a sharp current rise to a potential independent limiting current (i.e., sigmoid type behavior), which suggests diffusion through pinholes.[39,40] The origin of this type of the voltammogram can be attributed to the oxidation/reduction of Au substrate perhaps through more uniformly distributed pinholes (similar to a microarray electrode). NDS modified Au (Au/NDS) shows a behavior close to that of DDS, except that the cathodic reduction peak is not as pronounced. These peak shape changes along with an increased peak separation suggests that the reduction of the oxide film is more irreversible for NDS than for DDS. Nevertheless, the magnitude of the oxidation current is significantly greater presumably due to the large defective nature of the monolayer. This could be attributed to the rigid nature of fused rings present in NDS while DDS and DDSe allows conformational flexibility during organization. This comparison of the voltammetric behaviour clearly

indicates that among these molecules, NDS shows poor compactness and defective monolayers. The same trend is also confirmed by the order of change in differential capacitance values estimated from Fig. 2.2a.

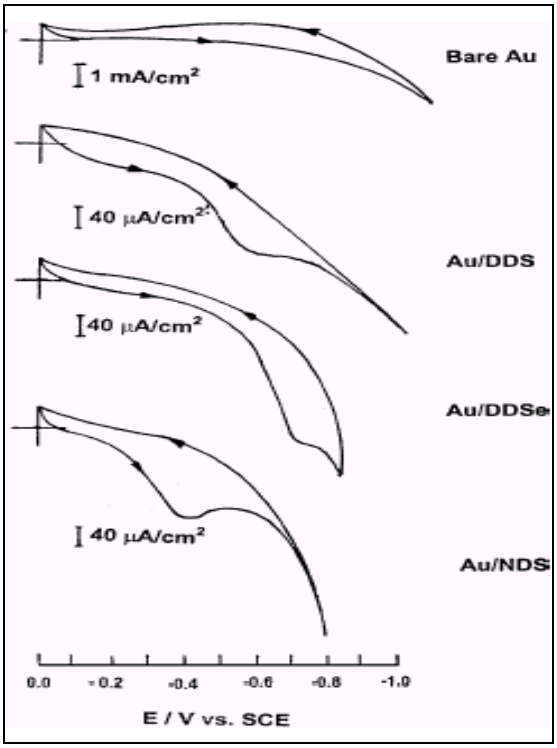

Figure 2.2b Cyclic voltammogram of bare gold and DDS, DDSe, and NDS-modified gold substrates in the potential range of 0 to –1.0 V, in 0.1 M KOH (reference: SCE; counter electrode: platinum disk; scan rate: 0.2 V/s)

In order to compare the electrochemical stability of these monolayers with respect to reductive desorption in alkaline medium, cyclic voltammograms were recorded in the negative potential range. Fig.2.2b shows the cyclic voltammetric response of the bare gold surface and of three monolayer-coated electrodes (DDS, DDSe and NDS), at a scan rate of 200 mV/s, in the potential range from 0.0 to -1.0 V vs. SCE. The electrodes modified with DDS, DDSe and NDS show a reductive desorption peak at -0.65 V, -0.73 V and -0.49 V vs. SCE. This behavior can be explained on the basis of the earlier work by Porter et al[41] on electrode reactions of disulfide monolayers on gold, in aqueous

solution. The difference in the reductive potential values also supports the relative compactness of DDS monolayer since it is more difficult to desorb, perhaps due to the fact that it has been formed by a more facile cleavage of S-S, in contrast to the easier desorption of NDS. DDSe shows an intermediate behaviour and the low degree of the structural integrity of the NDS monolayer may be attributed to the presence of pin holes, grain boundaries, trapped solvent molecules etc., as also supplemented by the increased broadness of the reductive desorption peak.

To determine if the above change in reductive desorption behaviour is only related to molecular structure and packing or if it is a function of time, scan rate dependent voltammograms were taken (Fig. 2.3) in the same electrolyte for DDS, DDSe and NDS monolayer modified electrodes. The voltammetric response in current with increase in scan rate for all molecules were found to be similar as all peak potentials were found to shift more cathodic with higher scan rates. For example, Fig. 2.3a shows such a scan rate dependent voltammogram for DDS modified Au electrode, where the peak seems to broaden with scan rate. DDSe also shows similar behaviour (Fig. 2.3b) but for NDS (Fig. 2.3c), the shift in potential with increase in scan rate is substantially more confirming poor degree of structural integrity. In addition, at higher scan rates the peaks are sharper and all these observations including the pronounced asymmetric shape at 500 mVs^{-1} scan rate, are in agreement with the more irreversible nature of the reductive desorption of NDS molecule. For all the cases, a plot of the current peaks I_p, with scan rate gives a straight line (insets of Fig.2.3), but not passing through the origin, perhaps due to deviations from the ideal surface confinement caused by the appearance of pin holes, grain boundaries, trapped solvent etc. or due to the not reversible formation of the species involved in the voltammograms. This can be compared with voltammetric response for diffusing species, where the peak current normally varies with the square root of the scan rate. The higher slope of I_p vs. scan rate

plot for DDSe is also in good agreement with the less defective monolayers due to the better coverage.

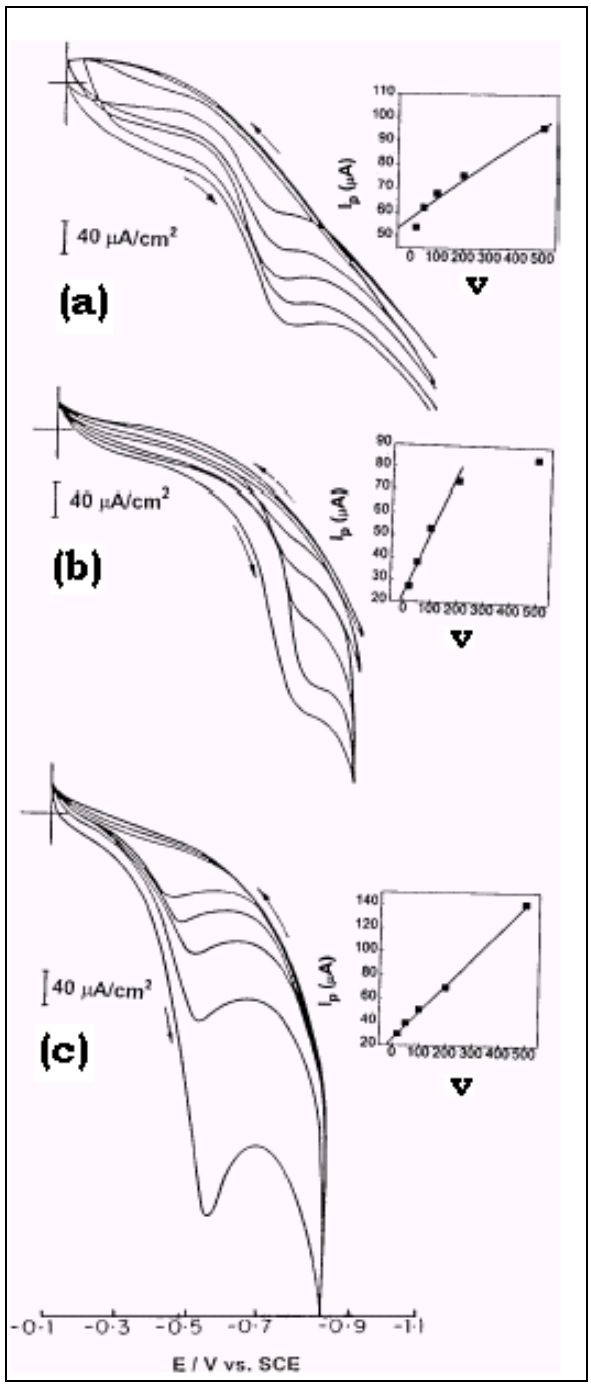

Figure 2.3 The cyclic voltammogram taken in 0.1 M KOH at various scan rates (0.05 to 0.5 V/s) for (a) DDS, (b) DDSe, and (c) NDS – modified gold electrodes ; inset shows variation of peak current with scan rate.

2.3.3 Scanning Tunnelling Microscopy (STM)

STM is an important tool to study nanoscopic structure of SAMs to a high degree of accuracy and the relationship between molecular structure, compactness and nature of the adsorbed molecules can be well understood using this technique.[42]

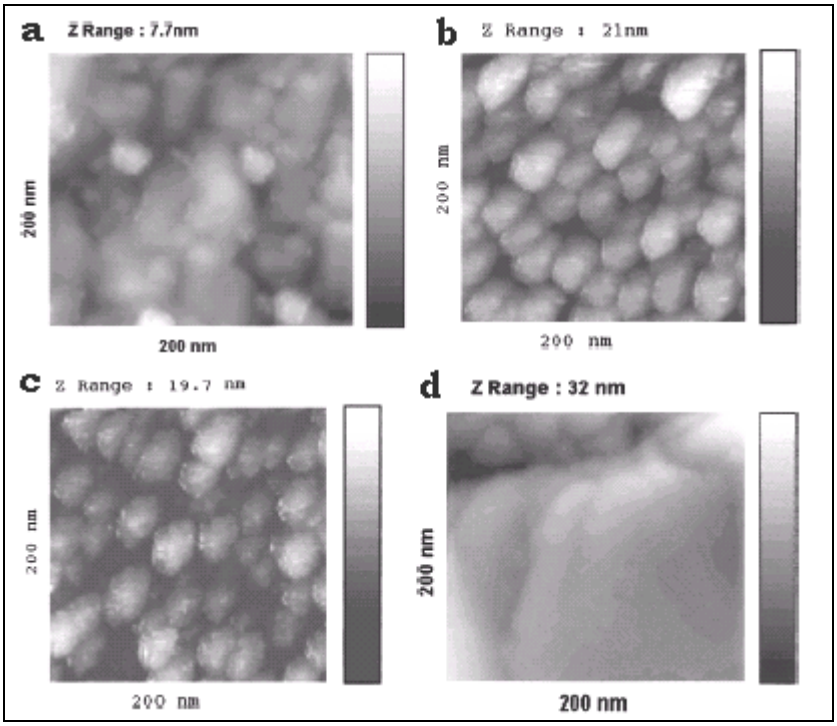

Figure 2.4 STM images of (a) bare gold and (b) DDSe, (c) DDS, and (d) NDS-modified SAMs on gold substrates; all images were obtained in the constant current mode.

For example several STM studies of SAMs using long chain thiols on Au(111) surfaces clearly illustrate the surface structure as well as subtle changes on annealing.[43] STM images shown in Figure 2.4 (a, b, c & d) also indicate the difference in the nature of the monolayer for these three molecules on Au surface.

In the case of gold coated glass (Fig. 2.4a), the surface does not show any periodicity or terraces, while crystalline structure is visible with granular

size variation from 30 to 60 nm having deep gorges and hills (no single crystal surfaces were used). Relative to bare gold, DDSe functionalized gold surfaces show (Fig. 2.4b) uniform size domains bundled together with a size ranging from 25 to 30 nm and nearly similar patterns have been observed for DDS modified gold surfaces (Fig. 2.4c). For NDS, no such periodic domains have been observed (Fig. 2.4d), the surface being covered with larger domains, showing a continuous coverage of the surface with NDS. The streaks are probably from the smaller domains and pinholes are clearly visible in all images. These STM images are qualitatively similar to those reported earlier for other organoselenium and organosulfur monolayers.[11]

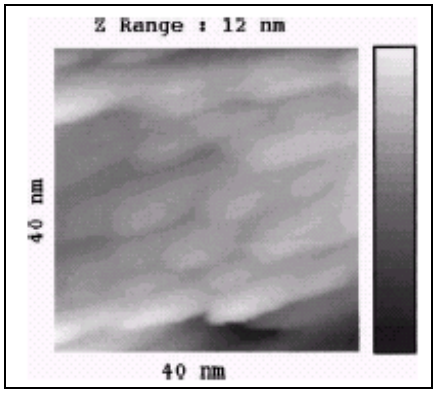

Figure 2.5 Magnified STM image of a NDS molecule after scanning a representative domain of a small area in constant current mode when the tunneling current was kept at 200 Å and the bias voltage was 100 mV.

Fig. 2.5 displays a high resolution STM pattern of NDS, which reveals a periodic domain (i.e., less than 10 nm in size). Significantly no such small domains are seen for DDS and DDSe monolayers. This is due to the rigidity of naphthalene ring in NDS, which hinders the monolayer formation. The orientational flexibility of rings in DDS and DDSe is missing in NDS. This illustrates the importance of geometric constraints for the formation of a compact monolayer. STM images of DDSe monolayers on gold, at various

scan ranges (Fig. 2.6) confirms that the entire surface has uniform coverage. Domains of similar size are present, despite the presence of pinholes. Similar patterns are also observed for DDS monolayers as shown in Fig. 2.7. Thus, voltammetric data in combination with the QCM results suggests that while monolayer formation by adsorption from solution is fast for DDS, the reductive desorption is faster for NDS, in alkaline medium.

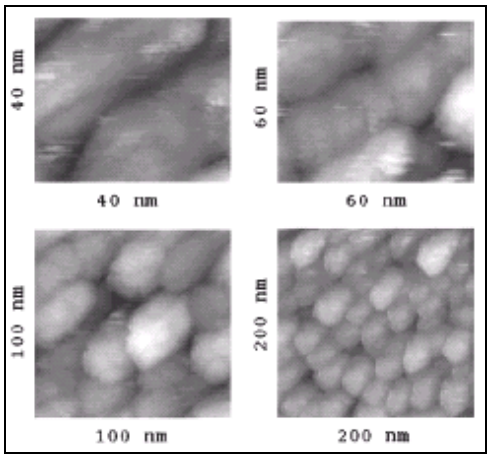

Figur 2.6 STM images of DDSe-modified gold at different scan ranges, keeping the tunneling current (200 pA) in constant current mode by applying a bias voltage of 100 mV.

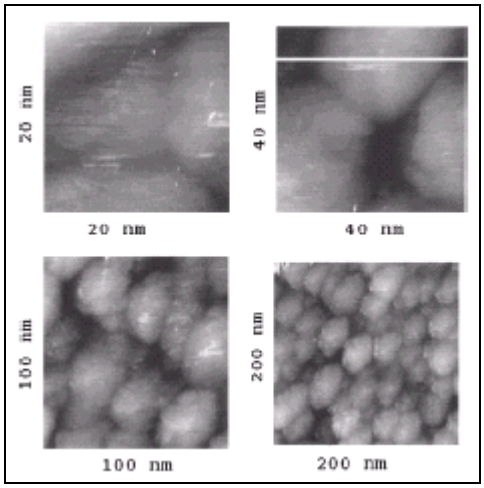

Figure 2.7 STM images of DDS-modified gold at different scan ranges, keeping the tunneling current (200 pA) in constant current mode by applying a bias voltage of 100 mV.

2.4 EFECTIVE UTILIZATION OF ω-TERMINATED SAMs FOR CERAMIC FILM FORMATION

2.4.1 X-Ray diffraction analysis

The XRD patterns of the dry as-deposited and annealed zirconia films, prepared potentiodynamically on SAM-covered and bare gold surfaces, are shown in Figure 2.8 and 2.9, respectively. The XRD pattern (Fig. 2.8a) of the as-deposited (room temperature) sample on a SAM functionalized surface indicates a highly oriented monoclinic nature for the ZrO_2 film. More specifically, this data shows two major peaks (●) belonging to the (111) and (222) planes of zirconia, perhaps due to the strong (111) preferred orientation of the gold film induced by the hexagonal structure of the dithiol SAM. Annealing of the film at 100 °C (Fig. 2.8b) shows a marked decrease in intensity of all the zirconia peaks, whereas the intensities of the gold peaks (■) appear to increase. A further increase in annealing temperature to 200 °C (Fig. 2.8c) reveals that the ZrO_2 peaks are completely diminished, leaving the remaining gold peaks only. We believe that the SAM provides a strong periodic field for the orientation of zirconia nuclei and this order is lost when the monolayer is thermally decomposed. The crystallites may take a random orientation (rather than becoming amorphous) and the probable reason for the loss of reflection is due to the formation of amorphous ZrO_2 on the annealed surface. In contrast to Fig. 2.8a, the XRD pattern of ZrO_2 coated on a bare gold surface (Fig. 2.9a) shows relatively intense gold peaks along with zirconia peaks. The annealing of the film at 300 °C (Fig. 2.9b) shows a similar decrease in the intensity of zirconia peaks but no disappearance, unlike the case of the functionalized surface, indicating the influence of the thiol monolayer on crystallinity.

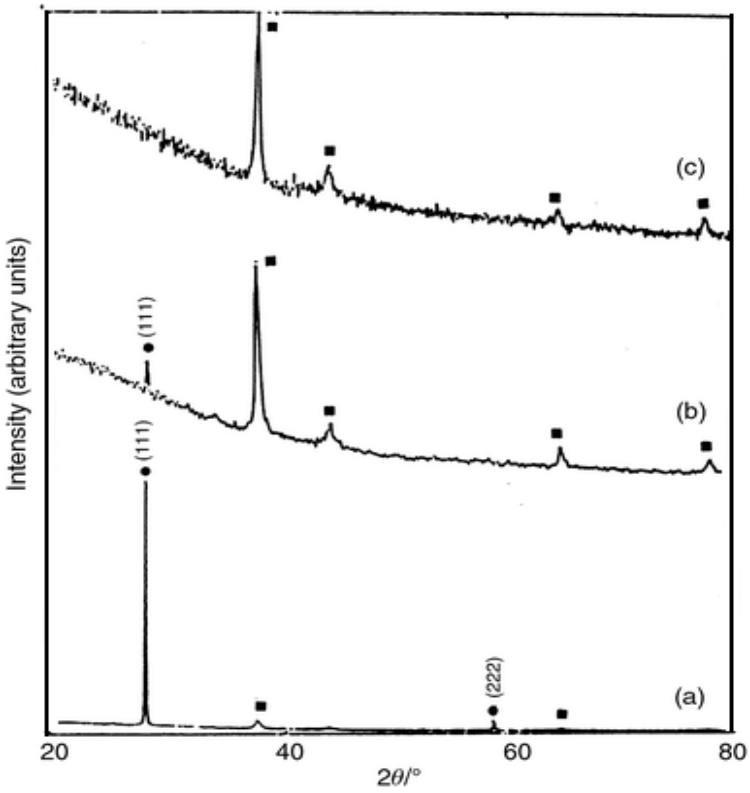

Figure 2.8 XRD pattern of zirconia films on a PDT SAM coated gold surface by potentiodynamic cycling (a) at room temperature, (b) calcined at 100 °C, and (c) after annealing at 200 °C. The peaks corresponding to the underlying gold substrate are marked by (■) while those of zirconia are indicated by (●).

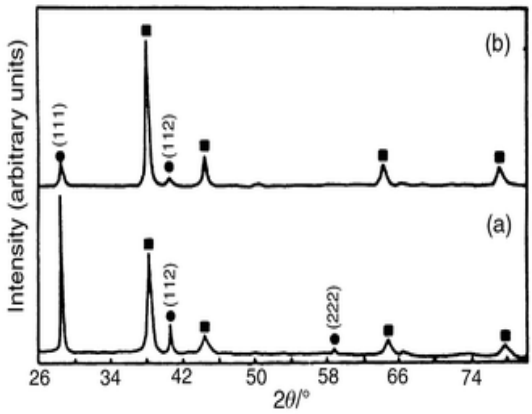

Figure 2.9 XRD pattern of zirconia films prepared on a bare gold substrate (a) at room temperature and (b) annealed at 300 °C. Similar marks are given for zirconia and gold peaks as indicated above.

The change in crystallite size was calculated using the line broadening of the (111) peak with the aid of the Scherrer equation.[44] The crystallite size was

found to be 40–50 nm for as-deposited samples in both the cases. Interestingly, the annealed samples show a decrease in particle size (20–30 nm) upon heating, in contrast to the amorphous to polycrystalline progression known in zirconia films.[45-47] It is unlikely to have undergone a transition from crystalline to amorphous by annealing and hence the disappearance of the preferred orientation indicates that the ordering of the SAM enables unique crystalline features during nucleation.

2.4.2 Cyclic voltammetry

A significant change in double layer capacitance as approximately estimated from fast scan voltammetry is a commonly used procedure to evaluate monolayer formation and quality.[48] Fig. 2.10 shows such a superimposed cyclic voltammogram taken at 500 mV/s for a bare gold electrode (a), a gold electrode modified with dithiol (b) and a gold electrode modified with dithiol after adsorption of Zr ions (c), all using 1 M aqueous KCl solution. The dithiol SAM formation is evident from the significant decrease of the nonfaradaic current (Fig. 2.10b,c). More importantly, the passivation of the surface is complete after Zr^{4+} attachment. An approximate calculation of the double layer capacitance from this data on the basis of reported surface roughness[49] yields 40 μF/cm^2 for bare gold, whereas 5.5 and 2.1 μF/cm^2 are obtained for the dithiol-modified electrode and the Zr-attached SAM surface, respectively. These values obtained for bare gold and SAM-covered gold are comparable to the respective values reported earlier and the change in capacitance corresponds to similar SAMs with 99% surface coverage.[50] As capacitance is determined by dielectric permittivity, the thickness of the adsorbed layer and the packing density of the adsorbed molecule, a further reduction after Zr attachment suggest that either the Zr species from the solution has increased the separation of charge between the electrode surface and plane of closest approach or decreased the polarizibility of the intervening medium.

In order to understand the difference in ZrO_2 film formation on bare and functionalized Au surfaces from Zr^{4+} ions in solution, cyclic voltammetry was also conducted in a 1 M KCl solution containing a 5 mM aqueous solution of zirconyl oxychloride. Fig. 2.11 shows a representative superimposed cyclic voltammogram at 200 mV/s using gold-coated glass and SAM-functionalized gold-coated glass as working electrodes respectively. An irreversible reduction peak at 0.9 V *vs.* SCE is clearly seen in both the cases. The minor oxygen reduction peak observed for the bare electrode is absent on the SAM-covered gold electrode. The potential range for CV in this case is the same as that used for zirconia preparation. The type of cyclic voltammetric response remains unchanged even after ten continuous potential cycles. The double layer capacitance (14 μF/cm^2 for bare gold and 5.6 μF/cm^2 for the SAM funtionalized gold surface) observed using a 200 mV/s scan rate at the end (Fig. 2.12) suggests that the monolayer is intact even after the cathodic formation of ZrO_2. Gold-coated glass substrates kept for 12 hours in $ZrOCl_2$ solution, washed and immersed in KCl showed a response like Fig. 2.12a, without any significant change in double layer capacitance, indicating that there is no surface functionalization in the absence of a dithiol monolayer.

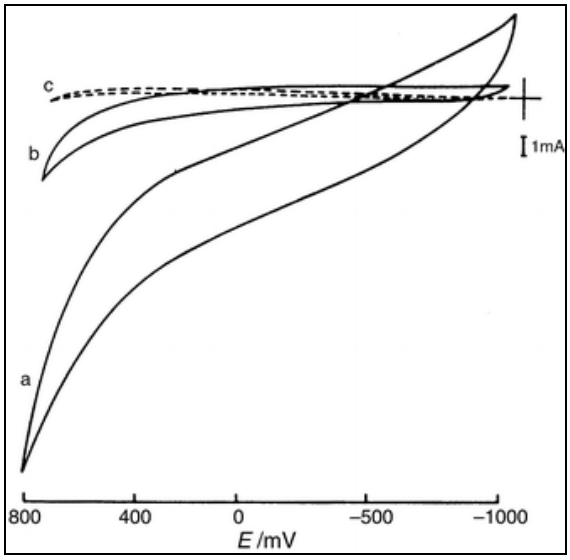

Figure 2.10 Superimposed cyclic voltammogram in 1 M KCl (a) at a bare gold electrode, (b) at a gold electrode modified with a SAM of PDT, and (c) after attachment of Zr from 5 mM $ZrOCl_2$ on the SAM surface with a typical scan rate of 500 mV/s.

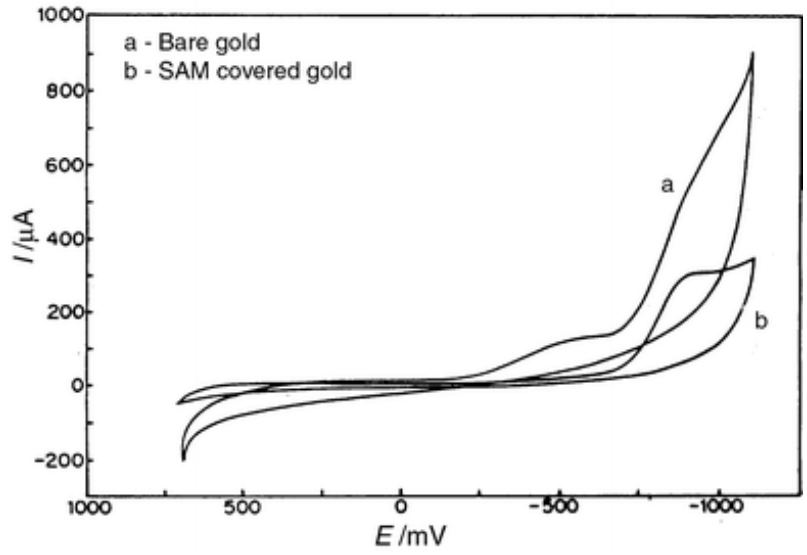

Figure 2.11 Superimposed cyclic voltammogram in 1 M KCl and 5 mM zirconyl oxychloride aqueous solution (a) at a bare gold electrode, and (b) at a SAM functionalized gold electrode, with a typical scan rate of 200 mV/s.

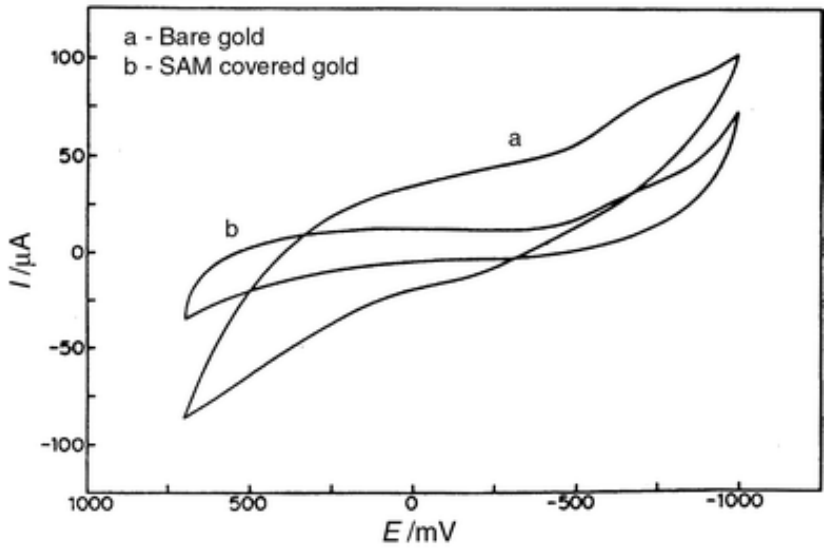

Figure 2.12 Superimposed cyclic voltammogram in 1 M KCl (a) at a bare gold electrode, and (b) at a SAM functionalized gold electrode after subsequent adsorption of Zr ions from 5 mM $ZrOCl_2$ on both the surfaces, with a typical scan rate of 200 mV/s.

It is instructive to compare all the features present in Fig. 2.11 to the voltammetric response obtained for a Pt working electrode in a similar solution.[30] Although the Pt working electrode shows a reversible couple at $E_{1/2}$

of 0.49 V *vs.* SCE along with the same anodic and cathodic peak current, Au shows only an irreversible reduction at 0.9 V, irrespective of the presence of a monolayer. A comparison of the electrochemistry of $ZrOCl_2$ on Au and Pt electrodes indicates that the mechanisms of ZrO_2 formation are different on these two electrode surfaces. Zirconia formation by reduction is thought to occur *via* the following plausible scheme.[30]

$$ZrOCl_2 + e^- \leftrightarrow ZrOCl + Cl^-$$
$$2ZrOCl + 2H_2O \leftrightarrow 2ZrO_2 + 2HCl + H_2$$

However, the actual mechanism may be more complex for a number of reasons. First, $ZrOCl_2$ is not a simple molecule containing Zr–Cl bonds, it is a tetrameric hydrolysis product in which all bonds of Zr are to O (hydrolysis of water). Although Zr can exhibit the +3 oxidation state in compounds such as $ZrCl_3$, such compounds are completely unstable in water. In aqueous environments, Zr^{III} is instantaneously oxidised to Zr^{IV} and all Zr–Cl bonds are hydrolysed to form Zr–O bonds. The resulting hydrolysis products are only soluble in strong acids or strong base. Hence, the reaction scheme given above may not be possible for gold. An alternate explanation to realise the electrochemical activity for dissolved $ZrOCl_2$ which promotes ZrO_2 formation is that water molecules coordinated to Zr are being electrolysed to produce H_2 and more anionic oxygens. Such oxygens would be more active for polymerisation than the coordinated water molecules. The observed electrochemical potentials are in the right range to be consistent with such a scheme. Another factor could be that if electrolysis is creating pH gradients near the electrode surfaces, it can also stimulate the nucleation of ZrO_2 simply by changing the pH. The Zr species need not be a direct participant in the electrochemical reaction itself.

The decreased current values indicated in Fig. 2.11 for the dithiol-functionalized electrode can be understood either in terms of an increase in the ohmic resistance due to monolayer formation or merely a reduction in

nucleation sites due to the partitioning of the available area. The SAM head groups might be expected to form a stable complex with dissolved zirconia species. The sulfate head group is known to be capable of displacing coordinated water molecules to form a stable complex. Since the –SH terminating alkane thiol group has a pK_a of about 9, a neutral –SH is present initially in the solution, which then reacts with tetrameric $ZrOCl_2$ to produce ZrO attached to the SAM surface, eliminating HCl. The short chains possibly avoid the problem of dithiol looping on the gold surface[51] providing free thiol on the surface to anchor the zirconium ions. The Zr attachment on the terminal functional group (–SH) rather than ZrO_2 formation on defects and pinhole regions is supported by the shape of the voltammograms, as there is no indication of spherical diffusion control.[52]

2.4.3 Current–time transients

Since the above cyclic voltammetric features (Fig. 2.11) suggest reductive ZrO_2 formation on both bare and functionalized Au surfaces with identical thermodynamic features (*i.e.* peak potential), current–time transients were used to study the difference in nucleation and growth aspects of the oxide film. Fig. 2.13 shows such a current–time response measured after stepping the potential from the open circuit value to 1.2 V *vs.* SCE, optimised primarily on the basis of voltammetry performed for the ZrO_2 formation. Although there is a pronounced maximum and a thousand-times decrease in the magnitude of the current for the case of the functionalized Au surface, the chronoamperometric data can be systematically analyzed after separating them into two regions (I and II in Fig. 2.13). The first region (*i.e.* time between 0 to t_o) corresponds to a sharp decrease in the current for both types of electrodes, whereas the second part of the curve shows distinct changes in nucleation behaviour before reaching a final steady state current. For region ($t < t_o$), both the electrodes indicate a linear relationship between I and $t^{1/2}$ (inset (I), Fig. 2.13) suggesting the mechanism of instantaneous nucleation corresponding to the growth of hemispherical nuclei kinetically controlled by planar or spherical

diffusion. However, both the lines do not intersect the origin, perhaps due to deviation from an ideal Cottrell diffusion process. The increase in the slope for the SAM-covered gold substrate may be partly due to the difference in the charging behaviour (double layer capacitance change) and nucleation sites.

The second region ($t > t_o$), on the other hand, indicates a peak at the beginning for the SAM-covered gold substrate, whereas a slow decrease only is observed for bare gold, finally reaching a steady value. The peak is not sharp and could be associated with the reductive desorption of dithiol monolayers, as simple alkanethiols at Au(111) surfaces are known to desorb beyond 1.0 V in aqueous electrolytes.[53] The nucleation of ZrO_2 on the SAM surface can be delayed due to the linkage of Zr to the surface, while such a restriction is not present for the case of bare Au. The kinetics is also different as the nature of the process elucidates a linear relationship between $\ln(I_o\text{-}I)$ and $\ln(t\text{-}t_o)$ for the bare electrode, while a sigmoidal relation is observed for the SAM covered gold electrode (inset (II), Fig. 2.13).

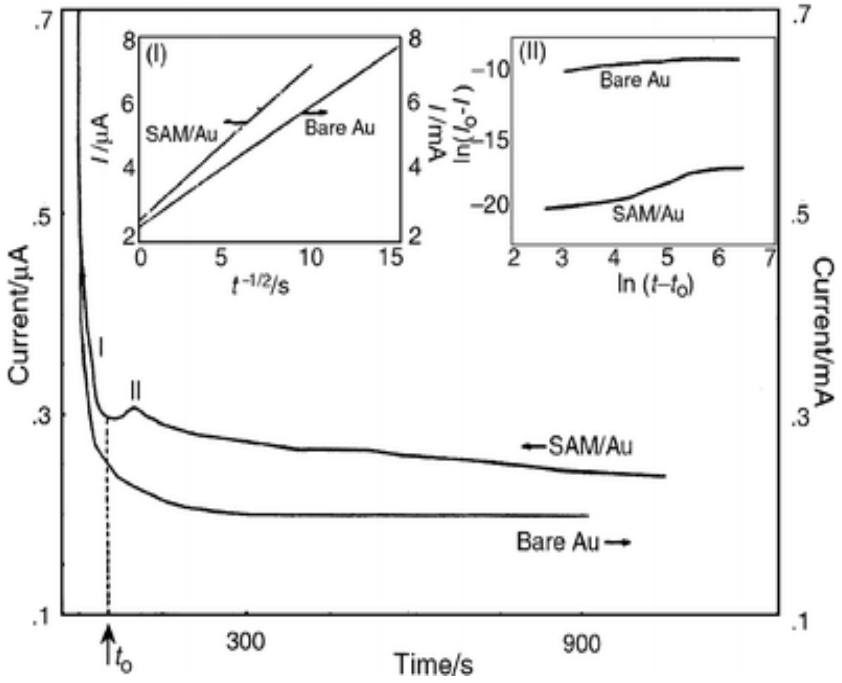

Figure 2.13 Current–time transients for (I) the SAM functionalized electrode, and (II) the bare gold electrode, as indicated in the figure illustrating the behaviour observed at potential 1.2 V. The solution was 1 M aqueous KCl + 5 mM $ZrOCl_2$. At t = 0 the potential was stepped from 0 to 1.2 V. The inset (I) indicates the plot of current *vs.* $t^{1/2}$ ($t < t_o$) for the same composition and similar electrodes as described above and inset (II) describes the variation of $\ln(I\text{-}I_o)$ with respect to $\ln(t\text{-}t_o)$.

This indicates that the potentiostatic formation of ZrO_2 is driven by progressive nucleation which is controlled by planar diffusion in the case of bare Au and by spherical diffusion in the case of the SAM-covered Au electrode. The difference in kinetics is due to constraints, such as pinholes and structural defects offered by the SAM,[48] probably controls the rate of nucleation, leading to improved crystallinity of ZrO_2 film on SAM-covered gold.

2.4.4 Impedance measurements

Despite the ambiguities of model-dependant interpretation, impedance measurements based on the response of an electrochemical cell to a small amplitude alternating signal offers a convenient method to study monolayer[54] structure and integrity. For example, the process of monolayer formation and the subsequent covalent attachment of Zr^{4+} from aqueous solution to the SAM-covered surface was followed by impedance measurements in the presence of a redox active probe, $Fe(CN)_6^{-4/3}$. In such systems, two distinct frequency regions can be separated in the presence of external redox agents like $Fe(CN)_6^{-4/3}$ using the simplest Randles' equivalent circuit.[55] In the low-frequency region, mass transfer *via* diffusion has to be taken into account, whereas, the micro-array behaviour of the pinholes within the passivating monolayer disturb the expected $\omega^{-1/2}$ dependence of Warburg impedance.[56] Defects or pinholes in the monolayer which are far apart from each other deviate from the semi infinite diffusion[27] and therefore spherical diffusion seems to be valid as overlap of diffusion layer is not achieved.[57]

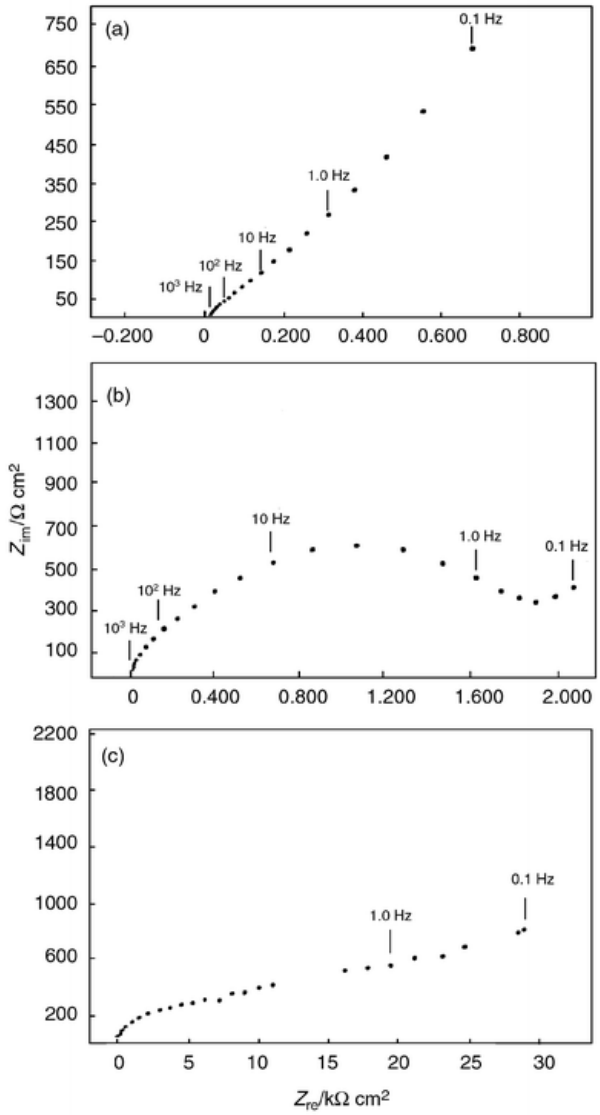

Figure 2.14 Impedance plots at a dc bias of 0.22 V in 5 mM $K_3Fe(CN)_6$ + 5 mM $K_4Fe(CN)_6$ in 0.5 M aqueous KF solution for (a) a bare gold electrode, (b) a gold electrode with a pentane-1,5-dithiol SAM, and (c) a gold electrode with a pentane-1,5-dithiol SAM after Zr attachment on the SAM surface from a 5 mM solution of $ZrOCl_2$. Frequency range used is 100 kHz to 100 mHz with a 5 mM rms signal at five steps per decade.

A comparison of the impedance plots of bare gold (Fig. 2.14a) and monolayer-coated gold (Fig. 2.14b) shows the effect of adsorbed dithiol monolayer on the ac response of gold electrodes. The impedance spectrum for bare gold is not well defined (probably due to a fast electrode reaction) and the absence of a semicircle precludes any quantitative calculation. In sharp contrast, identification of a well defined semicircle for SAM-covered gold

allowed us to calculate useful parameters, as it is known that at higher frequency the diameter of the semicircle corresponds to the R_{ct} of the monolayer coated electrode.[50] From the analysis of the spectrum in Fig. 2.14b, charge transfer resistance of 2109 Ωcm^2 is obtained with a corresponding approximate electrode coverage of 99%.[58] This result shows that the dithiol has formed a highly compact and organised monolayer assembly on the Au surface to give a good platform for further adsorption of Zr^{4+} from the solution.

Fig. 2.14c shows the impedance plot of the Au/SAM electrode after adsorption of Zr^{4+} ion. Comparison with Fig. 2.14b indicates a more dispersed impedance response. The expected semicircle at higher frequencies is not well defined in this case, although an approximate semicircle fit gives a charge transfer value of 9277 Ωcm^2. This drastic difference in impedance response of the two electrodes can be attributed to the attachment of Zr^{4+} from solution to the dithiol SAM covered surface which hinders the penetration of the redox probes. Since the monolayer acts as a barrier for ion permeation, adsorption of Zr ion on the SAM covered surface can make the electrode surface more passive and as a result of the electrostatic interactions, the permeation rate of ions becomes still lower.

2.4.5 X-Ray photoelectron spectroscopy

X-Ray photoelectron spectroscopic analysis of a Au substrate with dithiol monolayer formation and subsequent Zr attachment shows two peaks for sulfur core level spectra. The peak at lower binding energy after deconvolution shows two gaussian pairs consisting of spin–orbit components separated by a difference of 1.1 eV (Fig. 2.15a). The least-squares fit shows that there are two species of sulfur separated by 4.4 eV. The lower peak at *ca.*163 eV is in good agreement with that reported[59] earlier for chemisorbed thiol and dithiol monolayers on Au. The sulfur peak at *ca.* 167 eV is due to sulfate or sulfonic

acid moieties[60] formed due to X-ray beam damage of the free thiols (*i.e.* not linked to Zr species) during the measurements.[61]

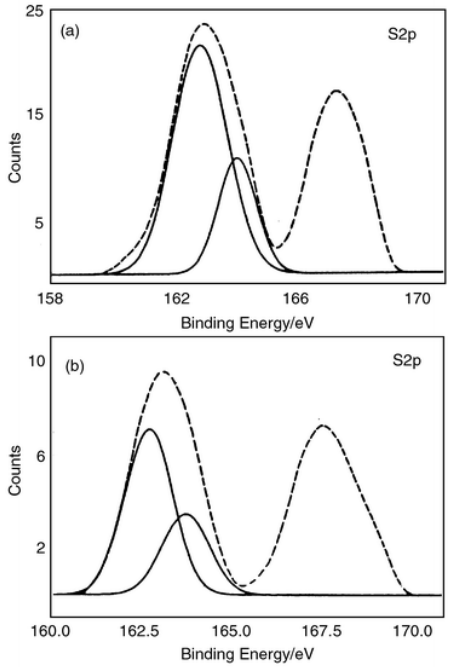

Figure 2.15 X-Ray photoelectron spectra of (a) the S 2p core level after subsequent Zr adsorption on the self-assembled monolayer functionalized Au surface, and (b) the S 2p core level after potentiodynamic cycling between 1.2 and +0.8 V.

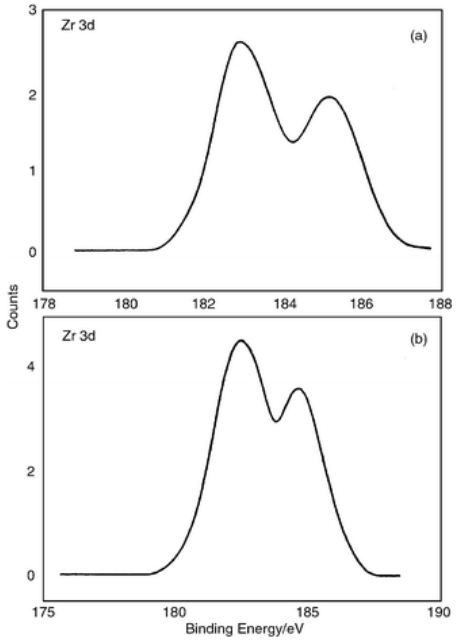

Figure 2.16 X-Ray photoelectron spectrum of (a) the Zr 3d core level after subsequent Zr attachment on the SAM covered Au surface, and (b) the Zr 3d core level after potentiodynamic cycling between 1.2 and +0.8 V for the SAM functionalized Au surface.

The evidence of sulfur peak after the potential cycling demonstrates that the underlying dithiol monolayer is stable during the formation of ZrO_2 (Fig. 2.15b). Although the relative cross section of sulfur is very small, the binding energy values are particularly sensitive to the chemical environment of sulfur. The Zr 3d signal on a SAM covered gold surface before (Fig. 2.16a) and after (Fig. 2.16b) potentiodynamic cycling consists of a Zr $3d_{5/2}$ peak at *ca.* 182.4 eV and a Zr $3d_{3/2}$ peak at 185.6 eV, whereas the XPS data of a bare gold substrate dipped in a zirconyl oxychloride aqueous solution indicates no such peaks, revealing no Zr attachment on the bare gold surface before or after the cycling.

2.4.6 Scanning electron microscopy

Scanning electron microscopy performed on ZrO_2 obtained after potentiodynamic cycling on bare and functionalized Au surfaces shows interesting morphological features. First, distinct zirconia crystals possessing an average size of 5–10 μm can be seen on the SAM coated Au surface (Fig. 2.17a), suggesting the formation of uniform and sharp-edged crystals at room temperature. More significantly, the distinct separation between crystals (5–10 μm) due to Zr attachment on the SAM is missing for ZrO_2 formed on a bare gold substrate (Fig. 2.17c), where ZrO_2 particles distributed continuously with an average interparticle distance of 5 μm suggest random nucleation. Even maintenance of 1.2 V for several hours (Fig. 2.17d) shows continuous growth of ZrO_2 films as compared to that for the functionalized interface. This type of variation in crystal habit exhibited by a given organic molecule is known to result from variations in the conditions under which the substance crystallised. This highlights the significance of SAMs in controlling the directional growth of the solid materials at the interface. This is specially significant for biomimetic processing of materials since several reports[62] have recently shown that the manipulation of the surface energies is possible through SAM formation to favour heterogeneous growth and nucleation.

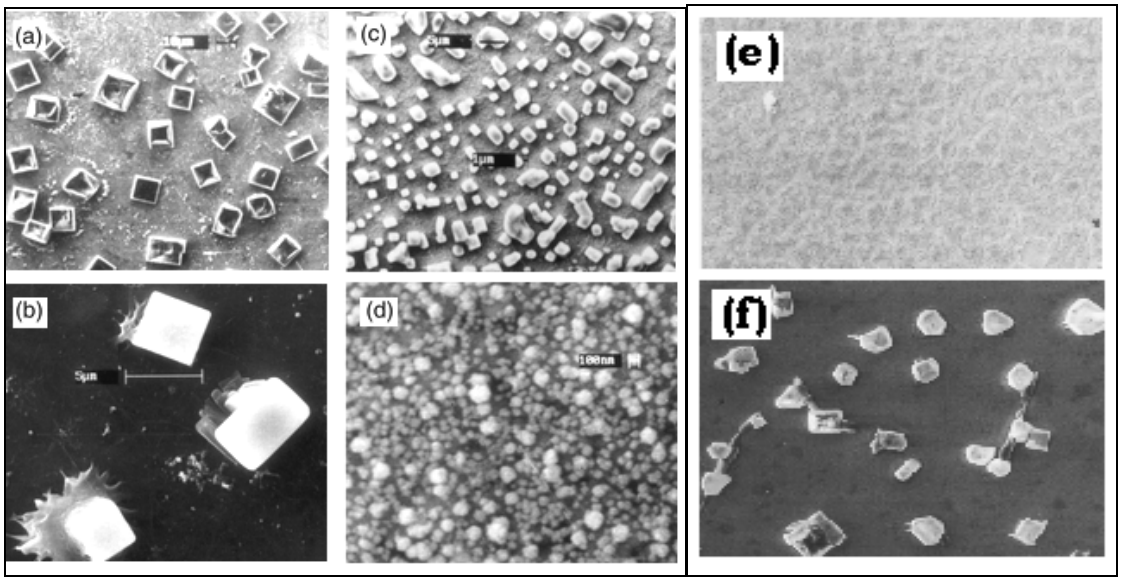

Figure 2.17 Micrographs of microcrystalline zirconia on (a) a gold coated glass substrate derivatized with a SAM of pentane-1,5-dithiol, (b) a SAM functionalized gold surface with higher resolution, (c) a bare gold substrate, and (d) a bare gold substrate cycled for longer time. The samples were prepared by potentiodynamic cycling at a scan rate of 200 mV/s over a potential range of +0.7 to 1.1 V *vs.* SCE. (e) illustrates the effect of -CH_3 terminated SAM, (f) –NH_2 terminated SAM, respectively on ZrO_2 nucleation under identical potentiodynamic cycling.

All the above results indicate that microcrystalline zirconia with better topographic control can be grown at room temperature on SAM surfaces. The difference in nucleation and growth kinetics due to Zr attachment on the dithiol functionalized Au surface is primarily responsible for this, as evidenced in the current–time transients. The role of SAMs in this context is to be compared with the role of organic materials as manipulators of morphology, leaving an imprint of their original presence even after complete oxidation at high temperature.[63,64] We believe that this morphology difference is explained by the ability of SAMs to favour certain growth directions, as manifested from the relative microscopic evidence of crystals obtained in the absence of SAMs.

2.5 CONCUSIONS

In this chapter we demonstrate the role of two important parameters affecting the kinetic stability of SAMs namely geometric constraints and substrate-head group interaction. The facile S-S cleavage in DDS is one of the main reasons for the enhanced stability of the monolayer as also illustrated by

the structurally similar DDSe. By contrast, NDS forms a thermally unstable and less ordered monolayer, presumably due to the structural rigidity. We also reveal that the morphology of ceramic materials can be controlled using SAMs *via* Zr attachment on self-assembled monolayers of dithiol on an Au surface followed by a simple potentiodynamic cycling to give microcrystalline, monoclinic ZrO_2 at room temperature. The results discussed here also suggest the possible use of self-assembled monolayers to effectively modify the morphology of ceramic thin films with promising applications in a wide range of fields including electrochemical sensors, electrocatalysis and ceramic coatings. A similar functionalization strategy could also be extended to prepare tetragonal or cubic zirconia at room temperature, with control of appropriate electrolyte composition.

2.6 REFERENCES

1. Ulman, A., "*An Introduction to ultrathin organic films from Langmuir-Blodgett to Self-assembly.*" Academic Press, San Diego, CA, 1991. pp. 237.
2. Nuzzo, R.G.; Allara, D.L. *J. Amer. Chem. Soc.* **1983**,*105*, 4481.
3. Hickman, J.J.; Ofer, D.; Laibinis, P.E.; Whitesides, G.M. *Science* **1991**, *252*, 688.
4. Nuzzo. R.G.; Zegarski, B.R.; Dubois, L.H. *J. Amer. Chem. Soc.* **1987**, *109*, 733.
5. Ulman, A. *Chem. Rev.* **1996**, *96*, 1533.
6. Fenter, P.; Eberhardt, A.; Eisenberger, P. *Science* **1994**, *266*, 1216.
7. Patai, S.; Rappoport, Z. "*Organic Selenium and Tellurium Compounds*." John Wiley & Sons: New York, 1986, Vol.1. pp. 44.
8. Bandyopadhyay, K.; Sastry, M.; Paul, V.; Vijayamohanan, K. *Langmuir* **1997**, *13*, 866.
9. Oesch, U.; Janata, U. *J. Electrochimica Acta* **1983**, *28*, 1237.
10. Samant, M.G.; Brown, C.A.; Gordon II, J.G. *Langmuir* **1992**, *8*, 1615.
11. Dishner, M.H.; Hemminger, J.G.; Feher, F.J. *Langmuir* **1997**, *13*, 4788.
12. Bandyopadhyay, K.; Vijayamohanan, K. *Langmuir* **1998**, *14*, 625.
13. Bryant, M.A.; Pemberton, J.E. *J. Am. Chem. Soc.* **1991**, *113*, 3629.
14. Murty, K.V.G.; Venkataramanan, M.; Pradeep, T. *Langmuir* **1998**, *14*, 5446.
15. Bain, C.D., Troughton, E.B., Tao, Y.T., Evall, J., Whitesides, G.M., and Nuzzo,
    R.G. *J. Am. Chem. Soc.* **1989**, *111*, 321.
16. Frey, B.L.; Hanken, D.G.; Corn, R.M. *Langmuir* **1993**, *9*, 1815.
17. Brust, M.; Blass, P.M.; Bard, A.J. *Langmuir* **1997**, *13*, 5602.
18. Bunker, B.C.; Rieke, P.C.; Tarasevich, B.J.; Campbell, A.A.; Fryxell, G.E.; Graff, G.L.; Song, L.; Liu, J.; Virden, J.W.; McVay, G.L. *Science* **1994**, *264*, 48.
19. Bell, C.M.; Yang, C.H.; Mallouk, T.E. *Materials Chemistry (An Emerging Discipline)*, ed. L. V. Interrante, L. A. Casper and A. B. Ellise, 1995, p. 211.
20. Agarwal, M.; De Guire, M.R.; Heure, A.J. *J. Am. Ceram. Soc.* **1997**, *80*, 2967.
21. Rao, C.N.R. *J. Mater. Chem.* **1999**, *9*, 11.

22. Lee, H.; Kepley, L.J.; Hong, H.; Akhtar, S.; Mallouk, T.E. *J. Phys. Chem.* **1988**, *92*, 2597.
23. Mann, S.; Nicholas, H.C.; Frankel, R.B.; Bazylinski, D.A.; Jannasch, H.W. Nature **1990**, 343, 258.
24. Shin, H.; Collins, R.J.; De Guire, M.R.; Heure, A.H.; Sukenik, C.N. *J. Mater. Res.* **1995**, *10*, 3692.
Rieke, P.C.; Marsh, B.D.; Wood, L.L.; Tarsevich, B.J.; Liu, J.; Song, L.; Fryxell, G.E. *Langmuir* **1995**, *11*, 318.
25. Gamage, S.A.; Smith, R.A.J. *Tetrahedron* **1990**, *46*, 2111.
26. Bandyopadhyay, K.; Vijayamohanan, K.; Venkataramanan, M.; Pradeep, T. *Langmuir* **1998**, *15*, 5314.
27. Bain, C.D.; Troughton, E.B.; Tao, Y.; Evall, J.; Whitesides, G.M.; Nuzzo, R.G. *J. Am. Chem. Soc.* **1989**, *11*, 321.
28. Bain, C.D.; Evall, J.; Whitesides, G.M. *J. Am. Chem. Soc.* **1989**, *111*, 7155.
29. Bandyopadhyay, K.; Sainkar, S.R.; Vijayamohanan, K. *J. Am. Ceram. Soc.* **1999**, *82*, 1622.
30. K. Bandyopadhyay and K. Vijayamohanan, *Langmuir* **1998**, *14*, 6924.
31. Lakshminarayanan, V. *Curr. Sci.* **1998**, *74*, 413.
32. Sauerbrey, G. *Z. Phys.* **1959**, *155*, 206.
33. Buttry, D.A.; Ward, M.D. *Chem. Rev.* **1992**, *92*, 1355.
34. Porter, M.D.; Thomas, B.B.; Allara, D.L.; Chidsey, C.E.D. *J. Am. Chem. Soc.* **1987**, *109*, 3559.
35. Miller, C.; Cudent, P.; Grätzel, M. *J. Phys. Chem.* **1991**, *95*, 877.
36. Sabatini, E.; Rubinstein, I. *J. Phys.Chem.* **1987**, *91*, 6663.
37. Icenhower, D.E.; Urbach, H.B.; Harisson, J.H. *J. Electrochem. Soc.* **1970**, *117*, 1500.
38. Whiteman, R.M. *Anal. Chem.* **1981**, *53*, 1127A.
39. Amatore, C.; Saveant, J.M.; Tessier, D. *J. Electroanal. Chem.* **1983**, *147*, 39.
40. Chuan-Jian, Z.; Porter, M.D. *J. Am. Chem. Soc.* **1994**, *116*, 11616.

41. Burgess, I.; Jeffrey, C.A.; Cai, X.; Szymanski, G.; Galus, Z.; Lipkowski, J. *Langmuir* **1999**, *15*, 2607.
42. Dishner, M.H.; Peter, T.; Hemminger, J.C.; Feher, F.J. *Langmuir* **1998**, *14*, 6676.
43. B. D. Cullity and C. Cohen, *Elements of X-ray diffraction*, Addison-Wesley Publishing Co. Inc., 1956.
44. Yao, T.; Inui, T.; Ariyoshi, A. *J. Am. Ceram. Soc.* **1996**, *79*, 3329.
45. Preusser, S.; Stimming, U.; Wippermann, K. *Electrochim. Acta* **1996**, *39*, 1273.
46. Gal-Or, L.; Silberman, I.; Chaim, R.J. *J. Electrochem. Soc.* **1991**, *138*, 1939.
47. Porter, M.D.; Bright, T.B.; Allara, D.L.; Chidsey, C.E.D *J. Am. Chem. Soc.* **1987**, *109*, 3559.
48. Bandyopadhyay, K.; Vijayamohanan, K.; Shekhawat, G.S.; Gupta, R.P. *J. Electroanal. Chem.* **1998**, *447*, 11.
49. Sabatani, E.; Rubinstein, I.; Maoz, R.; Sajiv, J. *J. Electroanal. Chem.* **1987**, *219*, 365.
50. Bain, C.D.; Biebucky, H.A.; Whitesides, G.M. *Langmiur* **1989**, *5*, 723.
51. Milchev, A. *Contemporary Physics* **1991**, *32*, 321.
52. Zhong, C.-J.; Porter, M.D. *J. Electroanal. Chem.* **1997**, *425*, 147.
53. Sabatani, E.; Cohen-Boulakia, J.; Bruening, M.; Rubenstein, I. *Langmuir* **1993**, *9*, 2974.
54. Sluyters-Rehback, M.; Sluyters, J.H. *Electroanalytical Chemistry*, ed. A. J. Bard, Dekker, New York, 1970, vol. 4.
55. Finklea, H.O.; Sinder, D.A.; Fedyk, J.; Sabatani, E.; Gaini, Y.; Rubinstein, I. *Langmuir* **1993**, *9*, 3660.
56. Tokuda, K.; Gueshi, T.; Matsuda, H. *J. Electroanal. Chem.* **1979**, *102*, 41.
57. Approximate coverage (θ) of the dithiols on gold electrode can be measured using charge transfer resistance of bare (R_{ct}) and monolayer coated (R_{ct}') gold electrode by using the relation = 1 [R_{ct}/R_{ct}']. R_{ct}s are calculated from the

impedance plane plot at higher frequency in the presence of both the oxidized and reduced species present in the solution. Charge transfer resistance is expected to increase at monolayer covered electrode due to inhibition of electron transfer compared to bare electrode.

58. Castner, D.G.; Hinds, K.; Grainger, D.W. *Langmuir* **1996**, *12*, 5083.
59. Mekhalif, Z.; Riga, J.; Pireaux, J.J.; Delhalle, J. *Langmuir* **1997**, *13*, 2285.
60. Henglein, A. *Top. Curr. Chem.* **1988**, *143*, 113.
61. Liu, J.; Feng, X.; Fryxell, G.E.; Wang, Q.; Kim, Y. *Adv. Mater.* **1998**, *10*, 161.
62. Kresge, C.T.; Leonowicz, M.E.; Roth, W.T.; Vartuli, J.C.; Beck, J.S. *Nature* **1992**, *359*, 710.
63. Messersmith, P.B.; Stupp, S.I. *Chem. Mater.* **1995**, *7*, 454.

Chapter 3

Multilayered Ag nanocluster arrays using sequential self-assembly of dithiol molecular interconnects on Au (111) surface*

The major theme of this thesis revolves around the organization of nanoparticles using various interactions and this chapter demonstrates one of them. A superlattice of silver nanoclusters (core size ~ 2 nm) was prepared using the sequential self-assembly of 1,5-pentanedithiol (PDT) and octanedithiol (ODT) on an Au (111) substrate. The formation of highly ordered silver nanocluster array was confirmed using AFM, STM and also by the longitudinal periodicity observed in the low angle X-ray diffraction pattern. In contrast to the behaviour of dithiol self-assembled monolayers (SAM) on gold substrates, which gives only blocking behaviour, the superlattice exhibits interesting electrochemical properties in terms of redox accessibility of silver nanoclusters with respect to potential cycling. The layer-dependent studies using QCM suggests that for ODT/Ag array the mass uptake for Ag nanoparticles decreases by *ca.* 20% with number of layers and there is a linear increase in Ag x-ray photoelectron intensity.

*A portion of this chapter has been published in: **J. Mat Chem.** *11*, 1710-1714 (2001), and another part has been communicated to **Colloids and Surfaces A** (2002).

3.1 INTRODUCTION

Different methods of organising quantum dot superlattices of metals and semiconductors have received significant interest in recent times as the tailoring of particle sizes and interparticle separation can, in principle, cause unique magnetic, optical and electronic behaviour.[1-5] For example, several nanocluster assemblies organised in different length scales have been found to be promising due to their potential applications in many diverse areas such as optoelectronic devices, single electron transistors and chemical sensors.[4-8] One of the principal objectives is to accomplish the design of broadly applicable synthetic schemes that produce superlattices of nanoparticles where the particle size as well as the interparticle coupling can be controlled.[9]

Self-assembled monolayer (SAM) formation offers a simple and flexible method for organising nanoclusters on noble metal surfaces. Using SAM there have been several attempts recently to obtain a systematic arrangement of metal and semiconductor nanoparticles in different dimensions in contrast to the use of sophisticated and expensive method molecular of beam epitaxy which is widely used for superlattice formation. Self-organised 2-D nanoparticle superlattices of semiconductors[10,11] and metals[12-15] as well as 3-D assemblies of nanoparticles[16,17] have been constructed and analysed. One of the important advantages of this approach is that the tailoring of band structure can be accomplished by selecting appropriate organic molecules to protect nanoclusters. Since many metallic and semiconducting clusters (Au, Ag, CdS, CdSe *etc.*) have high affinity for amine and thiol moieties, both the size and the interparticle separation can be controlled by changing the organic spacer. While it has been generally proved that both Ag and Au nanoclusters can be organised on a SAM surface, the sequential extension of this organisation to demonstrate novel optical and electrochemical properties is rather unknown. Two-dimensional organisation of these clusters requires the control of the interparticle coupling and in comparison with semiconductors, metal clusters have strong dispersion interactions.[18] The nature of these interactions is

indicative of the dependence of superlattice formation on particle size and also the degree of interparticle coupling through the bridging ligand.

In chapter 2 we have demonstrated the usefulness of ω-terminated SAM in obtaining crystalline thin ceramic oxide films along with some structural studies of aromatic disulfides. In this chapter, we have demonstrated the fabrication of layer-by-layer self-assembly of ordered uncapped silver nanoclusters using a 1,5-pentanedithiol SAM as a building block on a gold substrate. More specifically, the role of the protective monolayer coating in controlling both the particle–particle interaction and the electron transfer properties of Ag clusters is investigated using X-ray diffraction (XRD), photoluminescence and electrochemistry after repeated SAM formation and cluster organisation. Although superlattices of alkanethiolate passivated silver nanoclusters have been reported earlier,[18,19] this is the first report of a repeated multilayer superlattice with photoluminescence and electrochemical characterisation. In continuation, we have also demonstrated the extension of such an approach using a longer organic spacer molecule to compare our previous results. We illustrate the fabrication of Ag nanocluster arrays (size 1.4 ± 0.4 nm) using sequential SAMs of 1,8 octanedithiol, where, the presence of longer organic molecule (1.2 nm) can lead to a considerable degree of order in the superlattice formation. Since the particle size control plays a key role in such an organization due to their strong dispersion interaction, it is essential to understand if a sequential approach can be adapted to extend the organization of superlattice with a different cell parameter. Although, earlier work had shown the multilayer formation of Au nanoclusters using dithiol,[20] their electrical and electrochemical behavior were not investigated. In addition, the length of the molecular interconnect was not considered as a parameter in that study despite its importance, the relative merits and demerits of this type of nanocluster organization with respect to other electrostatic and hydrophobic modes is also taken into account.[21]

3.2 EXPERIMENTAL

3.2.1 Materials

Vacuum deposited 200 nm Au (purity 99.99%) film was prepared using the procedure described in chapter 2 (section 2.2.1). 1,5-Pentanedithiol, 1,8-Octanedithiol, $AgNO_3$ and $NaBH_4$ obtained from Aldrich were used as received. The layer-by-layer formation of a silver quantum dot superlattice on a SAM surface was carried out in the following manner.

3.2.2 SAM/Ag Nanoparticles Mono/Multilayer Formation

A SAM of 1,5-pentanedithiol was formed on an Au surface from a 1 mM ethanolic solution of the respective compounds for 24 h, followed by washing with ethanol and drying in a jet of argon. The details of the preparation and characterisation of these dithiol monolayers have been described earlier (chapter 2 section 2.2.3). The SAM covered gold surface was then introduced into a dilute aqueous dispersion of uncapped silver nanoclusters, instantaneously prepared by the controlled reduction of 10^{-4} M aqueous $AgNO_3$ solution using the desired amount of $NaBH_4$ by following reported procedures.[22] After the adsorption of silver particles (typically for 2 h), the substrate was washed with ethanol and dried in air. The second layer of dithiol SAM was formed by immersing this substrate in an ethanolic solution of 1,5-pentanedithiol for several hours followed by subsequent adsorption of silver clusters as explained before. These steps were repeated to obtain multilayer superlattices of two and four layers of silver clusters (hereafter specified as 2L and 4L respectively). The same procedure has been applied to get the assemblies with 1,8 octanedithiol as linker molecule. The self-assemblies thus prepared were characterised by low angle XRD, cyclic voltammetry (CV), AFM, STM, TEM and photoluminescence.

3.2.3 Uv-vis Spectroscopy

The presence of metal nanoclusters in the initial solution was analysed using optical absorption spectrophotometry. The absorption spectra were recorded on a Hewlett Packard 8452 diode array spectrophotometer with 2 nm spectral resolution at room temperature. The procedure for the sequential self-assembly was repeated in the same fashion with a longer dithiol molecule (ODT) for the structural analysis and organizational capability in comparison with smaller PDT molecule.

3.2.4 X-ray Photoelectron Spectroscopy (XPS)

Self-assembly on the gold substrate was confirmed by XPS studies. XPS measurements were carried out on a VG MicroTech ESCA 3000 instrument at a pressure >1 × 10^{-9} Torr. For ODT/Ag array, the general scan and Ag 3d, C 1s, S 2p, and O 1s core-level spectra were recorded with unmonochromatized Mg Kα radiation (photon energy = 1253.6 eV) at a pass energy of 50 eV and an electron takeoff angle (angle between electron emission direction and surface plane) of 60^{o}. The overall resolution was ~1 eV for the XPS measurements. The core-level binding energies (B.E.) were aligned taking the Au peak as 83.9 eV.

3.2.5 Atomic Force Microscopy (AFM)

The assembly of silver cluster arrays on the SAM coated gold surface was identified by AFM imaging under ambient conditions using a Nanoscope II (Digital Instruments, USA) in the tapping mode. The AFM was initially calibrated using mica and then using a gold coated Si wafer. The first layer of the nanocluster arrays grown on the Au coated Si wafer was used for actual imaging. Silicon tip cantilevers with a force constant of 20–100 N/m and a resonance frequency around 200–400 kHz were used. The nominal tip radius was less than 10 nm. The AFM tip was guided to the middle of the sample

before imaging. The images presented contain 256 × 256 data points collected within several seconds. The images were scanned from different areas of the sample to verify continuity in the structure. The error estimates on the horizontal and vertical distances were ±0.1 Å and ±0.05 Å respectively. To avoid tip-related artefacts, imaging was performed with minimal (up to 7 nN) force.

3.2.6 Electrochemical and Photoluminescence Studies

The details of the electrochemical measurements discussed in this chapter are identical to that given in chapter 2 (section 2.2.5) except that the standard three electrode cell had Ag nanoclusters organised on a gold substrate as the working electrode. The scans were recorded with an instrumental accuracy of ±1 mV and ±5 μA. Photoluminescence (PL) measurements were performed on a Perkin-Elmer (LS50) photoluminescence spectrophotometer. The emission spectra were collected between 300–800 nm using a 250 nm excitation and a 290 nm filter with a spectral resolution of ±3 nm at room temperature.

3.2.7 Quartz Crystal Microbalance (QCM)

The frequency counter used was an Edwards FTM5 instrument operating at a frequency stability and resolution of ±1 Hz. For the 6 MHz crystal used in this investigation, this translates into a mass resolution of 12 ng/cm^2. The frequency changes were converted to mass loading using the standard Sauerbrey formula.[23] All the measurements were performed *ex-situ* after thorough washing and drying of the crystal prior to frequency measurements. Before the deposition the crystals were cleaned using pirhana solution (section 2.2.3), washed thoroughly with the solvent used for the SAM formation and dried under ambient condition. The frequency change due to adsorption was converted directly to mass and plotted with time. One of the major limitation of

this measurement is the gradual shift in the base line. To overcome this, the mass change observed for a blank experiment (only with solvent) without monolayer was subtracted from all the experimental data. This blank experiment to some extent provided the inherent drift to the system.

3.2.8 Other measurements

X-Ray diffraction (XRD) measurements were performed at room temperature using a Rigaku Miniflex with filtered CuKα radiation (λ = 1.5404 Å). The scanning 2θ range was set between 1.5° and 5° at a scan rate of 0.5° per min. The details of the STM experiments have already been described in the previous chapter (section 2.2.6). TEM measurements were carried out on a JEOL model 1200EX instrument operated at an accelerating voltage of 120 kV after adsorbing Ag clusters on a copper grid. The normal incidence selected area electron diffraction (SAED) pattern was also obtained.

3.3 SYNTHESIS AND COVALENT ASSEMBLY OF Ag NANOPARTICLES

3.3.1 Optical absorption of silver hydrosol

Since the majority of the reported procedures for Ag cluster preparation use either capping agents or surfactants for the stabilisation of clusters in solution, it is extremely important to characterise the uncapped Ag cluster solution prior to the adsorption on the SAM surface. Fig. 3.1a illustrates the optical absorption spectra of the as-prepared cluster solution along with similar data obtained after 150 (Fig. 3.1b) and 270 min respectively (Fig. 3.1c). An intense plasmon absorption band at approximately 390 nm is observed for the silver particles.

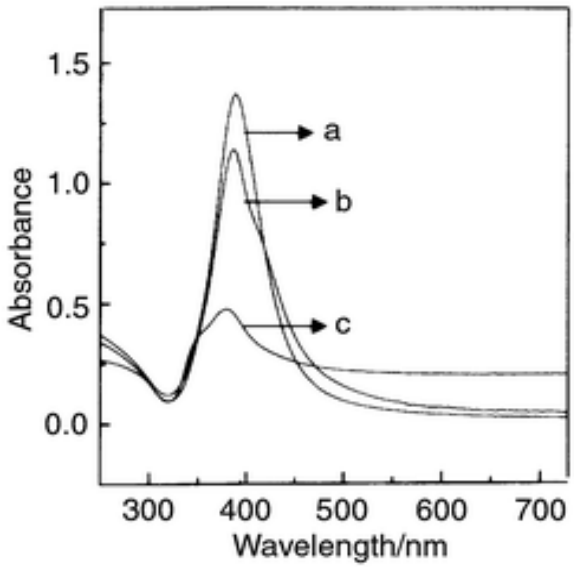

Figure 3.1 Time dependent optical absorption spectra of uncapped silver clusters in aqueous solution: (a) as prepared, (b) after 150 min, (c) after 270 min.

This band signifies that the clusters contain very few silver atoms. Such a band at 380 nm has already been observed for colloidal particles with a diameter around 1 nm.[24,25] In comparison, our clusters show an average diameter of 0.55 nm as estimated from the half width of the surface plasmon band.[26] As the clusters are uncapped, this plasmon resonance absorption can only provide information about the particle size of the clusters in the sol, which however, cannot be considered as a true measure of the size. Systematic monitoring of the optical absorption of the silver sol every 30 min shows that it is stable only for 120 min. For example, the absorption of the same cluster solution after 150 min. (Fig. 3.1b) shows changes in the shape of the absorption band. Interestingly, the peak maximum is observed at the same wavelength but with reduced intensity. This along with the presence of a red shifted shoulder presumably suggests the deterioration of the cluster solution after two hours. The agglomeration of particles can be distinctly seen as a shoulder appearing at 300 nm in Fig. 3.1c, although the existence of clusters is apparent by the band at 390 nm which is substantially reduced in intensity. Since size effects limit the lifetime of the clusters in aqueous solution as reflected by the coalescence, disproportionation and oxidation of clusters,[27] a

fresh solution was always prepared for sequential organisation on the SAM covered surface.

3.3.2 Identification of superlattice formation

Fig. 3.2 shows the sulfur core level X-ray photoelectron spectrum of a SAM covered gold film. In order to determine the S 2p binding energies as accurately as possible, a non-linear least squares fit of the data was performed using two gaussian pairs consisting of spin–orbit components ($2p_{3/2}$ and $2p_{1/2}$) with a separation of 1.15 eV. The least squares fit indicates that there are two sulfur species separated by 6 eV.

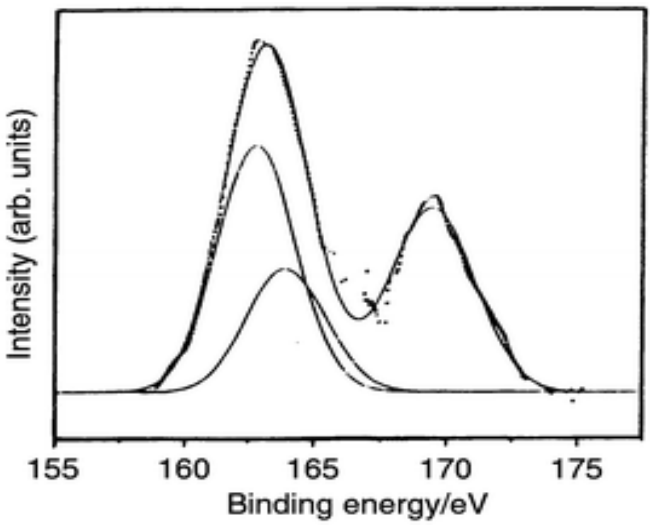

Figure 3.2 X-Ray photoelectron spectra for the dithiol functionalized Au surface: S 2p core level region of dithiol monolayer on gold together with non-linear least squares Gaussian fits showing spin–orbit components (*ca.* 163 corresponding to $2p_{3/2}$) with a separation of 1.15 eV and a peak (*ca.* 167 eV) due to sulfate/sulfonic acid moieties.

The lower peak at *ca.* 163 eV is in good agreement with that reported earlier[28] for chemisorbed thiol and dithiol monolayers on Au and Ag. The second peak at *ca.* 167 eV is thought to be due to sulfate or sulfonic acid moieties[29] formed

due to X-ray beam induced damage of free thiols. Both sulfate and sulfonic moieties seem to be present from the XPS as this peak appears more distorted.

The AFM raw image (Fig. 3.3a) of the first layer of silver clusters obtained after the adsorption of clusters indicates a highly ordered and closely packed array of silver nanoclusters appearing as nanorods in the FT filtered image (Fig. 3.3b). The protrusions coming out of the radius of the tip are likely to cause an enhancement in the resolution as observed. This anisotropically ordered arrangement is attributed to the diffusion of the unprotected silver clusters across the SAM, due to strong dispersion interactions between metal clusters. The cluster arrays having a width of 6.5 Å and height of 20 Å are clearly seen in the enlarged and processed image.

Fig. 3.4 shows the low angle XRD pattern of four layers of Ag nanostructures on a SAM functionalized gold substrate. The diffractogram reveals a significant peak at 2.08° illustrating the sequential organisation of Ag clusters on the SAM surface. This peak corresponding to the longitudinal repeat distance of 42 Å suggests interesting organisational changes in the cluster shape after adsorption on the dithiol template. An approximate calculation of the cluster height from the difference between the assessed periodicity and the dithiol length (*ca.* 9 Å from ellipsometric measurements assuming a refractive index of 1.5 for dithiol SAM) gives 32 Å. Although this estimated cluster height is considerably larger than that observed in the AFM image, this discrepancy could be attributed to various reasons such as the presence of multiple layers, large errors involved in the ellipsometric measurements of small molecules *etc.*

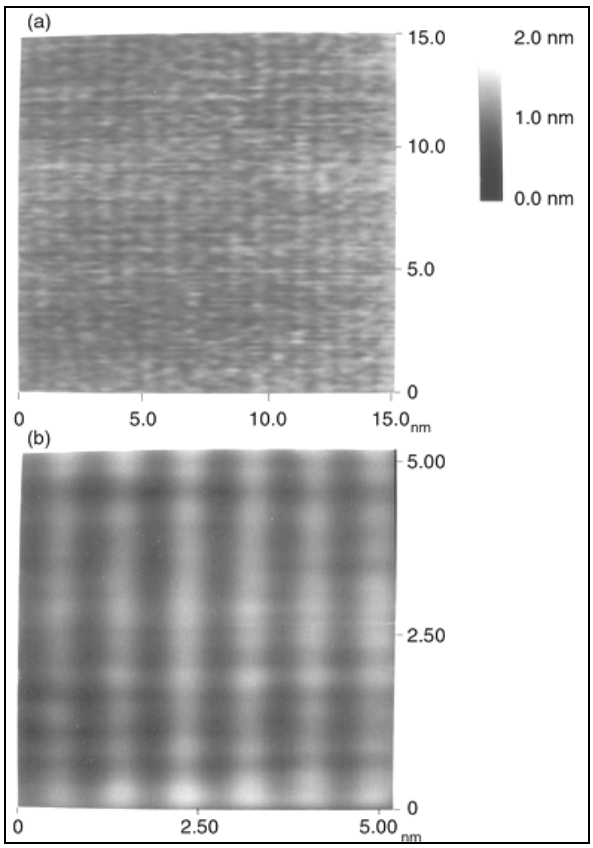

Figure 3.3 AFM image of the first layer of silver nanoclusters on SAM coated gold. The images presented contain 256 × 256 data points collected within several seconds. (a) Raw image, (b) enlarged and Fourier transform-filtered image.

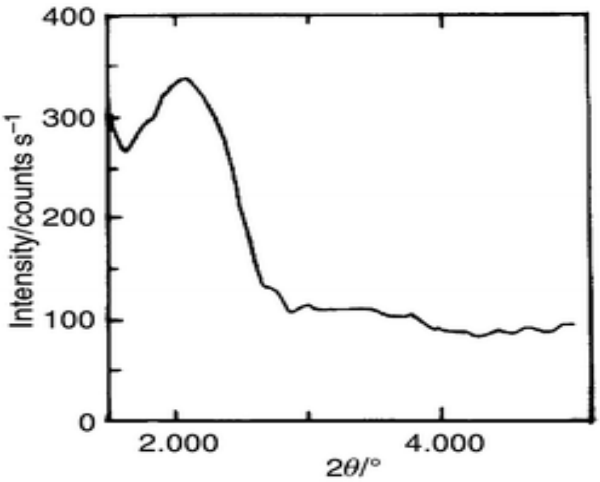

Figure 3.4 Low angle X-ray diffractogram of four layers of Ag nanostructures on a SAM functionalized gold substrate taken at a scan rate of 0.5°/min.

3.3.3 Cyclic voltammetry

The processes of adsorption of dithiol and subsequent Ag cluster attachment in various stages have been followed by measuring the cyclic voltammetric response of these modified electrodes in 1 M aqueous KCl solution. Fig. 3.5 shows such a superimposed cyclic voltammogram of a gold electrode modified with a dithiol SAM (a), and after the adsorption of Ag clusters in two stages (b and c) in the potential range of 1.0 to +0.8 V. The significant reduction in capacitance upon SAM formation as manifested in the comparison of the CVs for the bare and SAM covered surfaces has been discussed several times previously.[30] An approximate calculation of the double layer capacitance (at *E* = 250 mV *vs.* SCE) value from this response taken at 500 mV/s scan rate indicates a capacitance change from 25 μF/cm^2 for bare gold (not indicated in the figure for clarity) to 1.2 μF/cm^2 for the dithiol modified gold electrode (Fig. 3.5a) suggesting the compact nature of the primary monolayer.

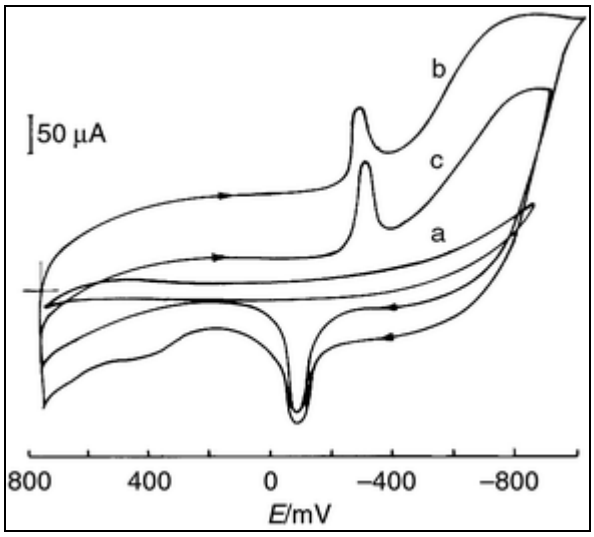

Figure 3.5 Superimposed cyclic voltammograms in 1 M KCl for (a) a gold electrode modified with a SAM of 1,5-pentanedithiol, and after (b) one layer and (c) two layers of silver nanocluster superlattice formation on the SAM surface with a typical scan rate of 500 mV/s.

Two-dimensional organisation of Ag nanoclusters on this primary SAM surface drastically increases the differential capacitance from 1.2 to 35 μF/cm^2(Fig. 3.5b) while a slight decrease is observed for a repeated sequence of SAM

formation and Ag nanocluster organisation (Fig. 3.5c). A geometric variation alone (*i.e.,* area under the peak and separation) cannot account for these interesting changes in differential capacitance and perhaps a more important reason is the abrupt change in dielectric constant before and after silver nanocluster formation.

Consequently more importance should be given to the presence of a sharp reversible peak after Ag nanocluster organisation, which in combination with the above change in double layer capacitance suggests that Ag clusters act as a nanoelectrode array collectively enabling the passage of electrons through the SAM barrier. Although the blocking effect of the SAM is retained in the anodic region of Fig. 3.5b, a sharp reversible peak is observed around E° = 100 mV *vs.* SCE with a peak to peak separation of 190 mV and a peak current ratio approaching unity. Apart from demonstrating the redox accessibility of Ag nanoclusters, a comparison of this formal potential with the standard value corresponding to the Ag/Ag^+ couple (+0.779 *vs.* SCE) suggests the importance of quantum size effects.[24] Since the silver clusters are surface bound, one ideally expects all the characteristic signatures of voltammetric response of an electrochemically reversible redox reaction (peak current, I_p, proportional to scan rate; peak potentials and wave shapes for the cathodic and anodic surfaces identical and the full width at half maximum (FWHM) equal to 90.61/*n* mV, where *n* is the number of electrons transferred) although deviations due to non-idealities such as particle–particle and adsorbed particle–organic dipole interactions can occur.

Organisation of the second layer of Ag nanoclusters (Fig. 3.5c) does not change the position of both the peaks and this similarity of $E_{1/2}$ values also suggests that the size of the Ag nanoclusters in the second layer is not drastically different from the size in the first layer. The full widths at half maximum are also identical but the actual peak current and coverage for both oxidation and reduction peaks for the second layer are more (*e.g.* the

calculated coverage values of the cathodic peak for second and first layers are 30.3 μC/cm^2 and 25.1 μC/cm^2 respectively). An approximate calculation of the charge under the peak for both the first and second layers also shows less charge for the anodic peak, probably due to electrostatic repulsion between the oxidised form of clusters. Fig. 3.6 shows the cyclic voltammograms of a dithiol monolayer with one layer of Ag nanoclusters taken at various scan rates (without any correction due to ohmic drop) in 1 M aqueous KCl solution in the potential range of 1.0 to +0.8 V. The reversible redox couple can be observed at all scan rates, although a 100 mV/s scan rate gives optimum features of highest peak current and lowest peak potential separation. Compared to the anodic peak potentials, the cathodic peak potentials are found to shift more with scan rate and a stronger binding of thiols to the reduced form of the clusters may be one of the contributing factors.

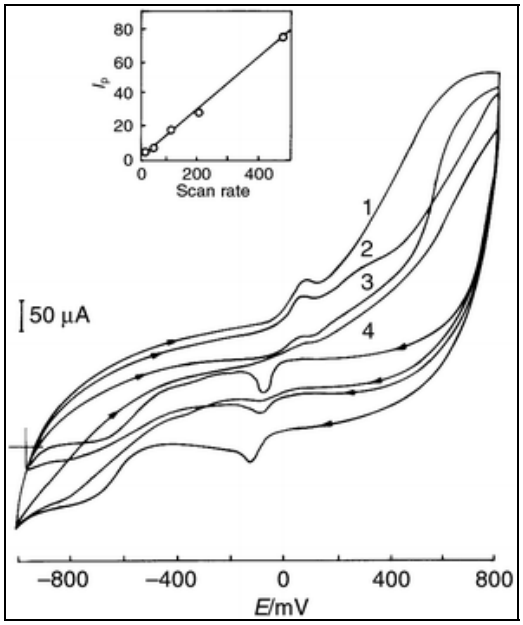

Figure 3.6 Cyclic voltammograms of a dithiol functionalized gold electrode with one layer of Ag nanoclusters taken at various scan rates in 1 M aqueous KCl solution in the potential range of 1.0 to +0.8 V. (1) 50, (2) 100, (3) 200 and (4) 500 mV/s.

The inset of Fig. 3.6 shows that the voltammetric peak current is proportional to the potential scan rate, which is consistent with the expectation that the silver

clusters are surface bound. Further confirmation arises from the diminishing separation between the anodic and cathodic peaks (E_p) as the scan rate decreases. Comparison of the observed FWHM with the theoretically expected value of 90.61/*n* mV suggests the involvement of two electrons in the redox reaction of the clusters if the theory of the voltammetric response for the surface wave is applicable. Beyond the anodic peak corresponding to silver cluster oxidation, the increase in background current can be explained by the slow oxidation of the dithiol molecules.

The high degree of reversible behaviour observed at 200 mV/s ($I_{pa}/I_{pc} \approx 1$, ΔE_p = 45 mV) is found to be adversely affected by repeated cycling. For example, Fig. 3.7 shows cyclic voltammetric data for a two-layer assembly of ordered nanostructures at this scan rate for five successive cycles. Although diminishing peak currents with increasing number of cycles have been observed for both anodic and cathodic peaks (see inset Fig. 3.7) there is an important difference. The decrease for the cathodic case is more abrupt (*e.g.*: 1st to 2nd to 3rd cycle) compared to the anodic case which could be attributed to many reasons such as different electrostatic surface potentials of the clusters, rearrangement of thiol molecules on the surface, the possibility of destruction of the SAM by reductive desorption, *etc.* As the number of cycles increases, there can be a significant loss of Ag clusters to solution and the final shape in the anodic side suggests a plateau current possibly due to the presence of large defects (microelectrode behaviour). Approximate calculation of the area under the peak (20–30 μC/cm^2) for the voltammogram taken at 100 mV/s provides the accessible concentration of Ag clusters more for cathodic, perhaps due to the increased amount of oxidised clusters accessible for reduction. The reversible peak in the initial few cycles clearly indicates that protected Ag clusters act as an array of nanoelectrodes enabling the passage of electrons through the SAM barrier.

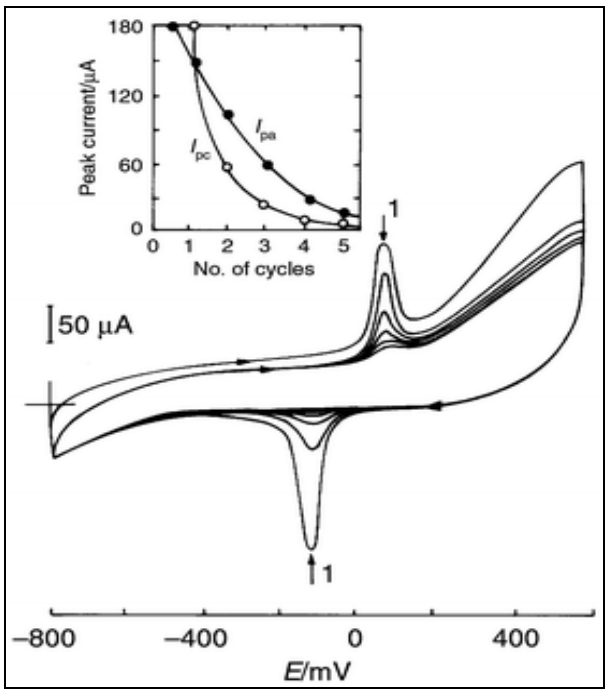

Figure 3.7 Cyclic voltammogram for a two layer assembly of ordered nanostructures on a dithiol modified gold electrode at 200 mV/s in the potential range of 1.0 to +0.8 V for five successive cycles.

3.3.4 Photoluminescence studies

Fig. 3.8 shows the room temperature emission spectra of silver cluster superlattices of two and four layers. The superlattice structure manifests a conventional quantum well structure. The electronic charge distribution then can be expected to be delocalized along the direction normal to the well layer,[31] for the barrier thickness (here dithiol thickness of 9 Å) is sufficiently small to allow electronic coupling between wells. Owing to this coupling the broadening of the quantized electronic states of the wells occurs giving rise to new broadened and delocalized quantized states called minibands. The three distinct transitions in the emission spectra at 320, 400 and 620 nm manifest as minibands in the superlattice structure whereas the silver cluster solution exhibits no such bands. This is also probably one of the reasons for the observation of efficient charge transport normal to the layers as in agreement with the presence of sharp peaks in the CV. No significant change in the PL

spectrum has been observed with the number of layers, which is consistent with the above explanation.

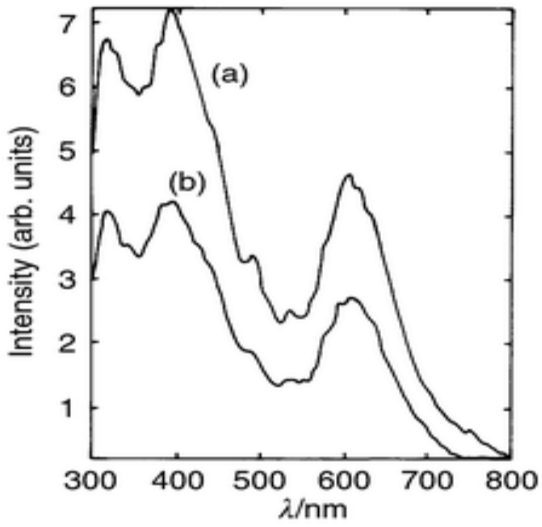

Figure 3.8 Photoluminescence spectra of (a) two layers and (b) four layers of Ag nanocluster superlattices on a SAM functionalized surface taken at room temperature (not corrected for the instrument).

3.4 Effect of Chain length on Ag array formation

3.4.1 Adsorption Kinetics

The sequential nanocluster organization using covalent interactions of octanedithiol SAM and silver nanocluster was monitored by QCM as their layer-by-layer formation can cause corresponding steps in mass changes. In addition this type of an experiment can also provide valuable kinetic information about the different rates of monolayer formation and subsequent cluster organization. For example, if the dynamic nature of SAM causes continuous exchange between molecules on cluster surfaces and substrate surfaces during the time scale of organisation, this would be reflected in the mass change. Fig. 3.9 shows such a combined data for the sequential adsorption of C8-dithiol molecules and silver nanoclusters. In the first case of dithiol monolayer formation on planar Au (111) surface (SAM I) a typical mass increase upto 1000 ng/cm^2 indicates a 99% saturation coverage attainment

within few minutes. This value obtained after saturation coverage of monolayers of ODT is in agreement with the reported values for other dithiol molecules. The possibility of looping of dithiols is insignificant here due to the use of C5 to C8 molecules as discussed elsewhere.[32]

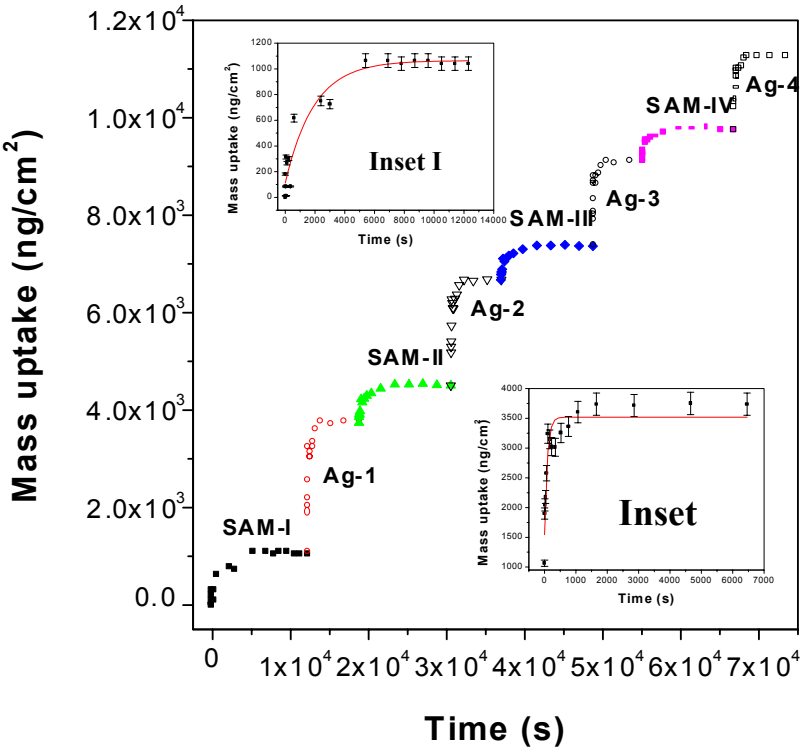

Figure 3.9 The layer by layer mass change with time for subsequent simple octanedithiol and freshly prepared Ag nanoclusters adsorption on Au (111) surface indicated by SAM- and Ag-1 respectively. **Inset I** indicates the langmuir fit for the mass uptake of octanedithiol molecule, **Inset II** shows the mass uptake with time for the covalent organization of Ag nanoparticles on SAM functionalized Au (111) surface.

Regarding the second step of cluster organisation on dithiol SAM, although Ag nanoclusters[33a] of the order of 1.5-2 nm can in principle give a mass uptake upto 4 μg/cm^2, we found the measured value as 2.7 μg/cm^2 indicating about 20% coverage, which can reasonably account a cluster-cluster spacing of *ca.* 1 nm estimated from STM, for the first layer. The small surface

coverage is close to the value of 30% obtained by Natan et al[33b] for self-assembled colloidal particle films and may be rationalized in terms of strong interparticle repulsive interactions. In consecutive layers, the cluster coverage decreases very fast (*ca.* 20% per layer) confirming the increased disorder and possible slanting of the monolayers on the faceted surface of the nanoclusters. There is also a possibility that smaller clusters are preferentially organized in the first layer although we do not have any clear evidence. In comparison, dithiol SAM formation interestingly shows a decrease of only 10% mass with subsequent layers due to more flexible orientations of molecules on nanoparticle surfaces as compared to 2D Au (111) surface. For example, the initial coverage of 10^{13} molecules/cm^2 becomes 10^{10} molecules/cm^2 after four layers of the cluster attachment.

An approximate estimation of the free energy of adsorption (ΔG_{ads}=-$RTlnK_{eq}$) for octanedithiol for all layers, ΔG_{ads} = -5.2 kcal/mol, is in agreement with earlier reports (inset I; shown for one layer only for brevity).[34] Considerable fluctuations in the quartz crystal resonant frequency are noticed for 1 mM concentration over a long time of interval and the precautions necessary to analyse this type of information have been reviewed earlier.[35] In comparison to the well known kinetics of SAM formation, the Langmuir fit for the nanocluster adsorption on a dithiol functionalized surface reveals a surprisingly faster response (Inset II). Initially the mass increases very fast (up to 120 sec) followed by a slight decrease, before attaining a gradual saturation. The important parameters calculated from the Langmuir equation $\theta = (a/b)(1-\exp(-bx))$; where $a = k_a c$ and $b = k_d + k_a c$ are in agreement with those reported earlier.($k_a = 8 \times 10^3$ $M^{-1}s^{-1}$; $k_d = 0.8078$ $M^{-1}s^{-1}$; $K_{eq} = 1000.711$).[34] In contrast to earlier results for the electrostatic organization of nanoclusters where a slow mass uptake is observed,[21] the naked clusters are observed to adsorb fast with most of the mass change occurring within a couple of minutes (even faster than the dithiol molecules!). The slight decrease after a fast organization of the

nanoclusters may be due to the removal of some nanoparticles which are not strongly linked to dithiols.

3.4.2 Surface Coverage by Ag Nanoparticles

In order to examine the change in oxidation state of silver nanoclusters before and after organization and also to confirm the formation of thiolate bond formation during monolayer formation, X-ray photoelectron spectra of these multilayer assemblies organized on Au (111) surfaces were carried out. These results are shown in Fig. 3.10. The intensity of Ag 3d peak (Fig. 3.10a) increases with layers of clusters while the Au 4f intensity from the substrate accordingly decreases due to the limited escape depth of the photoelectrons. The intensity of the C 1s and S 2p levels of dithiol (at 285 eV and 163.9 eV) also increases with the number of depositions. Interestingly, three C1s components are clearly seen at 282.2 eV, 285 eV and 286.9 eV respectively, which may be tentatively assigned to alkyl chain carbon, chamber carbon due to contamination and carbon coordinated to thiol group respectively (Figure 3.10a (v), after deconvoluting for one of the layers).[36]

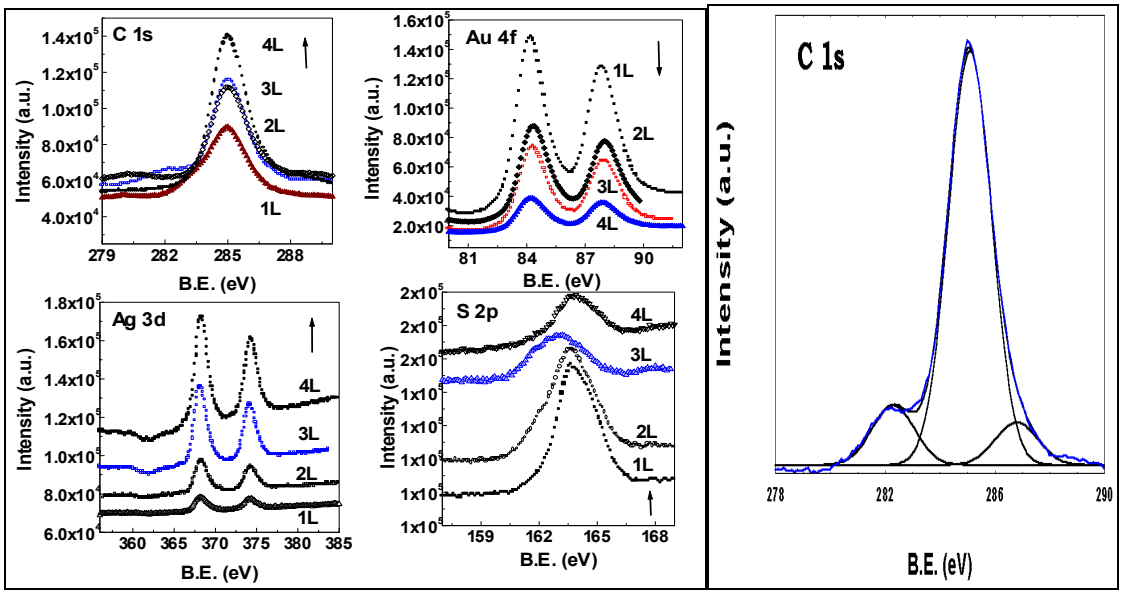

Figure 3.10a The XP spectra of Ag 3d, C 1s, Au 4f and S 2p, respectively. 1L, 2L, 3L and 4L indicates the number of layers after the layer-by-layer subsequent organization of Ag nanoparticles and octanedithiol molecules on Au(111) surface. C 1s peak for the first layer is deconvoluted using Gaussian fit.

The XP spectra of Ag nanocluster covered SAM surface shows two sulfur species after a nonlinear curve fitting (Figure 3.10b) procedure for the S 2p core level corresponding to a spin-orbit splitting of 1.15 eV and $2p_{3/2}/2p_{1/2}$ intensity ratio of 2 respectively.). The S $2p_{3/2}$ signal of 163.9 eV is a typical characteristic binding energy value of unbound sulfur.[21] The additional component of S 2p observed at a B.E. of 161.8 eV is in agreement with the reported B.E. of thiolate bond with Ag.[36] Growth of the low B.E. component is therefore a clear indication of the covalent Ag particle attachment to the SAM surface. Bound thiol signal seems to diminish in the 4th layer (4L), perhaps due to the decrease in the number of bound thiols on the top layers which confirms the QCM results indicating lower cluster coverage at higher layers.

More interestingly, the oxidized sulfur species (S $2p_{3/2}$ >166 eV) not seen for the first two layers, is intense for the 3L and 4L samples suggesting diminished stability.[37a] This could be attributed to the increase in sulfate or sulfonic acid moiety on the modified surface with more number of layers.[37] The intensity ratio of the S 2p components shows that only 40% of surface thiol is taking part in the linkage with Ag nanoparticles. On the other hand QCM studies suggest, ~20% surface coverage assuming a spherical particle of diameter 1.4 nm and the reason for this discrepancy is not clear although the size of adsorbed clusters being not spherical (e.g., elongated) can be one possibility. The linear plot of intensity enhancement of Ag and S (or metal coverage) signals with the number of layers along with a linear decrease in the Au 4f signal intensity confirms the multilayer structure. The Ag 3d spectrum (Figure 3.10a) clearly shows the presence of only one component (B.E. $3d_{5/2}$ = 368 eV with spin-orbit splitting = 6.1 eV and Ag $3d_{5/2}$/Ag $3d_{3/2}$ intensity ratio = 1.5). The fact that an additional component due to thiolate linkage of silver atom is not seen is in consonance with the observation of Brust et al that there is no evidence of peak shifting in dodecanethiol stabilized gold colloidal particles.[20]

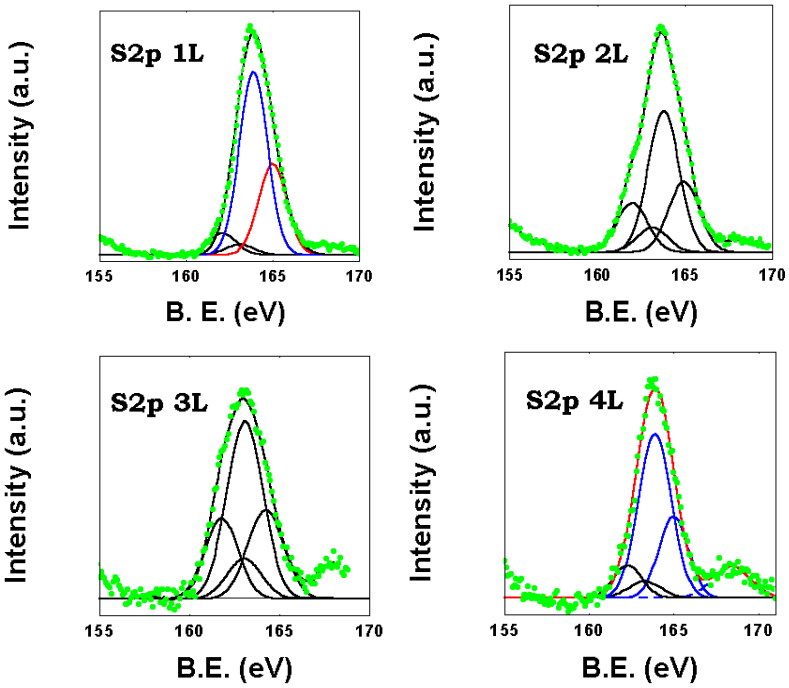

Figure 3.10b The comparative XP spectra for sulfur 2p after the four layer organization of Ag nanoparticles on the octanedithiol modified Au (111) surface.

3.4.3 Electrochemical Studies

The processes of adsorption of dithiol and subsequent Ag cluster attachment in various layers can be effectively followed by measuring the cyclic voltammetric (CV) response of these modified electrodes in 0.1 M aqueous KCl solution. Fig. 3.11 shows such a superimposed cyclic voltammogram of a gold electrode modified after the adsorption of freshly prepared Ag clusters in four layers (indicated by 1L, 2L, 3L etc.) in the potential range of -0.6 to +0.6 V. The significant reduction in capacitance upon SAM formation as manifested in the comparison of the CVs for the bare and SAM covered surfaces has been discussed several times previously.[38] However, in our study with C5-dithiol we revealed that two-dimensional organization of Ag nanoclusters on this primary SAM surface causes an increase of differential capacitance from 2.1 to 40 $\mu F/cm^2$ despite an increase in the distance of closest approach.

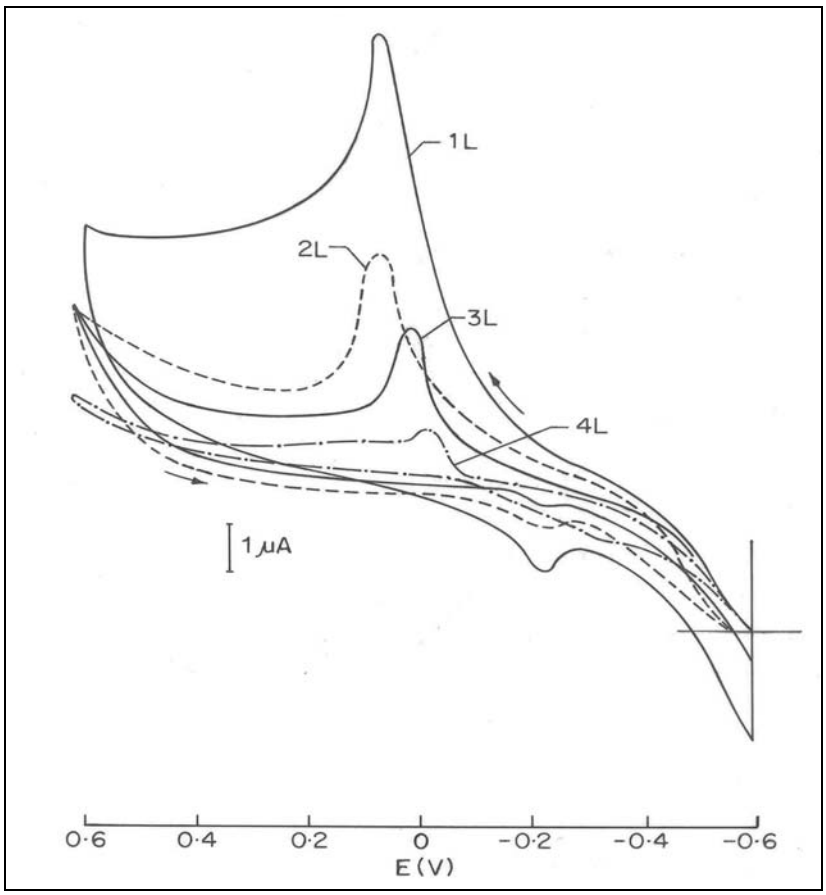

Figure 3.11 Superimposed cyclic voltammogram of a gold electrode modified after the adsorption of freshly prepared Ag clusters in four layers (indicated by 1L, 2L, 3L and 4L) in the potential range of -0.6 to +0.6 V. The voltammograms were taken in 0.1 M KCl at the scan rate of 200 mV/s.

In comparison with those results for C5 dithiol-Ag array assembly the present voltammetric results of C8 dithiol -Ag assembly show a consistent decrease in the double layer capacitance with number of layers, perhaps due to the systematic variation of distance of closest approach. This is also in agreement with the variation of peak current with the number of layers confirming the difficult redox accessibility of Ag particles of buried layers for the electron transfer. Our results however, contradict the electrochemical behavior of colloidal multilayers with electroactive species incorporated between the particles layers[39] fabricated by alternate dipping method, where the peak current is found to increase linearly with number of layer as all sites are

accessible for the electron transfer. The discrepancy observed for our results suggests that in a covalent assembly, the Ag clusters are buried between the monolayers after strong bonding which creates a large energetic barrier for charge transfer as well as charge compensation.[40] In other words, the assembly behaves less conductive with more layers, resulting in the decrease of accessible Ag sites and hence smaller voltammetric current. This may also account al least, in part, for the cathodic shift of the formal potential of the Ag nanoclusters with more layers.

To illustrate these effects in greater details, scan rate dependent voltammogram were taken for a one-layer assembly of Ag nanoparticles as a typical example (Fig. 3.12). Surprisingly, the reversible couple observed at higher scan rates (100 mV/s) is not visible at lower scan rate (10 mV/s) due to the inaccessibility of electron transfer rate constant at faster time scales. In contrast to C5-Ag assembly reported earlier (section 3.3.3), the oxidation potential is found to be shifted more positive with scan rate and the longer alkane chain may be one of the contributing factors. The linear increase in the faradaic current with scan rate, rather than a square root dependence, confirms that the species are surface confined. Further support arises from the diminished separation between the anodic and cathodic peaks as the scan rate decreases and the value of peak width (ΔE_p = 60 mV) suggests the involvement of one electron transfer in agreement with theoretically expected value of 59.01/n. The increase in the background current at higher scan rates also suggests the slow oxidation of the dithiol molecules.

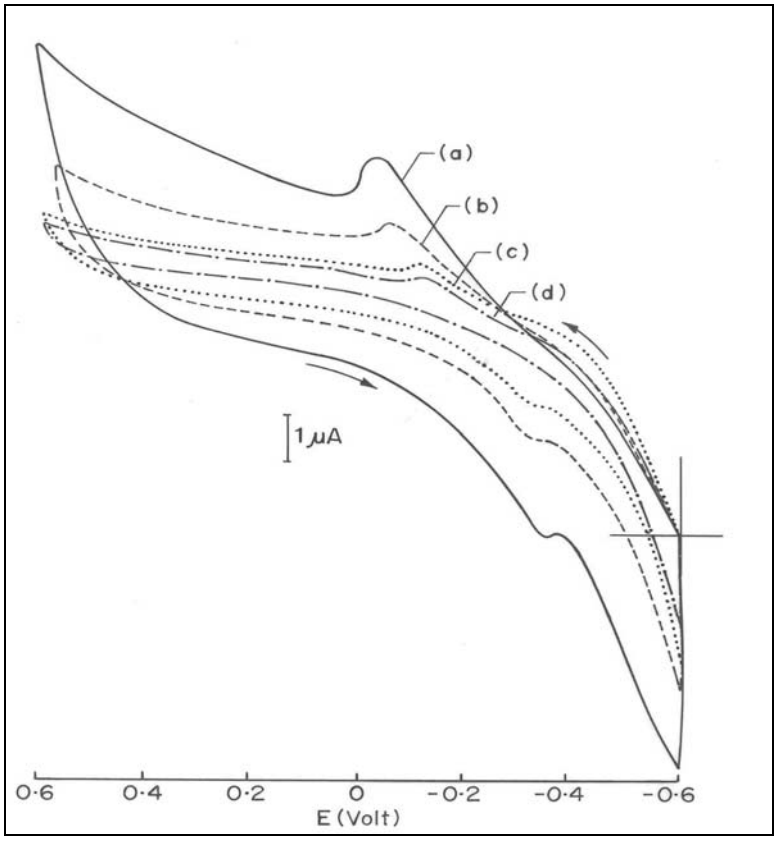

Figure 3.12 Scan rate dependent cyclic voltammograms recorded in 0.1 M KCl between the potential – 0.6 to +0.6 using one layer Ag nanoclusters modified Au (111) surface as working electrode. (a) 100 mV/s, (b) 50 mV/s, (c) 20 mV/s and (d) 10 mV/s, respectively.

3.4.4 Identification of Array formation

One of the important evidence for the long-range order in these cluster assemblies can be obtained from low angle x-ray diffraction. In figure 3.13, we show the changes on a typical low angle x-ray peak of the multilayer structure (four alternate layers indicated by 1L, 2L and 3L etc.) formed by the sequential adsorption of 1.4 nm Ag nanoclusters and dithiol SAMs. The peak at 3.4^{o} corresponds to a 2.28 ± 0.5 nm repeating unit in the ODT/Ag multilayers and agrees well with the geometric dimensions of both clusters (Ag particle diameter is 1.4 nm) and dithiol molecules; also the difference corresponds to the thickness of the monolayer reported earlier from ellipsometry

measurements.[38] Similar results earlier reported for Pt and Au nanoparticle superlattices show a spacing of about 2 nm.[15]

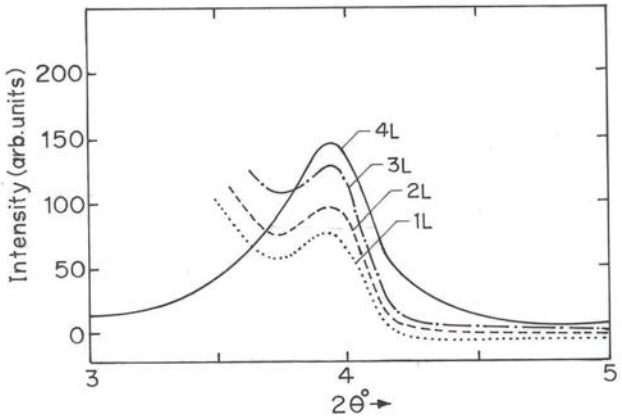

Figure 3.13 The small angle x-ray diffraction pattern of the three dimensional (3D) partial superlattice of Ag nanoparticles on dithiol SAM functionalized Au (111) surface after four such organizations.

Self-assembly is governed by a net balance between adsorption and desorption equilibria. Various interactions between nanoparticles and molecular layers (dithiol) governs the spontaneous layer-by-layer self-assembly of ultra-thin films including electrostatic and covalent interactions between substrates and SAM molecules in addition to subtle forms of hydrogen bonding, van der Waals interaction, hydrophobic or π-π type of interaction. The combined nature of the weak interactions between the chains and covalent structure of organic molecules on Au surface can be understood by imaging the Ag array formation using TEM and STM. For example Figure 3.14 shows a TEM image which reveals the size distribution of the silver nanoparticles with a standard deviation of 0.3. TEM image (Fig. 314a) demonstrates the mean diameter of the nanoparticles as 1.4 nm, along with the average interparticle spacing of 1 nm. Figure 3.14b is the SAED, which further confirms the hexagonal close-packed (hcp) structure.

A comparison of the above results with the image obtained by scanning tunneling microscopy (STM) for a single layered sample confirms the formation of ordered arrays over distances which are consistent with the length of dithiol molecule used (Fig. 3.15). More specifically the molecular resolution STM images of the array (on a gold coated mica substrate) as large as 200 Å on a side shows clear evidence for one molecule step height representing adjacent domains of Ag nanoparticle in the array. The inability to detect multilayer features above the plane of molecularly resolved arrays in STM suggests that deposits with two layer thickness may be insufficiently conductive to permit tunneling to resolve at that level. STM images characterized as large arrays with uniform height and molecular resolution are monolayer deposits some disordered regions are seen perhaps due to the damage resulting from fast diffusion after solvent evaporation.

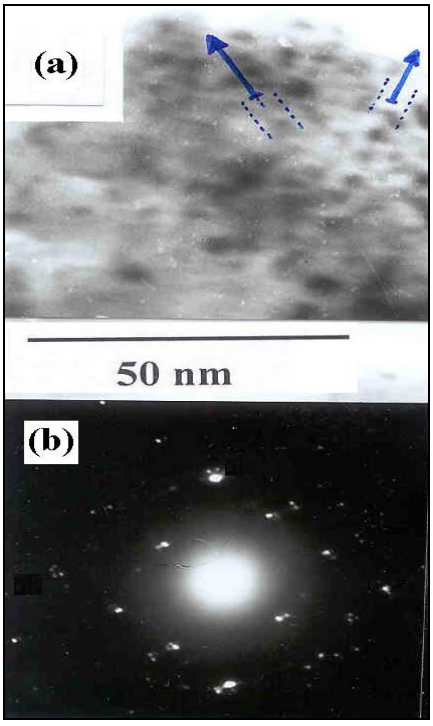

Figure 3.14 (a) Transmission electron micrographs obtained from one layer of Ag nanoclusters adsorbed on an electron microscope grid from the dilute nanocluster solution, (b) The SAED for the Ag particles. Arrow indicates the guideline to understand the partial array formation on copper grid.

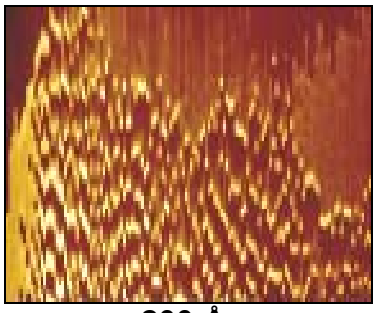

Figure 3.15 STM image for a single layer of Ag nanoparticles on mica coated gold substrate modified with octanedithiol.

3.5 SUMMARY AND CONCLUSIONS

These results imply a methodology for the sequential organization of self-assembled monolayers and silver nanoclusters from aqueous solution to form a superlattice structure at room temperature. In particular, this type of layer-by-layer deposition of arrays of silver clusters on a dithiol SAM overcomes several diffusional and orientational restrictions to finally form a nanorod like superstructure as indicated by AFM imaging. It also raises subtle questions about the acquired order, cluster diffusion and electron coupling across the passivating barrier. The mechanism of electron transfer (tunnelling or hopping) also needs further investigations since these silver clusters can be addressed electrochemically as demonstrated by voltammetry.

3.6 REFERENCES

1. Collier, C.P.; Vossmeyer, T.; Heath, J.R. *Annu. Rev. Phys. Chem.* **1998**, *49*, 371.
2. Harfenist, S.A.; Wang, Z.L.; Whetten, R.L.; Wezmar, I.; Alvarez, M.M. *J. Phys. Chem.* **1996**, *100*, 13904.
3. Elghanian, R.; Storhoff, J.J.; Munic, R.C.; Letsinger, L.R.; Mirkin, C.R. *Science* **1997**, *277*, 1078.
4. Nakanishi, T.; Ohtani, B.; Uosaki, K. *J. Phys. Chem. B* **1998**, *102*, 1571.
5. Kagan, C.R.; Murray, C.B.; Bawendi, M.G. *Phys. Rev. B* **1996**, *54*, 8633.
6. Guzelian, A.A.; Katari, J.E.B.; Kadavanich, A.V.; Banin, U.; Hamad, K. *J. Phys. Chem.* **1996**, *100*, 7212.
7. Yin, J.S.; Wang, Z.L. *Phys. Rev. Lett.* **1997**, *79*, 2570.
8. Rao, C.N.R.; Kulkarni, G.U.; Thomas, P.J; Edwards, P.P. *Chem. Soc. Rev.* **2000**, *29*, 27.
9. Wang, Z.L.; Harfenist, S.L.; Whetten, R.L.; Bentley, J.; Evans, N.D. *J. Phys. Chem. B* **1998**, *102*, 3068.
10. Alvarez, M.M.; Khoury, J.T.; Schoatt, T.G.; Shafigullin, M.N.; Vezmar, I.; Whetten, R.L. *J. Phys.Chem. B* **1997**, *101*, 3706.
11. Murray, C.B.; Kagan, C.R.; Bawendi, M.G. *Science* **1995**, *270*, 1335.
12. Mayya, K.S.; Sastry, M. *Langmuir* **1999**, *15*, 1902.
13. Korgel, B.A.; Fitzmaurice, D. *Adv. Mater.* **1998**, *10*, 661.
14. Musick, M.D.; Keating, C.D.; Lyon, L.A.; Botsko, S.L.; Pena, D.J.; Holliway, W.D.; McEvoy, T.M.; Richardson, J.N.; Natan, M.J. *Chem. Mater.* **2000**, *10*, 2869.
15. Vijayasarathi, K.; Thomas, P.J.; Kulkarni, G.U.; Rao, C.N.R. *J. Phys. Chem. B* **1999**, *103*, 399.
16. Taleb, A.; Russier, V.; Courty, A.; Pileni, M.P. *Euro. Phys. J. B* **1999**, *59*, 13350.
17. Simon, U.; Flesch, R.; Wiggers, H.; Schon, G.; Schmid, G. *J. Mater. Chem.* **1998**, *8*, 517.

18. Heath, J.R.; Knobler, C.M.; Leff, D.V. *J. Phys. Chem. B* **1997**, *101*, 189.
19. Ohara, P.C.; Heath, J.R.; Gelbart, W.M. *Angew. Chem.* **1997**, *36*, 1078.
20. Brust, M.; Bethell, D.; Kiely, C.J.; Schiffrin, D.J. *Langmuir* **1998**, *14*, 5425.
21. Shipway, A.N.; Lahav, M.; Gabai, R.; Willner, I. *Langmuir* **2000**, *16*, 8789.
22. Schmid, G. *Clusters and Colloids*, Wiley VCH, New York, 1994.
23. Sauerbrey, G. *Z. Phys. Chem. (Munich)* **1959**, *155*, 206.
24. Henglin, A. *J. Phys. Chem.* **1993**, *97*, 5457.
25. Mostafvi, M.; Keghouche, N.; Delcourt, M.; Belloni, J. *Chem. Phys. Lett.* **1990**, *167*, 193.
26. Kreibig, U.; Genzel, L. *Surf. Sci.* **1985**, *156*, 678.
27. Brust, M.; Flink, J.; Bethell, D.; Schiffrin, D.J.; Kiely, C.J. *J. Chem. Soc. Chem. Commun.* **1995**, 1655.
28. Castner, D.G.; Hinds, K.; Grainger, D.W. *Langmuir* **1996**, *12*, 5083.
29. Mekhalif, Z.; Riga, J.; Pireaux, J.J.; Delhalle, J. *Langmuir* **1997**, *13*, 2285.
30. Miller, C.; Cuendet, P.; Grätzel, M. *J. Phys. Chem.* **1991**, *95*, 877.
31. Nozik, A.J.; Parsons, C.A.; Dunlavy, D.J.; Keyes, B.M.; Ahrenkiel, R.K. *Solid State Commun.* **1990**, *75*, 297.
32. Kohli, P.; Taylor, K.K.; Harris, J.J.; Blanchard, G.J. *J. Am. Chem. Soc.* **1998**, *120*, 11962.
33. (a) Shipway, A.N.; Katz, E.;Willner, I. *ChemPhysChem* **2000**, *1*, 18. (b) Grabar, K.C.; Smith, P.C.; Musick, M.D.; Davis, J.A.; Walter, D.G.; Jackson, M.A.; Guthrie, A.P.; Natan, M.J. *J. Am. Chem. Soc.* **1996**, *118*, 1148.
34. Schessler, H.M.; Karvovich, D.S.; Blanchard, G.J. *J. Am. Chem. Soc* **1996**, *118*, 9645.
35. Schmacher, R. *Angew. Chem. Int. Ed. Engl.* **1990**, *29(4)*, 329.
36. Laibinis, P.E.; Whitesides, G.M.; Allara, D.L.; Tao, Y.T.; Parikh, A.N.; Nuzzo, R.G. *J. Am. Chem. Soc.* **1991**, *113*, 7152.
37. a) Castner, D , D. G.; Hinds, K.; Grainger, D. W. *Langmuir* **1996**, *12*, 5083. b) Mekhalif, Z.; Riga, J.; Pireaux, J. -J.; Delhalle, J. *Langmuir* **1997**, *13*, 2285.

38. Porter, M.D.; Bright, T.B.; Allara, D.L.; Chidsey, C.E.D. *J.Am. Chem. Soc.* **1987**, *109*, 3559.

39. Shipway, A.N.; Lahav, M.; Willner, I. *Adv. Mater.* **2000**, *12*, 993.

40. Smith, C.P.; White, H.S. *Anal. Chem.* **1992**, *64*, 2398.

Chapter 4

Hydrophobic Organization of Monolayer Protected Au Nanoclusters on Thiol Functionalized Au (111) Surface*

This chapter deals with a novel hydrophobic organization of 4.8±0.5 nm core diameter Au clusters in contrast to normal organization using covalent and electrostatic interactions where specific bifunctional molecules are used. This unique method of organization is demonstrated using Quartz Crystal Microbalance (QCM), UV-vis spectroscopy, Cyclic Voltammetry (CV), X-ray Photoelectron Spectroscopy (XPS), X-ray Diffraction (XRD) and I-V measurements. All the results strongly suggest that there is a slow attainment of saturation coverage (10^{10} clusters/cm^2) of Au nanoclusters on SAM functionalized Au (111) substrate and the equilibrium constant (K_{eq}) is three times less compared to that for the monolayer formation using dodecanethiol. The in-plane conductivity of these arrays of gold nanoparticles demonstrate clear Coulomb blockade effect with larger band gaps for clusters passivated with longer chain length, where the fractional residual charges Q_o on the centre electrode is varied without an external electrode. A model based on double-barrier tunnel junction has been used to explore the observed features.

*A part of this chapter has been published as an Article in **Langmuir** *17*, 7383-89 (2001) and another portion has been communicated to **J. Appl. Phys.**

4.1 INTRODUCTION

Nanoclusters display a diverse set of size and shape dependent electronic properties that make them particularly attractive candidates for several applications in the area of molecular electronics.[1-5] Extensive research activities during the last few years have facilitated the successful preparation and characterisation of metallic and semiconducting nanoclusters using different approaches.[1] Recent efforts are directed towards understanding their individual and co-operative behavior mainly due to their potential applications as single-electron transistors, chemical sensors etc.[6] The precise organization of identical nanoclusters at controlled length scales is therefore significant for many of these applications involving collective behavior.

As illustrated in chapter 1, self-assembled monolayer (SAM) formation offers a simple and flexible method for organising nanoclusters on selected substrates.[7-9] In this approach an organic molecule with specific functional groups on both ends [i.e., bifunctional molecules, X-$(CH_2)_n$-Y, where X and Y represent similar or different functional groups such as -NH_2, -COOH, -SH, -CN etc.] is selected in such a way that one group attaches on the substrate while the other is linked intimately to the cluster. For example, the covalent Au-S interaction (thiolate bond) is used for organising nanoclusters on Au(111) substrates as demonstrated by the use of various organic dithiols.[10] Long chain dithiols allow relatively stable and well ordered cluster assemblies, while some aromatic dithiols and short chain aliphatic dithiols do not allow close packed and stable assemblies due to the high mobility of the clusters.[11] In addition to dithiols, other bifunctional molecules containing carboxyl, amino and few other selected groups can also be used for such type of nanocluster organization, although substrate selection plays a key role. Techniques such as XPS, AFM, STM and HRTEM have been used to study the surfaces and microscopic characteristics of these monolayers and the monolayer-cluster

nanostructures.[12,13] Electrochemical methods have also been eminently used to characterise the structure and properties of these organized systems.[14]

Our earlier results (chapter 2 and 3) reveal that self-assembled monolayers having free thiol group at the surface can organize other molecules and nanoclusters from solution. It was shown that dithiol molecule adsorbs on the surface of gold with the tilted orientation of alkyl chains, having one thiol group bonded to the gold as thiolate and the other free at the surface. This freely available -SH group can anchor naked nanoparticles by exposure to nanoparticle solutions as illustrated in the previous electrochemical/photoluminescence studies (chapter 3, section 3.3.3 and 3.3.4). Such an organization can be very effective to control interparticle spacing, surface coverage and the extent of distribution of nanoparticles on modified Au (111) surface. This controlled organization is the most important parameter to understand the electrical behavior of organized nanoparticles. Such an organization will help to understand the band gaps and the surface states created in the 2D surface through the hydrocarbon molecule. The mechanism responsible for such an ordered organization is not very clear although change in surface functional group and thickness of the SAM forming molecule are some of the possible reasons. An investigation to the origin and nature of the surface modified and bare nanoparticles via the adsorption of hydrocarbon molecules is therefore of both fundamental and practical importance.

In this chapter, we show that even hydrophobic interactions can be used to organize metallic nanoclusters on SAM surfaces by exposing them to aprotic cluster solutions. Since surface hydrophobicity[15a] plays an important role in many biological systems,[15] such type of nanocluster organization can find significance in designing complicated multilayer structures having promising applications in biomolecular electronics. For example, hydrophobic interactions play an important role in governing the stability of native

conformations of macromolecules in biological systems like simple helix in ployglutamic acid and more complicated intermolecular interactions in the blood plasma or membrane lipoproteins.[16] In contrast to strong electrostatic or covalent interactions, these weak intermolecular forces provide sufficient flexibility for biological functions. Semiconducting nanoclusters like CdS and CdSe, possessing interesting optical properties, could also be organized on transparent substrates by applying the same methodology. We use XPS, QCM and CV as the characterization tools to compare the relative merits and demerits of this type of nanocluster organization with respect to other electrostatic and covalent modes. The room-temperature electron transfer behavior in ordered arrays shows that when the nanoclusters are organized at a small spatial distance of ~1 nm in one, two or three dimensions a typical example of the double tunnel junction (DBTJ) is formed in series with the Q-dots at the centre (equivalent circuit for organized Au nanoclusters shown in the figure 4.1) to manifest single-electron tunnelling. These systems give rise to a capacitance, C, in such away that the charging energy is always greater than the thermal energy (k_BT), where e is the fundamental charge unit and k_B is the Boltzmann's constant. In the presence of an external field, the system shows attofarad capacitance (10^{-18} F)[17,18] before an electron tunnels through the system resulting in steps in the I-V characteristics popularly known as Coulomb blockade or Coulomb staircase. The threshold voltage is found to increase with a decrease in the cluster core size and the remarkable degree of flexibility offered by the tunable surrounding barriers helps to build such single electron circuits of different complexity.[19] This model is different from the electrostatic models of simple quantum dots of semiconductors where the dots are described as embedded bulk structures in accordance with the chosen parallel coupling of the dots and bulk capacitance to explain the negative differential capacitance.[20]

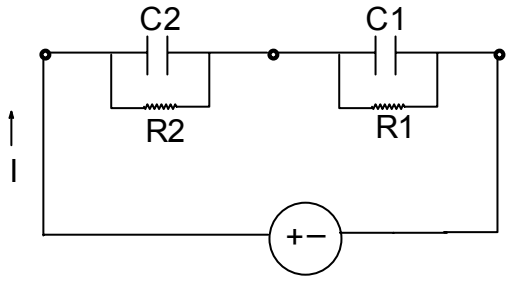

Figure 4.1 Equivalent circuit for the double barrier tunnel junction (DBTJ) constructed using Au MPCs organized through hydrophobic interaction between the alkyl chains of nanocluster and planar Au (111) surface. DBTJ is generally treated as two capacitors with capacitances and resistances C_1,R_1 and C_2,R_2 placed in series and driven by an voltage source.

Several experimental illustrations of Coulomb blockade for ensembles of silver and gold nanoparticles anchored through covalent and electrostatic forces have been reported earlier.[19,21,22] Theoretical treatments[17b,22] of current steps in the I-V characteristics of small two junction systems and 2D Q-dot superlattice reveal that Coulomb blockade and staircase size exclusively depend on the interparticle separation and that the tunneling is quenched with the redistribution of density of states when interparticle separation is of the order of ~0.5 ± 0.2 nm.[23] These and several other studies demonstrate that in contrast to the tunnel junctions formed by lithography (~100 nm) where millikelvin range temperature is needed to suppress thermal fluctuations, the use of chemically synthesized nanoparticles (MPCs) with tailored organic molecules can cause Coulomb blockade at room temperature. Here we explore the chain length dependence of the passivating organic molecule on the tunneling characteristics using a kelvin probe in conjunction with transmission microscopy studies to reveal the crucial role played by the shape, size, thickness of barrier molecules and density of defects on electrical transport. The I-V characteristics obtained using a single micrometer controlled Hg drop is compared with the results obtained using STM. The transport studies of these organized superstructures are in agreement with the semiclassical model of the two-tunnel junction *(including fractional residual charges Q_o and other parameters)* and the exact form can be obtained after subtracting positive feedback current when the mercury drop touches the surface modified with the

MPCs. Nanoclusters of *ca.* 5 nm in size are utilized in order to demonstrate the Coulomb blockade effect in chemically directed organization of clusters through weak van der Waals interaction using dc conductivity measurement.

4.2 EXPERIMENTAL

4.2.1 Materials

Dodecanethiol (99%), $HAuCl_4.3H_2O$ and sodium borohydride were obtained from Aldrich and used as received. In all the experiments deionized water from Milli-Q system was used. Self-assembled monolayer of the C_{12} thiol was formed on an Au (111) film from 1 mM ethanolic solution of the compound following established methods (chapter 2, section 2.2.3).

4.2.2 Nanoparticle Synthesis

The nanoclusters were synthesized following the modified Brust synthesis route.[24] In brief, 0.0985 gm of gold salt was dissolved in 50 ml water and this was mixed with 100 ml toluene containing 0.2 ml of dodecanethiol (ca. 10 mM) as the capping agent. The biphasic mixture under low temperature (ice bath) was stirred for 30 min. and then the gold salt was reduced using 0.1 M aqueous $NaBH_4$ in the presence of thiol at the aqueous-nonaqueous interface. Upon the slow addition of $NaBH_4$, the pale yellow color of gold salt turned dark brown indicating the Au cluster formation and then after rigorous stirring for 2 h, the Au^o clusters were found to be shifted to the organic phase turning the upper layer dark brown. The dark brown powder obtained after separation and drying was redispersed in toluene for further experimentation. The above described procedure was repeated for pentanethiol, octanethiol, benzyl thiol and phenyl thiol surface passivating agents respectively to see the effect of chainlength and conjugation on electron transfer behavior.

4.2.3 SAM Fabrication and Hydrophobic Organization of MPCs

All the substrates used for the present experiments were prepared by evaporating 200 nm thick gold film on glass to get Au (111) films as described earlier (chapter 2, section 2.2.2). SAMs of pentane (C_5), octane (C_8), dodecane (C_{12}), phenyl (Ph) and benzyl (PhC_2) thiols were formed on Au (111) surface and on mercury drop respectively, using 1 mM ethanolic solution of respective thiols as described earlier (chapter 2, section 2.2.3). Close inspection of the molecular confirmation using a variety of diverse tools had provided evidence for SAM alignment with the long molecular axis tilted away from the surface normal by 30^o in the monolayers.[7] Further studies have revealed the monolayer as a good insulator with a relatively small bulk dielectric constant of 2.5-3 and a conductivity of the order of $10^{-15}\Omega^{-1}cm^{-1}$ per molecule.[25] Monolayers comprised of hydrocarbon chains greater than C8 proves to be good insulators while smaller chainlengths and aromatic thiols generally show pinholes and defects due to the variation in packing consideration and interchain van der Waal interaction.[25]

4.2.4 Hg Drop I-V Setup

Au nanocrystals organized through hydrophobic interactions on a SAM modified Au (111) surface shows a Q-dot density of *approx.* 10^{10} clusters/cm^2 along with a minor change in length due to interdigitation. Since sulfur atoms in the Au/thiol junction forms a rather long barrier of about 2 eV energy and abundant pinhole in SAMs generally limit the area of molecular junction to very small (10 $Å^2$), a large contact area using a micrometer controlled mercury drop was used for all the I-V measurements. Thus a DBTJ was prepared by lowering a 0.5 mm diameter mercury drop (prefunctionalized with respective thiols from 1 mM ethanolic solution as mentioned above by just dipping the drop for 5-10 min. in the solution followed by extensive washing) suspended from a wire lead onto the cluster monolayer. The conductivity was measured (Figure 4.2), with SAM modified substrate ground and the voltage was applied through the

functionalized Hg drop. The drop was gently left as it is, once the contact was initially established with an offset current varying with the chainlength and molecular structure. Although the monolayer on Au (111) has less pinholes and defects compared to other substrates,[7] the high surface tension and the modification of Hg surface with thiol monolayers should in principle, reduce the possibility of short circuits at large pinholes regions (Figure 4.3). The DC voltage was applied using Keithley voltage source and current was measured using Keithley 485 picoammeter (± 0.1 nA) at room temperature. The in-plane conductivity measurements were carried out at ambient conditions using a part of the film (2 mm x 10 mm) for contact through gold. The remaining part of the film (8 mm x 10 mm) was used for SAM formation and the cluster dispersion. The I-V measurements were taken when the contact is established with 5 nA set point current (referenced to SAM covered Au (111) surface). We found that the current fluctuates between 3 to 5 nA for a very small period (few minutes) and subsequently stabilizes to constant value. Nevertheless, keeping for long time (several hours) in contact causes shortening due to the amalgamation of the Hg drop with Au.

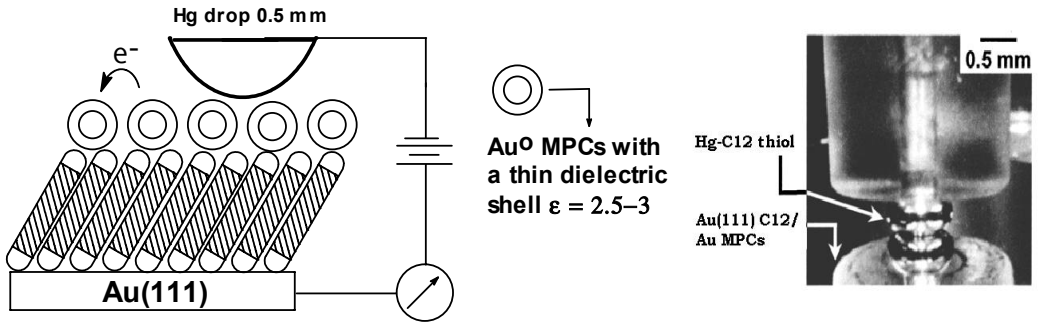

Figure 4.2 (A) Schematic cartoon representing the measurement of electronic properties using kelvin probe, the Hg drop (~0.5 mm in size) was always modified with the respective thiol of which Au MPCs of the order of size 4.5±0.5 nm are taken. (B) Macroscopic picture of the Hg drop in contact with the MPCs organized using C_{12}-thiol monolayer on Au(111) surface.

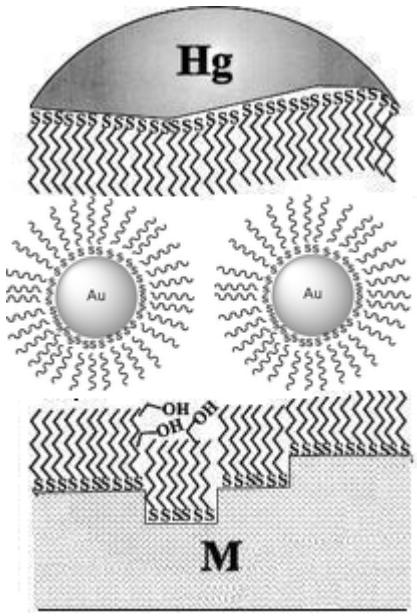

Figure 4.3 Schematic representation of a Hg-SAM/Au MPCs/SAM-metal (M) junction, where M is an Au(111) polycrystalline surface. The liquid Hg-SAM surface comes into conformational contact with the SAM-metal surface through Au MPCs of various chain lengths; indeed, the presence of solvent (ethanol) between the SAM layers is indicated.

4.2.5 Other Measurements

An Elchema electrochemical nanobalance (with 0.1 Hz resolution) interfaced with a computer was used to monitor subtle mass changes during SAM formation and subsequent Au MPC adsorption. The details have been described in chapter 2, (section 2.2.4). All the XRD patterns were recorded on a RIGAKU Miniflex instrument using Cu Kα radiation (λ=1.5404 Å) with a resolution of 0.2^o. The scanning 2θ range was set between 1.5^o to 6^o at a scan rate of 0.5^o per minute. FTIR measurements of the gold particle modified film were made on a Shimadzu PC-8201 instrument in the diffuse reflectance mode at a resolution of 4 cm^{-1}. XPS measurements were carried out on a VG MicroTech ESCA 3000 instrument at a pressure >1 × 10^{-9} Torr (chapter 3, section 3.2.4). The core-level binding energies (BE) were aligned taking the adventitious carbon peak as 285 eV. Cyclic Voltammograms were obtained using a Scanning Potentiostat Model 362 and a Recorder Model RE0151 using a standard three-electrode cell. The Au nanocluster organized Au(111)

substrate was the working electrode, a platinum foil was the counter electrode and a Saturated Calomel Electrode (SCE) served as the reference electrode, as described earlier (chapter 3, section 3.2.6). The scans were recorded with an instrumental accuracy of ±1 mV and ±5 μA. TEM measurements were carried out on a JEOL model 1200EX instrument operated at an accelerating voltage of 120 kV after re-dispersing Au clusters on a copper grid. The normal incidence selected area electron diffraction (SAED) pattern was also obtained to verify the crystallinity of the clusters.

4.3 A Novel Strategy for the Nanocluster Organization on 2D SAM Surface

4.3.1 Nanocluster Assembly

The Au MPCs prepared by the above experimental procedure were characterised by TEM and Uv-vis spectroscopy. Fig. 4.4(a) shows the electron micrograph obtained from Au nanoclusters dispersed on an electron microscope grid from the nanocluster solution. A fairly uniform distribution of well-dispersed particles is seen. The size distribution statistics (Fig. 4.4 (c)) determined from the micrograph appears to be Gaussian, with the main peak at around 4.8 nm. Fig. 4.4 (b) shows the selected area electron diffraction (SAED) of Au MPCs. The well-defined crystalline structure is rather obvious from the spot pattern which corresponds to an fcc lattice with a= 4.074Å.[26a]

In comparison to the results of Hostetler et al,[26b] using similar reaction conditions (room temperature, same Au/R-SH ratio) we got slightly larger particles probably due to the faster rate of reduction. Also confirmed from TEM studies are patterns of small clusters around larger one for polydispersed MPCs while long-range and orientational order is seen in gold monodispersed MPCs.[26b,4] Although the images are not very distinct, the shapes are not clearly spherical agreeing well with the results demonstrated by Murray et al.[26b]

UV-Vis spectroscopy of these gold clusters show a surface plasmon band at 525 nm (Fig. 4.5) indicating a particle size larger than 3 nm[27a], which is in agreement with our TEM results. The origin of the surface plasmon band and its width properties follow theoretically predicted behavior,[27b] and agree well with the previously reported results for similar systems in water, hexane and toluene.[27c]

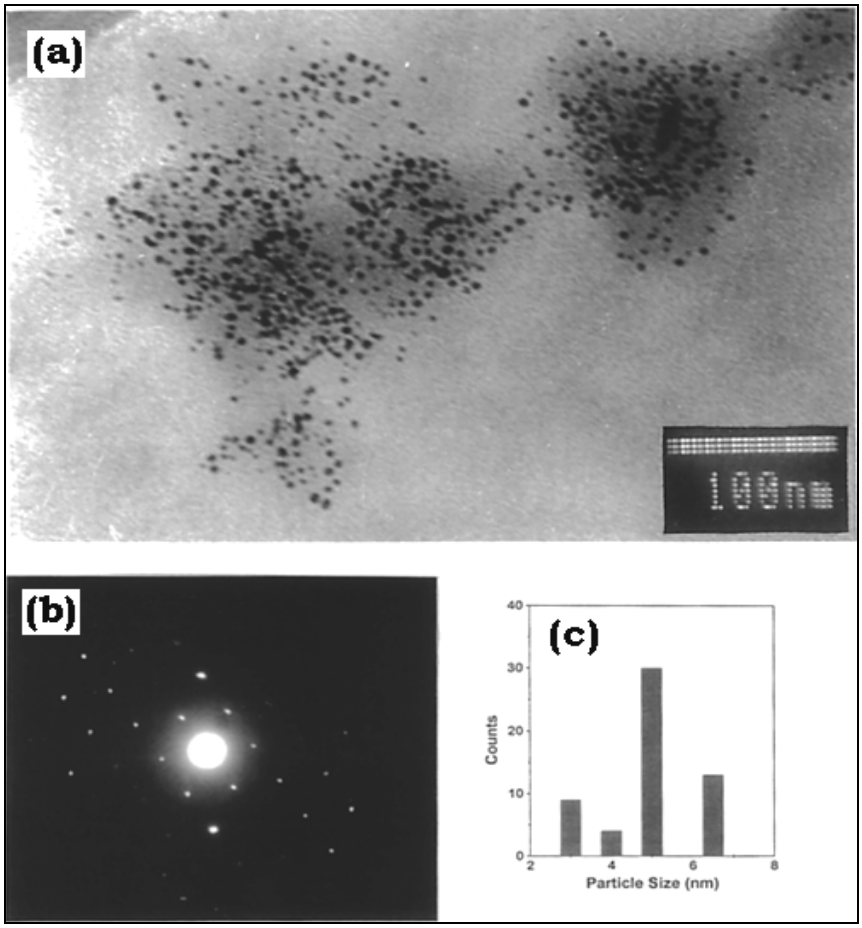

Figure 4.4 (a) Transmission electron micrographs obtained from Au nanoclusters dispersed on an electron microscope grid from the dilute nanocluster solution. The (b) and (c) shows the SAED and the histogram for the particle size distribution respectively (Standard deviation σ = ±10%).

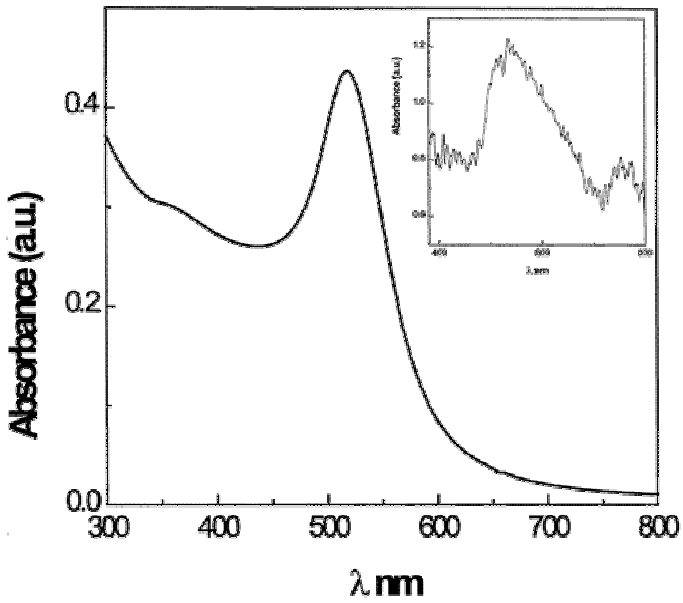

Figure 4.5 The UV-vis spectrum of 4.8 nm Au nanoclusters for Au MPCs in toluene. The inset indicates the UV-vis spectrum after hydrophobic organization on dodecanethiol functionalized Au(111) surface.

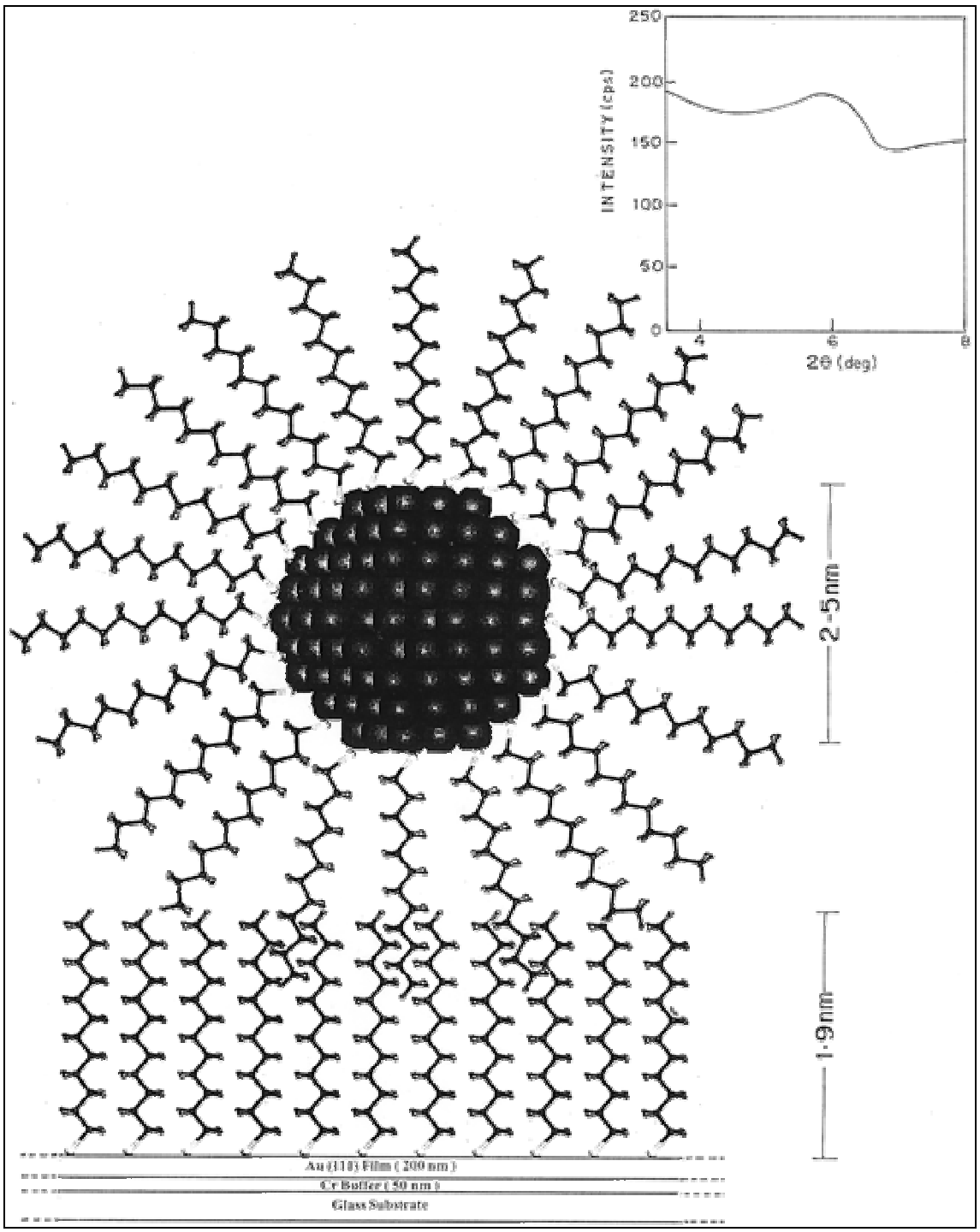

Figure 4.6 Schematic drawing of the dodecanethiol protected single Au nanocluster after the hydrophobic organization in an artificial upright adsorption geometry including an arbitrary number of methylene chains considered for the interdigitation. Inset: The small angle x-ray diffraction pattern of the two dimensional (2D) partial superlattice of Au MPCs on SAM functionalized Au(111) surface after first such organization.

Fig. 4.6 shows a schematic representation of the organization of Au MPCs on a dodecanethiol functionalized Au (111) surface. After such a hydrophobic organization the surface plasmon peak is significantly broadened and redshifted (Fig. 4.5 inset) as compared to that observed for Au clusters in toluene, revealing the aggregation of nanoclusters on the SAM surface; similar behavior has also been reported for the coupled gold particles in solution[28a,b] as well as on solid substrate indicating interparticle plasmon coupling.[28c] Also, the broad-band feature for the hydrophobically organized array is similar to semicontinuous thin gold films.[28c]

The inset of Fig. 4.6 illustrates the organization of clusters on SAM functionalized surface using small angle x-ray diffraction. The peak corresponding to the 'd' spacing of 7.7 nm represents the length scale between two adjacent clusters which is slightly smaller than the size of the two chainlengths of dodecanethiol. An approximate calculation based on these results and taking twice the chainlength of dodecanethiol as about 4 nm, suggest that about three methylene chains are interdigitated on the SAM surface. As compared to 4.2 nm Au particle array demonstrated by Rao et al[11b] the hydrophobic array is larger in interparticle separation.

In order to understand the hydrophobic organization of Au MPCs, FTIR has been found to be very useful. The modified surface due to cluster organization shows several clearly resolved peaks indicating ordered and dense crystalline bulk alkanes: especially for all the C-H stretching regions (Fig. 4.7a). The high degree of conformational order is best evidenced by the position of the symmetric (d^+) and antisymmetric (d^-) CH_2 stretching peaks. Average value of 2847 ± 1 and 2916 ± 1 cm^{-1} for these peaks indicate an extremely high percentage of all-trans conformations.[29] The values measured for such type of hydrophobic organization is interestingly similar to that of layered materials as well as well ordered solid n-alkanes.[30]

For the spectrum in the region 1400-1500 cm^{-1}, for 2D-SAM alkanethiolates, only the all-trans scissoring mode has been observed,[31] while after 3D-SAM formation, typically four bands are seen in this region (methylene scissoring (δ) at ~1458 cm^{-1}; methylene antisymmetric bending (α) at ~1452 cm^{-1} and CH_2-S methylene scissoring (δ) at ~1424 cm^{-1}). Very weak CH_3 symmetric bending vibration (~1375 cm^{-1}) which has been observed in 2D SAM[29] is found to be well resolved after the adsorption of clusters on SAM surface (Fig. 4.7b) as reported earlier.[29,30] Presence of large number of bands between 1200-1380 cm^{-1} corresponding to either twisting-rocking or wagging progression modes, is a strong evidence for the micro-environment of the alkanethiol monolayers on gold clusters as demonstrated by Murray et al.[32]

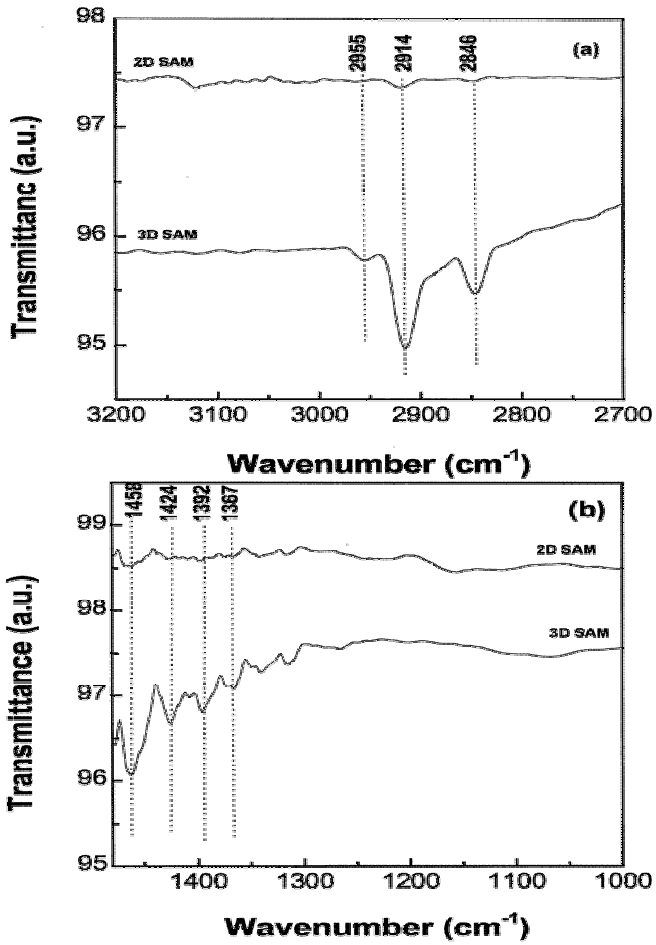

Figure 4.7 The FTIR spectra recorded from a one-layer Au MPCs film on functionalized Au(111) substrate: (a) in the range of 2700-3200 cm^{-1} and (b) in the range of 1000-1600 cm^{-1}. The main resonances are identified in the figure and discussed in the text with reference to 2D-SAM alkanethiolates on gold surface.

Fig. 4.8 shows x-ray photoelectron spectra of C1s, Au 4f and S 2p, for dodecanethiol covered Au(111) surface before (a) and after (b) MPCs organization. The peak position, line shape and peak to peak separation of 3.6 ± 0.1 eV are the standard measure of the Au oxidation state.[33] The B.E. for Au 4f doublet (83.9 and 87.5 eV) are consistent with Au^{o} oxidation state. If Au^{+} were present, it would have appeared as a peak (or at least a shoulder on the Au^{o} $4f_{5/2}$ peak) near 84.9 eV. The intensity of the peak is increased four times after cluster adsorption.

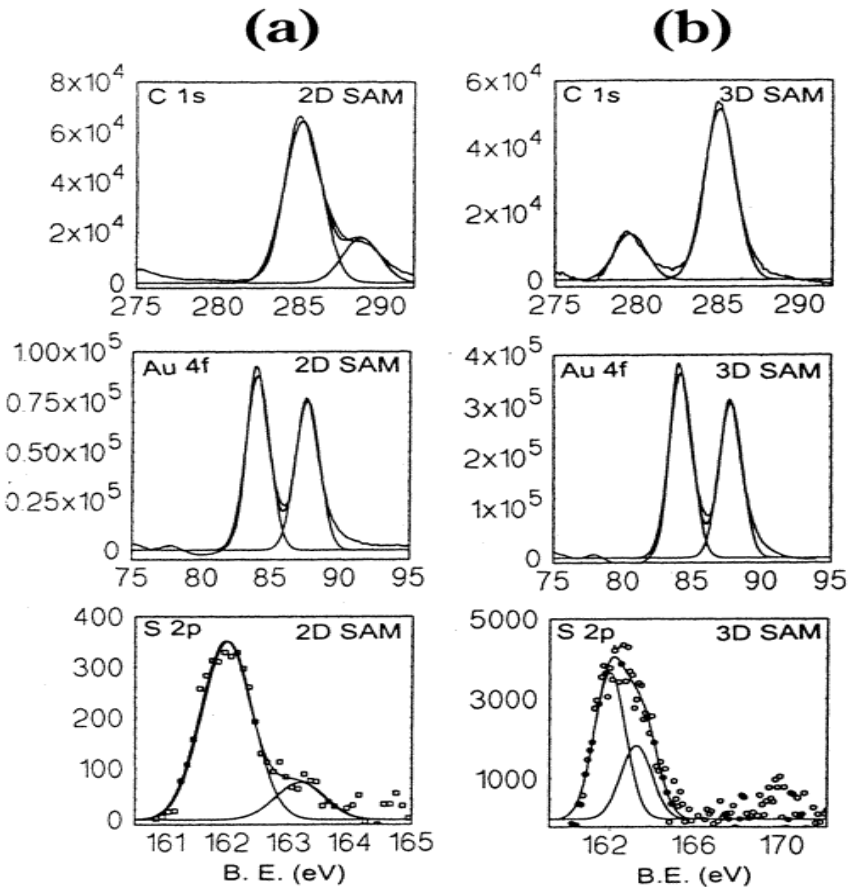

Figure 4.8 The XP spectra of C 1s, Au 4f and S 2p respectively, (a) for dodecanethiol covered Au(111) surface (2D SAM) and (b) for the monolayer protected clusters adsorbed on SAM surface (3D SAM).

The S $2p_{3/2}$ B.E. for 2D and 3D SAM appear at 162.0 and 162.2 eV (Fig. 4.8c) respectively. The shift in B.E. for S, after cluster adsorption may be due to the possibility of charging arising from the insulating nature of the monolayers.

Only after 2D SAM formation, the B.E. of the sulfur peak is in agreement with those of the previously reported values. The shift in B.E. is neither due to the presence of free alkylthiol nor disulfide, as their B.Es. are expected much larger than 163 eV. The peak at 168 eV may be attributed to the thiolate moiety on the cluster surface due to the beam induced damage.[33b]

4.3.2 Adsorption Kinetics

The hydrophobic interaction between the 2D SAM and MPCs (3D SAM) surfaces is also confirmed by the results of the QCM studies. Fig. 4.9 displays the comparative variation of mass change with time for simple dodecanethiol adsorption on Au(111) surface at different concentrations.

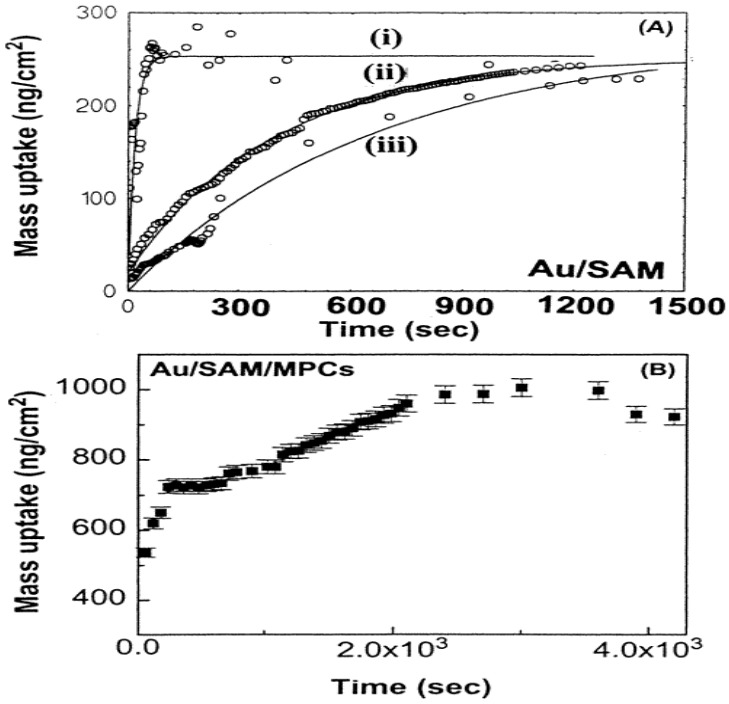

Figure 4.9 (A) The comparative variation of mass change with time for simple dodecanethiol adsorption on Au(111) surface at different concentrations. (i) 2.5 x 10^{-3}M; (ii) 2.5 x 10^{-4} and (iii) 2.5 x 10^{-5}. (B) The mass uptake with time for the hydrophobic organization of Au MPCs on SAM functionalized Au(111) surface.

Typical mass increase (Fig. 4.9a; for 2.5 x 10^{-3} M) shows the kinetics of SAM formation indicating that the saturation coverage has been attained within few minutes. This saturation value of mass (254 ng/cm^2) after correction for

blank indicates that *ca.* 1.26 x 10^{-9} moles has been adsorbed corresponding to 99% coverage. In order to study the kinetics of SAM formation quantitatively, this data was fitted with Langmuir adsorption isotherm for different concentrations of thiol.[34] Comparatively, for lower concentrations (b: 2.5 x 10^{-4}M and c: 2.5 x 10^{-5}M), the adsorption seems to be slow perhaps due to more reorganization. An approximate estimation of the free energy of adsorption for dodecanethiol (ΔG_{ads} = -4.2 kcal/mol) is in agreement with earlier reports.[34] Considerable fluctuations in the quartz crystal resonant frequency are noticed for 2.5 x 10^{-3} M over a long time of interval and the precautions necessary to analyse this type of information have been reviewed earlier.[35]

In comparison, Fig. 4.9B indicates the mass uptake with time during the hydrophobic organization of MPCs on SAM functionalized surface. As compared to the kinetics of SAM formation (Fig. 4.9A), the cluster adsorption is extremely slow. More interestingly, the time-dependence of mass uptake shows two distinct regions, a fast initial step is followed by a sigmoidal behavior, perhaps due to cluster insertion. For example, in the initial step (500 s) *ca.* 125 ng/cm^2 mass uptake has been effected while the second region shows a sigmoid increase upto 995 ng/cm^2. The first stage could be attributed to the exchange of thiol which is followed by a slow adsorption of clusters. After saturation coverage, there occurs a slight decrease in mass possibly due to the partial removal of clusters that form multilayers. The important parameters calculated from these results are briefly summarized in Table-I.

Table-I A comparison of the adsorption kinetics of dodecanethiol SAM and Au clusters (on SAM functionalized surface) after hydrophobic organization.

Parameters	**SAM on Au(111) surface**	**Au MPCs adsorption on SAM functionalized (p.s. 4.8±0.5 nm)[a]**
K_a ($M^{-1}s^{-1}$)	10^4	2.5 x 10^3
K_b ($M^{-1}s^{-1}$)	8.91	11.35
K_{eq}	1011.1	237.35
ΔG (kcal/mol)	-4.8 kcal/mol	-3.2 kcal/mol

[a]Particle size (p.s.) is determined from TEM. The standard deviation for the TEM measurement is 10%.

As compared to dodecanethiol organization on flat Au(111) surface, the organization of hydrophobic clusters on SAM surface is less favourable since the driving force for the adsorption of these MPCs on the organic surface arises due to weak interactions coupled by the reduction in the surface tension. The mass change of 750 ng/cm^2 obtained after MPCs hydrophobic organization corresponds to a particle surface coverage of 1.3 x 10^{10} clusters/cm^2, assuming 4.8 nm diameter (TEM result) and 1.6 nm^3 per Au atom. This corresponds to a surface coverage of ~18%. This small surface coverage is nearly similar to the value of 15% obtained by Natan et al[36] for self-assembled colloidal gold particle films and may be rationalized in terms of strong interparticle repulsive interaction. Nevertheless, the mass increase clearly suggests that alkanethiol protected clusters are organized on the SAM surface using the hydrophobic effect. The gain in free energy on the transfer of MPCs from solution to the SAM surface provides the driving force for this type of nanocluster organization. Since the hydrophobicity of aminoacids can be estimated,[37] cluster organization using amino acids as monolayers will help to understand more details.

4.3.3 Electrical/Electrochemical Properties

The adsorption of hydrophobic MPCs on 2D SAM functionalized surface was also investigated for their electrochemical behavior as Au MPCs show good redox behavior in aqueous electrolytes (Fig. 4.10). For example, cyclic voltammogram taken at 200 mV/s shows an anodic peak at +0.5 V and a cathodic peak at -0.15 V indicating the redox activity of clusters after hydrophobic organization on SAM surface (Fig. 4.10). During voltammetric measurements the final potential was never allowed to exceed +0.8 V since SAM is reported to undergo oxidative damage.[38a] The calculated $E_{1/2}$ value, 0.65 V, is comparable to that reported earlier by Willner et al for Au MPCs functionalized on ITO electrode.[38b]

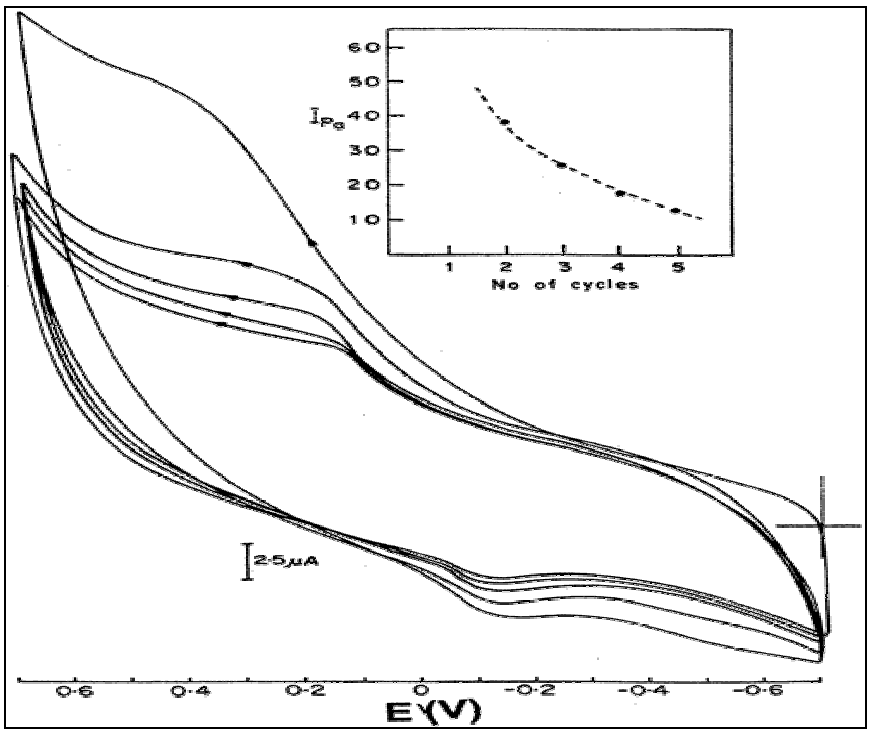

Figure 4.10 Cyclic voltammogram taken at 200 mV/s in 0.1 M KCl using Au MPCs organized SAM surface as working electrode. Inset shows the variation of anodic peak current with number of cycles.

The peak width (FWHM), ΔE of ~ 60 mV suggests one electron process ($Au_n \rightarrow Au_n^+ + e^-$). The sigmoidal nature of the voltammogram indicates the passivation of the surface due to the presence of monolayers. A plot of the anodic current (after correction for the capacitive current), I_p with the number of cycle shows that I_p decreases exponentially (inset) as only less gold surface is exposed to the clusters after the reorganization of the organic molecules. This is in agreement with the tentative scheme that has been proposed earlier.[38c]

Fig. 4.11 shows cyclic voltammograms using SAM modified Au(111) as working electrode before (a) and after (b) the adsorption of clusters. For comparison purpose a separate voltammogram is shown for clusters dispersed in the same solution using SAM functionalized Au(111) electrode as the working electrode (c). The voltammograms were recorded in 1:1 acetonitrile:toluene mixture(v/v) containing 0.1 M $TBAF_6P$ between the potential -1.0 to +1.0.

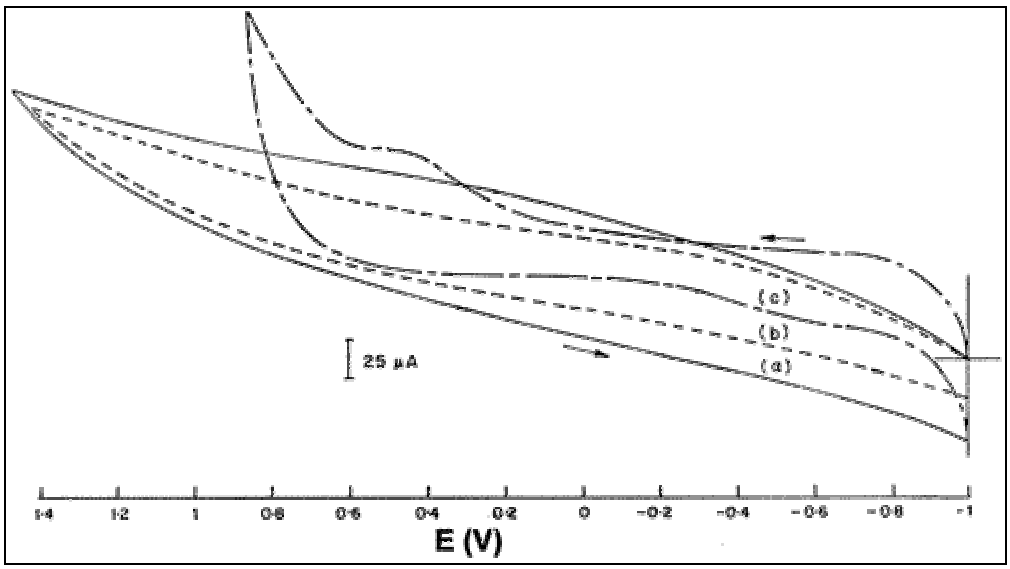

Figure 4.11 Cyclic voltammograms recorded in 1:1 acetonitrile:toluene mixture containing 0.1 M $TBAF_6P$ between the potential -1.0 to +1.0 using SAM modified Au(111) as working electrode (a), after adsorption of the clusters on SAM functionalized surface (b), and after dispersing the clusters in the solution (c).

The thiol SAM functionalized Au electrode shows no redox activity as predicted and the capacitance reduction (2.5 $\mu F/cm^2$) compared to bare gold (30 $\mu F/cm^2$) confirms the formation of a compact monolayer. After the cluster adsorption (Fig. 4.11 b) the redox accessibility of the clusters is not seen, perhaps because the electron transfer is diminished by the passive nature of the monolayers. However, surprisingly the double layer capacitance is also decreased after the adsorption of the clusters. A typical value of 1.5 $\mu F/cm^2$ is estimated from the constant slope of the plot of non-faradaic current with scan rates. Interestingly, after dispersing the clusters in the solution (Fig. 4.11 c), a reversible peak is observed confirming the redox accessibility of the clusters in the solution. In the first cycle a large anodic peak is seen at 0.45 V corresponding to the oxidation of the clusters while the reverse scan shows only a small cathodic peak around -0.62 V, may be due to the leaching of the oxidised clusters to solution. In the second cycle, the anodic current decreases sharply perhaps due to the adsorption of the clusters on the passivated surface and then in next few cycles it attains a steady value. There is an asymmetry in

the peaks (area under anodic curve ~ 10^{-9} moles while area under cathodic peak is ~ 10^{-10} moles) and anodic currents are significantly larger. This implies that oxidation is more favoured since the clusters are not completely protected due to the reductive desorption of thiol. Thus the dynamic nature of the thiol molecules attached on the cluster is considered to be responsible for this difference. Nevertheless, an electrochemical coverage of 10^{-9} moles/cm^2 agree well with the value of 10^{10} clusters/cm^2 from QCM results considering that the clusters have an average number of 3000 atoms as shown in the TEM results.

Fig. 4.12 shows a comparison of the current-voltage (I-V) curves for dodecanethiol SAM covered gold before (a) and after (b) cluster organization. For all the samples reproducible I-V curves could be obtained only upto $\pm$1.5 V. In contrast to the linear behavior observed for bare gold (not shown), SAM functionalized gold substrate shows clear non-linear I-V characteristics which can be explained due to the presence of a metal-insulator-metal type of a junction. Hence the current is expected due to tunnelling through this barrier, which may lead to a positive value of non-linearity.[39] In comparison, the I-V curve for Au MPCs organized on SAM surface (Fig. 4.12 b) establishes a double barrier tunnel junction (contact-metal cluster as first junction and the metal cluster-metal substrate as second junction with the insulating barrier in between). At room temperature, the I-V is strongly non-linear, with a region of suppressed current near zero voltage. At higher voltages the current approaches two linear asymptotes, which are displaced from the origin by +0.25 and -0.25 V, respectively which is larger by 0.05 V as compared to SAM covered surface. This could be attributed to the coulomb blockade effect, which basically arises due to the charge quantization in nanoclusters capable of small quantum charge fluctuations when electron transfer occurs as only in units of 'e'.[40] The gap width is larger than the SAM functionalized surface possibly due to the slow electron transfer through the nanoclusters. For the case of organized clusters the even barrier for electron-transfer between nanoclusters can be tuned by controlling the long-range nature of hydrophobic forces using

appropriate chainlengths. I-V measurements at low temperature are essential to unravel the nature of hydrophobic interaction, which are much stronger than the expected van der Waals interactions at nm length scale and its exponential decay with distance.

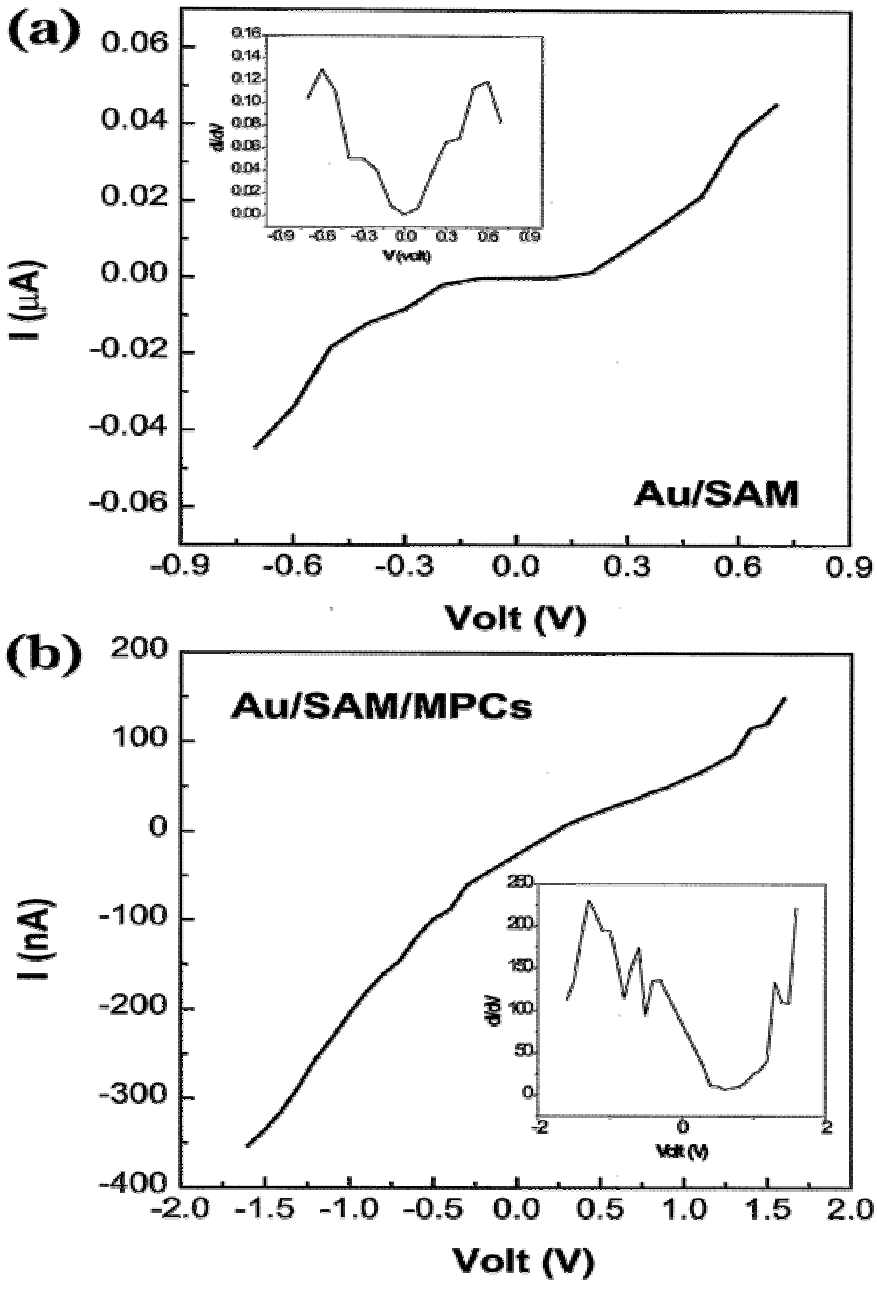

Figure 4.12 The current-voltage curves for (a) dodecanethiol SAM covered gold and (b) SAM covered gold after hydrophobic cluster organization. Inset shows the respective differential conductances before and after MPCs organization.

4.4 Electrical behavior of Hydrophobically Organized Q-dot arrays: Effect of Chain length and molecular structure of the Passivating Organic Molecule

The electronic properties of both monolayer-protected nanoclusters and cluster arrays depend on several parameters such as core size, nature of the organic molecule, especially its electronic structure, chain length, functional group and the type of interaction between cluster-molecule and molecule-molecule junctions. Bonding between cluster surface and the monomolecular layer is covalent while the interaction between MPCs and monolayer-covered surface is predominantly due to van der Waal's interaction. Interparticle separation (distance between the surface of the metallic cores of the nanoclusters) systematically changes from C5 to C12 that enables to study the distance-dependent electron transfer through the hydrocarbon chain. The determination of a detailed mechanism for electron transfer through self-assembled MPCs seems to be a difficult problem especially if different orientations of hydrocarbon chains are considered. In the absence of temperature variation, we may not be able to separate out several possible mechanisms. Nevertheless, we fit the model with electrical measurements that allow us to study the tunneling current with the shape of the I-V, the band gap width and the effect of molecular structure.

We start with the model of Hanna and Tinkham[22] where two-junction system is treated with fractional charge Q_o on central electrode without an external electrode and their result are in full agreement with orthodox theory including these additional parameters. This model is found to be compatible with the data obtained using Kelvin probe method; however, it is important to understand the effect of such a large assembly where, $R_2/R_1 > 1$, with $Q_o > e/2$ which alters when electron tunnels from one junction to another and

$$I(V) = 1/R_2C_s\,[-(n_oe-Q_o)+C_1V-e/2IVI]$$

with $I(V) = 0$ when $(-e/2+n_oe-Q_o)/C_1 \leq V \leq (e/2+n_oe-Q_o)/C_1$, where $C_s=C_1+C_2$; these equations are basically used to determine the features of experimental I-

V characteristics. Thus tunneling events are dependent on the change in the energy of each electron as it tunnels from one cluster-molecule junction to the other.

Before analyzing the results it is important to mention the assumptions involved in these calculations. 1) The electron transfers from the electrode to several nanoclusters are considered and not from electrode one to another; 2) The voltage source is assumed to give charge as fast as possible; 3) Misalignment in Fermi levels due to the charge offset or impurities are neglected; 4) the effect of grainy surface of Au is not taken into account and finally, 5) the particle size distribution should be narrow (Standard Deviation < 3%), or otherwise, the effect may become ohmic due to the drastic variation in charging energy. Apart from these assumptions, few features are also important like, if C_2/C_1 or R_2/R_1 approaches 1, then steps will be disappeared; if R and C are equal on both sides, electron should tunnel with identical rates. By optimizing these two ratios we get materials with different dielectric properties. Keeping all these in mind, our experimental configuration enables us to average the steps to Ne/RC so that each cluster will act as a DBTJ to give an additive current.

The current-voltage behavior predicted by the above model could be used to understand the experimental I-V characteristics of hydrophobically organized clusters. For example, a typical I-V curve obtained for the case of C12-Au MPCs is shown in Fig. 4.13a with the fitted curve (solid line) and the conductance spectrum. A large blockade (a potential gap of 625 mV in zero current region) is observed for these well separated MPCs followed by a sharp increase (two linear asymptotes are seen) in the current on both negative and positive potential sides. These results agree very well with the orthodox theory.[22,23] For such an array, a fractional charge Q_o may exist on the cluster, permitting an asymmetry in the I-V characteristics, included in the fitting routine. The coulomb blockade as determined from I-V measurements is in accordance with the previously reported results of Wang et al[21], which reveals that for a 5

nA set current $C_1<C_2$. The distance from the mercury drop to the cluster array R_2 was estimated from the fitting. The other parameters (R_1, C_1, and Q_0) were also calculated by changing C_2, as we change the cluster-Hg drop distance, by varying the chainlength and the molecular structure. The current values are in the same range as have been confirmed by independent STM measuements.[18,21]

The narrow size distribution of C12-Au clusters could be confirmed by the TEM image shown in Fig. 4.13b. The particles used for the hydrophobic organization are found to be very well dispersed from each other. The particles are of the order of 4.8 nm ± 0.5 nm (1:2 Au/RSH molar ratio) size. These particles were found to have narrow gaussian distribution with compact separated crystalline core. The selected area electron diffraction (SAED) of Au MPCs reveals a well-defined crystalline structure rather obvious from the spot pattern.

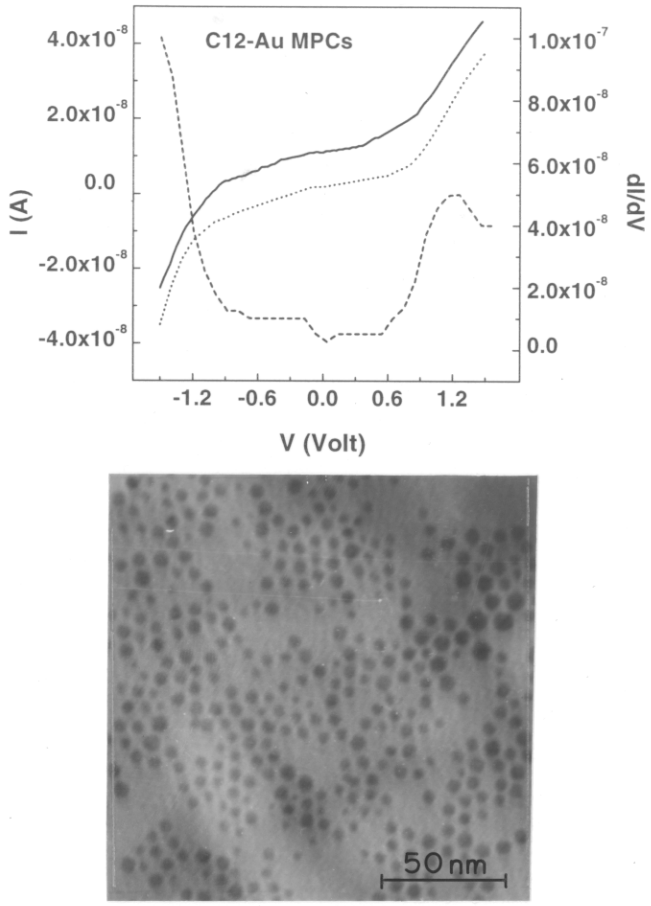

Figure 4.13 a) I-V curve (dotted line) of C12-Au MPC taken after hydrophobic organization and solid line indicate their theoretical fitting. The differential conductance is also shown for these Au MPCs (dashed line). The voltage is taken between 1.5 V to –1.5 V and the set current was 5 nA. The parameters for fitted curve are C_1 = 0.5E-19 F, C_2 = 0.88E-19 F, R_1 = 10.0 MΩ, and R_2 = 15.5 MΩ. b) TEM image of C12-thiol stabilized Au particle of sizes 4.8 nm ± 0.5 nm dispersed on an electron grid from the dilute solution of the cluster.

When the distance between the Hg-drop and particles on SAM modified substrate is changed by varying the length of the passivating molecule, we could tune C_2 so that the systematic change in the nature of I-V could be studied. For example, the I-V curve for C_8-Au MPCs (Fig. 4.14a) indicates that the current suppression region near zero voltage is reduced to 500 mV as compared the case of C12-Au MPCs, followed by two linear regions at both potentials sides. In addition, the asymmetry is reduced and two linear asymptotes come closer by 125 mV. The asymmetry may arise due to the

energy levels arising from the quantum size effect. The decrease in R exhibits the lower charging energy and the comparison with only SAM/Metal surface shows exponential behavior as reported by Whitesides et al.[41] The gap arises from the quantum size effect that opens up an energy gap near the fermi level of the particle called the Kubo gap. The results demonstrated by Heath et al for Q-dot superlattice (i.e. many electron system with gap δ) shows that the Coulomb gap was quenched when the capping was changed from C12 to C5 i.e. when the cluster interparticle separation is varied from 1.8 nm to 0.5 nm.[23]

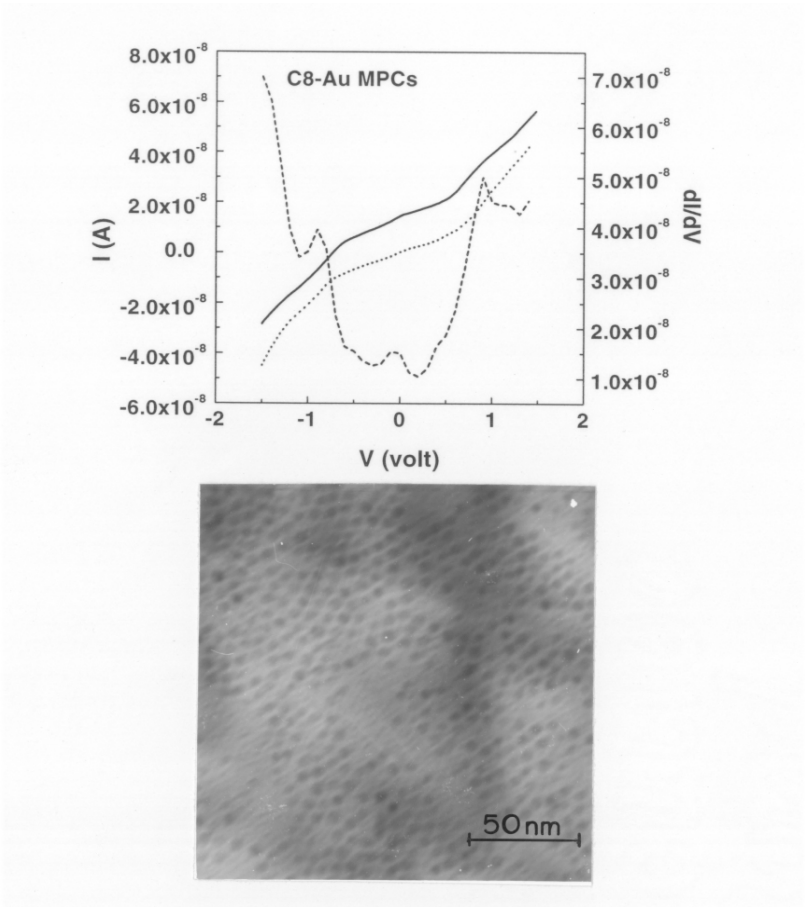

Figure 4.14 a) I-V curve (dotted line) of C8-Au MPC taken after hydrophobic organization and solid line indicate their theoretical fitting. The differential conductance is also shown for these Au MPCs (dashed line). The voltage is taken between 1.5 V to –1.5 V and the set current was 5 nA. The parameters for fitted curve are C_1 = 0.89E-19 F, C_2 = 1.0E-19 F, R_1 = 9.9 MΩ, and R_2 = 15.0 MΩ. b) TEM image of C8-thiol stabilized Au particle of sizes 4.8 nm ± 0.5 nm dispersed on an electron grid from the dilute solution of the cluster.

In order to determine the junction parameters, the curves were fitted, considering the set point current of 5 nA, the C_2 becomes larger as Hg-MPC distance decreases but R_2 also decreases. The fitting parameters are mentioned in the figure with the Q_o value of 0.2e. The fitting value of C_1 is in close proximity with the experimental results. This is supported by the TEM image which shows particles as separate as C12-Au MPCs with nearly the same size (Fig. 4.14b).

A further decrease in the particle-Hg tip distance by selecting the C5-thiol as passivating molecule reveals a minima in the coulomb gap size by 155 mV for Au-C5 MPCs (Fig. 415a). In comparison to the case of C12 and C8-Au MPCs, the zero current region is reduced with two linear asymptotes at higher voltages following Ohm's law and it becomes more symmetric on both sides of the blockade region. The fitting reveals a further decrease in the R value along with an increase in C_2 and the fractional residual charge changes to more negative value as distance between the Hg drop and the MPCs decreases. This is attributed to the fluctuation mechanism.[42] This residual charge is assumed to arise due to the difference between the work functions of the working electrodes as it is easy to understand that charge may get localized due to the surface states arising under the electric field. In contrast to the images of C12 and C8- Au MPCs, TEM results of C5-Au MPCs (Fig. 4.15b) suggest closer particles to form ordered lumps, supporting the linear nature of the I-V characteristic when chainlength decreases below C6.[23]

In order to understand the effect of conjugation on the electron transfer behavior through organized clusters, two organic molecules containing a π-electron cloud were selected. The inclusion of pi-cloud shows an increase in the charge density and the non-linearity as well as asymmetry reduces with very narrow gap as compared to alkanethiol-Au MPCs (Fig. 4.16 and 17a). The conductance gap is reduced to 225 mV and 325 mV for Ph-Au and PhC2-Au MPC, respectively; mostly it looks linear on both sides of higher potentials. The

fitting of the curve shows negative value of Q_o with R_2~R_1 and increased C_2 as compared to C_1. These results indicate that the presence of pi-cloud has enhanced the current density, possibly due to less compact packing leading to more pinholes and defects in these 3D nanostructures. Interestingly, the linearity in I-V behavior is also reflected in the TEM images of these two particles where bigger clusters are evident compared to normal alkanethiol passivated MPCs (Fig. 4.16 and 17b), cross-linked presumably due to π-π stacking.

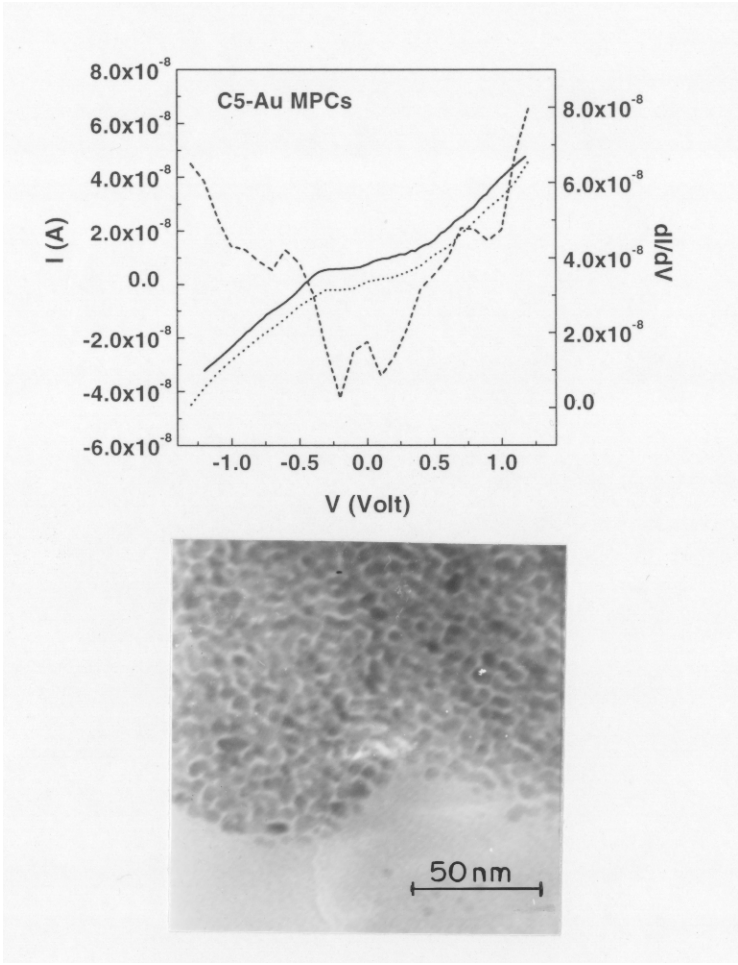

Figure 4.15 a) I-V curve (dotted line) of C5-Au MPC taken after hydrophobic organization and solid line indicate their theoretical fitting. The differential conductance is also shown for these Au MPCs (dashed line). The voltage is taken between 1.3 V to –1.3 V and the set current was 5 nA. The parameters for fitted curve are C_1 = 0.05E-19 F, C_2 = 1.0E-19 F, R_1 = 9.7 MΩ, and R_2 = 10.5 MΩ. a) TEM image of C5-thiol stabilized Au particle of sizes 5-6 nm ± 0.5 nm dispersed on an electron grid from the dilute solution of the cluster.

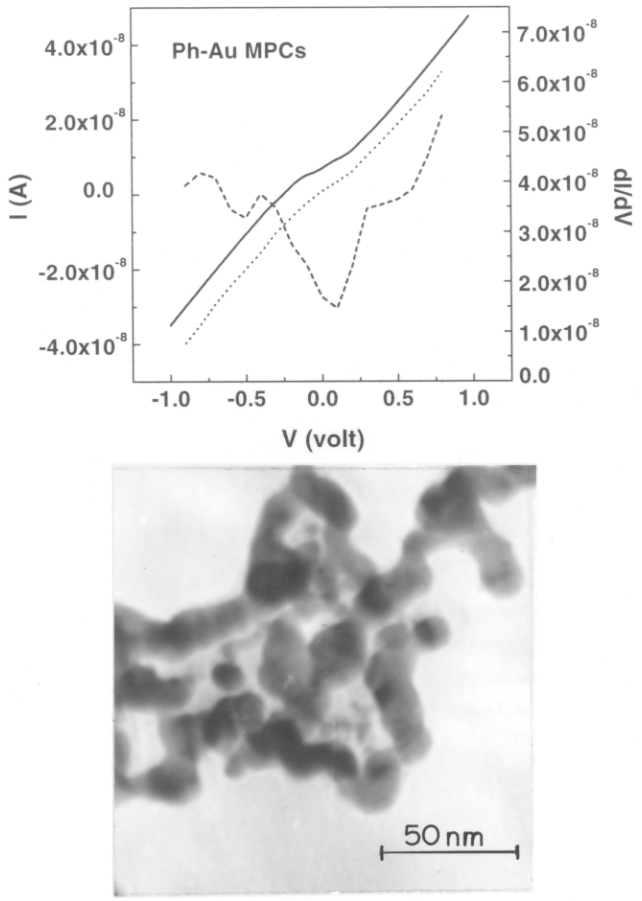

Figure 4.16 a) I-V curve (dotted line) of Ph-Au MPC taken after hydrophobic organization and solid line indicate their theoretical fitting. The differential conductance is also shown for these Au MPCs (dashed line). The voltage is taken between 1.0 V to –1.0 V and the set current was 5 nA. The parameters for fitted curve are C_1 =1.0E-19 F, C_2 = 1.5E-19 F, R_1 = 9.6 MΩ, and R_2 = 10.0 MΩ. b) TEM image of Ph-thiol stabilized Au particle of sizes 7-8 nm ± 0.5 nm dispersed on an electron grid from the dilute solution of the cluster.

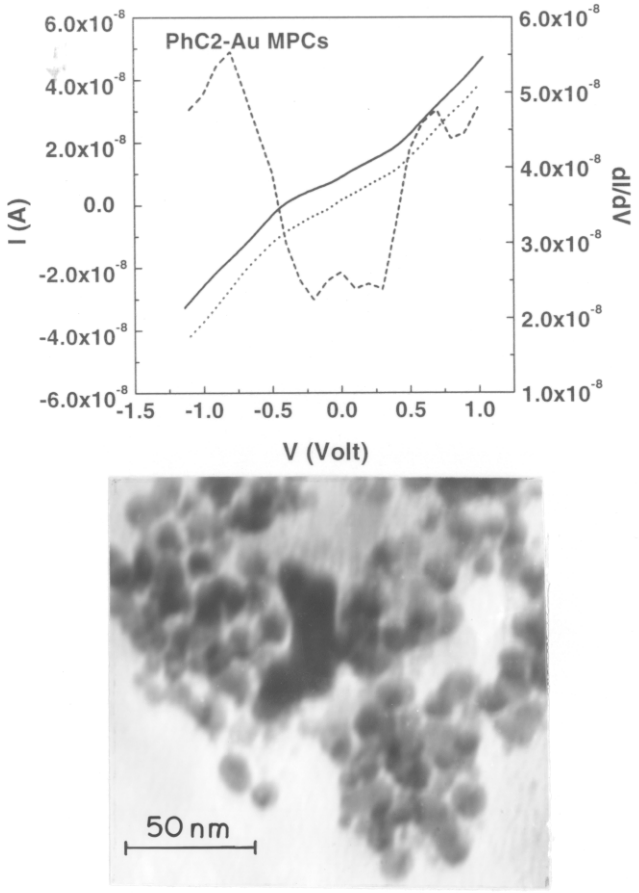

Figure 4.17 a) I-V curve (dotted line) of PhC2-Au MPC taken after hydrophobic organization and solid line indicate their theoretical fitting. The differential conductance (dashed line) is also shown for these Au MPCs. The voltage is taken between 1.1 V to –1.1 V and the set current was 5 nA. The parameters for fitted curve are C_1 = 1.0E-19 F, C_2 = 0.75E-18 F, R_1 = 10.0 MΩ, and R_2 = 10.2 MΩ. b) TEM image of PhC2-thiol stabilized Au particle of sizes 7-8 nm ± 0.5 nm dispersed on an electron grid from the dilute solution of the cluster.

All these experiments (Table-I) suggest that the hydrophobically organized arrays show non-linear I-Vs depending on the length of the alkane chain. The conductivities increase by two order of magnitude for each C4 length as in agreement with the results proposed by Murray.[43] More interestingly, the magnitude of asymmetry gradually reduces as hydrocarbon chain length decreases, as expected from the change in charging energy (Figure 4.18). In comparison, for MPCs passivated with conjugated aryl thiol molecules the I-V is nearly linear due to the increased overlap between particles resulting from the π-system of the organic molecule. It is worth noting

that the gap width changes from 625 mV to 225 mV when the molecular length changes from C12 to C5. Further, the magnitude of the Coulomb gap potential at room temperature can be tuned by the junction thickness (i.e. length of the organic spacer molecule) as in agreement with the predictions of the model. Interesting aspect is that perhaps some wider undistinguished peaks in dI/dV-V give hint to the existence of high disorder produced by conjugation.

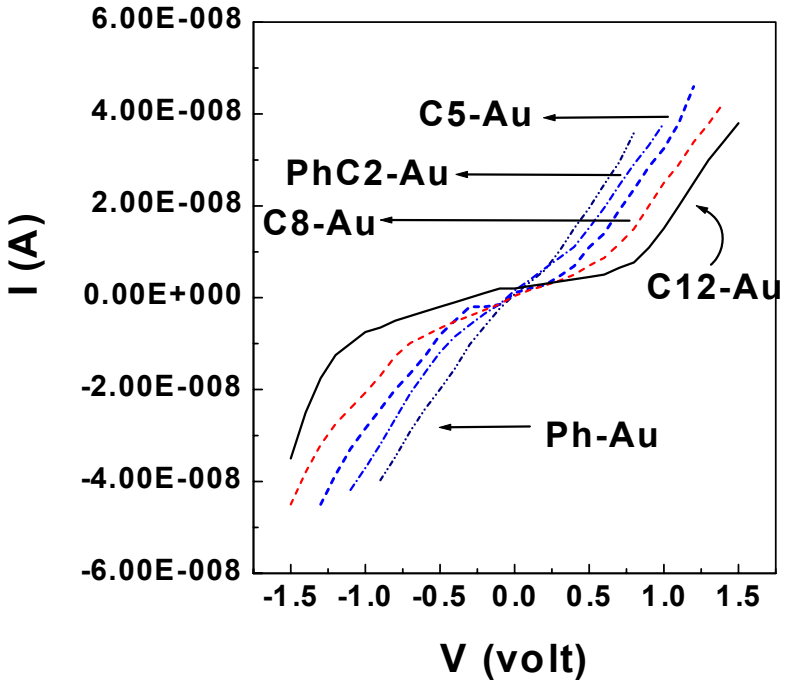

Figure 4.18 Superimposed I-V curves of various MPCs taken after hydrophobic organization on respective SAM modified Au (111) surfaces. C5, C8, C12, PhC2 and Ph-Au indicate pentane, octane, dodecane, benzyl, and phenyl thiol monolayer protected Au nanoclusters respectively.

Table-I: Parameters calculated from the fitting of the experimental I-V curve for different MPCs and width of the zero conduction regions for different cases.

Parameters	C12-Au	C8-Au	C5-Au	PhC2-Au	Ph-Au
C_1	0.5E-19	0.89E-19	0.05E-19	1.0E-19	1.0E-19
C_2	0.88E-19	1.0E-19	1.0E-19	1.5E-19	0.75E-18
R_1	10.0M	9.9M	9.7M	9.6M	10.0M
R_2	15.5M	15.0M	10.5M	10.0M	10.2M
C_s	2.38E-19	3.54E-19	4.05E-19	5.0E-19	9.6E-19
ΔE (mV)	625	500	345	325	225

One of the limitations of the above I-V measurements is the lack of sensitivity due to the large area of contact compared to the individual cluster size. Although it is desirable to use an STM tip for contact, we believe that the application of a micromanipulator has helped to minimize the errors associated with the large area of contact during these I-V measurements. The characteristic I-V features were repeated for selected few systems (such as different size Au nanoclusters) with an STM tip for contact and the same extent of non-linearity was confirmed despite high sensitivity and molecular resolution. In certain cases there is also a wide variation in interparticle separation and hence electrical measurements may represent average behavior of an ensemble of particles. Nevertheless, comparison of the results of the blank experiments with SAM (Hg/Molecule/Metal surface contact) alone clearly suggests coulomb blockade electron-transfer behavior of nanoclusters as in agreement with the results of few other investigators.[18,41]

4.5 CONCLUSIONS

A novel hydrophobic organization of Au MPCs on organic surfaces is demonstrated using dodecanethiol SAM on Au(111) surface. The electronic and optical properties of these films show that the Au colloids maintain their individual character. Cyclic voltammetric studies confirm the redox accessibility of these monolayer protected Au clusters on SAM functionalized surface. This type of organization of nanoclusters using controlled hydrophobic forces will act as a model system for studying several phenomena like specificity of molecular recognition and adsorption effect in biomolecules and biomolecular aggregates. The results of a simple kelvin probe study of the electronic properties of an array of Au nanoparticles with the size of 4.8 ± 0.5 nm demonstrate that length of the organic molecule and molecular structure (e.g. conjugation) of the passivating molecule along with core size plays a crucial role in controlling the coulomb blockade behavior. A systematic variation of chainlength shows coulomb blockade effect with larger band gap (gap width ~625 mV) for MPCs

passivated with longer chain length where the fractional residual charges Q_o on the center electrode is varied without an external electrode. The aromatic nature of phenyl ring demonstrates nearly linear I-V characteristics. These results help to understand the electronic behavior of molecular junctions especially in tuning single electron tunneling behavior by varying the molecular structure and chain length of the organic SAM forming molecule.

4.6 REFERENCES

1. Templeton, A.C.; Wuelfing, W.P.; Murray, R.W. *Acc. Chem. Res.* **2000**, *33*, 27.
2. Gittins, D.I.; Bethell, D.; Schiffrin, J.; Nichols, R.J. *Nature* **2000**, *408*, 67.
3. Collier, C.P.; Saykally, R.J.; Shiang, J.J.; Henrichs, S.E.; Heath, J.R. *Science* **1997***, 227*, 1978.
4. O'hara, P.C.; Leff, D.V.; Heath, J.R.; Gelbart, W.M. *Phys. Rev. Lett.***1995**, *75*, 3466.
5. Halperin, W.P. *Rev. Mod. Phy.* **1986**, *58(3)*, 533.
6. a) Feldheim, D.L.; Keating, C.D. *Chem. Soc. Rev.* **1998**, *27*, 1. b) Elghanian, R.; Stovhoff, J.J.; Mucic, R.C.; Hetsinger, R.L.; Mirkin, C.A. *Science* **1997**, *277*, 1078.
7. Ulman, A. *An Introduction to ultrathin organic films from Langmuir-Blodgett to Self-asembly*: Academic Press, CA, 1991.
8. Hickman, J.J.; Ofer, D.; Laibnis, P.E.; Whitesides, G.M. *Science* **1991**, *252*, 688.
9. Bandhyopadhyay, K.; Mayya, S.; Vijayamohanan, K.; Sastry, M. *Langmuir* **1997**, 13, 5244.
10. (a) Colvin, V.L.; Schlamp, M.C.; Alivisatos, A.P. *Nature* **1994**, *370*, 354. (b) Murry, C.B.; Kagan, C.R.; Bawendi, M.G. *Science* **1996**, *270*, 1335. (c) Nakanishi, T.; Ohtani, B.; Uosaki, K. *J. Phy. Chem. B* **1998**, *102*, 1571. (d) Brust, M.; Etchenique, R.; Calvo, E.J.; Gordillo, G.J. *Chem. Commun.* **1996**, 1949.
11. (a) Vijayasarathy, K.; Thomas, P.J.; Kulkarni, G.U.; Rao, C.N.R. *J. Phy. Chem. B* **1999**, *103*, 399. (b) Vijayasarathy, K.; Raina, G.; Yadav, R.T.; Kulkarni, G.U.; Rao, C.N.R. *J. Phy. Chem. B* **1997**, *101*, 9880.
12. Bourg, M.; Badia, A.; Lennox, R.B. *J. Phy. Chem. B* **2000**, *104*, 6562.
13. Chen, S.; Murray, R.W. *Langmuir* **1999**, *15*, 682.
14. Bandyopadhyay, K.; Vijayamohanan, K. *Langmuir* **1998**, *14*, 6924.
15. (a) Israelachvili, J.N. *Intermolecular and Surface forces*; Academic Press: New York, 1992. (b) Yang, Z.; Galloway, J.A.; Yu, H. *Langmuir* **1999**, *15*,

8405. (b) Su, T.J.; Green, R.J.; Wang, Y.; Murphy, E.F.; Lu, J.R.; Ivkov, R.; Satija, S.K. *Langmuir* **2000**, *16*, 4999. (c) Sigal, G.B.; Mrksick, M.; Whitesides, G.M. *J. Am. Chem. Soc.* **1998**, *120*, 3464.

16. Zhdanov, V.P.; Kasemo, B. *Langmuir* **2001**, *17(18)*, 5407.
17. (a) Dorogi, M.; Gomez, J.; Osifchin, R.; Andres, R.P.; Reifenberger, R. *Phy. Rev. B* **1995**, *52*, 9071. (b) Amman, M.; Wilkins, R.; Ben-Jacob, E.; Maker, P.D.; Jaklevic, R.D. *Phy. Rev. B* **1991**, *43*, 1146.
18. Thomas, P.J.; Kulkarni, G.U.; Rao, C.N.R. *Chem. Phys. Lett.* **2000**, *321*, 163.
19. Ancona, M.G.; Kruppa, W.; Rendell, R.W.; Snow, A.W.; Park, D.; Boos, J.B. *Phy. Rev. B* **2001**, *64*, 033408.
20. Chiquito, A.J.; Pusep, Y.A.; Mergulhao, S.; Galzerani, J.C.; Moshegov, N.T. *Phy. Rev. B* **2000**, *61*, 5499.
21. Wang, B; Wang, H.; Li, H.; Zheng, C.; Hou, J.G. *Phy. Rev. B* **2000**, *63*, 035403.
22. Hanna, A.E.; Tinkham, M. *Phy. Rev. B* **1991**, *44*, 5919.
23. Medeiros-Ribeiro, G.; Ohlberg, D.A.A.; Williams, R.S.; Heath, J.R. *Phy. Rev. B* **1999**, *59*, 1633.
24. Brust, M.; Walker, M.; Bethell, D.; Schiffrin, D.J.; Whyman, R.; *J. Chem. Soc. Chem. Commun.* **1994**, 801.
25. Rampi, M.A.; Schueller, O.J.A.; Whitesides, G.M. *Appl. Phys. Lett.* **1998**, *72*, 1781.
26. (a) Torigoe, K.; Esumi, K. *J. Phy. Chem. B* **1999**, *103(15)*, 2862. (b) Hostetler, M.J.; Wingate, J.E.; Zhong, C.-J.; Harris, J.E.; Vachet, R.W.; Clark, M.R.; Londono, J.D.; Green, S.J.; Stokes, J.J.; Wingall, J.D.; Glish, G.L.; Porter, M.D.; Evans, N.D.; Murray, R.W. *Langmuir* **1998**, *14(1)*, 17.
27. (a) Brust, M.; Bethell, D.; Kiely, C.J.; Schiffrin, D.J. *Langmuir* **1998**, *14(19)*, 5426. (b) Link, S.; El-Sayed, M.A. *J. Phys. Chem. B* **1999**, *10*, 8410. (c) Hutter, E.; Fendler, J.H.; Roy, D. *J. Phys. Chem. B* **2001**, *105*, 11159.
28. (a) Brust, M.; Bethell, D.; Schiffrin, D.J.; Kiely, C.J. *Adv. Mater.* 1995, *7*, 795. (b) Mirkin, C.A.; Lestinger, R.L.; Mucic, R.C.; Storhoff, J.J. *Nature*

1996, *382*, 607. (c) Shipway, A.N.; Lahav, M.; Willner, I. *Adv. Mater.* **2000**, *12(13)*, 993.

29. Snyder, R.G.; Stranss, H.L.; Elliger, C.L. *J. Phy. Chem.* **1982**, 16, 5145.
30. MacPhail, R.A.; Strauss, H.L.; Snyder, R.G.; Elliger, C.A. *J. Phy. Chem.* **1984**, *88*, 334.
31. (a) Nuzzo, R.G.; Fusco, F.A.; Allara, D.L. *J. Am. Chem. Soc.* **1987**, *109*, 2385. (b) Nuzzo, R.G.; Dubois, L.H.; Allara, D.L. *J. Am. Chem. Soc.* **1990**, *112*, 558.
32. Hostetler, M.J.; Stokes, J.J.; Murray, R.W. *Langmuir* **1996**, *12*, 3604.
33. (a) Mekhalif, Z.; Riga, J.; Pireaux, J.; Delhalle, J. *Langmuir* **1997**, *13*, 2285. (b) Colvin, V.L.; Goldstein, A.N.; Alivisatos, A.P. *J. Am. Chem Soc.* **1992**, *114*, 5229.
34. Schessler, H.M.; Karvovich, D.S.; Blanchard, G.J. *J. Am. Chem. Soc* **1996**, *118*, 9645.
35. Schmacher, R. *Angew. Chem. Int. Ed. Engl.* **1990**, *29(4)*, 329.
36. Grabar, K.C.; Allison, K.J.; Baker, B.E.; Bright, R.M.; Brown,K.R.; Freeman, R.G.; Fox, A.P.; Keating, C.D.; Musick, M.D.; Natan, M.J. *Langmuir* **1996**, *12*, 2353.
37. Hoffman, D.L.; Suslick, K.S. *J. Am. Chem. Soc.* **2000**, *39*, 5418.
38. (a) 1. H. O. Finklea, K. Yoon, E. Chamberlain, J. Allen, and R. Haddox J. Phys. Chem. B, **2001**, *105 (15)*, 3088. (b) Shipway, A.N.; Lahav, M.; Willner, I. *Adv. Mater.* **2000**, *12(13)*, 993. (c) Sabatani, E.; Rubinstein, I. *J. Phys. Chem*. **1987**, *91,* 6663.
39. Stratton, R. *J. Phy. Chem. Solids* **1962**, *23*, 1177.
40. Wang, B.; Xiao, X.; Huang, X.; Sherg, P.; Hon, J.G. *Appl. Phy. Lett.* **2000**, *77(8)*, 1179.
41. Holmlin, R.E.; Haag, R.; Chabinyc, M.L.; Ismagilov, R.F.; Cohen, A.E.; Terfort, A.; Rampi, M.A.; Whitesides, G.M. *J. Am. Chem. Soc.* **2001**, *123*, 5075.
42. Dubois, J.G.A.; Gerritsen, J.W.; Shafranjuk, S.E.; Boon, E.J.G.; Schmid, G.; van Kempen, H. *Europhys. Lett.* **1996**, *33*, 279.
43. Hostetler, M.J.; Wingate, J.E.; Zhong, C.J.; Harris, J.E.; Vachet, R.W..; Clark, M.R.; Londono, J.D.; Green, S.J.; Stokes, J.J.; Wignall, G.D.; Glish, G.L.; Porter, M.D.; Evans, N.D.; Murray, R.W; *Langmuir* **1998**, *14*, 17.

Chapter 5

Insulator to metallic Transition in Disordered Quantum Dot Superstructures of Au, Ag and Cu*

This chapter deals with the insulating to metallic transition (IMT) in disordered superstructures. The transition from insulating to metallic behavior is observed at low temperatures for protected nanocluster arrays of Cu, Ag and Au. The disappearance of Kubo gap at low temperature in these systems, where the inter-particle spacing (0.5-1 nm) is less compared to the nanocluster dimensions (6-12 nm), is explained to effect the transition due to strongly coupled charge fluctuations and cluster vibrations.

*Publications based on this chapter have appeared in **Appl. Phys. Lett.** *79*, 689-691 (2001). and **Appl. Surf. Sci.** *182*, 338-344 (2001).

5.1 INTRODUCTION

In recent years there has been a large effort to understand the structure and properties of metallic quantum dots.[1-3] The individual and collective electronic properties of both bare as well as protected nanoclusters have been investigated with respect to size/carrier confinement and several important devices for molecular electronics such as Single Electron Transistors (SET) have been developed.[3] The confinement of electronic wave function causes discreteness of energy levels and more importantly, the average spacing of successive quantum levels (Kubo gap, δ) can be controlled to make a system metallic or nonmetallic. Since δ is given by $4E_f/3n$, where E_f is the Fermi energy of bulk metal and n is the number of valence electrons in the nanoclusters, a change in 'n' by size tuning can lead to the control of δ compared to the value of thermal energy. For example, δ can vary with r^{-3} for spherical particles, as their density of states is proportional to volume. The low temperature behavior of these systems will be more interesting as the spacing δ may become larger than k_BT, and the life time, τ of the electronic states will be much larger than $\hbar/\delta$, thus making the system insulating. At the same time, disorder in the monolayer can create localization and this can be responsible for the temperature dependence as explained by Variable Range Hopping (VRH) theory.[4] The temperature dependence of the conductivity in disordered insulating systems below percolation threshold can be described by a simple Arrehnius-type formula implying activated charge transport, $\rho = \rho_o \exp(-E_a/RT)$, where ρ_o is a constant and E_a is the electrostatic activation energy for charge transport; But as T_c reaches, it fits to Motts VRH[4] conduction rule described by the equation $\rho(T) \propto \exp(-T_o/T)^{\varphi}$, where φ describes the dimensionality of the system and $kT_o=18\alpha^3/N(E)$, so $\xi=1/\alpha$ is localization length. This modified distance gives hopping distance comparable to the lattice spacing.

A few theoretical attempts have been made earlier to study the electronic structure of monolayer protected clusters (MPCs) in the simultaneous presence of interaction and disorder.[5-7] When there is large interparticle separation (D>2r), the clusters behave like a Mott insulator with a Coulomb gap described by the charging energies of individual nanoparticle sites. On the other hand when the distance between the adjacent clusters is very small (D<<2r) compared to their size, strong quantum mechanical exchange coupling can cause the disappearance of Coulomb gap, causing insulator-to-metal transition (IMT) (Fig 5.1).[4-8] Since the charging energy scales inversely with particle size, the IMT is experimentally easier to observe in superlattices composed of the larger clusters. This is to be contrasted with transition metal oxides, where IMT is normally accomplished by the variation of charge carrier density through altering the composition using substitution chemistry.

In chapters 3 and 4 we have demonstrated two methods of organization of nanoclusters on functionalized Au (111) surface with the emphasis on the role played by the organic molecule interconnects. In this chapter we demonstrate a reversible, IMT in capped nanoclusters of Cu, Ag and Au using the temperature dependent electrical resistivity measurement. We find that the low temperature properties appear to be determined by Coulomb blockade effects, where, in order to tunnel onto the cluster, electrons should overcome the cluster charging energy, [$E_c = e^2/2C(r)$, where C is the capacitance of the individual cluster], with an integral number of electrons on it, in contrast to the previous experiments on various transition metal oxide systems. Although several theoretical suggestions and preliminary experimental data have been made recently about inter-linked nanoclusters using organic molecules as model systems to study Mott-Hubbard IMT[9,10], this is the first such direct experimental evidence based on low temperature resistivity measurements.

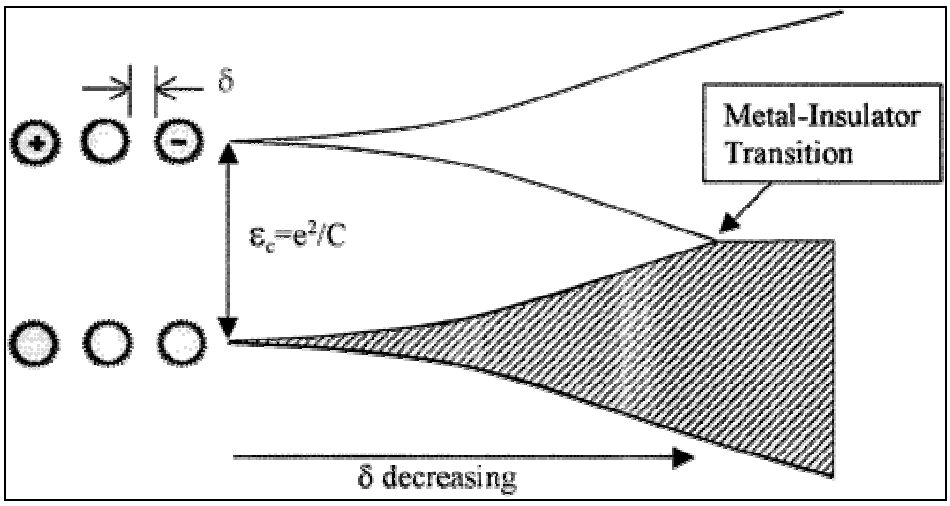

Figure 5.1 Representation of the effects of interparticle separation distance on the electronic structure of the QD superlattice. The energy to separate a positive and a negative charge barrier is the width of the Coulomb gap for a single particle, and is equal to e^2/C. As interparticle separation is reduced, exchange interactions lead to the development of energy bands, and eventually the formation of a metallic solid.[8]

5.2 EXPERIMENTAL

5.2.1 Materials

Chloroauric acid, silver nitrate, copper chloride, sodium borohydrate, 1-dodecane thiol, tridecyl amine, and lauric acid (99.9%; Aldrich make) were used as received. All other reagents for the experimental wok were obtained from standard sources and were used without further purification.

5.2.2 Cluster Synthesis and Low-temperature Conductivity Measurement

Copper, silver and gold capped nanoclusters were synthesised using modified Brust synthesis route.[11] In brief, the respective metallic salts were dissolved in mM concentration in deionised water and the capping agent (dodecane thiol, lauric acid or tridecyl amine) was taken separately in toluene in 1:2 ratio. After vigorous stirring for 30 minutes, this biphasic mixture was reduced slowly by dropwise addition of aqueous 0.1 M $NaBH_4$ solution. The stirring was continued till the transfer of metallic ions to nonaqueous layer was complete. The layer was separated and dried under N_2 atmosphere at 50-60^oC.

The particle size was determined using UV-Vis absorption maximum to be ranging from 8 to 12 nm and was confirmed by High Resolution Transmission Electron Microscopy (HRTEM). The average spacing between the clusters was found to be 0.65±0.05 nm. The electrical resistivity measurements were performed between the temperatures 300 and 8 K under vacuum better than 10^{-5} torr (APD Cryogenic System) on the pellets (8 mm x 2 mm) of the dried powder (Figure 5.2, Scheme I) collected after several experiments performed under identical condition, using the standard four-probe method (Fig. 5.2 (i)) using compressed He. All the experiments were repeated several times with different nanocluster samples prepared and stored under identical conditions using gold and silver contacts and the probes were kept equidistant. Some more experiments were performed using thin films of the clusters on Au(111) surfaces. Fig. 5.2(ii) indicates a layout for the charge transport mechanism in disordered Q-dot superstructure. The charge transfer is phonon assisted when the distance between the clusters is very less as compared to the cluster size. Fig. 5.2(iii) indicates the equivalent circuit diagram from top view for the first layer of the solid.

The toluene solutions of the copper, silver and gold particles were concentrated under reduced pressure using rotary evaporator which yielded a black, yellowish and brownish solids respectively which was repeatedly washed with ethanol and filtered to remove uncoordinated capping molecules in the powder. The resulting powder could be readily dissolved in different organic solvents such as chloroform, carbon tetrachloride, benzene, and so forth without any apparent change in the particle size distribution, and these solutions were characterized using UV-vis spectroscopy measurements carried out on a Hewlett-Packard 8452A diode array spectrophotometer at a resolution of 2 nm. All experimental data were corrected for toluene background absorption.

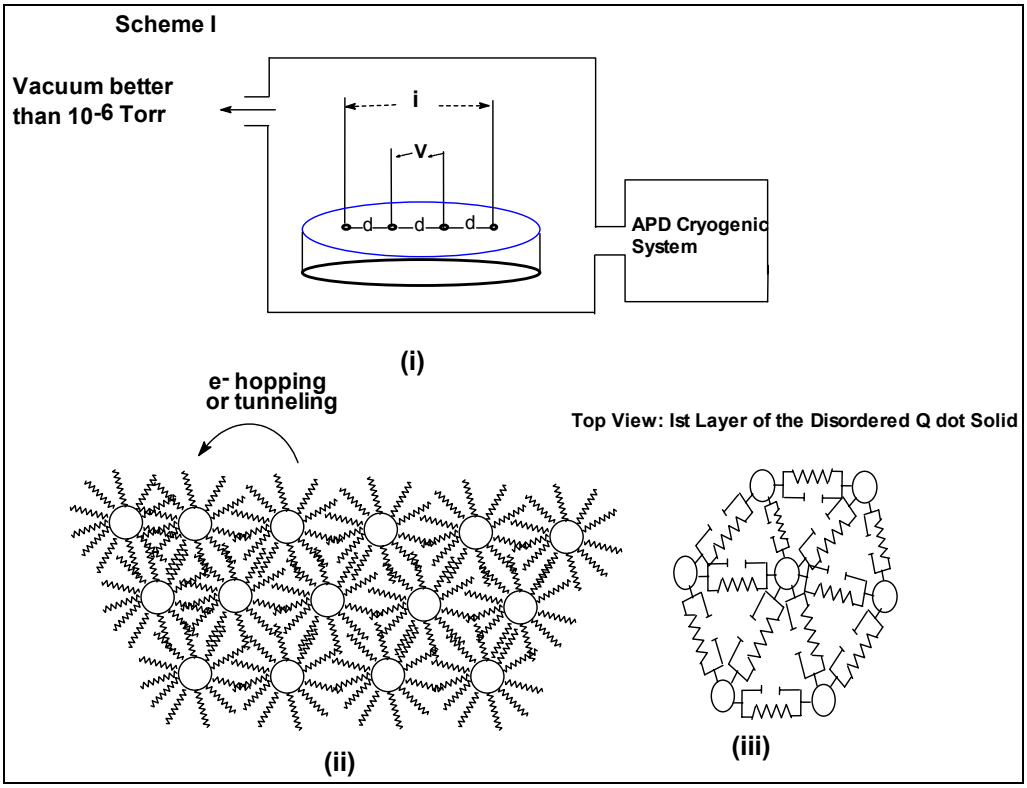

Figure 5.2 (Scheme I) (i) Schematic representation for the four-probe conductivity measurement performed at vacuum better than 10^{-6} torr. The current 'i' is supplied across outer two probes and voltage V is measured across the inner two probes. (ii) A portion of the superstructure formed indicating the tunneling of the electron at low temperature. (iii) Equivalent circuit diagram of the first layer of the superstructure (Top view).

5.2.3 Transmission Electron Microscopy (TEM)

The TEM experiments were performed on a Philips CM200 FEG microscope equipped with a field emission gun with an accelerating voltage of 120 kV. The magnification was 389000x and the coefficient of spherical aberration was 1.35 mm. The images were digitized in sizes of 256 x 256 pixels with a pixel size of 0.03994 nm. Atomically resolved images were thus possible. Images were stored in a computer after digitization and further processed. Power spectra were calculated so that structural analysis such as interplanar distances, angle between planes could be determined. A drop of liquid containing nanoparticles was placed on an amorphous carbon film (3nm thick), deposited on a commercial copper grid for electron microscope. After the liquid

evaporated the grid was introduced in the electron microscope and images as well as power spectra were recorded.

5.3 PROPERTIES OF Q-DOT SUPERSTRUCTURES OF Au, Ag AND Cu

5.3.1 Uv-vis spectroscopy of capped Au, Ag and Cu Sols

Nanosized particles exhibit unique optical properties with an exponential-decay (Mie scattering profile) with decreasing photon energy. Some transition-metal nanoparticles also show a distinct surface-plasmon band. For instance, nanosized Cu particles typically exhibit a surface-plasmon peak at around 566 nm.[12] Figure 5.3 (a) shows the absorption spectrum of freshly prepared Cu nanoparticles protected with dodecanethiol monolayers. For freshly prepared Cu sample small plasmon absorption is clearly visible at 569 nm with a small shoulder in the visible range. According to Pileni et al,[13a,b] the surface plasmon band appearing around 570 nm indicates the particle size is larger than 4 nm. Gold clusters show a surface plasmon band at 521 nm (Fig. 5.3b) indicating large particle formation,[14a] which is indicative of our TEM results. The origin of the surface plasmon band and its width properties follow theoretically predicted behavior,[14b] and agree well with the previously reported results for similar systems. For thiol capped Ag nanoclusters, the characteristic surface plasmon band around 440 nm is observed similar to the reported results for silver nanoclusters using several other preparation conditions.[14c] The broadening of the spectrum arises due to the smaller size of the particles than the mean free path of the electron (>52 nm for silver). A rough estimation of the particle size on the basis of the available optical absorption for silver nanocluster indicates the average size of 12 nm.[14c] This is in excellent agreement with the below mentioned results of TEM.

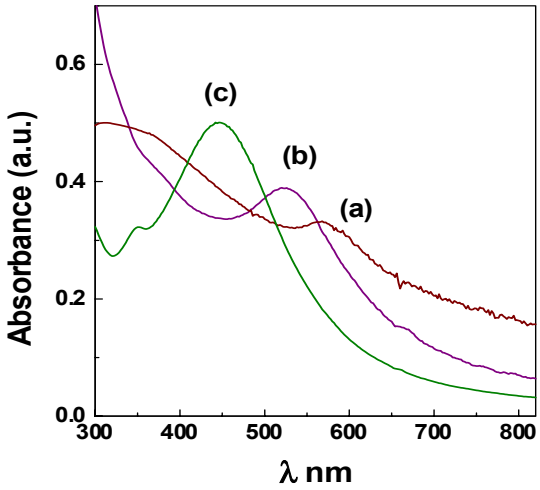

Figure 5.3 Superimposed optical absorption spectra of freshly prepared (a) Cu, (b) Au and (c) Ag nanoparticles protected with capping agents of 1-dodecanethiol in toluene medium.

Fig. 5.4 shows the superimposed optical absorption spectra of Cu nanoclusters protected with capping agents of tridecyl amine (a) and lauric acid (b) in toluene medium. Both the spectra display only a featureless Mie scattering around 570 nm with the surface plasmon peak at very short wavelength, i.e., approx. 289 nm for different capped clusters suggesting the presence of very small separated Cu clusters (< 4 nm in size). This might be, at least in part, attributed to the small particle size (<2 nm), as the surface-plasmon peak is known to be broadened and depressed with decreasing particle size.[15] Balogh and Tomalia have earlier reported[15b] such short wavelength plasmon for Cu nanoclusters, in contradiction to Pileni et al[13] suggesting that the surface plasmon band should appear around 570 nm, if the particle size is larger than 4 nm. Interestingly, dodecane thiol protected clusters (Fig. 5.3a) show a sharp intense plasmon peak while lauric acid capped clusters show the lower wavelength peak perhaps originating due to the extent of delocalization caused by size variation. Also, for lauric acid capped nanoclusters the decrease in the absorbance indicates the decrease in the copper particle quantity revealing the possibility of oxide formation with time on the copper particle surface.[16] Other than the Cu clusters only capping agent and reducing agents were present in the solvent and therefore we believe that

the plasmon band due to Cu clusters in the solvent is the primary reason[13]. Another additional feature, prominent in these short wavelength plasmon peaks is the presence of a shoulder at lower wavelength arising due the flocculation of the Cu clusters after dispersion in the solvent.

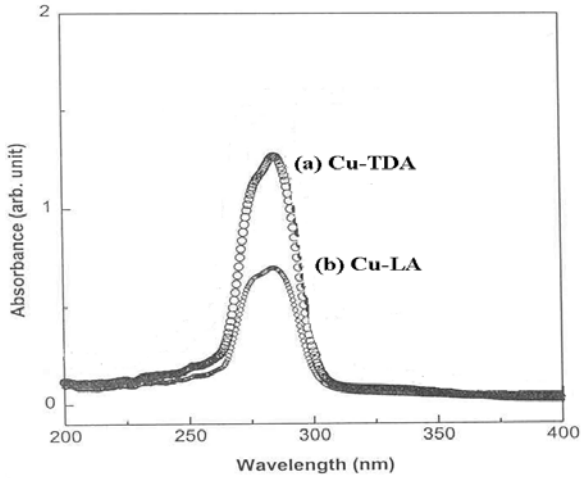

Figure 5.4 Superimposed optical absorption spectra of Cu nanoparticles protected with capping agents of (a) tridecylamine and (b) lauric acid in toluene medium.

5.3.2 High Resolution Transmission Electron Microscopy

TEM images of all samples after drying and redispersing in toluene are shown in Fig. 5.5 in lower resolution mode. From the TE micrographs, it is clear that most of the gold particles are spheroid in shape and they are in the size regime of *approx.* 7-12 nm (Fig 5.5a). The histogram for the particle size distribution shows uniformity. In sharp contrast to dodecanethiol capped copper clusters, gold nanoclusters are found to be smaller, attributed to the strong Au-SH interaction; the particle size distribution gives about 8 nm (Standard Deviation = 10%) size and interestingly the short distance between the clusters could be explained using the interaction of nonpolar part of the capping molecule (Fig. 5.5b). The well-defined crystalline structure is already shown in

the previous chapter which corresponds to fcc lattice with a= 4.074Å (section 4.3.1). The particle size is controlled by increasing the Au:thiol ratio to 1:2.

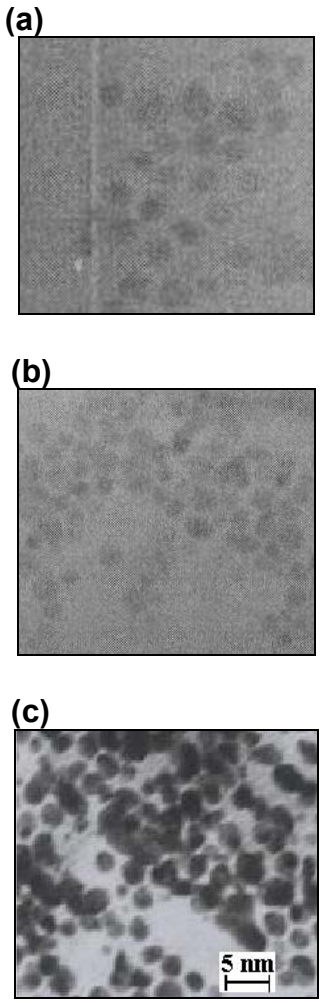

Figure 5.5 TEM images of dodecanethiolcapped (a) copper, (b) gold and (c) silver nanoparticles after drying and redispersing in toluene. The magnification bar is similar for all nanoparticles. The films were drop-casted from the toluene solutions onto carbon-coated "Formvar" films on Cu-grids.

In comparison, the Ag clusters show good agglomerates of size around 12 nm at lower resolution but with a faceting (Fig. 5.5c). The present analysis indicates that the size of silver clusters prepared via the two-phase synthesis should be comparable to that of silver clusters prepared via other preparation

routes[14c] confirming the UV-vis results. Nonetheless, comparing the mean and median values, the particles prepared via the two methods seem to be more homogeneously distributed than those prepared via the earlier method.[14c] In fact, Heath et al[17] reported recently that dodecanethiol-derivatized Ag nanocrystals exhibited a quite broad size distribution when they were prepared by a two-phase liquid/liquid method.

Fig. 5.6 shows the high-resolution TEM images for dodecane thiol (a), tridecyl amine (b) and lauric acid (c) capped copper clusters illustrating the crystallinity of all the samples; the faceting in the grain is also seen clearly. In addition to these well-dispersed particles (Fig. 5.5a), TEM measurements also show the presence of various very large (>15 nm) particles of irregular shape, some of which exhibit very well-defined faceted morphology (Figure 5.6a). The chain-like features of nearby particles are due to the formation of nanoparticle bilayer structures where the top layer sits at the 2-fold saddle sites between neighbouring particles.[18] In the close-up of the clusters, parallel lines with the interplanar spacing of 2.82 Å can be seen, corresponding to the lateral projection of (111) planes of Cu_2O; also the interplanar spacing for LA capped nanoclusters is found to be 2.4 Å. On the contrary, tridecyl amine capped nanoclusters show spacing of 1.08 Å, indicating the possibility of compression in the lattice. This lateral fringe is seen uniformly over the entire interior of the clusters.

These studies confirm the assignment to the cubic phase and enable us to ascertain the particle size distribution. Most of the clusters are cubic in nature and reveals that half of the particle is decahedrally oriented along the 5-fold axis. For tridecyl amine capped clusters (Fig. 5.6b) cubic morphology is evident. While in the case of Cu-LA capped clusters, the fcc nature is more prominent with hexagonal faceting. Previously in reverse micelle microreactors, Pileni et al[13] observed the formation of copper nanoparticles of varied shapes

but with the majority being either spherical or cylindrical, which was partly interpreted by the varied shapes of the micellar support. This is in contrast to the present observations where the surface morphological evolutions occurred in air without apparent matrix support.

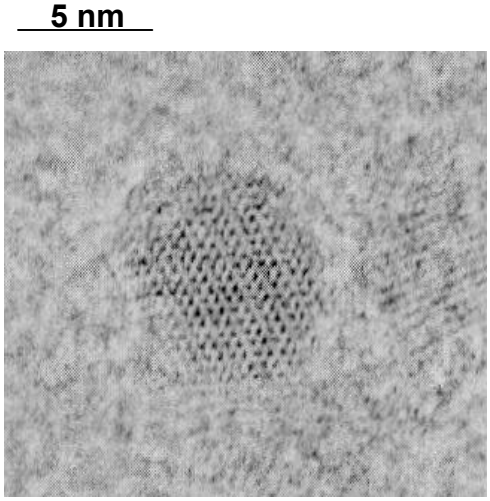

Figure 5.6a The high resolution TEM image for dodecanethiol capped copper nanoparticles after dispersing the toluene solution on a copper grid coated with carbon.

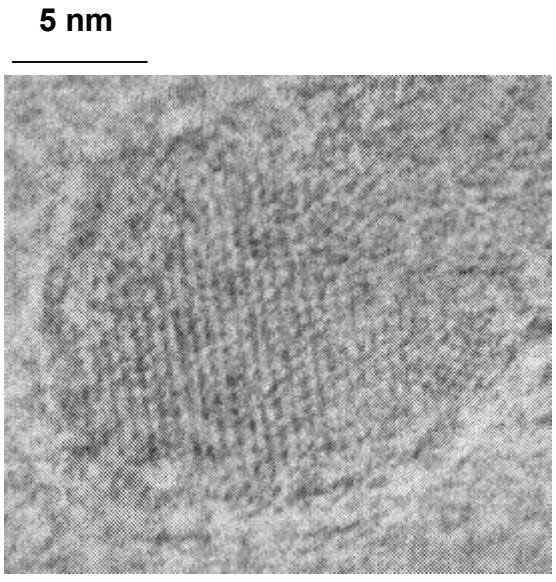

Figure 5.6b The high resolution TEM image for tridecylamine capped copper nanoparticles after dispersing from toluene on a copper grid coated with carbon.

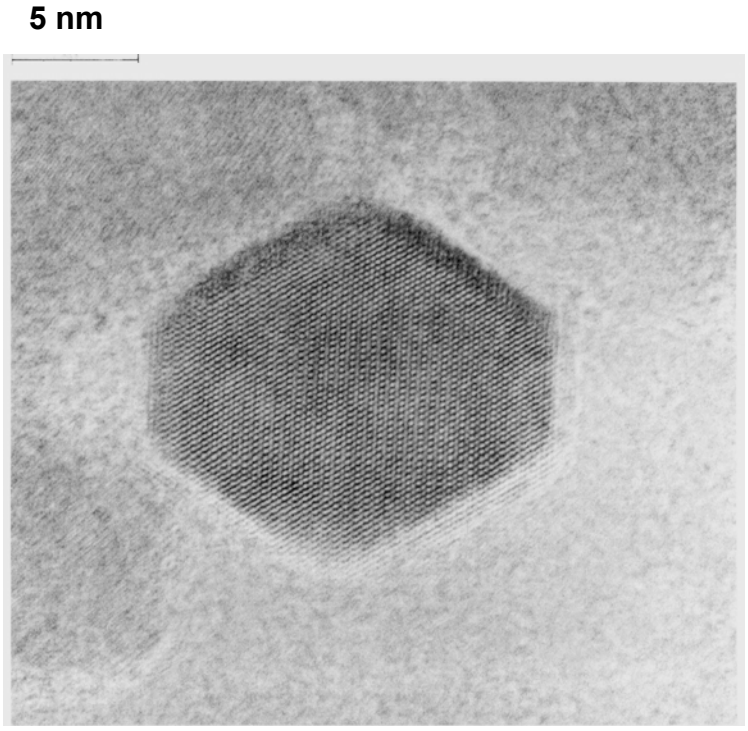

Figure 5.6c The high resolution TEM image for lauric acid capped copper nanoparticles after dispersing from toluene on copper grid coated with carbon. The magnification bar is similar for all nanoparticles.

5.3.3 Low-temperature Conductivity Measurement

The key to the control of capped nanocluster behavior is the selection of the functional group as well as the length of the capping agent. Electron diffraction patterns[19] of alkane thiolates on Au(111) show that the symmetry of the 'S' atom is hexagonal with an area per molecule of 0.214 nm^2. More significantly, the low conductivity of alkane thiolate monolayers make them excellent nanoscale insulators and dielectrics.[20] Finally, the use of this approach will enable us to easily control the spacing (2 to 10 nm) between clusters by varying the length of the surface passivating or monolayer forming molecule. We have selected thiol capped nanoclusters based on these reasons

and the available experimental evidence of monoelectron conduction, manifested as coulomb staircase phenomena.[21]

Figure 5.7 shows the comparison of the temperature dependence of resistivity (ρ) for similar sized dodecane thiol capped copper (a), gold (b) and silver (c) clusters, their room temperature (300 K) ρ values being 1.5, 3.5 and 12 MΩ cm, respectively. Particularly interesting is the temperature independence ($d\rho/dT=0.015$ Ωcm/K), characteristic of weak electron-phonon coupling, shown for Ag and Au nanoclusters. As the temperature decreases all show metallic behavior although the transition temperature (T_c) varies significantly. For example, Cu cluster shows an insulating to metal transition at 272 K, while for Au and Ag nanoclusters the T_c shifts to 200 K and 180 K respectively. This variation of T_c (Cu>Au>Ag) cannot be explained on the basis of compactness and defects on the capping layer as the insulating nature and capping efficiency decreases in the order Au>Ag>Cu, for similar sized protected clusters. Nevertheless, a gradual decrease in the resistivity in copper nanoclusters prior to the transition suggests a fast ordering in the monolayers, perhaps arising from the fragility of the defects in the organic layer on the copper surface. In comparison, the Au clusters show a steady temperature independent value upto 190 K with a sharp transition at 200 K, suggesting a relatively compact and ordered monolayer. Interestingly, the Ag clusters show a shoulder before the transition, which can be considered as a first order transition owing to the disordered state of the Ag MPCs.

The exact origin of this phenomena for Ag clusters is yet to be investigated. The above variation in the T_c for similar sized clusters may be correlated to the Kubo gap through the Fermi energy of the respective metals. Assuming that the similar size gives rise to same n values, δ should directly change with E_F and this indeed will be reflected in the variation of T_c. This is supported by the fact that the IMT is found to be at 272 K for Cu nanoclusters,

which has the bulk E_F of 7 eV. While for Au and Ag clusters the Fermi energy is of the order of 5.5 eV and IMT is in the range of 180-200 K.

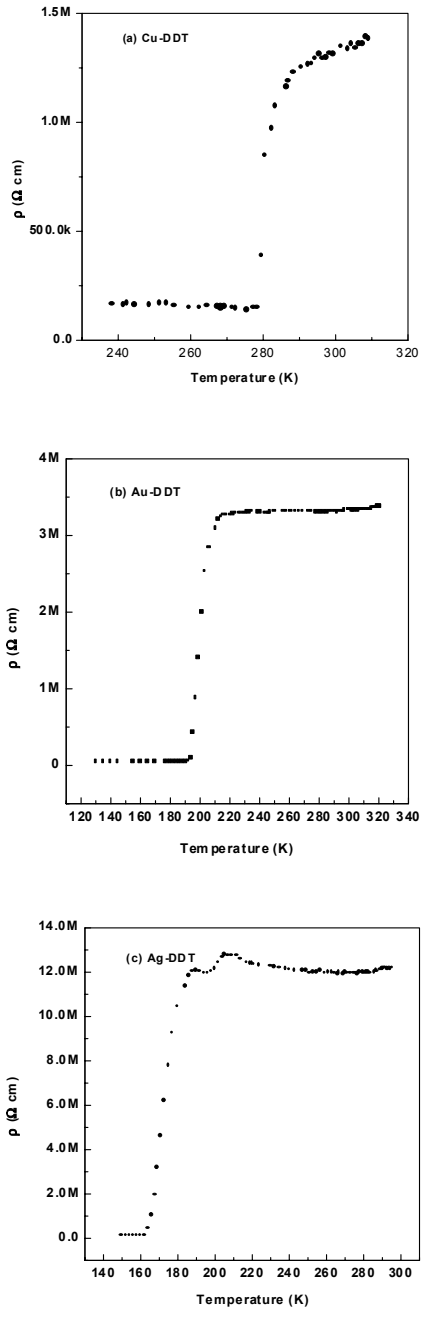

Figure 5.7 Comparison of the temperature dependence of resistivity (ρ) for similar sized dodecanethiol capped copper (a), gold (b) and silver (c) clusters.

Table-I Comparison of calculated Kubo gap, capacitance and charging energy with size for Cu, Ag and Au clusters

Cluster Type	**E_F (eV)**	**Kubo gap $\delta = 4E_F/3n$ (meV)**	**Capacitance[a] C (aF)**	**Charging Energy $E(r) = e^2/2C$ (meV)**	**T_c (K)**
Cu (11 nm)	7.01	1.339	1.82	44	272
Ag (12 nm)	5.5	1.47	1.68	50	180
Au (8 nm)	5.52	1.22	0.488	164	200

[a]The capacitance is estimated considering the nanoparticles as a model sphere with a thin dielectric shell using the equation $C=4\pi\varepsilon_o\varepsilon_r rR/R-[r(1-\varepsilon_r)]$, with the help of a geometric model and taking $\varepsilon_r=3$

An approximate calculation of 'δ' based on the experimentally determined sizes of the clusters (Table - I) shows that it is of the order of about 2 meV and $k_BT>\delta$ even at room temperature (k_BT = 25 meV). For bigger clusters having about 10^3 atoms, E_c can be calculated as follows. Assuming the clusters as 'spheres with a thin dielectric shell', C (r) can be obtained with the help of equation, $C=4\pi\varepsilon_o\varepsilon_r rR/R-[r(1-\varepsilon_r)]$, using known value of ε_r, r and R (where R = r + length of the organic molecule). Taking ε_r as 3 (justified on the basis of experimentally measured values of 2.8-3.1 for hydrocarbon chain lengths having 10-14 carbon atoms[22]), C can be of the order of 2 aF. E_c varies between 50-150 meV which is 5 times less than that of the particles of the 3 nm size showing E_c of the order of 0.3 eV[8], there will be an easier path (very low Kubo gap) for the transfer of electron and hence the state will be metallic. This confirms the prediction of Henrichs et al[10] that bigger particles will be easily accessible for the metallic transition at low temperature. The experimentally observed values of D/2r for all these clusters are in excellent agreement with the earlier predictions of the Anderson transition to a delocalized electronic phase when $D/2r<1.4$.[23]

One of the crucial aspect of all the above clusters is that they have 10-15 nm size and are interlinked by the fragile organic thiol molecules where the length of the molecule is significantly small as compared to r. The precise location of the nanoclusters cannot be fixed due to the orientational and conformational flexibility of the organic matrix and also due to the elastic moduli of the matrix, reported to be 3 orders of magnitude lower than that of normal solids.[22] According to Gorelik et al[24], these type of nanoclusters can vibrate with a typical frequencies of 10^{10} to 10^{11} Hz and when we compare this with the normal RC time constants of these clusters (RC=10^{-10}-10^{-11} s, where C is the capacitance of the metallic cluster which is of the order of 10^{-18}-10^{-19}F.) this means that charge fluctuation and cluster vibrations becomes strongly coupled in such systems. This can be controlled by changing the organic molecule (both length as well as the functionality) and hence we have selected three different capping agents for a representative example of Cu clusters (Figure 5.8).

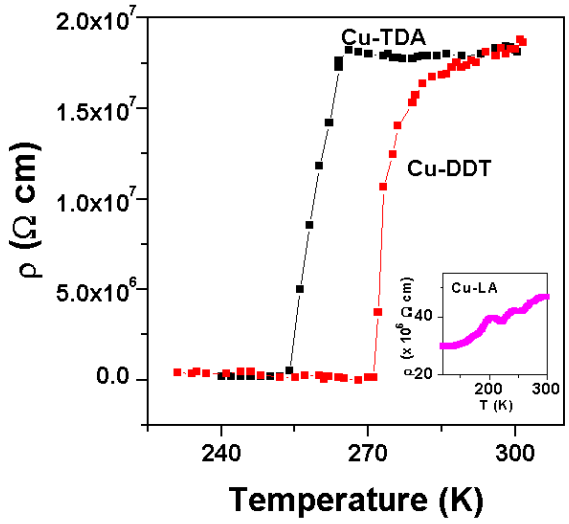

Figure 5.8 Superimposed resistivity vs. Temperature (K) plot for copper clusters with different capping agents. Cu-LA indicates copper clusters capped with lauric acid, Cu-DDT indicates dodecanethiol capped copper clusters and Cu-TDA indicates the tridecyl amine capped clusters.

The resistivity curve for Cu-DDT shows a gradual decrease upto the transition temperature (272 K). The ρ observed for Cu-DDT is of the order of 2 M Ωcm revealing an insulating nature of this monolayers. At 272 K, ρ decreases sharply and the array goes to the metallic state with typical ρ value of 20 Ωcm. Perhaps, as temperature decreases the hopping of the electron enhances the conductivity in these organically capped nanoclusters. In comparison, the resistivity of TDA capped clusters show a transition at 255K while LA capped clusters show a gradual decrease in ρ and remains in the MΩ range upto 25K indicating the ordering of monolayers. Although all the molecules have about 1.9 nm length,[25] this behavior may result from changes in the orientations of the organic molecule, which can alter the extent of disorder and hence the coupling of the clusters.

5.4 CONCLUSIONS

In conclusion, our experimental data provides strong evidence for reversible insulator to metal transition in MPCs when the inter-particle separation is much smaller than the size of clusters. The disorder due to the size and shape of the Q dots and the orientational changes of the organic molecule is used to correlate the variation in the conductivity with temperature. The gold nanoclusters show better results as compared to Ag and Cu clusters because of the limited stability at ambient condition. For example, the silver cluster solution with organic thiol capping, after few weeks show Ag_2S impurity while Cu lauric acid solution shows contamination with copper oxide. Further detailed experiments on the electrical behavior of these clusters as a function of size is essential after eliminating these impurities.

5.5 REFERENCES

1. Templeton, A.C.; Wuelfing, W.P.; Murray, R.W. *Acc. Chem. Res.* **2000**, *33*, 27.
2. Xia, Y.; Gates, B.; Yin, Y.; Lu, Y. *Adv. Mater.* **2000**, *12(10)*, 693.
3. Collier, C.P.; Saykally, R.J.; Shiang, J.J.; Henrichs, S.E.; Heath, J.R. *Science* **1997**, *277*, 1978.
4. Mott, N.F.; Davis, E.A. *Electronic Processes in Noncrystalline Materials*, Clarendon Press: Oxford, UK, 1971.
5. Remacle, F.; Levine, R. *J. Amer. Chem. Soc.* **2000**, *122,* 4084.
6. Lambe, J.; Jaklevic, R.C. *Phy. Rev. Lett.* **1969**, *22*, 1371.
7. Cavicchi, R.E.; Silsbee, R.H. *Phy. Rev. B* **1988**, *37*, 706.
8. Shiang, J.J.; Heath, J.R.; Collier, C.P.; Saykally, R.J.; *J. Phys. Chem. B* **1998**, *102*, 3425.
9. Hubbard, J. *Proc. R. Soc.* **1963**, *276*, 238.
10. Henrichs, S.; Collier, C.P.; Saykally, R.J.; Shen, Y.; Heath, J.R. *J. Amer. Chem. Soc.* **2000**, *122(17)*, 4077.
11. Brust, M.; Walker, M.; Bethell, D.; Schiffrin, D.J.; Whyman, R.; *J. Chem. Soc. Chem. Commun.***1994***,* 801.
12. Creighton, J. A.; Eadon, D. G. *J. Chem. Soc., Faraday Trans.* **1991**, *87*, 3881.
13. (a) Tanori, J.; Pileni, M.P. *Langmuir* **1997**, *13*, 639. (b) Petit, C.; Lixon, P.; Pileni, M.P. *J. Phys. Chem. B* **1993**, *97*, 12974. (c) Pileni, M. P.; Gulik-Krzywicki, T.; Tanori, J.; Filankembo, A.; Dedieu, J. C. *Langmuir* **1998**, *14*, 7359.
14. (a) Brust, M.; Bethell, D.; Kiely, C.J.; Schiffrin, D.J. *Langmuir* **1998**, *14(19)*, 5426. (b) Link, S.; El-Sayed, M.A. *J. Phys. Chem. B* **1999**, *10*, 8410. (c) Henglein, A. *Acc. Chem. Res.* **1993**, *97*, 5457.
15. (a) Bohren, C. F.; Huffman, D. R. *Absorption and Scattering of Light by Small Particles*; John Wiley & Sons: New York, 1983. (b) Balogh, L.; Tomalia, D.A. *J. Am. Chem. Soc.* **1998**, *120*, 7355.

16. Salkar, R.A.; Jeevanandam, P.; Kataby, G.; Aruna, S.T.; Koltypin, Y.; Palchik, O.; Gedanken, A. *J. Phys. Chem. B* **2000**, *104*, 893.
17. Heath, J. R.; Knobler, C. M.; Leff, D. V. *J. Phys. Chem. B* **1997**, *101*, 189.
18. Chen, S.; Sommers, J.M. *J. Phys. Chem. B* **2001**, *105 (37)*, 8816.
19. Rampi, M.A.; Schueller, O.J.A.; Whitesides, G.M. *Appl. Phys. Lett.* **1998**, *72*, 1781.
20. Haag, R.; Rampi, M.A.; Holmlin, R.E.; Whitesides, G.M. *J. Amer. Chem. Soc.* **1999**, *121*, 7895.
21. Rao, C.N.R.; Kulkarni, G.U.; Thomas, P.J.; Edwards, P.E. *Chem. Soc. Rev.* **2000**, *29*, 27.
22. Polymeropoulos, E.E.; Sagiv, J. *J. Chem. Phy.* **1978**, *69(5)*, 1836.
23. Remacle, F.; Collier, C.P.; Heath, J.R.; Levine, R.D. *Chem. Phy. Lett.* **1998**, *291*, 453.
24. Gorelik, L.Y.; Isacsson, A.; Voinova, M.V.; Kasemo, B.; Shekhter, R.I.; Johnson, M. *Phy. Rev. Lett.* **1998**, *80(20)*, 4526.
25. The chain length of dodecanethiol ($CH_3(CH_2)_{11}SH$) and tridecylamine [$CH_3(CH_2)_{12}NH_2$] are 18.74 Å and 19.93 Å respectively. Although Lauric acid [$CH_3(CH_2)_{10}COOH$] also has 18.24 Å, the presence of oxygen in the carboxyl group may allow the oxide formation on the cluster surface.

Chapter 6

Conclusions and Future Prospects

This last chapter deals with the significant conclusions of the present study of nanocluster organization. It also outlines several general limitations of such chemically synthesized organized assemblies along with suggestions for the improvement of chemical stability and size dispersion. Finally the future prospects for next 5-10 years is presented within a broad perspective, keeping in view of the plethora of fundamental and technological interest shown by physicists, chemists, biologists, electronic engineers etc., in these classes of hybrid materials.

The recent progress in the development of new methods for the organization of nanoparticles has been phenomenal in achieving the desired characteristics as revealed in this study and also by several other reports.[1-3] Self-assembled monolayer formation has proven to be the origin and the backbone of the synthesis of several unique classes of hybrid materials with promising potential in nanoelectronics. In particular, SAM of bifunctional molecules are very effective for organizing clusters at room temperature as demonstrated using various ω-terminated organic molecules. As molecular interconnects, their flexibility to tune chainlength and terminal functional group play crucial roles for the ordered superstructure formation and most of the size and shape dependent properties of clusters, useful for several electronic components are not adversely affected by these organic molecules.

Although there are well-established methods to get the nanoparticles and organized structures, in most cases their stability is not adequate.[4] In this regard, we focused our attention on the covalent assembly of stable Ag nanoparticle array on Au (111) modified with pentanedithiol and octancedithiol monolayers. Highly ordered silver nanocluster array formation was confirmed using various scanning probe microscopic techniques and also by the longitudinal periodicity observed in the low angle X-ray diffraction pattern. In contrast to only blocking behavior of SAMs, the superlattice exhibits interesting electrochemical properties in terms of redox accessibility. Miniband formation observed through PL studies confirms the quantum well type of behavior in this assembly.

Subsequently, we were the first to demonstrate that even hydrophobic interactions could be used to organize Au nanoclusters with controllable cluster-cluster spacing. Since hydrophobic interaction provides a major unifying concept in understanding the structure and functions of several biological systems, this remarkable way of cluster organization may help to design the nanocluster arrays for biomolecular electronics. The hydrophobic method to

achieve well ordered and close-packed arrays were studied for electron transfer process which demonstrate clear Coulomb blockade effect with larger band gaps for clusters passivated with longer chain molecules while nonlinearity decreases for passivating organic molecule having aromatic nature. A systematic study of the electrical behavior of these organized clusters shows reversible insulator to metal transition at low temperature when the inter-particle separation is much smaller than the size of clusters. The disorder due to the size and shape of the quantum dots and the orientational changes of the organic molecule is used to correlate the variation in the conductivity with temperature.

All our studies indicate that the construction of three-dimensional superstructures with nanoparticles and organic molecules is possible with high degree of order and precision. These structures may become the ultimate candidates for communication in artificially created biological systems using nanotechnology. Due to their tunable size, unique properties and interlinking capability, they seem to be promising candidates to replace several facets of current technology. More attention is needed to synthesize new functional materials apart from selected metallic and semiconducting clusters (Au, Ag, CdS, CdSe, ZnS, PbS etc.), as there is a long way to go.

In addition to the synthetic routes for surface modification, several key questions and challenges must be addressed, even though steady progress has been observed during the last decade. For the nanocluster organization to be used as building blocks to design electrical and optical properties, more accurate control is needed. Specific attention is required in many areas like:

1) Assembling nanoclusters into symmetrically and spatially well defined arrays to control the electromagnetic interaction between the particles in the array.

2) Establishing reliable, good electrical contacts with nanoclusters which can be individually addressed.
3) Understanding the surface chemistry of nanoparticle/organic molecule interface. This is especially significant because surface bound molecules affect the optical and electrical properties of nanoclusters which can be favorably used for potential applications.
4) Since these clusters have limited thermal stability, fundamental studies towards improving their stability in air and solution are urgently needed. Kinetics control using solvent, mixed monolayers, change of ionic strength and temperature is essential to get the exact size, morphology and shape of nanoparticles.
5) The role of matrix in encapsulated nanoclusters is still unclear which severely affects the electrical/optical properties of these nanoclusters and their arrays.

6) The relative stability of different structural phases is altered in nm regime, affected by both thermodynamic and kinetic features. Variations may arise from many reasons including surface energies, absence of defects or electronic quantum size effects. There is an immediate need to know more about the thermodynamic and kinetic phases of nanostructures.

New discoveries are expected and needed in studies of single molecule nanoparticle interfaces for nanoassembly. Apart from the assemblies and utilization, the synthesis is an area where research will be focused to get precisely well controlled pure materials, because many properties of nanostructures depends on obtaining precise building blocks, means of creating and analyzing purity. Large scale synthesis will also be a prerequisite otherwise the area will be limited to very few applications. There is great opportunity in next decade that all these synthesis and techniques would be integrated with biological applications at interface. Specific biomolecule guided assemblies using DNA, proteins etc. along with size and shape tuned clusters

would be useful for drug delivery, gene therapy and immuno therapy using suitable biosensors. Diverse nanoparticle assemblies with tailored optical/electromagnetic response in the infrared and submillimeter-wave spectral regions would be designed and fabricated. Thin-film device structures with passive or active control of electromagnetic properties in any region of choice from the visible to the millimeter-wavelength might be developed. Fabrication of an array-based all-optical device would be possible based on surface enhanced Raman response. The electronic properties of assemblies, such as applied field response, interparticle interactions and collective effects could be theoretically investigated.

Apart from the reduction in size, the reduction in cost and energy consumption is going to put a great impact on environment and society. This will enable us to make several fascinating nano electronic circuitry and components for specific applications. Several fundamental scientific issues like electron transfer, exciton diffusion and plasmon coupling etc. would be solved which would help to design nano devices accordingly. Some of the most important applications, which will be revolutionized, would be sensors, optical devices, biomedical drug delivery in the area of healthcare, climate control and energy storage in devices. Thus it is hoped that the next 10-15 years may see unprecedented change in nanotechnology affecting directly our day-to-day life due to several innovative biomedical and electronic devices.

REFERNCES

1. Huynh, U.; Dittmer, J. J.; Alivisatos, A. P. *Science* **2002**, *295*, 2425.
2. (a) Wuelfing, W. P.; Murray, R. W. *J. Phys. Chem. B* **2002**, *106(12)*, 3139. (b) Hicks, J. F.; Young, S.; Murray, R.W. *Langmuir* **2002**, *18(6)*, 2288. (c) Huang, Tao; Murray, R. W. *J. Phys. Chem. B* **2001**, *105(50)*, 12498.
3. (a) Sun, S.; Anders, S.; Hamann, H. F.; Thiele, J.U.; Baglin, J. E. E.; Thomson, T.; Fullerton, E. E.; Murray, C. B.; Terris, B. D. *J. Am. Chem. Soc.* **2000**, *124(12)*, 2884. (b) Murray, C. B.; Sun, S.; Doyle, H.; Betley, T. *MRS Bulletin* **2001**, *26(12)*, 985.
4. Paulini, Ralph; Frankamp, Benjamin L.; Rotello, Vincent M. *Langmuir* **2002**, *18(6)*, 2368.

LIST OF PUBLICATIONS

1) Self assembled monolayers and their Applications, K. Vijayamohanan and **M. Aslam**, *Appl. Biochem. & Biotech.* 96/1-3, 25-39 (2001).

2) Comparative Behavior of Aromatic Disulfides and Diselenide monolayers on Ploycrystalline Gold films using Cyclic Voltammetry, STM and QCM, **M. Aslam**, K. Bandyopadhyay, I.S. Mulla and K. Vijayamohanan, *J. Colloid and Interf. Sc.* 234, 410-417 (2001).

3) Mechanism of Zirconia Formation on Bare and Functionalized Gold Surface at Room Temperature. **M. Aslam**, Sushama Pethkar, I.S. Mulla and K. Vijayamohanan, *J. Mater. Chem.* 14(7), 1737 (2000).

4) Hydrophobic Organization of Monolayer Protected Au Clusters on Thiol Functionalized Au(111) Surface, **M. Aslam**, I.S. Mulla and K. Vijayamohanan, *Langmuir* 17, 7487 (2001).

5) Insulator-Metal Transition in Coulomb blockade Nanostructures, **M. Aslam**, I.S. Mulla and K. Vijayamohana, *App. Phy. Lett.* 79(2), 689, (2001).

6) Preparation and Characterisation of silver quantum dot superlattice using sequential self-assembled monolayers of pentane dithiol, Sushama Pethkar, **M. Aslam**, I.S. Mulla and K. Vijayamohanan, *J. Mater. Chem* 11**,** 1710 (2001).

7) Preparation and Electrical Characterisation of Dodecanethiol Monolayer Protected Silver Nanoclusters, **M. Aslam**, N. K. Chaki, I.S. Mulla and K. Vijayamohanan, *Appl. Surf. Sci.* 182(3-4), 338-344 (2001).

8) Formation of Cu and Cu_2O Nanoclusters by the variation of the Surface Ligand: Preparation, Structure and Insulating to Metallic Transition, **M. Aslam**, I.S. Mulla and K. Vijayamohana, *J. Colloid Interf. Sci.* (in press).

9) Application of self-assembled monolayers in materials chemistry, N.K. Chaki, **M. Aslam**, J. Sharma and K. Vijayamohanan, *Proc. Chem. Sci.* 113 (5/6), 1-12 (2001).

10) Device Application of Self-assembled monolayers and Monolayer-Protected Nanoclusters, **M. Aslam**, N. Chaki, J. Sharma, I.S. Mulla and K. Vijayamohanan, *Curr. Appl. Phys.* (2002).

11) Multilayered Ag nanocluster arrays using sequential self-assembly of dithiol molecular interconnects on Au (111) surface, **M. Aslam**, I.S. Mulla, A.B. Mandale, K. Vijayamohanan, submitted to *Colloids and Surfaces A*.

12) Electrical behavior of Hydrophobically Organized Q-dot arrays: Effect of Chain length and Molecular structure of the Passivating Organic Molecule, **M. Aslam**, I.S. Mulla and K. Vijayamohanan submitted to *J. Appl. Phys.*

13) New Evidence for the lateral Motion of Monolayer Protected Nanoclusters on functionalized HOPG Surfaces, **M. Aslam**, I.S. Mulla and K. Vijayamohanan submitted to *J. Phys. Chem. B.*

14) Soluble Au@TiO_2, Au@ZrO_2, Ag@TiO_2, Ag@ZrO_2 core-shell nano articles: one step synthesis, characterization, spectroscopy and optical limiting properties, Renjis T. Tom, A. Sreekumaran Nair, Navinder Singh, **M. Aslam**, C. L. Nagendra, Reji Philip, K. Vijayamohanan, T. Pradeep, submitted to *Chem. Mater.*

15) Guided Assembly, properties, and applications of organized nanoclusters on self-assembled monolayers K. Vijayamohanan, **M. Aslam** and G. Ramanath, *Chem. Mater.* (*Invited Review*)